

41 0628753 6



ProQuest Number: 10183432

All rights reserved

INFORMATION TO ALL USERS

The quality of this reproduction is dependent upon the quality of the copy submitted.

In the unlikely event that the author did not send a complete manuscript and there are missing pages, these will be noted. Also, if material had to be removed, a note will indicate the deletion.



ProQuest 10183432

Published by ProQuest LLC (2017). Copyright of the Dissertation is held by the Author.

All rights reserved.

This work is protected against unauthorized copying under Title 17, United States Code
Microform Edition © ProQuest LLC.

ProQuest LLC.
789 East Eisenhower Parkway
P.O. Box 1346
Ann Arbor, MI 48106 – 1346

Biomimetic Routes to Nanoscale-Toughened Oxide
Ceramics

Olivier Deschaume

A thesis in partial fulfilment of the
requirements of The Nottingham Trent University
for the degree of Doctor of Philosophy

16th October 2006

333014

THE NOTTINGHAM TRENT UNIVERSITY LLR	
SHARE LOAN	PH.D/BNS/CG
	DES

Acknowledgements

I would like to address special thanks to my supervisor, Professor Carole C. Perry, for the opportunity to carry on this project, support, advice and endless patience in improving my writing.

I also would like to thank Dr. Kirill Shafran for his insightful comments and for his help and guidance throughout this project.

I am much indebted to members of the Inorganic Chemistry Research Group, Drs. David Belton, Heather Currie, David Eglin, Siddharth Patwardhan, Neil Shirtcliffe, and Simon Thompson as well as Ms Agathe Fournier, Mr Paul Roach and Mr Graham Tilburey for their support and help. I am also grateful to all technical staff at the Nottingham Trent University Chemistry, Biomedical and Natural Sciences for their help and support with various equipment and sample characterisation.

Finally, I would like to especially thank my parents and fiancée Marie for their continuous moral support and encouragement throughout the years.

CONTENTS

<i>Part I Literature survey: aluminium aqueous solution speciation and biomimetic approaches to materials science</i>	1
<i>1. Aluminium speciation in aqueous solutions</i>	2
1.1 Hydrolysis and condensation of metal cations	2
1.1.1 Properties of water as a solvent	2
1.1.2 Hydration of ions and the structure of solutions	6
1.1.3 Acid-base properties of ions in aqueous solution	7
1.1.4 Model of the acid-base behavior of cations	8
1.1.5 Mechanism and kinetics of hydroxylation	10
1.1.6 Condensation and precipitation in aqueous solution	11
1.2 Aluminium hydrolysis and condensation: aluminium polycations	15
1.2.1 The core-link model	17
1.2.2 The cage-like model	18
1.3 Aluminium hydroxides and oxides	24
1.3.1 Formation of the zero-charge precursor	25
1.3.2 Nucleation	26
1.3.3 Growth	28
1.3.4 Ageing	31
<i>2. Interaction of aluminium with biomolecules</i>	40
2.1 Interaction of aluminium polycations with biomolecules	40
2.2 Aluminium ion interactions with aminoacids	41
2.3 Absorption of aluminium by the human body	42
2.4 Effects of aluminium on human and plant physiology	43

3. <i>The biomimetic approach</i>	46
<i>Part II Materials and methods</i>	62
4. <i>Solution state and colloidal characterisation techniques</i>	63
4.1 Potentiometric techniques	63
4.1.1 Definition of potentiometry	63
4.1.2 Potentiometric equipment and single-point measurement pro- cedures	64
4.1.3 Potentiometric titrations. Principles and instrumentation . . .	65
4.1.4 Uses of potentiometric techniques in the present work	67
4.1.5 Potentiometric titrations for standardisation of stock solutions of acids and alkalis	67
4.1.6 Single-batch potentiometric titration setup	68
4.1.7 Time-resolved potentiometric titrations	68
4.1.8 Multi-batch titrations	69
4.1.9 The ion exchange experiments	69
4.2 UV-Vis spectroscopy	74
4.2.1 Principles and instrumentation of UV-Vis spectroscopy	74
4.2.2 Measurement of protein concentration	75
4.2.3 Aluminium quantification and speciation	76
4.3 ²⁷ Al NMR spectroscopy	84
4.3.1 Operational techniques	84
4.3.2 Phase correction	85
4.3.3 Missing intensity	86
4.3.4 Quantification and referencing	87
4.3.5 The Spectroscopic parameters of aluminium-27	88
4.3.6 Analytical procedures	92
4.4 Photon correlation spectroscopy	92
4.4.1 Principles and instrumentation of dynamic light scattering . .	93
4.4.2 Standard operating procedures	99

4.4.3	Dynamic light scattering in Al hydroxide suspensions and Al- elastin systems	100
4.4.4	Dynamic light scattering and zeta potential measurements in Al-BSA systems	100
4.5	Conductometry	101
4.5.1	Principles and equipment	101
4.5.2	Experimental procedure	102
4.6	Viscosity measurements	102
4.6.1	Viscosity definition	102
4.6.2	Methods of viscosity measurement	103
4.6.3	Viscosity measurement using the SV-10	104
5.	<i>Solid state characterisation techniques</i>	106
5.1	Powder X-ray diffraction	106
5.1.1	Principles and instrumentation of PXRD	106
5.1.2	Preparation and measurement of the solid samples for PXRD	108
5.2	Thermogravimetric Analysis	109
5.2.1	Design features	109
5.2.2	Data presentation	110
5.2.3	Effects of experimental environment	110
5.2.4	The thermal behavior of aluminium compounds	112
5.3	Electron Microscopy	115
5.3.1	Introduction	115
5.3.2	Microscope characteristics	116
5.3.3	Electrons versus light	118
5.3.4	Transmission Electron Microscopy	118
5.3.5	Scanning Electron Microscopy	124
6.	<i>Data fitting techniques: The least squares minimisation</i>	132
6.1	The objective function	132
6.2	The weighted normal equations method	134
6.3	Resolution of the normal equations	135

6.4	The linear approximation to a non-linear system	137
6.5	Non-linear refinement	140
 <i>Part III Results and discussion</i>		148
7.	<i>Preparation of high purity aluminium systems by static anion exchange</i> . .	149
7.1	Multi-batch experiment on Al ion hydrolysis	149
7.1.1	the choice of conditions	149
7.2	Target synthesis of the Al ₁₃ -mer	156
7.3	Target synthesis of Al ₃₀	159
7.4	Synthesis of Al hydroxide nanoparticles with tuneable sizes	161
7.5	Concluding remarks	163
8.	<i>Conditions of large polycations formation: an NMR study</i>	167
8.1	²⁷ Al NMR treatment algorithms	167
8.1.1	The local integration algorithm	167
8.1.2	Automatic treatment algorithm	169
8.2	Application of Automated ²⁷ Al NMR treatment to kinetic studies . .	175
8.2.1	Preparation of initial samples	175
8.2.2	The kinetic study	177
8.3	Conclusion	190
9.	<i>Preparation of monodisperse Al hydroxides</i>	194
9.1	Introduction	194
9.2	Results and discussion: for low degree of neutralisation	195
9.3	The case of more extensive neutralisation	201
9.4	Conclusions	206
10.	<i>Destabilisation of Al species: Effect of BSA and soluble elastin, resulting materials</i>	208
10.1	Al-BSA systems	208
10.1.1	Physical properties and pH of the Al-BSA solutions	208
10.1.2	Dynamic light scattering	210

10.1.3	Residual concentrations of BSA and aluminium ions	213
10.1.4	Re-dissolution experiments and ^{27}Al solution NMR	215
10.1.5	TGA measurements	218
10.1.6	Results of powder X-ray diffraction	220
10.1.7	SEM observations	222
10.2	Al-Elastin systems	224
10.2.1	Physical properties and pH of the Al-Elastin solutions	224
10.2.2	Dynamic light scattering	225
10.2.3	Residual concentrations of elastin and aluminium after cen- trifugation	227
10.2.4	^{27}Al solution NMR	228
10.2.5	SEM observations	230
10.3	Conclusions of Al-protein interactions study	233
10.3.1	Al-BSA interactions	234
10.3.2	Al-elastin interactions	238
 <i>Part IV Conclusions and further work</i>		 241
 <i>Appendix</i>		 252

LIST OF FIGURES

1.1	Energy diagram and representation of Water Molecular orbitals.	3
1.2	Charge-pH diagram for metal cations in solution.	8
1.3	The most frequent types of hydroxo bridges.	14
1.4	Species predicted by the core-links model [37].	17
1.5	The structure of aluminium dimer, and its polyhedral representation drawn from crystallographic data obtained by Johansson et al. [57].	18
1.6	The structure of aluminium trimer, and its polyhedral representation.	19
1.7	The mechanism of Al ₁₃ -mer formation, inspired from [25].	20
1.8	The polyhedral view of the flat Al ₁₃ -mer characterised by Seichter et al. [64].	21
1.9	Polyhedral view of the different Baker-Figgis isomers of the Al ₁₃ -mer Keggin-type ion characterised by means of single-crystal XRD. α drawn from Baur [70], δ from the Na-capped Al ₁₃ -mer characterised by Nazar [71](also present in Al ₃₀ -mer structure) and ϵ from the data of Johansson [72].	22
1.10	Polyhedral representation of the Al ₃₀ -mer characterised simultaneously by Nazar [71]and Allouche [69].	24
1.11	Al ₃₀ -mer formation mechanism suggested by Allouche, involving the formation of the δ -Al ₁₃ isomer by 'capping' of an ϵ -Al ₁₃ molecule [69]	24
1.12	Charge-electronegativity diagram showing five classes of behavior for the zero-charge metal ion species. In domains I and V, the element remains monomeric and soluble. In domain II and IV, elements condense respectively by olation or oxolation, whereas both mechanisms can occur in field III [25].	25
1.13	Change (a) in the number and sizes of particles formed in solution and (b) in the concentration C of the soluble precursor of the solid phase during precipitation [25].	26

1.14	A: Variation in the free enthalpy of formation of nuclei as a function of the number of precursor molecules n , (a) $S < 1$, (b) and (c) $S_c > S_b > 1$. B: Nucleation rate n and growth rate c as a function of the precursor concentration. The labeled zones correspond to those in Figure 1.13 [25].	27
1.15	Left: Surface nucleation with (a) two-dimensional growth of the nuclei or (b) spiral growth around defect. Right: Predominant growth mechanisms as a function of precursor concentration [25].	31
1.16	Possible reaction mechanisms for the formation of gibbsite or bayerite during evolution of an amorphous gel at $\text{pH} < 5$ and $\text{pH} > 8$ [25].	37
3.1	Different strategies of the nanotectonic approach to materials synthesis [159].	47
3.2	SEM picture of the ordered structure of nacre (mother-of-pearl) giving rise to unique mechanical properties [160, 161].	47
3.3	Different explanations of the mechanical properties of nacre: (A) the presence of proteins holding the material together [162] and (B,C) the presence of microstructure giving rise to a higher energy dispersion during deformation [163].	48
4.1	A classical UV-Vis spectrometer arrangement.	75
4.2	The ferron molecule and scheme of a typical $[\text{Al}] = f(t)$ curve after mixing of Al solution with ferron, from which speciation information can be obtained.	77
4.3	Acid digestion monitored over time by means of ferron assay	78
4.4	The ferron data treatment optimisation algorithm	82
4.5	A full FT system.	85
4.6	The autocorrelation function (logarithmically spaced channels)	96
4.7	Functional block diagram of the N4Plus DLS instrument [71].	97
4.8	The SV-10 Vibro viscometer.	105
5.1	Cross-section of the JEOL 2010 transmission electron microscope used during this project.	120
5.2	Schematic representation of: The scanning electron microscope principle (left hand side) and the origin of the signal obtained in a SEM experiment.	126

- 5.3 Cross-section of the JEOL JSM 840A column. 128
- 7.1 The pH of the suspensions of anion exchange resin as a function of time elapsed after AlCl_3 solution addition (A). Examples of the first derivative curves calculated from the original pH data (B). 151
- 7.2 Conductivity (A) and chloride ion concentration (B) monitored during the ion exchange synthesis of a sample with $h=2.6$ upon anion exchange process. 152
- 7.3 (A) Evolution of hydrolysis ratio and (B) of the difference actual-theoretical h ratio as a function of the theoretical h . Actual h calculated from $\text{Cl}^-/\text{Al}^{3+}$ ions concentration measurements. 153
- 7.4 ^{27}Al NMR peak areas from different solutions prepared by dilution of a 0.2M Al_{13} -mer solution validating the ability to carry out quantitative speciation determination. The peak areas have been determined also for solutions diluted with pH 4 (pH of the initial solution) HCl solution, and did show any major differences. 154
- 7.5 ^{27}Al NMR spectra of the samples prepared using static anion exchange (A) and speciation diagram (B) derived from the quantification of ^{27}Al NMR spectra and ferron assay (Ref.= aluminate standard). 155
- 7.6 (A) Evolution of pH and conductivity, as well as (B) Al speciation as determined from a ferron kinetic assay over the synthesis of a high purity Al_{13} -mer by means of ion exchange. 157
- 7.7 Materials resulting from the classical drying of the Al_{13} solution in a 50ml tube (left), and on an hydrophobic surface synthesised from MTEOS(right). 157
- 7.8 PXRD patterns of the freeze-dried $h=2.45$ sample (a), and the major lines of the PXRD pattern of Al_{13} sulfate salt [21](b). 158
- 7.9 ^{27}Al solution NMR spectra (A) of the initial (1) and re-dissolved (2) sample at $h=2.5$; ^{27}Al NMR spectra (B) obtained on an Al_{13} solution before (a) and after (b) the second ion exchange step. 158
- 7.10 ^{27}Al solution NMR spectra of the Al_{13} solutions aged for 42h at 85°C (A) and the dynamic diagram of Al speciation (B) (Ref.= aluminate standard). 160

7.11	Al speciation determined by means of ferron kinetic assay as a function of time in the Al_{13} solutions aged for 42h at 85°C.	160
7.12	The ^{27}Al solution NMR spectrum of the as-prepared Al hydroxide ($h \approx 3.0$) (A) and the dynamic particle size distribution of the Al hydroxide suspensions as measured with DLS aged for 200h 25°C(B).	161
7.13	(A) TEM image of a 200nm hydroxide particle sol obtained by means of ion exchange followed by accelerated aging at 60°C, and normal light images of the bottom of 15ml sample tubes containing (B) Stöber silica and (C) the Al hydroxide mimic of opal.	163
7.14	The results of the implementation of the anion exchange technique for the synthesis of Al species model systems [25].	164
8.1	our local integration algorithm	168
8.2	Example of the use of an exponential window function.	170
8.3	Spectrum obtained after FFT of apodised FID trace, and the iterative phasing algorithm implemented.	171
8.4	Evolution of the minimum of the spectral window considered as a function of variation step for the four phasing process iterations, and spectrum obtained after phasing.	172
8.5	^{27}Al NMR spectrum of a sample containing Al monomer, Al_{13} and Al_{30} -mer prior to phasing, and the evolution of the minimisation parameter as a function of variation step for the four iterations of our phasing algorithm.	173
8.6	Shape of the peak functions used for the fitting of ^{27}Al NMR spectral features	174
8.7	3D representation of a set of 43 spectra after pre-treatment, and an example of 'fit' taken among this set.	175
8.8	Al speciation monitored by means of ^{27}Al NMR during the synthesis of Al chlorohydrate solutions prior to kinetic study: (A) stacked spectra and (B) Al speciation diagram, both obtained from our automatic treatment technique.	176
8.9	Evolution of hydrolysis ratio over time of exchange as determined from Cl^- and Al^{3+} concentration measurements.	177

- 8.10 Stacked representation of the spectra evolution over Al₃₀-mer production as a function of time at the three different heating temperatures and respective hydrolysis ratios 2.13, 2.37, 2.43 and 2.52. Spectra obtained from automatic treatment. 179
- 8.11 Summary of the Al₃₀-mer production as a function of time, determined from peak-fitting of the peak positioned at 70ppm in NMR spectra acquired at three different temperatures and respective hydrolysis ratios: (a)2.14, (b)2.37, (c)2.43, (d)2.52. 180
- 8.12 Arrhenius plots for the Al₁₃-Al₃₀-mer conversion with different initial h. . 181
- 8.13 Summary of the evolution of Al concentration corresponding the 10ppm peak attributed to part of octahedrally coordinated Al in Al₃₀-mer, for different temperatures and respective hydrolysis ratios: (a)2.14 , (b)2.37 , (c)2.43 , (d)2.52. 183
- 8.14 Summary of the Al₁₃-mer concentration evolution as a function of time at three different temperatures and respectively hydrolysis ratio: (a)2.14, (b)2.37, (c)2.43, (d)2.52. 184
- 8.15 Summary of the 'capped'-Al₁₃-mer concentration evolution as a function of time at three different temperatures and respectively hydrolysis ratio: (a)2.14, (b)2.37, (c)2.43, (d)2.52. 186
- 8.16 Evolution of the monomer concentration versus heating time at three different temperatures and respectively hydrolysis ratio: (a)2.14, (b)2.37, (c)2.43, (d)2.52. 187
- 8.17 Evolution of the concentration of small oligomeric Al species (dimers, trimers) versus heating time at three different temperatures and respectively hydrolysis ratio: (a)2.14, (b)2.37, (c)2.43, (d)2.52. 188
- 8.18 Monomer peak position as a function of heating time at three different temperatures and respectively hydrolysis ratio: (a)2.14, (b)2.37, (c)2.43, (d)2.52. 189
- 8.19 Evolution of the AIP₃ species concentration versus heating time at three different temperatures and respectively hydrolysis ratio: (a)2.14, (b)2.37, (c)2.43, (d)2.52. 190

- 9.1 ^{27}Al NMR spectra (A) and derived speciation diagram (B) over ion exchange synthesis of the initial Al hydroxide sol. 196
- 9.2 (A) pH and conductivity of the solution over the ion exchange process, and (B) evolution of the pH on aging the sols at different Al concentrations and temperatures for 60h. 197
- 9.3 (A) Evolution of conductivity and (B) viscosity in the sols during aging at different Al concentrations and temperatures for 60h. 198
- 9.4 Evolution of Al hydroxide particle size after dilution to 0.4, 0.2, and 0.05Mol/L Al over aging of the resulting sols at 25, 40 and 60°C for 60 hours. 199
- 9.5 Evolution of Al speciation as determined from ferron kinetic assay in 0.4 Mol/L Al sols aged at 25, 40 and 60°C for 60 hours. 200
- 9.6 (A) pH and conductivity of the solution over the ion exchange process, and (B) evolution of the pH over aging of the sols at different Al concentrations and temperatures for 60h. 202
- 9.7 Al Speciation monitored by means of ^{27}Al NMR over ion exchange time leading to an Al hydroxide batch virtually free of Al_{13} -mer: (A) Stacked spectra and (B) corresponding speciation diagram from automated spectra treatment. 202
- 9.8 (A) Evolution of conductivity and (B) viscosity in the sols over aging at different Al concentrations and temperatures for 60h. 203
- 9.9 Evolution of Al hydroxide particle size after dilution to 0.4, 0.2, and 0.05Mol/L Al over aging of the resulting sols at 25, 40 and 60°C for 60 hours. 204
- 9.10 Evolution of Al speciation as determined from ferron kinetic assay in 0.4 Mol/L Al sols aged at 25, 40 and 60°C for 60 hours. 205
- 10.1 Conductivity (A), pH (B) and viscosity (C) of Al species-BSA samples prepared with various BSA concentrations. 209

- 10.2 Evolution of mean particle sizes of Al species-BSA samples as a function of BSA concentration measured by DLS at a scattering angle of 90° . (A) Al hydroxide-BSA samples with different Al hydroxide particle sizes, (B) Al hydroxide-BSA samples prepared from 82 nm Al hydroxide with adjusted pH; (C) Al₁₃-mer-BSA and Al₃₀-mer-BSA samples. 211
- 10.3 Zeta potential measurements carried out on (A) Al polycations-BSA systems and (B) 82nm Al hydroxide-BSA. 213
- 10.4 Free BSA concentration (A) and aluminium ion concentration (B) in the supernatant solutions of the Al hydroxide-BSA samples after centrifugation. 214
- 10.5 ²⁷Al solution NMR spectra of the Al₁₃-mer-BSA (A) and Al₃₀-mer-BSA (B) samples as a function of total BSA concentration. T=25°C. The peak at 80ppm arises from internal reference solution of aluminate-ions in D₂O. 216
- 10.6 Quantification of the ²⁷Al solution NMR spectra of the Al₁₃-mer-BSA (A) and Al₃₀-mer-BSA (B) samples as a function of total BSA concentration. T=25°C. 217
- 10.7 Thermogravimetric 'weight loss' curves (A)(normalised against final weight), the first derivative thermogravimetric (DTG) curves (B), an example of the peak fitting used for semi-quantitative analysis of the DTG curves (C), and DTG peak areas as a function of BSA concentration (D). 219
- 10.8 XRD patterns obtained from the Al-BSA materials prepared. (a) Al₁₃-BSA 0 mg/ml; (b) Al₁₃-BSA 25 mg/ml; (c) Al₃₀-BSA 0 mg/ml; (d) Al₃₀-BSA 25 mg/ml; (e) Al hydroxide (d ≈ 26 nm)-BSA 0 mg/ml; (f) Al hydroxide (d ≈ 26 nm)-BSA 25 mg/ml. 221
- 10.9 SEM pictures of Al-BSA hybrid materials prepared by freeze-drying from Al hydroxide and Al polycations with various BSA amounts. 222
- 10.10 Physical Measurements carried out on the Al-Elastin systems. 225
- 10.11 Evolution of average particle size as a function of Elastin concentration in the systems: (a) In the presence of Al hydroxide, (b) In the presence of Al polycations. 226

- 10.12 Residual concentrations observed in the supernatant of samples centrifuged at 13000rpm for 30 min as a function of total elastin concentration (A) Elastin concentration as a percentage of elastin added, measured by a Bradford assay (B) Al concentrations measured by means of ICP. 228
- 10.13 ^{27}Al NMR spectra of (A) Al_{13} -elastin and (B) Al_{30} -elastin samples at 25°C. 229
- 10.14 Al speciation determined by local integration of the ^{27}Al NMR spectra of A Al_{13} -elastin and B Al_{30} -elastin samples. 229
- 10.15 SEM images of the freeze-dried pure Al hydroxide suspension (A-B) centrifuged at 13000rpm for 30min and (C) Without preliminary centrifugation. 231
- 10.16 SEM images of freeze-dried pure elastin solution. 231
- 10.17 SEM images of the freeze-dried Al hydroxide-elastin 20mg/ml sample (A) centrifuged at 13000rpm for 30min and (E) Without preliminary centrifugation; elemental mapping of the same regions using respectively (B-F) $\text{CK}\alpha_{1-2}$, (C-G) $\text{OK}\alpha_1$ and (D-H) $\text{AlK}\alpha_1$ energies. 231
- 10.18 SEM image of the freeze-dried pure Al_{13} -mer sample (A) centrifuged at 13000rpm for 30min and (E) Without preliminary centrifugation; elemental mapping of the same regions using respectively (B-F) $\text{OK}\alpha_1$, (C-G) $\text{AlK}\alpha_1$ and (D-H) $\text{ClK}\alpha_1$ energies. 232
- 10.19(a) SEM image of the Al_{13} -mer-elastin 20mg/ml sample (A) centrifuged at 13000rpm for 30min and (E) Without preliminary centrifugation; elemental mapping of the same regions using respectively (B-F) $\text{OK}\alpha_1$, (C-G) $\text{AlK}\alpha_1$ and (D-H) $\text{ClK}\alpha_1$ energies. 232
- 10.20 SEM image of the pure Al_{30} -mer solid-state sample (A) after centrifugation treatment, (B) without centrifugation; elemental mapping of the region (B) using respectively (C) $\text{OK}\alpha_1$, (D) $\text{AlK}\alpha_1$ and (E) $\text{ClK}\alpha_1$ energies. 233
- 10.21(a) SEM image of the Al_{30} -mer-elastin 20mg/ml sample SEM image of the freeze-dried pure Al_{13} -mer sample (A) centrifuged at 13000rpm for 30min and (E) Without preliminary centrifugation; elemental mapping of the same regions using respectively (B-F) $\text{OK}\alpha_1$, (C-G) $\text{AlK}\alpha_1$ and (D-H) $\text{ClK}\alpha_1$ energies. 234
- 10.22 Schematic representation of the interactions of BSA with various Al species. 237

LIST OF TABLES

- 1.1 Partial charge on the water molecule in the coordination sphere of aluminium as a function of the hydrolysis ratio of the cation. 9
- 8.1 Pre-exponential factor A and activation energy E_a determined on the basis of the different kinetic constant values obtained for Al_{13} - Al_{30} -mer conversion. 181
- 10.1 Evolution of weight loss fractions corresponding to the detected weight loss peaks and residual fraction after heat treatment (expressed as percentages of total sample weight) as a function of the initial BSA content of the sample. 220

ABSTRACT

In this work, a novel anion exchange technique has been developed and optimised in order to prepare extra-pure, hydroxide-free solutions of aluminium polyoxocations (Al_{13} and Al_{30}) as well as for the preparation of nanosized, highly monodisperse aluminium hydroxide particles in the particle size range 20-200nm. In order for the evolution and composition of the resulting systems to be monitored, an array of characterisation techniques including ^{27}Al NMR, dynamic light scattering, potentiometry, conductometry and UV-Vis spectroscopy, have been implemented and complemented with successful data treatment strategies. The quantitative data obtained indicates that the static anion exchange method is a soft, environmentally friendly, low-cost, energy-saving and convenient procedure for the preparation of Al-containing model systems. The Al species obtained can be used for high-precision model studies on Al speciation, and serve as nanosize precursors to a variety of Al-containing materials. The use of these pure Al precursors has a clear advantage in materials synthesis arising from an improved understanding and better control of Al speciation. In a second development of the project, the model systems have been used in a nanotectonic approach to biomimetic materials synthesis, with possible applications to the optimisation of Al-containing materials such as ceramics or composite films. Bearing this aim in mind, the interactions of the prepared aluminium species with the model protein BSA and a bioelastomer, elastin, were monitored and the resulting composite materials characterised. The methodology developed for the synthesis and characterisation of pure Al species and Al species/biomolecule systems is a robust base for further studies spanning research fields such as Chemistry, Biology or Environmental sciences, and possess a large potential for application to industrial products and processes.

Part I

LITERATURE SURVEY: ALUMINIUM AQUEOUS
SOLUTION SPECIATION AND BIOMIMETIC
APPROACHES TO MATERIALS SCIENCE

1. ALUMINIUM SPECIATION IN AQUEOUS SOLUTIONS

1.1 *Hydrolysis and condensation of metal cations*

In order to fully understand the mechanisms and structures underlying the inorganic aspects of the study undertaken during this PhD, this introduction to aluminium speciation in aqueous solution includes general aqueous chemistry concepts and aluminium solution speciation peculiarities. This chapter very logically begins with an introduction to the two principal components of the system, water and metal cations. The interactions of these components in solution will be described and the different possible mechanisms underlying the aqueous speciation of Al^{3+} reviewed.

1.1.1 *Properties of water as a solvent*

Water is a reaction medium and a solvent of choice in the laboratory as well as on an industrial scale. The polarity of the water molecule is responsible for its good solvation power, i.e. its ability to attach itself on to ions as a result of electrical dipolar interactions. Water is also an ionizing liquid, i.e. able to polarize a covalent bond because of its Lewis base (electron donor) character. Its high dielectric constant makes water a dissociating medium because the decrease in electrostatic forces between solvated cations and anions allows their easy dispersion in water (the attractive force F between two charges q and q' separated by a distance r is given by Coulomb's law $F = qq'/4\pi\epsilon_0r^2$).

These properties may be predicted from the electronic structure of water. The symmetry of the water molecule is C_{2v} and its Molecular Orbitals (MOs) can be expressed as linear combinations of the Atomic Orbitals (AOs) of the oxygen atoms (2s, 2p) and of the hydrogen atom (1s) according to the Linear Combinations of Atomic Orbitals (LCAO) method. They exhibit one of the symmetries that cor-

respond to the four irreducible representations of the C_{2v} group (A_1 , A_2 , B_1 , B_2). Theoretical calculations give the following expressions for the four MOs of lowest energy [1]:

$$2a_1 \quad 0.85(2s) + 0.13(2p_z) + 0.81(1s_a + 1s_b), \quad E = -36eV$$

$$1b_2 \quad 0.54(2p_y) + 0.78(1s_a - 1s_b), \quad E = -19eV$$

$$3a_1 \quad 0.46(2s) - 0.83(2p_z) - 0.33(1s_a + 1s_b), \quad E = -14eV$$

$$2b_1 \quad (2p_x), \quad E = -12eV$$

Each of the occupied MOs contains two electrons, whereas the antibonding MOs of higher energy ($4a_1$, $2b_2$) are empty. The high polarity of the water molecule, which explains the solvation of ions, is due to the electronegativity difference between oxygen and hydrogen. The propensity of oxygen to attract the electronic charge is much greater than that of hydrogen. The high coefficients of the oxygen AOs in the expression for the occupied MOs point to the fact that the electron density is shifted towards oxygen [2]. The electronic charge carried by each of the atoms (partial

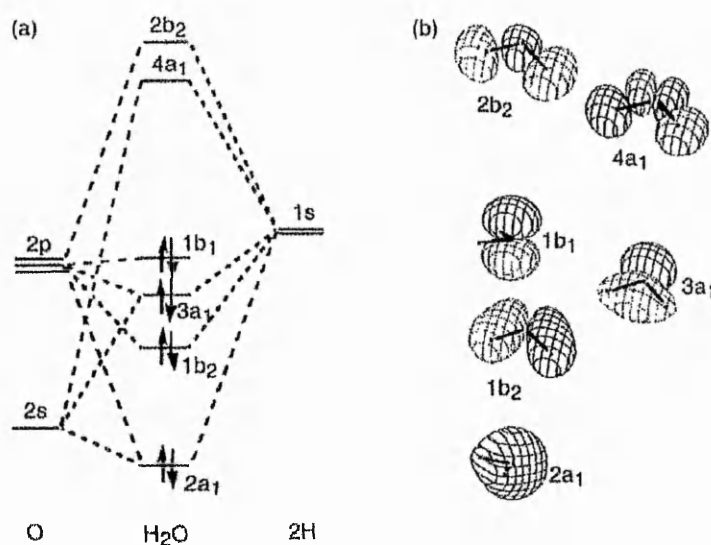


Fig. 1.1: Energy diagram and representation of Water Molecular orbitals.

charge) may be calculated from the expression of MOs given above. The 'partial' charge of an atom in a combination is defined by the total atomic population, which includes its formal charge (degree of oxidation) and half the overlap charge due to

bonds with other atoms, the overlap charge being considered localized on to the atoms [1]. In order to provide a rational explanation of the main chemical processes (hydrolysis, condensation, and complexation) involved in the aqueous chemistry of metal cations, Livage and co-workers developed the 'partial charge model' [3], based on the principle of electronegativity equalization stated by R. T. Sanderson [4] as follows: "when two or more atoms initially different in electronegativity combine, they adjust to the same intermediate electronegativity in the compound". According to L. Pauling electronegativity means the power of an atom in a molecule to attract electrons to itself [5]. Later on, Parr and co-workers showed that the electronegativity χ is related to the electronic chemical potential μ as follows $\chi = -\mu$ [6]. This provides a theoretical basis to Sanderson's assumption. The main consequence is that both the electronegativity χ_x of a given atom X and its partial charge δ_x vary when the atom is chemically combined. These two parameters must be related. A linear relationship is usually assumed as follows:

$$\chi = \chi_x^0 + \eta_x \delta_x \quad (1.1)$$

where η_x is the hardness of atom X as introduced by Pearson [7]. Hardness is related to the softness $\sigma_x = 1/\eta_x$ which provides a measure of the polarizability of the electronic cloud around X [8]. Softness increases with the size of the electronic cloud, i.e. with the radius r of X. Therefore, hardness varies as $1/r$. According to the Allred-Rochow scale, electronegativity is proportional to Z_{eff}/r^2 [9]. Hardness may then be approximated as:

$$\eta = k\sqrt{\chi^0} \quad (1.2)$$

where k is a constant that depends on the electronegativity scale. It can be shown that $k = 1.36$ when Pauling electronegativities are expressed in the frame of Allred-Rochow's model. The total charge 'z' of a given chemical species is equal to the sum of the partial charges of all individual atoms $z = \sum \delta_i$. This together with the previous equations leads to the following expressions for:

$$\text{the mean electronegativity [3]: } \chi = \frac{\sum_i \sqrt{\chi_i^0} + 1.36z}{\sum_i 1/\sqrt{\chi_i^0}} \quad (1.3)$$

$$\text{and the partial charge: } \delta_i = \sigma_i(\chi - \chi_i^0) \quad (1.4)$$

The previous equation can also be written as: $\delta_i = \sigma_i(\chi - \chi_i^0)$ (1.5)

$$\text{where } \sigma_i = (1.36\sqrt{\chi_i^0})^{-1} \quad (1.6)$$

This model was also chosen by Shafran in his PhD work [10] to determine the likelihood of formation of aluminium and zirconium species in water. Although this model is relative and approximate, it does provide a simple estimation of the charges on atoms in a combination. According to equation (1.3), the average electronegativity of the water molecule is

$$\chi = \frac{2\sqrt{\chi_H^*} + \sqrt{\chi_O^*}}{(2/\sqrt{\chi_H^*}) + (1/\sqrt{\chi_O^*})} = 2.49$$

and the partial charges

$$\delta(H) = \frac{\chi - \chi_H^*}{1.36\sqrt{\chi_H^*}} = +0.2 \quad \delta(O) = \frac{\chi - \chi_O^*}{1.36\sqrt{\chi_O^*}} = -0.4$$

However, the size difference between atoms, as well as the dipole moments of free pairs, must also be taken into consideration [11] to determine the molecular dipole moment. The Lewis base character of water is due to the electrons in the $3a_1$ MO. This MO is essentially built on the hybridization of the 2s and $2p_z$ AOs of oxygen. It is strongly delocalized towards the outside of the molecule, as indicated by the high coefficients of the corresponding AOs and their negative contributions in the combination. The water molecule behaves like a donor ligand of a σ pair, which explains its ionizing properties and its aptitude to coordinate Lewis acids (complexing properties). However, the non-bonding b_1 MO entirely localized on oxygen exhibits a very weak π donor character and does not allow the creation of a bond. The physical peculiarities of water such as high boiling and melting points, and fast proton and hydroxyl diffusion can be explained by the existence of hydrogen bonds between water molecules. The ionizing and dissociating power of liquid water leads to the self-dissociation of the molecules:



responsible for its amphoteric properties. The oxonium ion H_3O^+ is a planar or slightly pyramidal molecule. Its solvation by water molecules occurs through hydrogen bonds and creates $[\text{H}_3\text{O} \cdot n\text{H}_2\text{O}]^+$ entities. The structural information obtained using diffraction techniques points to the presence of four water molecules

($n = 4$) in a tetrahedral or pyramidal configuration around H_3O^+ , one of the water molecules interacting very weakly. The solvated proton can therefore be considered as a 'molecular' entity $[\text{H}_9\text{O}_4]^+$, itself solvated by other water molecules through weaker hydrogen bonds. The hydroxyl ion HO^- exists in solution as a 'molecular' entity $[\text{H}_7\text{O}_4]^-$, itself solvated by other water molecules.

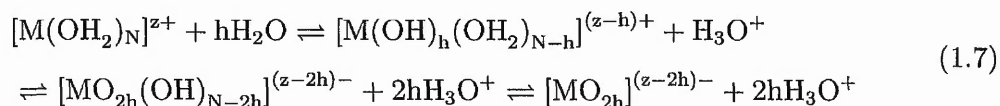
1.1.2 Hydration of ions and the structure of solutions

The attraction and organization of water molecules around ions subjected to dipolar interactions occur over several layers. The number of water molecules contained in these layers, as well as the number of the layers influenced by the presence of the ion increase with its polarizing strength, defined as the z/r^2 ratio. Two main hydration layers, or spheres, are generally accepted, e.g. the first hydration 'sphere', of water molecules in contact with the ion, and the outer and more distant layers. The effect of water on an ionic solid such as an alkali halogen in MX is limited to the simple dispersion of solvated ions as $\text{M}^+ \cdot n\text{H}_2\text{O}$ ($4 < n < 8$) and $\text{X}^- \cdot m\text{H}_2\text{O}$ ($m = 6$) at any pH. Small-size, high-charge cations such as aluminium ($z = 3$, $r = 0.57\text{\AA}$) develop strong electrostatic interactions with water and have a large hydration energy ($-\Delta H^0 = 4700\text{kJ}\cdot\text{Mol}^{-1}$ for Al^{3+}), such that the geometry of the hydrated cations is well defined. Structural investigations [12, 13] point to an octahedral symmetry for $[\text{Al}(\text{OH}_2)_6]^{3+}$. The interactions between the water molecules and Al^{3+} are the result of the σ -donor ligand role of the water molecules, through the overlap of the $3a_1$ MO with the d orbitals of the cation. Hence, the bond exhibits a strong covalent character and the hydrated cations are really coordination complexes. The lability of the water molecule is an important parameter as it strongly influences the kinetics and mechanisms of metal ion speciation. The lability of the water molecule in the first hydration sphere of Al^{3+} is low (exchange rate constant $= 1\text{s}^{-1}$) when compared to other cations. This exchange rate is much faster for water molecules in the second hydration sphere, and complicates the characterisation of this layer. Nevertheless, for the majority of cations, the immediate environment of the solvated ions consists of 12 water molecules. [12, 13].

1.1.3 Acid-base properties of ions in aqueous solution

Acid-base properties of cations in aqueous solution are highly related to hydrolysis and condensation reactions. Hydrolysis reactions are important in chemistry because they determine such behavior as: (1) the solubility of the metal ion (in the absence of other ligands), (2) the species actually present in solution and therefore the interactions with other complexing ligands or with solids, (3) the tendency for coagulation of colloids and other surface phenomena, (4) the oxidizability or reducibility of the metal to other valence states, (5) the transport and deposition of the metal in natural systems and technological applications, and (6) the toxicity of the element to organisms [14].

As seen earlier, the overlap of valence orbitals between the solvated ion and the water molecules allows an electron transfer from the $3a_1$ MO of water to the empty or partially filled d orbitals of the cation. The transfer, and intrinsically the strength of the M–O bond increases with polarizing strength. This electron transfer decreases the electronic density in the bonding $3a_1$ MO and weakens the O–H bond. The ionic character of the O–H bond increases and the positive charge on hydrogen increases. Concurrently, the positive charge on the cation decreases. Coordinated water molecules are stronger acids than water molecules in the solvent itself. They tend to de-protonate according to



These equilibria are known as the hydrolysis equilibria of the cation [15]. They depend on its intrinsic characteristics (formal charge, size, nature of the element), the acidity of the aquo-ion being dependent on the magnitude of the σ transfer. Therefore, a cation may be coordinated to three types of ligands: aquo (H_2O), hydroxo (HO^-) and oxo (O^{2-}) depending on the degree of polarisation of the oxygen atom. The hydrolysis equilibria may be displaced by changing the acidity of the medium. Therefore, it is possible, to a certain extent, to modify the nature of the coordination sphere of the cation. The possible modifications are shown on an experimental diagram indicating which ligand is present as a function of the charge of

the cation and the pH [16, 17]. In the aquo domain, all coordinated water molecules

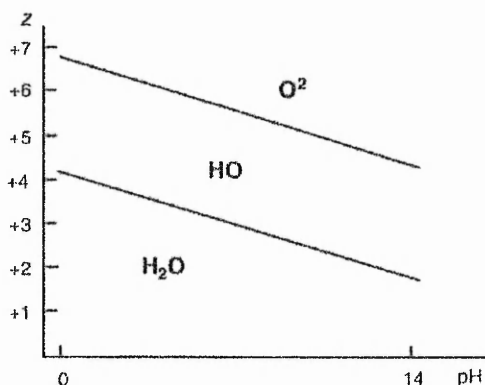


Fig. 1.2: Charge-pH diagram for metal cations in solution.

keep their proton, whereas in the oxo domain, oxygen cannot be protonated. In the hydroxo domain, at least one hydroxo ligand is present within the coordination sphere. Hence, as an element of medium formal charge ($z = 3$) Al^{3+} will polarize oxygen and form aquo- to hydroxo- complexes depending on the domain of acidity considered.

1.1.4 Model of the acid-base behavior of cations

The behavior of cations toward hydrolysis is very well known. It is described by thermodynamic equilibrium constants [15, 18–22] that allow for the calculation of the distribution of species as a function of the pH and the solution concentration. They can be combined with the complexing constants of the cation for any ligand [19]. However, the situation is very complex whenever condensation reactions occur because the relevant species produced are sometimes hypothetical and thermodynamic data becomes rare for polynuclear species. The partial charge model of Henry et al. is a simple quantitative approach to the problem. The problem is to define the nature of the coordination sphere of a cation of charge z and coordination N as a function of the pH of the medium. This is equivalent to calculating the hydrolysis ratio h of this element in the equilibrium:



It is logical to assume that an increase in the charge on the hydrogen of the water molecules coordinated to the cation weakens the O–H bond, resulting in a deprotonation. Using the Sanderson assumption of the equalization of the average electronegativities through a chemical reaction, the deprotonation reaction can be seen as a way to equalize the electronegativities of the hydroxylated complex and water. The following equations allow the determination of the limiting forms of the cations in solution in accordance with this electronegativity equalisation criteria.

At pH = 0, the hydrolysis ratio h of the complex $[M(OH_2)_N]^{z+}$ is given by

$$h = 1.36z - 0.24N - \frac{(2.621 - \chi_M^*)}{\sqrt{\chi_M^*}} \quad (1.8)$$

whereas at pH 14 we obtain

$$h = 1.14z + 0.25N' - \frac{0.836(2.341 - \chi_M^*)}{\sqrt{\chi_M^*}} \quad (1.9)$$

The results from these equations (Table 1.1) are in good agreement with experimental values [15]. One may note that in these equations the acidic nature of a cation is governed by three parameters: the charge z , the size (via the coordination number N) and the electronegativity. The most important factor is the formal charge of the cation. The limits of the existence domain of the aquo-hydroxo

Tab. 1.1: Partial charge on the water molecule in the coordination sphere of aluminium as a function of the hydrolysis ratio of the cation.

	$[Al(OH_2)_6]^{3+}$	$[Al(OH)(OH_2)_5]^{2+}$	$[Al(OH)_2(OH_2)_4]^+$	$[Al(OH)_3(OH_2)_3]$	$[Al(OH)_4(OH_2)_2]^-$
χ	2.754	2.675	2.588	2.487	2.373
δ_{H_2O}	+0.37	+0.26	+0.14	0	-0.16

$[M(OH_2)_{N-1}(OH)]^{(z-1)+}$ and oxo-hydroxo $[MO_{N-1}(OH)]^{(2N-z-l)-}$ forms as a function of z and the pH are easily calculated using $h = 1$ or $h = 2N - 1$ in the general partial charge expression [3]. The experimental pH-charge diagram is easily confirmed.

Generally, cations of formal charge z lower or equal to 4 such as Al^{3+} form aquo-hydroxo complexes $[M(OH)_h(OH_2)_{N-h}]^{(z-h)+}$ in an acid or neutral medium ($h \leq z$).

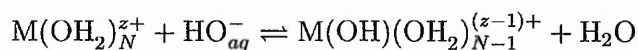
In an alkaline medium, they may exist in hydroxo forms $[M(OH)_x]^{(x-z)-}$.

However, no information regarding the respective amounts of species in solution can be obtained from the partial charge model. In a molecular entity, atoms of similar chemical nature are treated similarly. Consequently, the results are mere estimations that must be used with caution, particularly if structural peculiarities are present, such as the decrease in coordination number of aluminium species in basic medium. This reduction in coordination is explained by the decrease in polarization of the coordinated water with the decrease in overall charge of the complex.

In the zero-charge species, the water molecules carry a near zero partial charge, so it is difficult to say that they act as ligands. These molecules may be considered as belonging to the second hydration sphere. The partial charge of the water molecules in the hexacoordinated Al^{3+} complex of various hydration ratios decreases steadily until it becomes negative (Table 1.1). The latter situation is of course unrealistic because it would mean an electron transfer from the cation to the water molecule. In fact, ^{27}Al NMR spectra do show Al in coordination 4 in an alkaline medium [23], which confirms that, in these conditions, water molecules have lost their nucleophilic character owing to the decrease in the partial charge of the cation.

1.1.5 Mechanism and kinetics of hydroxylation

Owing to the strong lability of water observed for aquo complexes, hydroxylation through neutralization may be treated as a ligand exchange reaction by substitution:



However, the hydrogen bond network in the liquid ensures fast diffusion paths for the proton and the HO^- ion, so that the reaction may also proceed through a direct attack of the aquo ligand by the hydroxyl:



The kinetics of neutralization are extremely fast [15] and diffusion-controlled, which means that the reaction rate is limited only by the approach of the reactants. Hy-

drolysis is, strictly speaking, a neutralization carried out by the water molecule:



For this reaction [15] $\Delta H^0 = (75.2 - 9.6z)\text{kJ}\cdot\text{Mol}^{-1}$, $\Delta S^0 = (-148.4 + 73.1z)\text{J}\cdot\text{Mol}^{-1}$, from which $\Delta G_{298}^0 = (119.5 - 31.35z)\text{kJ}\cdot\text{Mol}^{-1}$. For elements with a charge z smaller than 4, ΔG^0 becomes negative, and the reaction is therefore spontaneous only if the temperature is higher than 298K. Therefore, it is necessary to heat the solution in order to carry out hydrolysis of the cation (forced hydrolysis or thermohydrolysis). This technique has been used in the preparation of particles of narrow size distribution [24]. However neutralization of a solution by addition of a base inevitably leads to local pH gradients, causing inhomogeneities in the hydrolysis products, which condense in an random manner. Often, they lead to amorphous solids and, under such conditions, the particle size is very heterogeneous because of the overlap of nucleation and growth kinetics in the solid phase. Heating of a solution to ca 50-100°C makes it possible, particularly with trivalent elements (Al, Fe, Cr) [24], to carry out hydrolysis homogeneously, in conditions close to thermodynamic equilibrium. Under such conditions, the slow speed of formation of the hydrolyzed precursors allows decoupling of the nucleation and growth steps from a kinetic standpoint. This allows narrow particle size distributions to be formed.

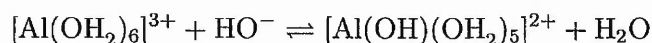
1.1.6 Condensation and precipitation in aqueous solution

The condensation of ions in aqueous solution creates entities in which identical or dissimilar cations are linked through various types of oxygenated bridge like HO^- or O^{2-} . The transition of the ion in solution to the solid comprises complex phenomena that are true inorganic polymerization reactions which must be treated with as much care as organic polymerizations [25]. In mildly acidic solution, the condensation of Al species will lead to discrete and soluble polycations such as Al dimers, trimers, Al_{13} -mer or Al_{30} -mer depending on the degree of condensation. The current opinion concerning the formation and structural peculiarities of aluminium polycations will be explained in more detail in a dedicated section below. For the present, the mechanisms underlying condensation reactions will be summarised.

Mechanism of the condensation reactions

By analogy to organic polymerization processes, one may identify several steps in inorganic condensation processes:

(a) *Initiation* The initiation step corresponds to the production of the first hydroxo-aquo monomers in solution. Let us consider the case of an initiation by addition of a base to an $[\text{Al}(\text{OH}_2)_6]^{3+}$ solution. The result is a first hydrolysis reaction:



As has been seen earlier, this hydroxylation may equally be obtained through thermohydrolysis. The hydroxylated complex is the precursor of the condensation products. The degree of hydrolysis of species taking part in condensation reactions, and therefore the condensation reactions themselves are strongly dependant on the properties of the medium. The nature of the mononuclear species present in solution is highly dependant on parameters such as metal concentration and acidity, as well as the ionic strength of the medium. Therefore the hydrolysis of $[\text{Al}(\text{H}_2\text{O})_6]^{3+}$ (hydrolysis ratio $h=0$) will lead to monomeric aluminium species of hydrolysis ratio $h=1, 2, 3$ and 4 , and respective formulae $[\text{Al}(\text{OH})(\text{H}_2\text{O})_5]^{2+}$, $[\text{Al}(\text{OH})_2(\text{H}_2\text{O})_4]^+$, $[\text{Al}(\text{OH})_3(\text{H}_2\text{O})_3]$, and $[\text{Al}(\text{OH})_4]^-$. The relative proportion of these species can be calculated for given conditions using the available thermodynamic data, well verified for monomeric and few polymeric species, and pH or h -dependant speciation diagrams can be built from the results of these calculations [15, 26, 27].

(b) *Propagation* Once the first hydroxylated species are formed in solution, condensation may take place and leads to oxygenated bridges between cations. In an acidic medium, the maximum cation coordination is always achieved in the aquo-hydroxo monomeric complex, and hence the reaction must proceed though nucleophilic substitution. This reaction may take place via one of three simple mechanisms: dissociation, association and a concerted mechanism or direct displacement [28].

Dissociative substitution is a two-step process involving the formation of a reduced-coordination intermediate. In the second step, the nucleophile completes the cation

coordination.

Associative substitution is also a two-step process, this time involving a high coordination intermediate. The creation of a bond with the nucleophile (first step) occurs prior to the release of the leaving group (second step). From an energy standpoint, this release is favored by the formation of a bond with the entering group in the transition state.

In a concerted or direct displacement mechanism, substitution is a one-step process, in which the leaving group and the nucleophile contribute simultaneously to the formation of the transition state. The formation of the bond with the nucleophile and the breaking of the bond with the leaving group are synchronous. Associative and direct displacement mechanisms are often difficult to distinguish, unless an intermediary compound can be identified directly. These mechanisms are called bimolecular nucleophilic substitutions, or S_N2 , because two partners are required at the transition state. Using the same logic, the dissociative mechanism is referred to as a monomolecular nucleophilic substitution, or S_N1 reaction.

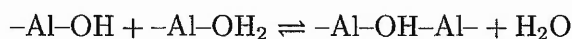
Condensation by substitution requires a charge donor, the nucleophile, which is able to attack the metal cation, which bears a positive charge and is an electron acceptor. The cation must also possess a leaving group. Ligands most easily removable bear a positive charge $\delta+$. In the case of aluminium, the lability of coordination water is low and condensation should proceed via an associative mechanism with temporary formation of a $[H_3O_2]^-$ bridging ligand.

In a non-complexing medium, two types of ligand are likely to exist in the coordination sphere of mononuclear aluminium species: the aquo (H_2O) and hydroxo (OH^-) ligands, whereas oxo (O^{2-}) ligands are observed in the particular case of polynuclear Keggin-type species.

(i) in aquo species such as $[Al(OH_2)_6]^{3+}$, the partial charges on the metal and the aquo ligand are positive [26]: $[Al(OH_2)_6]^{3+}$ $\chi = 2.757$, $\delta(Al) = +0.755$, $\delta(H_2O) = +0.372$. The aquo ligand has no nucleophilic character and may only play a role as a leaving group. Condensation of the aquo species alone does not occur since the water molecule never acts as a nucleophile.

(ii) In the aquo-hydroxo $[Al(OH)_h(OH_2)_{N-h}]^{(z-h)+}$ species, both nucleophile (OH^-)

and leaving (H_2O) groups are present. Usually, the hydroxo ligand bears a negative partial charge and is therefore a nucleophile. The presence of the aquo ligand allows a condensation reaction leading to the formation of hydroxo bridges:



The bridging OH groups formed are called 'ol' in order to distinguish them from terminal hydroxo ligands [29, 30]. The reaction leading to the formation of an hydroxo bridge is called 'olation'. The proton in the ol bridge of the transition state is more acidic than that of terminal hydroxo ligands. In addition to the presence of an hydroxo ligand bearing a negative charge in the cation coordination sphere, the electrophilic character of the cation is an important requirement for nucleophilic attack to take place. Indeed, examples demonstrate that condensation occurs only if the partial charge on the cation in the precursor is equal to or higher than 0.3 (Partial charge calculated from PCM). This empirical value defines the threshold for the onset of condensation, whatever the partial charge on the hydroxo ligand. Therefore, the criteria for condensation in solution are $\delta(\text{OH}) < 0$, $\delta(\text{Al}) > +0.3$. The most frequent hydroxo bridges are presented in Figure 1.3. The hydroxo ligand

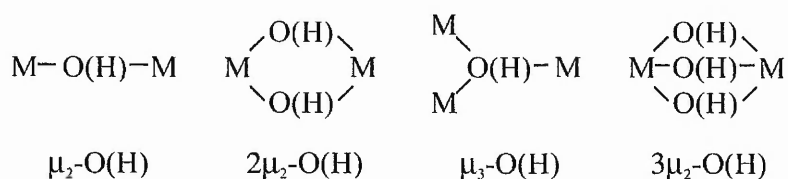


Fig. 1.3: The most frequent types of hydroxo bridges.

is able to form one, two or three bonds through the weakly bonding $3\sigma\text{MOs}$ and the non-bonding π orbitals. In the extreme case of Al_{13} -mers, four oxo ligands take part in $\mu_4\text{-O}$ bridges. The simple $\mu_2\text{-OH}$ bridge corresponds to corner-sharing coordination polyhedra, whereas the $\mu_2\text{-O(H)}$ double bridge corresponds to edge-sharing polyhedra. The $\mu_3\text{-O(H)}$ bridge, which links three polyhedra through single hydroxo or oxo bridges, is often observed. As the number of shared corners grows, the spacing between metal ions diminishes and the electrostatic repulsion becomes increasingly strong.

(c) *Termination* Condensation of hydroxylated and electrically charged complexes always ends at a more or less advanced stage, leaving discrete species in solution. As condensation causes water elimination, the change in composition of the reaction product modifies its average electronegativity, causing charge redistribution within its structure and, therefore, a change in the reactivity of the functional groups. Hence, OH ligands in the polymer may lose their nucleophilic character ($\delta(\text{OH}) > 0$) and cations may lose their electrophilic character ($\delta(\text{M}) < +0.3$).

In the case of the condensation of electrically neutral ions, the elimination of water never leads to a sufficient change in the average electronegativity and condensation may continue indefinitely until the precipitation of a solid (hydroxide, oxyhydroxide, more or less hydrated oxide or basic salt in the presence of complexing ligands). The condensation of zero-charged species will be described in the section devoted to aluminium hydroxides.

Additional to the acidity of the media, parameters such as electronegativity, size and electronic configuration affect acid-base properties and must be taken into account in order to clarify the behavior of elements such as aluminium.

1.2 Aluminium hydrolysis and condensation: aluminium polycations

The chemistry of aluminium polycations has recently gained renewed interest because of the multiple uses and relevance of such species in domains such as water treatment [31], catalysis [32], cosmetology [33], environmental sciences [34], geochemistry [35], medicine [36] to cite only some (see [37] for numerous other applications). Added to these fields of application, the small particle size and high surface charge of these species make them attractive for self assembly and composite design applications which might lead to the preparation of advanced materials. Several studies have indeed demonstrated the feasibility of Al polycation assembly with other inorganic building blocks such as tungsten or molybdenum polyanions [38–41] or with organic copolymers [42]. The main advantage of aluminium polycations being their stability compared to other elements oligomers and the possible prepa-

ration of materials containing Al having different configuration numbers [43]. As seen in the earlier part of the introduction, hydrolysis of the aluminium hexaaquo complex $[\text{Al}(\text{H}_2\text{O})_6]^{3+}$ (hydrolysis ratio $h=0$) leads to monomeric aluminium species from hydrolysis ratio $h=1, 2, 3$ and 4 , of respective formulae $[\text{Al}(\text{OH})(\text{H}_2\text{O})_5]^{2+}$, $[\text{Al}(\text{OH})_2(\text{H}_2\text{O})_4]^+$, $[\text{Al}(\text{OH})_3(\text{H}_2\text{O})_3]$, and $[\text{Al}(\text{OH})_4]^-$. After formation of OH^- ligands in the first coordination sphere of the metal ion, polymeric aluminium species can be formed from a succession of condensation reactions.

Jander and Winkel [44] were the first to suggest the existence of polynuclear Al species based on diffusion coefficients measured in solutions of basic Al salts. Twenty years later, Brosset [45] found that the simple monomeric hydrolysis scheme was inappropriate for interpreting his potentiometric titrations of aqueous Al^{3+} solutions, and was better considered in terms of a series of indefinite polynuclear complexes [37]. The subject of aluminium polycationic species has extensively been reviewed during the past decade [26, 35, 37, 46]. Aluminium speciation lacks structural proof of the existence of some of the species that can be hypothesized from the results of careful potentiometric experiments. For other species structural information is well known, but the mechanisms by which the species are formed remain the subject of controversy. The main controversies reside in the mechanism of formation and structure of these species [37]. Indeed, two theories respectively based on the assembly of hexameric cycles ('core-links') and on the assembly of oligomeric species leading to the formation of Keggin-type polycations ('cage-like') have been in coexistence for more than 50 years despite much opposition. Authors of the work [37] tried to unify these two theories, using the rate of base addition as a factor triggering one or other of the condensation mechanism. Indeed a larger amount of Keggin-type polycations can be obtained using slow titration techniques, the lack of these species in the case of fast alkali addition being attributed to the formation of aluminium hydroxide.

We decided to concentrate the efforts of interpretation and analysis of the results obtained during this project using the cage-like model, which fits better to both the experimental conditions and results (NMR proof of 4-coordinated Al). This model will therefore be explained in more detail in the following section. Nevertheless,

information on the core-links model is presented in order to leave to the reader an alternative way of interpretation and to leave room for discussion and extra (if necessary) complexity.

1.2.1 The core-link model

In 1952, Brosset interpreted his potentiometric titration data successfully using an early form of the 'Core-links' model [45]. Two years later, the same group suggested a series of 'Core-links' polymeric Al species $\text{Al}(\text{Al}_2(\text{OH})_5)_n^{(3+n)+}$ [47], on the basis of Sillen's theoretical 'Core-links' model [48]. Afterwards, Hsu and coworkers [49, 50] and Stol et al. [51] introduced and improved a 'gibbsite-fragment' model, also called the 'hexameric ring scheme'. The present 'Core-links' model is a combination of the early 'Core-links' model and the 'gibbsite-fragment' model. This model predicts a continuous distribution of species produced by hydrolysis-condensation following the hexameric ring model (Figure 1.4). Condensation of charged species occurs until formation of $[\text{Al}_{54}(\text{OH})_{144}]^{18+}$ after which a gel is formed from $[\text{Al}(\text{OH})_3]_n$ gibbsite or bayerite particles. Therefore the structure of the charged polymers in solution

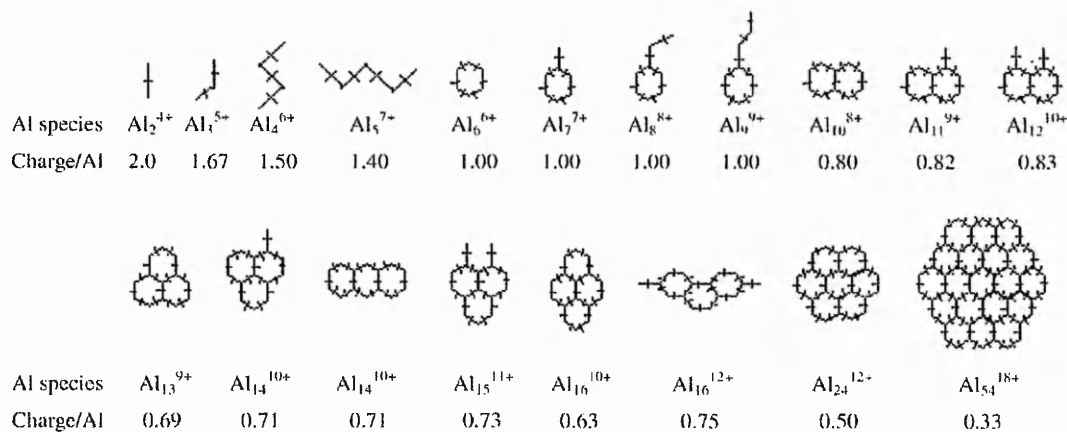


Fig. 1.4: Species predicted by the core-links model [37].

explains the sheet-like morphology of the particles observed [52, 53], by an assembly of either $\text{Al}_6(\text{OH})_{12}(\text{H}_2\text{O})_{12}^{6+}$ (hexamer rings) [54] or $\text{Al}_{10}(\text{OH})_{22}(\text{H}_2\text{O})_{16}^{8+}$ (decamer double rings) [55]. Despite its lack of direct validation, the 'core-links' model remains

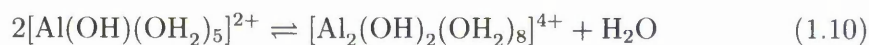
the model of choice in the field of geochemistry [56] because of the analogy between the polycations predicted and gibbsite structure.

1.2.2 The cage-like model

The current status on the formation and structure of aluminium polycations explained by the core-shell model of aluminium speciation will now be reviewed.

Aluminium dimers

The condensation of solvated aluminium starts by the formation of $[\text{Al}_2(\text{OH})_2(\text{H}_2\text{O})_8]^{4+}$ ($h=1$) through the formation of a μ_2 bridge between two $[\text{Al}(\text{OH})(\text{H}_2\text{O})_5]^{2+}$ ($h=1$) precursors. This reaction probably follows an associative nucleophilic substitution mechanism due to the low lability of the complexing water, as seen earlier [25].



The dimer has been isolated in the solid state as a sulphate salt and its structure determined by means of XRD by Johansson [57]. This species can be anticipated by homology with chromium dimers, the condensation processes of chromium being slow enough to be evidenced [25]. However, this species seems to be formed as an intermediate species [26] in solution. Al dimers were originally suspected in

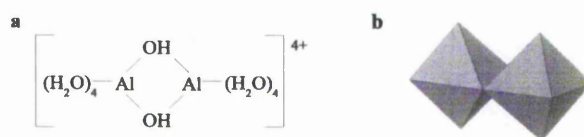


Fig. 1.5: The structure of aluminium dimer, and its polyhedral representation drawn from crystallographic data obtained by Johansson et al. [57].

hydrolyzed $\text{AlCl}_3/\text{NaOH}$ solutions [15, 58], but these species are difficult to identify by ^{27}Al -NMR and their presence was later questioned from potentiometric data [27]. Akitt and Elders later crystallized the dimer sulfate salts and redissolved them in dilute solution, which yields a peak near +4ppm in ^{27}Al -NMR spectra [59]. They concluded that the dimer present in the solid state disproportionates in solution to give a dimer of different h formulated as $[\text{Al}_2(\text{OH})_5]^+$ and monomer [23].

Aluminium trimers

Following an increasing h scale, the planar h=1.33 trimers $[Al_3(OH)_4(OH_2)_9]^{5+}$ (Fig.1.6) have been evidenced by means of potentiometric data acquired during titration of concentrated aluminium chloride solutions, and are structurally likely to be key building blocks for the larger clusters, but have not yet been isolated for solid-state structure determination. The planar trimer structure is present in other metal

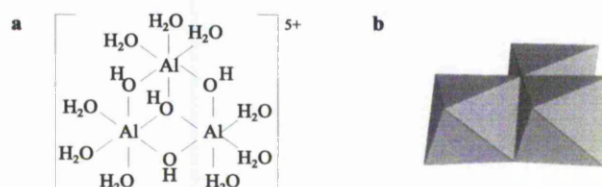
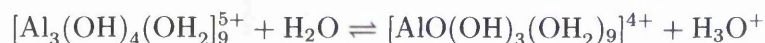


Fig. 1.6: The structure of aluminium trimer, and its polyhedral representation.

cation systems (Sn^{2+} , Pb^{2+} , Cr^{3+} , Fe^{3+} , In^{3+}) [14] since it is the structure most able to minimize electrostatic repulsions because of its geometry [25]. Evidence from potentiometric titrations [27, 60] indicate that the trimer complex exists in solutions at $4 < pH < 5$ but never reaches a large concentration, even in concentrated aluminium solutions, probably because of the fast formation of larger species. Despite the lack of structural information concerning the Keggin-type aluminium trimer, a ligated version of a planar trimer has been isolated and crystallized by Feng et al. [61] using citrate as the ligand.

Aluminium tridecamers

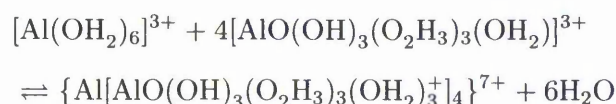
In the Al trimer structure, the oxygen atom in the μ_3 -OH bridge forms three bonds with cations and a fourth one with the proton. The small Al^{3+} cation has a larger polarizing effect on the oxygen of the μ_3 -OH bridge than on the oxygen from the μ_2 -OH, and therefore the μ_3 -OH bridge is more acidic. This causes dissociation of the μ_3 -OH bridge [25, 62]:



and makes the water molecules in the cis configuration (with respect to the μ_3 -O bridge) more acidic than the molecules in the trans configuration. Formation of the $[\text{H}_3\text{O}_2]^-$ ligand can also favor deprotonation of the aquo ligands in the cis configuration under moderate hydrolysis conditions ($h < 2.6$):



The μ_3 -O bridge of the trimer becomes able to act as a nucleophile towards a $h=0$ monomer but, because of steric effects, the central element cannot reach coordination 6 and Al adopts a tetrahedral coordination [25]. In the end, the following complex forms:



The four trimers coordinated to the central aluminium atom may subsequently undergo intramolecular condensation by olation for molecules in the cis configuration. This last step ensures the stability of the cation.



This reaction mechanism is supported by calculations using the partial charge model

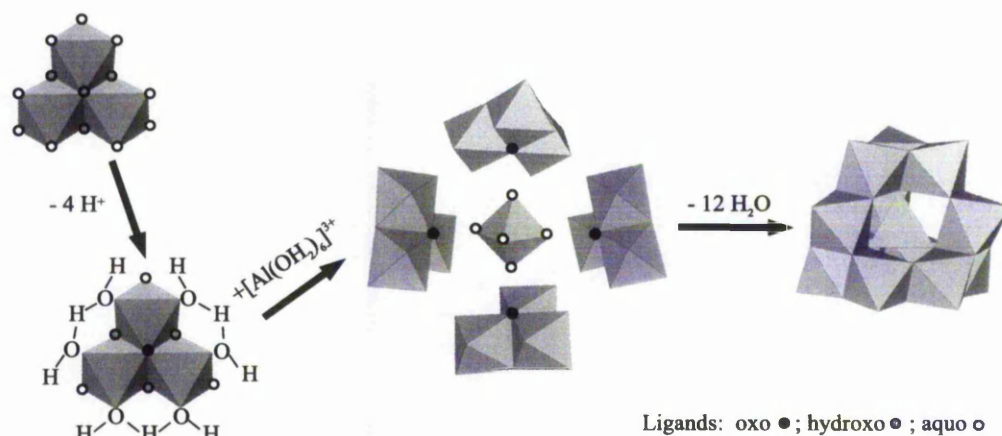


Fig. 1.7: The mechanism of Al_{13} -mer formation, inspired from [25].

and is in agreement with ^1H , ^{17}O and ^{27}Al NMR of moderately hydrolyzed solutions

obtained by Akitt [59], which indicate that only small oligomers, probably trimers, condense directly without intermediates during the formation of Al_{13} . The validity of this mechanism is strongly related to the ease with which Al can change its configuration from octahedral to tetrahedral, and to the empty d orbitals of the cation (electronic configuration $1s^2 2s^2 2p^6$) is maximizing the donor effect of the oxygen in the μ_3 -OH bridge of the trimer, an important prerequisite to the deprotonation of this bridge. For example, in the case of other cations such as chromium, the reaction of the trimer with the non-hydrolyzed precursors would lead to tetramers.

On the basis of ^{71}Ga NMR and potentiometry studies it is known that Ga and Al have parallel hydrolytic behavior. An alternative mechanism, built by analogy with a model of Ga_{13} formation based on a ^{71}Ga /EXAFS study [63], mentions the existence of oligomers with double corner sharing such as tetramers on the basis of the existence of bond lengths only possible for such species. This model explains the formation of the tridecameric species by the reaction of tetrameric and trimeric units. However, the existence of this particular bond length is not proof for the existence of such a tetramer. Indeed, the existence of a flat Al_{13} -mer such as the one crystallised by Seichter and others [64], where such a molecule (Fig.1.8), through rearrangement, could equally lead to the formation of Al_{13} or at least account for the presence of the measured bond length. In addition to these models, several

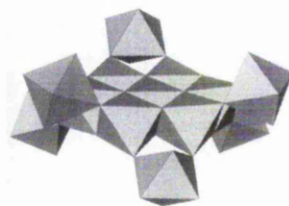


Fig. 1.8: The polyhedral view of the flat Al_{13} -mer characterised by Seichter et al. [64].

authors assume that tetrahedral aluminium $\text{Al}(\text{OH})_4^-$ is needed as a precursor for the formation of the Al_{13} moiety. Such a tetrahedral monomer would be formed at the injection point of the base due to the high local hydroxide concentration and be quickly stabilized by surrounding octahedral oligomers. This approach has been discussed by Morgado et al. [63, 65].

Polycations such as Al_{13} are usually based on Keggin structures and described in polyoxometalate chemistry [66]. The structure originally solved by Keggin in 1934 involved four 3-fold W_3O_{13} groups. Each WO_6 octahedron therein shares two edges with other WO_6 s and the four W_3O_{13} groups are attached to one another by corner sharing. The total assemblage contains 40 close-packed oxygens and has a tetrahedral pocket in its center for the heteroatom [66, 67].

Starting from the α -Keggin structure, a 60° rotation of one, two, three or four of the M_3O_{13} groups produces the β , γ , δ and ϵ Baker-Figgis isomers [67, 68] of the structure. Tungstate and molybdate polyanions usually exhibit α - and β -Keggin structures and can lead to pseudo-Keggin dimers by condensation [69]. Such dimerisation has never been observed for aluminium polycations, but three polycationic Al_{13} Keggin isomers are known: α - Al_{13} in the mineral zunyite, first solved by Linus Pauling in 1933, and later refined by others [70], δ - Al_{13} , found capped by Na^+ ions by Nazar et al. [71], and ϵ - Al_{13} , first observed by Johansson in the sixties [72] (figure 1.9). The δ -isomer differs from ϵ - Al_{13} in that one of the edge-sharing triads of octa-

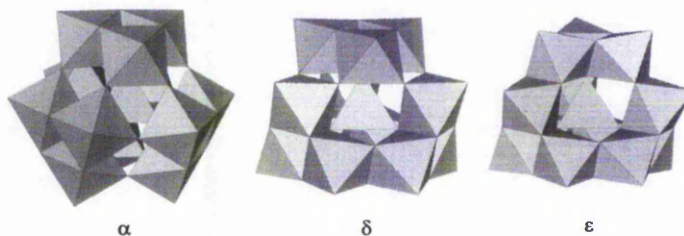


Fig. 1.9: Polyhedral view of the different Baker-Figgis isomers of the Al_{13} -mer Keggin-type ion characterised by means of single-crystal XRD. α drawn from Baur [70], δ from the Na-capped Al_{13} -mer characterised by Nazar [71] (also present in Al_{30} -mer structure) and ϵ from the data of Johansson [72].

hedrally coordinated aluminium atoms is rotated 60° with respect to the remainder of the cluster to form six shared vertices instead of three shared edges. This species has been observed by means of SAXS¹ [73], or DLS². In the Al_{13} -mer structure,

¹ Small Angle X-Ray Scattering

² Dynamic Light Scattering

distortion of the AlO_6 octahedra is significant, as indicated by the very large peak on the MAS ^{27}Al NMR spectrum of the polycation in the solid state [25].

Al₃₀-mer and larger Al-polyoxocations

Despite its occurrence and stability over a wide pH range, Al_{13} is not the largest and most energetically stable of the polycations characterised so far. Using a ferron spectrophotometric assay or GPC³ coupled or not to ^{27}Al NMR, researchers noticed that other species of higher stability were forming upon ϵ - Al_{13} -mer solution storage for several months, or when the same solution was heat-treated for a few days, or indeed when the polycation solution was prepared by reaction of metallic aluminium in AlCl_3 at high temperature [23, 74–76]. These researchers assumed the formation of larger polymers, but did not attempt to hypothesise the structure or formation mechanisms of such species. After having characterised large aluminium polycations by means of SAXS, Nazar et al. monitored this transformation using GPC coupled with ^{27}Al [77], separating three different Al polycation fractions containing Al in tetrahedral coordination. The elution sequence of the aluminium species was found to correspond to the three major peaks observed in the tetrahedral region of ^{27}Al NMR spectra. (e.g. 63, 70, 76 ppm). Almost a decade after this publication, the same group solved the structure of the species corresponding to the peak at 70ppm by means of XRD [69], another team obtaining similar results independently. The characterised species differ from the hypothesis of dimerisation of the Al_{13} -mer having a defect Al_{13} -mer as an intermediate. The crystal structure reveals a polycation with a formula $[\text{Al}_{30}\text{O}_8(\text{OH})_{56}(\text{H}_2\text{O})_{24}]^{18+}$, compensated by nine sulfate ions. The polycation (figure 1.10) results from the combination of two δ - Al_{13} units connected by a crown of four octahedrally complexed aluminium ions. The formula of the solid can therefore be rewritten as $[(\delta\text{-Al}_{13})_2\{\text{Al}_4(\text{OH})_8(\text{H}_2\text{O})_6\}](\text{SO}_4)_9$ [69]. A mechanism has been proposed for the formation of the Al_{30} -mer during the thermal treatment of an ϵ - Al_{13} -mer suspension [78](Fig.1.11). Initially, Some of the Al_{13} polycations dissociate into AlO_6 monomers and to un-dissociated ϵ - Al_{13} -mer. These species then attach to AlO_6 units and isomerise into the δ -form. Once isomerisation

³ Gel Permeation Chromatography

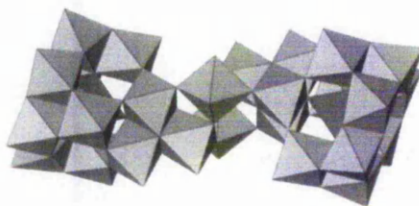


Fig. 1.10: Polyhedral representation of the Al_{30} -mer characterised simultaneously by Nazar [71] and Allouche [69].

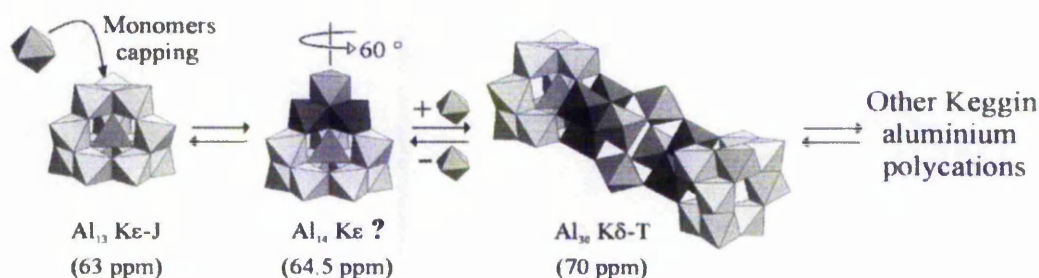


Fig. 1.11: Al_{30} -mer formation mechanism suggested by Allouche, involving the formation of the δ - Al_{13} isomer by 'capping' of an ϵ - Al_{13} molecule [69]

is complete the species are able to dimerise to form the Al_{30} -mer molecule. The theoretical h for Al_{30} -mer (2.40) is lower than that for the Al_{13} -mer (2.46). Al_{30} might not yet be the largest aluminium polycation able to form in aqueous solution. Indeed, as pointed out by Fu [77], the species corresponding to the 76ppm peak observed in ^{27}Al NMR spectra of heat-treated basic Al salts solutions has still not been assigned to a species. Many authors assume this species will have a larger size than Al_{30} -mer. However, structural studies of larger species are hindered both by synthesis and crystallisation difficulties arising from longer synthesis times and lower mobility of these giant polycations.

1.3 Aluminium hydroxides and oxides

The formation of a solid phase within the liquid phase involves four major steps, e.g. the formation of a zero-charge precursor, nucleation, growth and aging. These

steps can be understood using chemical and thermodynamic concepts. In the next section the nature of these steps will be described and the peculiarities observed in the case of aluminium hydroxide chemistry reviewed.

1.3.1 Formation of the zero-charge precursor

The formation of an hydroxide starts with the formation of a stable zero-charge precursor able to condense until formation of the solid phase. The hydroxylation speed and the nature of the zero-charge precursor depends on conditions such as pH or temperature, and whether the reaction takes place through the addition of a base, by thermohydrolysis, by an hydrothermal route or the thermal decomposition of a base such as urea [25]. According to the partial charge model of Henri et al., $\chi_{B,z} < \chi_M^* < \chi_{A,z}$ in $[\text{Al}(\text{OH})_3(\text{OH}_2)_3]^0$ (Fig.1.12), and hydroxo ligands are 'stable' because their negative charge prevents their acidic dissociation. Condensation is

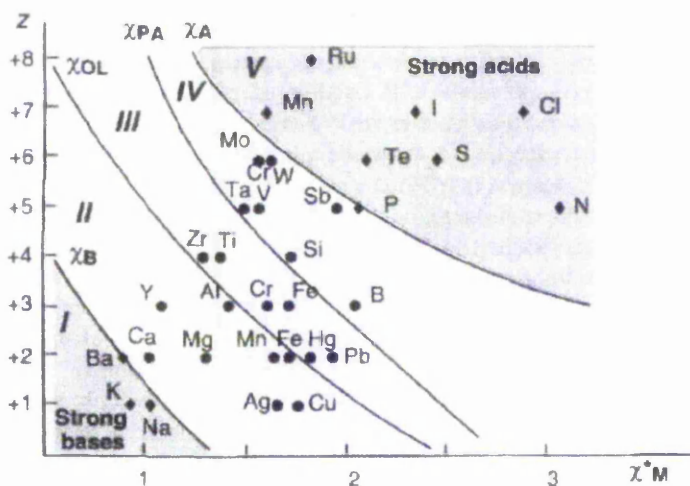


Fig. 1.12: Charge-electronegativity diagram showing five classes of behavior for the zero-charge metal ion species. In domains I and V, the element remains monomeric and soluble. In domain II and IV, elements condense respectively by olation or oxolation, whereas both mechanisms can occur in field III [25].

not hampered and $\text{Al}(\text{OH})_3$ is formed by condensation via olation and loss of water molecules. Moreover, depending on the synthesis procedure, the precursor to the solid phase can be a zero-charged tetrameric species, or precipitated salts. Therefore

the morphology, size and physical properties of the resulting phase will depend strongly on the synthesis conditions.

1.3.2 Nucleation

For the class of trivalent elements to which aluminium belongs, the zero-charge precursor exceeds a critical concentration C_{min} above $h=2.5$, for which the condensation rate increases abruptly, leading to the formation of nuclei throughout the solution (zone I, figure 1.13). The nucleation phenomenon can be explained using

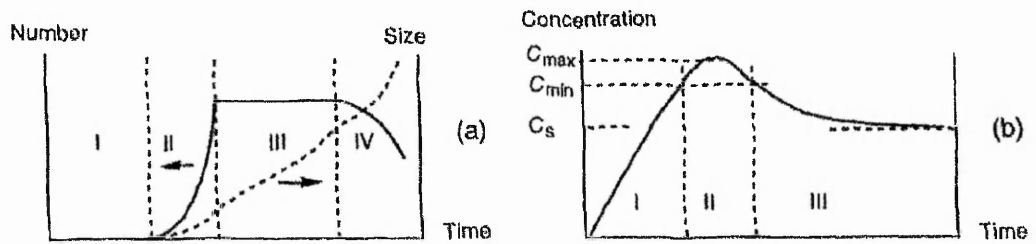


Fig. 1.13: Change (a) in the number and sizes of particles formed in solution and (b) in the concentration C of the soluble precursor of the solid phase during precipitation [25].

thermodynamic concepts. The free enthalpy change of nuclei P_n , formed from n precursors P includes a term due to the chemical potential difference ($\mu_s - \mu_L$) of the P entity in the solution and in the solid, respectively, as well as a term representing the energy required for formation of the surface of the nucleus [79]:

$$\Delta G = n(\mu_s - \mu_L) + A\gamma$$

where γ is the interfacial tension or energy, $\gamma = \partial G / \partial A$, and A is the surface area of the solid.

Assimilating activity and concentration, the chemical potential difference may be written as:

$$(\mu_s - \mu_L) = kT \ln(c_s/c_L) = -kT \ln S$$

where c_L is the precursor concentration in the solution, c_s is the solubility of the solid phase and $S = c_L/c_s$ is the supersaturation ratio of the solution.

The radius r of a spherical nuclei formed from n precursors of molecular volume v , is $r = (3nv/4\pi)^{1/3}$. The surface of the nucleus is $A = n^{2/3}(36\pi v^2)^{1/3}$ and the free enthalpy of nucleation can now be written as:

$$\Delta G = -nkT \ln S + n^{2/3}(36\pi v^2)^{1/3}\gamma \quad (1.11)$$

The surface tension γ is usually positive and the solution is usually supersaturated ($S > 1$). The first term of equation (1.11) is negative and the second is positive. Under these conditions of spontaneous precipitation, the formation of nuclei in homogeneous solution requires passage through a maximum in the free enthalpy (Figure 1.14). The number of precursor molecules n^* in the 'critical' nuclei present

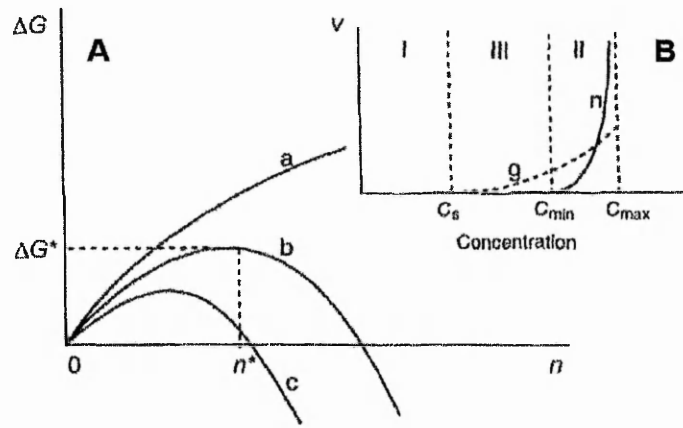


Fig. 1.14: **A:** Variation in the free enthalpy of formation of nuclei as a function of the number of precursor molecules n , (a) $S < 1$, (b) and (c) $S_c > S_b > 1$. **B:** Nucleation rate n and growth rate c as a function of the precursor concentration. The labeled zones correspond to those in Figure 1.13 [25].

for this maximum is given by $\partial(\Delta G)/\partial n = 0$, or

$$n^* = \frac{32\pi\gamma^3 v^2}{3(kT \ln S)^3} \quad (1.12)$$

and the corresponding change in free enthalpy is

$$\Delta G^* = \frac{n^*}{2} kT \ln S = \frac{16\pi\gamma^3 v^2}{3(kT \ln S)^2} \quad (1.13)$$

The radius of the critical nucleus is given by the Gibbs-Kelvin equation:

$$r^* = (3n^*v/4\pi)^{1/3} = \frac{2\gamma v}{kT \ln S} \quad (1.14)$$

From this equation, the size of the critical nuclei is smaller for higher supersaturation and smaller surface tension, the latter being a strong function of the physico-chemical conditions of the medium. The critical nuclei are in an unstable equilibrium with the solution. They correspond to a maximum of $\Delta G = f(n)$, which means that a small change in their size leads to either dissolution or growth because $\partial(\Delta G)/\partial n < 0$ in either case. In fact, the probability of growth of the nuclei is higher than that of dissolution, and precipitation is spontaneous.

From a kinetic standpoint, the nucleation rate constant J represents the number of nuclei formed per unit time per unit volume. It is expressed as [79]

$$J = J_0 \exp\left(\frac{-\Delta G_N}{kT}\right) \quad (1.15)$$

where J_0 is the frequency of collisions between precursor molecules (usually between 10^{10} and $10^{35} \text{ cm}^{-3} \text{ s}^{-1}$) and ΔG_N is the nucleation activation energy.

ΔG_N includes the energy barrier ΔG^* required for the formation of a stable nucleus (equation (1.13)) and ΔG^R , related to the type of the condensation reaction (usually of the order of 35 kJ mol^{-1}). Hence, the nucleation rate may be written as

$$J = J_0 \exp\left[\frac{\Delta G^* + \Delta G^R}{kT}\right] = J'_0 \exp\left[\frac{16\pi\gamma^3 v^2}{3(kT)^3 (\ln S)^2}\right] \quad (1.16)$$

with $J'_0 = J_0 \exp(-\Delta G^R/kT)$.

Nucleation is usually difficult to control using the concentration of the precursor, but it may nevertheless be efficiently controlled by a modification of the solid-liquid surface tension, for example by adsorption of anions or cations, and by variation of the pH or ionic strength of the precipitation medium.

1.3.3 Growth

For a concentration close to C_{min} , the nucleation rate is very small and precursors condense preferentially on existing nuclei, which causes their growth until the precursor concentration reaches solution saturation (the solubility limit of the solid phase, zone III, Figure 1.13). The rate of precursor condensation during precipitation is a function of the respective rates of precursor generation and nucleation. Nucleation and growth phases could therefore be consecutive or overlap and occur simultaneously if the precursor concentration stays higher than C_{min} . In this case, the first

nuclei will become much larger than the younger ones, leading to a large particle size distribution. In order to obtain monodisperse⁴ particle sols, the nucleation and growth steps must be decoupled to ensure that a singular nucleation phenomenon takes place, followed by a controlled growth via accumulation of all remaining matter. This implies that the nucleation rate should be much greater than the rate at which the precursor is generated. The average size of the final particles depends on the number of nuclei and the amount of matter available during the synthesis, but the breadth of the particle size distribution is linked to the mechanism of nucleus growth. The kinetic step that limits the growth rate may be either the diffusion of the precursor towards the surface or a surface reaction prior to incorporation [79].

Diffusion-limited Growth

This occurs when the reaction with the surface is very fast. The change in particle size with time is given by [79, 80]

$$\frac{dr}{dt} = \frac{D(C - C_s)v}{r} \quad (1.17)$$

where r is the radius of the particle (assumed spherical), D is the diffusion coefficient of the solute of molar volume v and concentration C , and C_s is the solubility of the solid.

The width of the size distribution Δr is given by [79, 80]

$$\frac{\Delta r}{r} = \left(\frac{r_0}{r}\right)^2 \frac{\Delta r_0}{r_0} \quad (1.18)$$

where r_0 and Δr_0 are the nuclei size and the width of the size distribution respectively.

The larger the growth, the smaller is the relative width of the distribution $\Delta r/r$. It is rare, however, for diffusion-limited growth to lead to monodisperse solutions because of the overlapping of nucleation and growth steps under high supersaturation conditions.

Growth Limited by a Surface Reaction

The rate-limiting step is the incorporation of the precursor on the surface of the nuclei, and an heterogeneous nucleation step must take place on the surface of the

⁴ a single narrow particle size distribution

particles in order to form two-dimensional nuclei. Primary homogeneous nucleation and surface nucleation are analogous, but the activation energy of the latter is smaller because only the outer limits of the nucleus participate in the creation of the surface.

Mononuclear mechanism: If the surface nucleation rate is much smaller than the two-dimensional growth rate for the surface nucleus, each new layer comes from a single nucleus. Growth takes place according to a 'mononuclear' mechanism which is a function of the surface area. The growth rate of the particles can be written [79]:

$$\frac{dr}{dt} = k_m r^2 C^m \quad (1.19)$$

Where k_m is the rate constant, and m is the approximate number of precursor molecules contained in the surface nuclei.

As their growth rate is proportional to the surface area, the larger particles grow faster. This mechanism leads to a broadening of the relative size distribution of the particles:

$$\frac{\Delta r}{r} = \left(\frac{r}{r_0} \right) \frac{\Delta r_0}{r_0} \quad (1.20)$$

Polynuclear mechanism: If surface nucleation and growth rates are similar, several nuclei form simultaneously and new layers begin to form prior to the previous ones being completely covered. This 'polynuclear' growth mechanism is independent of surface area [79, 80]. The polynuclear growth rate can be written:

$$\frac{dr}{dt} = k_p C^{(m+2)/3} \quad (1.21)$$

and the relative width of the size distribution is written as

$$\frac{\Delta r}{r} = \left(\frac{r_0}{r} \right) \frac{\Delta r_0}{r_0} \quad (1.22)$$

Other growth mechanisms: Other growth mechanisms may take place, such as spiral growth. This takes place from a structural defect such as a dislocation formed during nucleation or during the initial steps of growth. Subsequent growth maintains the defect by wrapping itself around it (Figure 1.15). This mechanism allows

the growth of particles on a singular defect, since it creates little or no increase in the solid-liquid interface and therefore the activation energy is very small and this mechanism may occur at very low supersaturation ($S \approx 1$). The three main growth mechanisms do not obey the same power laws of concentration and particle size (cf. Eqs.1.17, 1.19 and 1.21). Therefore, they will occur as the predominant mechanism over different concentration ranges (Figure 1.15). However, as precipitation pro-

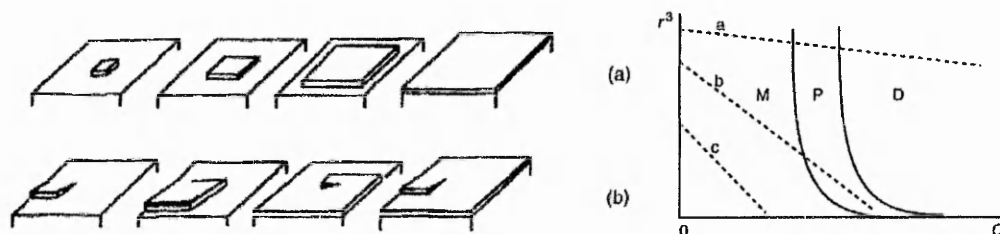


Fig. 1.15: Left: Surface nucleation with (a) two-dimensional growth of the nuclei or (b) spiral growth around defect. Right: Predominant growth mechanisms as a function of precursor concentration [25].

gresses, the medium concentration decreases and the particle size increases. Several mechanisms contribute to growth, and composite rate laws [79, 81] must be used to describe the evolution of the system.

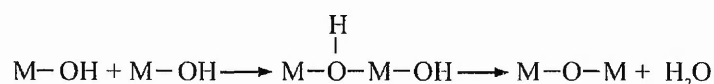
1.3.4 Ageing

After their growth, the primary particles are not necessarily stable. Ageing of the suspensions, which may take place over a very large time scale (hours, days or months), allows the system to tend towards or to reach this stability. Ageing is often associated with modifications of some physical or chemical characteristics of the particles. Some of the most frequently observed phenomena are described below.

Dehydration

Some hydroxides are not stable and their spontaneous dehydration, more or less rapid and extensive, generates oxyhydroxides $\text{MO}_x(\text{OH})_{z-2x}$ or hydrated oxides $\text{MO}_{z/2} \cdot x\text{H}_2\text{O}$ via oxolation reactions in the solid phase.

In the absence of aquo ligands, an hydroxo ligand may act as a leaving group if, through proton transfer in the transition state of a SN_2 mechanism, the formation of an aquo ligand is possible. The proton in the ol bridge of the transition state is more acidic than that of terminal hydroxo ligands and may migrate onto one of them to form the aquo ligand. For this reason, the negative charge on the oxygen of the hydroxo has to be relatively low to allow proton migration. The resulting aquo ligand may be eliminated if its partial charge is positive, and condensation occurs with the formation of oxo bridges through oxolation [29]:



considering this mechanism, the likelihood of dehydration and therefore the stability of the hydroxide can be related to water charge within the structure.

If $\delta(H_2O) < 0$ in the hydroxide, the hydroxo ligands are too negative and hence too weakly polarized by the cations for water to form. The hydroxide is stable.

If $\delta(H_2O) > 0$ in the hydroxide, oxygen in the hydroxo ligands is highly polarized by the cations. The formation of oxo bridges is favored. A structural change leads to the formation and elimination of water.

By introducing the criterion $\delta(H_2O)=0$ in the charge balance equation of the hydroxide (Equation 1.8), an electronegativity χ_{OL} emerges, which limits the domain ($\chi_B < \chi_M^* < \chi_{OL}$) within which cations may condense via olation only and form stable hydroxides from zero-charge precursors, oxyhydroxides or oxides are obtained via dehydration if olation and oxolation are competing mechanisms for $\chi_M^* > \chi_{OL}$. As one can see from figure 1.12, Al^{3+} is positioned at the borderline of these two domains, indeed we will see that aluminium tends to form hydroxides which then dehydrate to form oxyhydroxides such as γ - $AlOOH$ boehmite. It has been long observed that elements with a +2 charge precipitate as hydroxides, and those with a +3 charge as oxyhydroxides (the final stage in the ageing process being the formation of an oxide) [82]. This sequence is a clear illustration of the increasing polarization of the hydroxo ligands by the cation which is related to the covalent nature of the metal-oxygen bond. After heat treatment, an oxide is always obtained.

Increase in Particle Size

This is manifested by a shift in particle size distribution owing to the disappearance of the smaller particles leading to the growth of the larger ones. This evolution is possible because, if the liquid-solid interfacial tension is positive, true thermodynamic stability is reached only when all precipitated matter is gathered in a single particle. The surface area of the solid is therefore at a minimum (cf. Equation 1.3.2).

Ostwald ripening: The Gibbs-Kelvin equation (Equation 1.14) shows that, for a concentration corresponding to saturation, only particles with radius r are in equilibrium with the solution. For particles with $r < r$ the solution does not appear to be saturated and they must redissolve. For those particles with $r > r$ the solution is supersaturated and the particles must grow ($\partial\Delta G/\partial n < 0$). The process involves transport of matter through the solution in what are referred to as 'dissolution-crystallization' mechanisms or Ostwald ripening. This process can be very slow, because it occurs for very low concentrations ($S \approx 1$) and requires breaking of hydroxo bridges. This secondary growth therefore mostly proceeds through surface nucleation or spiral growth. In practice, the evolution of the system stops before all particles are transformed because the increase in the size of the particles decreases the rate of dissolution, and a pseudo-equilibrium is soon reached.

Particle aggregation: Decrease in the area of the solid-liquid interface may also occur via particle aggregation. It is favored when the physicochemical conditions of the medium (pH, ionic strength) minimizes the surface electrical charge of the particles and hence the repulsive forces existing between them. Particles aggregate, decreasing the area of the oxide-solution interface more easily and rapidly than crystalline growth. This phenomenon may occur during nucleation, or at any stage during growth, causing formation of dendrites, mosaic crystals or fractal structures [83]. Aggregation of primary particles bolsters the dissolution-crystallization equilibria because the areas close to the contact point between particles (concave surfaces) have smaller solubilities than the areas of positive curvatures (convex surfaces).

Therefore, the contact zones between particles fill themselves following dissolution-crystallisation until the solubility difference is minimised. The phenomenon is more predominant as the size of the primary particles is small. This may lead to coalescence⁵, chain stiffening of spherical particles and even their transformation into fibers or sticks [84].

Change in Crystal Type

In the case of a crystal that may exhibit various allotropes, the least stable and most soluble phase usually precipitates first. This metastable phase is transformed during ageing into a more thermodynamically stable phase. Equations 1.14 and 1.16 show respectively that, for a given supersaturation level S , the nucleus size is smaller and the nucleation rate is larger for a smaller solid-solution interfacial energy γ , since solubility is inversely proportional to interfacial tension [85] and precipitation of the most soluble phase is favored kinetically. Because of its solubility and metastable nature, the resulting phase recrystallizes to form the thermodynamically stable allotrope, usually through heterogeneous nucleation [86]. This phenomenon, known as the Stranski rule [87], is observed in the case of aluminium hydroxide for which the amorphous phase $\text{Al}(\text{OH})_3 \cdot x\text{H}_2\text{O}$ is transformed into boehmite first and bayerite later [88, 89].

Changes in Morphology

The morphology of particles formed by precipitation is very intricately connected to the experimental conditions of the synthesis. Recrystallization of a solid in suspension into a more thermodynamically stable species is frequently associated with a change in the shape of the particles. It is difficult to predict the shape of the particles in a solid because the same crystal structure may exist in various morphologies. A sphere is, from a thermodynamic point of view, the most favored geometry because its minimal surface/volume ratio decreases the free enthalpy of nucleation (cf. Equation 1.3.2). Small particles of many solids are very often spheroidal. However, particle anisotropy develops during growth, for structural or chemical reasons.

⁵ 'fusion' of the particles

Growth may be favored along preferential axes or crystallographic planes because the chemical reactivity of surface groups, on which the precursors bind, depends on many parameters such as local structure and electrostatic charge, as well as aggregation of primary particles. The last two factors are strongly linked to the pH of the solution and to the presence of complexing ions.

Peculiarities of Al(III) solid phases in aqueous solutions

During neutralization of acidic Al(III) solutions, particles seem to form by aggregation of very small nuclei, rather than by crystal growth [90]. As has been seen, the first stages of hydrolysis and condensation very often lead to stable and highly hydrated polycations. Different theories exist to explain their rearrangement leading to the hydroxide phase. One explanation being that they can act as a reservoir for monomers and another explaining the amorphous solid phase formed by an aggregation of these species caused by charge cancellation during neutralization. Internal modifications (dehydration, crystal rearrangement) allow subsequent nucleation of more stable phases [86, 91, 92]. Solid Al-containing phases may be formed following perturbation of a stable system through different techniques.

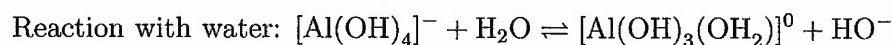
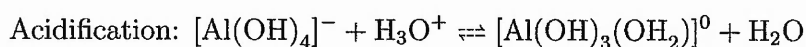
Condensation via acid or base addition at room temperature: During the addition of a droplet of a base to a solution, a strong pH gradient exists locally around the droplet because the mixing and homogenization are relatively slow (of the order of milliseconds in a turbulent medium) compared with the rate of exchange of the protons with the aquo complex ($k \approx 10^{10} \text{Mol}^{-1} \cdot \text{s}^{-1}$). Before reaching equilibrium, a collection of species of variable hydrolysis ratios can be formed, each of which has its own reactivity. Condensation via olation of these various forms occurs in an anarchical manner, in both time and space, which results in particles of very different sizes that do not necessarily correspond to thermodynamic equilibrium if kinetic constraints are involved. Therefore, alkalinisation of an aluminium nitrate solution around pH 6–7 with sodium hydroxide or ammonia causes the immediate formation of a translucent amorphous gel [93]. Upon aging, this gel undergoes rearrangements leading to crystallisation. The driving force for such rearrangements is mainly the

decrease in free enthalpy of the solid. Many authors attribute the formation of the gel to the aggregation of stable Keggin-like species such as the Al_{13} -mer. Upon crystallisation at room temperature, the NMR peak characteristic of the tetrahedral core of Keggin species progressively disappears [94]. The structures obtained vary depending on the crystallisation conditions, the reaction paths being related to changes in the solubility of the solid phase with the pH of the medium.

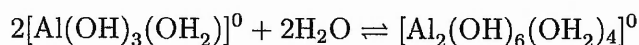
At pH 6–7, corresponding to minimum aluminium hydroxide solubility, matter transport through solution is difficult and reorganization of Keggin-type species is more easily accomplished within the solid. The transformation involves partial dehydration and leads to γ - AlOOH boehmite, in which the oxygen lattice is f.c.c. and similar to that of the Al_{13} -mer. Although boehmite is not the thermodynamically most stable phase at room temperature, it is probably kinetically stabilized because the system is constrained to evolve without heating and transforms on the lowest activation energy path.

For $\text{pH} < 6$, and $\text{pH} > 8$, the solubility of aluminium is appreciable. Gel transformation can occur via matter transport in solution, via classical aging. Slowly generated soluble species at small concentration, probably monomers, feed the formation of $\text{Al}(\text{OH})_3$ which is more stable than boehmite at room temperature (ΔG_{f298K}^0): $\text{Al}(\text{OH})_3 = -546$, γ - $\text{AlOOH} = -436 \text{ kJ} \cdot \text{mol}^{-1}$.

At $\text{pH} > 8$, the precursor of the hydroxide phase is probably the tetrahedral $[\text{Al}(\text{OH})_3(\text{H}_2\text{O})]$. Indeed, alkaline solutions contain mostly aluminate ions $[\text{Al}(\text{OH})_4]^-$, as confirmed by ^{27}Al NMR [95]. Through acidification or reaction with water:



the zero-charge species ready for condensation is formed. Addition and solvation cause an increase in the coordination of the Al^{3+} cations, which leads to the formation of oligomers in which Al^{3+} is hexacoordinated:



A reaction mechanism involving octahedral dimers $[\text{Al}_2(\text{OH})_6(\text{OH}_2)_4]^0$ whose further condensation by olation leads to the planes characteristic of the structure of the

hydroxide (Figure 1.16) can then be considered. At $\text{pH} < 6$, the soluble species are octahedral, so that the dimer $[\text{Al}_2(\text{OH})_6(\text{OH}_2)_4]^0$ may form directly to allow formation of the hydroxide from the gel along the same reaction path.

Depending on the pH of the medium, aluminium hydroxide crystallizes as gibbsite or as bayerite. Both structures are based on the stacking of identical layers of edge-sharing $\text{Al}(\text{OH})_6$ octahedra (Figure 1.16). In gibbsite, the order of the stacking is of the ABBA type (oxygen atoms of two adjacent sheets are face-to-face), whereas in bayerite, stacking is of the ABAB type (oxygen atoms form a hexagonal close-packed structure) [96, 97]. Within the sheets, hydrogen bonds between OH groups

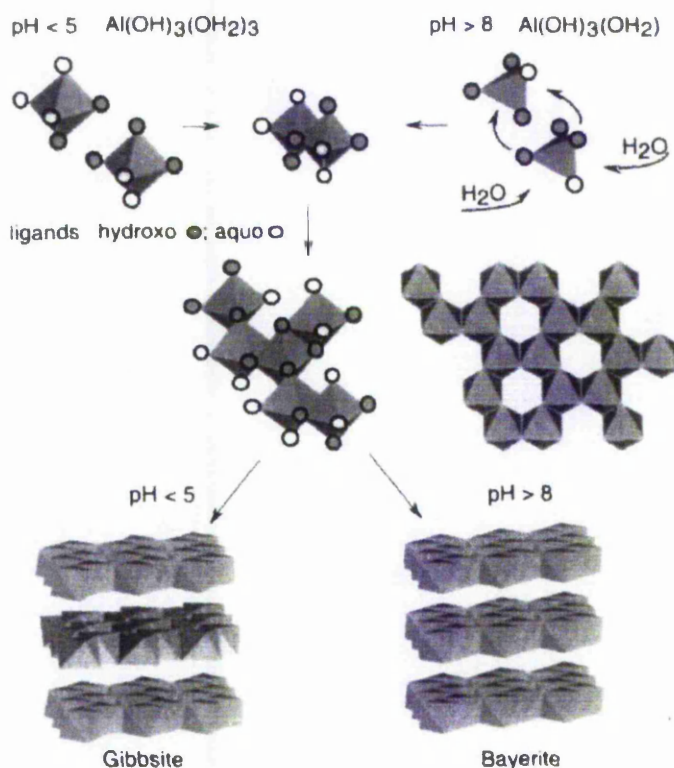


Fig. 1.16: Possible reaction mechanisms for the formation of gibbsite or bayerite during evolution of an amorphous gel at $\text{pH} < 5$ and $\text{pH} > 8$ [25].

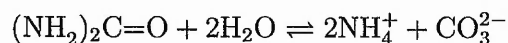
maintain the cohesiveness. It is probable that, depending on the pH , the charge on OH groups on the surface of the sheets could be somewhat different, which would tend to modify their solvation. As a consequence, their interaction through

hydrogen bonds is modified, thereby favoring one structure or the other. Gibbsite appears to be slightly more stable than bayerite (enthalpies of formation ΔH_{f298K}^0 are respectively -612.5 and -610.1 $\text{kJ}\cdot\text{Mol}^{-1}$).

Thermohydrolysis and other soft techniques: Rather than modifying the composition of the system abruptly, it is preferable to work near equilibrium, in a homogeneous system. Hexa-aquo complexes of trivalent elements are stable in an acidic medium at room temperature. Hydroxylation of these complexes by water may, however, take place by heat treatment. During the thermolysis process, deprotonation is slow. Species in solution may therefore condense during slow hydroxylation, forming intermediate species of similar structure to polycations. These entities may aggregate and condense to form a crystallized solid. Heating of an acidic solution of Al(III) ions to about $80\text{-}100^\circ\text{C}$ causes the formation of boehmite $\gamma\text{-AlOOH}$ [98, 99]. In this case, boehmite probably forms starting from $[\text{Al}_4\text{O}(\text{OH})_{10}(\text{OH}_2)_5]^0$ or $[\text{Al}_4(\text{OH})_{12}(\text{OH}_2)_4]^0$ tetramers. These are good structural models for the oxyhydroxide nuclei and they may be considered in a first approximation as the building blocks of the solid phase. During studies of the early stages of condensation of trivalent elements, it was observed that two forms of tetramer may result from an octahedron fixed on the compact $[\text{M}_3(\text{OH})_4(\text{OH}_2)_9]^{5+}$, flipping in one direction or another. The tetramer with a $\mu_4\text{-O}$ bridge (form III) appears favored in the case of aluminium because of the nucleophilic character of the $\mu_3\text{-OH}$ bridge. Condensation of $[\text{Al}_4\text{O}(\text{OH})_{10}(\text{OH}_2)_5]^0$ by olation and oxolation could lead directly to the formation of corrugated sheets characteristic of $\gamma\text{-AlOOH}$, containing $\mu_4\text{-O}$ and $\mu_2\text{-OH}$ bridges. Another reaction mechanism could involve the formation of boehmite from the planar tetrameric precursor rapidly forming double chains of octahedra, in a process similar to the formation of goethite. Connections between these chains could take place by oxolation between the $\mu_3\text{-OH}$ of one chain and the terminal ligands of another. This seems rather unlikely because the growth of 'fibrillar' boehmite particles is preferential along their c axis perpendicular to the corrugated planes of the lattice, rather than in the direction of the chains. Diaspore, isostructural with goethite, forms only under hydrothermal conditions (around 400°C , 400 bar [100],

conditions in which the physicochemical properties of water are very different from the standard conditions, and can affect drastically the structure and acidity of the oligomers). Therefore, the formation of double chains of octahedra from the planar precursor $[\text{Al}_4(\text{OH})_{12}(\text{OH}_2)_4]^0$ appears difficult.

Thermally unstable molecules such as urea can as well be used to allow soft control over the pH of the solutions:



which acts as a buffer and maintains the solution around pH 7.8. These reaction rates may be adjusted thermally, and it is possible to tune both the extent and the rate of hydrolysis, thereby controlling nucleation. This results in a narrow particle size distribution. Similarly, thermal decomposition of metallic complexes or basic salts allows regulation of the precursor concentration and control of the precipitation of the solid. Matijevic's research [101, 102] clearly demonstrates the efficiency of thermohydrolysis techniques.

2. INTERACTION OF ALUMINIUM WITH BIOMOLECULES

2.1 Interaction of aluminium polycations with biomolecules

Previous studies of amino acids, peptides and proteins interactions with aluminium have focused on the effects of aluminium on living organisms. The study of aluminium relation to biological molecules and processes is a relatively new topic in biology and medicine. The main reasons for this raising awareness are the use of Al-based actives and materials close to our everyday environment, and the observation of cases of aluminium toxicity. In addition to monomeric species, polymeric Al finds many applications such as antiperspirant actives and water treatment. Despite suspicions concerning the toxicity of antiperspirants, aluminium present in the blood plasma usually remains at a low level even in heavy users of these products [103, 104], although antiperspirant induced hyperaluminemia is reported [105, 106]. The animal toxicity of polymeric aluminium species have never been reported, although Rao et al. [107] detected Al_{13} in rat brains synaptosomes. Excellent reviews dealing with aluminium toxicity [108] and aluminium biochemistry and speciation in body fluids are available [109].

Environmental interest in the Al_{13} -mer stems largely from its reported phytotoxicity [110–112], polynuclear hydroxo-Al complexes being much more phytotoxic than the hexahydrated ion or mononuclear hydroxo-Al complexes [37], and the potential toxicity to fish [113–115]. It is also considered to provide a vector for transporting pollutants [116, 117] and for influencing pesticides [118]. Natural conditions for forming the Al_{13} -mer would be when acidic and low-organic-acid waters mix rapidly with a higher-pH solution. Such an environment could be found as dilution of acid rainfall percolating through soil into a higher-pH stream [117] or over a limestone terrain [119]. However, the critical pH window ($4.5 < \text{pH} < 6.5$) is difficult to sample

during a mixing event and the Al_{13} -mer is suppressed by constituents common in natural waters. It dissociates rapidly by bonding to phenolic compounds [120–123] and metals [124] and is flocculated by anions such as sulfate [125, 126] or humic acids [119, 127–129]. Although there are doubts as to whether these polyoxocations exist in natural waters, [130] the Al_{13} -mer has been detected in soil solutions [131], and its presence is inferred from the ^{27}Al NMR spectra of pollutant floc [117]. Despite the recent increase of interest concerning polymeric aluminium species interactions with biologically relevant ligands, the interactions of their monomeric counterparts has to date received more attention. Therefore the next part of this review will mainly summarise the available literature on the interactions of mononuclear aluminium species with biomolecules.

2.2 Aluminium ion interactions with aminoacids

$[\text{Al}(\text{H}_2\text{O})_6]^{3+}$ is the hardest of the trivalent metal ions existing in aqueous solutions (high charge to radius ratio). As this type of cation has the highest affinity for hard anions, the most likely binding sites of $[\text{Al}(\text{H}_2\text{O})_6]^{3+}$ in biosystems are oxygen donors, especially negatively charged donors such as groups containing O^{2-} and OH^- . Carboxylate, phenolate, catecholate and phosphate are the strongest Al^{3+} binders. Aminoacids have lower complexing ability compared to carboxylic acids due to the presence of the repulsive NH_3^+ group. The stability constants of Al^{3+} complexes formed with simple bidentate aminoacids such as glycine, alanine, serine, threonine, asparagine and glutamine are in the range $\text{Log } K=5.5$ to 5.9. Aminoacids often form monodentate complexes by binding to aluminium ions via their carboxylate group, or bidentate ones via the coordination by both carboxylic and amino groups [132].

The speciation of $[\text{Al}(\text{H}_2\text{O})_6]^{3+}$ in the presence of these biomolecules is influenced by the formation of the mononuclear complexes $\text{Al}(\text{LH})(\text{OH})^{2+}$ (LH denotes an aminoacid protonated at the amino end) and $\text{AlL}(\text{OH})^+$, and dinuclear complexes such as the dihydroxo-bridged $\text{Al}_2\text{LH}(\text{OH})_2^{4+}$. Under acidic conditions, the complexes formed with the tridentate (two carboxylate and one central NH_2 donor

groups) aspartic acid are about two orders of magnitude more stable than with simple aminoacids. The NH_2 group seems to play an important role in the strength of the interaction. However, Glutamic acid acts as a bidentate carboxylic ligand due to the lower stability of the larger chelate ring formed involving the NH_2 group [133]. The alcoholic-OH or phenolic-OH side chain groups of the amino acids in Serine, Threonine or Tyrosine-containing peptides can be easily phosphorylated and these posttranslational modifications occur in biological systems. Ser(P) has been shown to be capable of keeping Al^{3+} in solution, preventing precipitation even at pH 8. The most probable binding mode of Ser(P) is its tridentate chelation through (OPO_3^{2-} , NH_2 , COO^-) donors [134].

For larger molecules such as oligopeptides, the presence and relative position of suitable side-chain donors can also play an important role. For larger peptides or even proteins, a suitable spatial arrangement of appropriate donor groups, becomes an important factor for metal binding, and amide coordination is often encountered. The irreversible binding of Al in biological systems may occur in molecular aggregates, when the exchange reactions of Al^{3+} are slowed down by the formation of hydrolysed oxo- or hydroxo- bridged Al clusters surrounded by organic compounds.

2.3 *Absorption of aluminium by the human body*

Aluminium is encountered in high concentration in some food products such as tea or baking additives, and can also be absorbed during the antacid treatment of ulcers [134]. Aluminium oxide can be used as an additive increasing the immune response for vaccines [135], or as a constitutive material for prostheses [136]. It may be released from Al salt containing antiperspirants [36] or from food containers, as in the case of aluminium found in dietary milk due to its interaction with milk proteins [137]. After ingestion from food products, aluminium can be quickly adsorbed on the gastrointestinal tract mucus: the mucin proteins constituting this substance can be precipitated by aluminium [138] and the hydroxypolymerisation of Al can be controlled by intercalation of freshly formed $\text{Al}(\text{OH})_3$ into the hydrated mucin polymer [139]. The metal ion is then slowly released into the blood. Exogeneous

ligands such as citrate increase aluminium mucosal permeation. It has been proven that other dietary ligands encountered in food products (ascorbate, gluconate, lactate, malate, oxalate, succinate, tartrate, fluoride, glutamate, gallate, chlorogenate, caffeate and protocatechulate) increase aluminium absorption and increase the pH of precipitation from 4.5 to nearly 8. However, other species such as phosphate, silica, Na^+ and Ca^{2+} ions have been found to decrease aluminium uptake [140].

2.4 Effects of aluminium on human and plant physiology

The effects and toxicity of aluminium can be observed in different locations and over different time scales. Greater amounts of Al are encountered in decreasing order of importance in bone, liver, muscle and brain. An excessive Al concentration is found as aluminosilicates in the brain of patients suffering from Alzheimer's disease [140]. Intrinsic effects are when the element is found to disturb natural processes by fixation on biomolecules whereas the toxicity of aluminium is extrinsic in the case of the modification of permeability by fixation of the element on natural membranes. In this case, aluminium enhances the membrane (for example Blood-Brain Barrier) porosity to some peptides, for example, amyloid fragments. This modification could be due to the binding of Al to the negatively charged sites present on the membranes [132]. In blood serum, Al^{3+} ion is mainly bonded to transferrin and albumin, but low molecular mass complexes may play an important role in the transport of the element. Al^{3+} binds to vacant Fe^{3+} sites of transferrin via the coordination of two Tyr, one His, one Asp and a synergistic bidentate carbonate ion in a pseudo-octahedral geometry [141], disrupting the overall Iron-dependant cellular processes. Al^{3+} can then be found in ferritin [140], the protein responsible for iron storage in the organism. Serum albumin binds weakly to about three Al^{3+} by six oxygen ligands in an octahedral site, which might be the Ca^{2+} binding site [141]. The activity related to the binding of the brain protein calmodulin to more than 40 proteins and enzymes depends on the alpha helical conformation of the Ca^{2+} coordinated protein. The replacement of Ca^{2+} by Al^{3+} provokes a breaking of this configuration, with concomitant loss of activity [142]. At Al concentrations higher than physiolog-

ical, Al binding to peptides from the β -amyloid sequence induces a conformational change from random coil to β -sheet required for aggregation initiation, aggregated β -amyloid being a hallmark of Alzheimer's disease.

Aluminium has been found to affect some structural proteins present in animal muscle or in plants, in which we are particularly interested.

Since actin filaments bear a high negative charge, aluminium can destabilize the filaments by increasing the disassembly rate in the absence of actin binding proteins (Filamin, spectrin, and fimbrin) and bridge the negative charges of adjacent filaments in their presence [143].

The irreversible Al^{3+} binding and subsequent structural alterations (reduction of the β -sheet structure and increase in the coil-turn conformations) of the bioelastomer elastin makes it completely resistant to calcification. 'Elastic' tissues such as the large arteries owe their remarkable properties of extensibility and elastic recoil to this protein. Recent advances in understanding the mechanisms of self-assembly of the elastin polymer, and in the development of materials based on elastin are finding application in a variety of uses including the design of novel self-assembling materials and biomaterials [144].

Aluminium binding to collagen results in transverse striations and in an increased temperature of contraction of the protein [132].

Aluminium can also become toxic for plants growing in acidic soils [145]. Some plants avoid this toxicity by exudation of aluminium-sequestering agents such as malic or citric acids, which immobilize the metal outside the root [146]. In addition, when bonded to an aluminium hydroxide surface, some of these sequestering agents (chlorogenic and caffeic acids), as well as other proteins such as parabactin, an adhesive protein from the blue mussel, reduce the pitting corrosion by protecting the passivating oxide layer of Al metal. Catecholate groups of these molecules, such as the dopa residue, bind to both soluble and insoluble metals [147]. Aluminium has been shown to affect porphyrin biosynthesis and phosphorylating enzymes [148]. When bonded to plant membrane surfaces, it favors H^+ extrusion and increases NO_3^- uptake [149]. It can also disturb diverse cellular functions, generally by the conformational change induced on the binding proteins, as in the case of yeast

glucose-6-phosphate dehydrogenase inactivation, where it induces a conformational change from ordered (α -helix + β -pleated sheet) to random coil via binding to the Lys and His residues [150].

Few studies have investigated interactions of Al species with proteins and other biopolymers with regard to materials chemistry applications. Examples of such studies include interactions of Al ions with elastin, actin [151] and poly-L-glutamic acid [152]. Hem and co-workers [153–155] have studied interactions of commercial Al hydroxide adjuvants with BSA and other proteins as model antigens. A significant effect of the surface charge of Al hydroxide on predominantly electrostatic interactions with BSA has been demonstrated, as well as a substantial impact of the adjuvant material on the antigen activity.

3. BIOMIMETIC APPROACH TO NANOSCALE OXIDE CERAMICS

Currently materials science is interested in non-metallic materials such as plastics, ceramics, glass and carbon fibres, and mixtures of these components (composites). The discipline called bionics by continental Europeans, biognosis by Americans and biomimetics in the other countries is the science searching for inspiration and models for novel materials through the observation of natural materials [156]. The basic approach of biomimetic synthesis tries to imitate the special building mechanisms of biological systems to obtain composites that are ordered from the nanometer to the mesoscopic length scale. A first step in this field is represented by the examination of the influence of organic molecules on crystallisation. These model systems can be nonbiological systems such as bicontinuous microemulsions, self-assembled monolayers, amphiphiles, polyglycolides, and biological systems including collagen, glycosaminoglycans, and noncollageneous proteins [157]. Self-assembly implies the spontaneous organisation of molecules, molecular clusters, and aggregate structures into two-dimensional arrays and three-dimensional networks by attractive forces or chemical bond formation. Biomineralisation, Nature's self-assembly, provides a strikingly elegant and economic approach to the formation of 2D and 3D structures in desired sizes, shapes, and physical and chemical properties [158].

The 'bottom-up' or 'nanotectonic' approach is a biomimetic strategy used to obtain structural organization over different length scales through the use of preformed building blocks. The term 'nanotectonics' of crystal tectonics regroups the use of shape-directed assembly and programmed assembly of nanoparticles comprising surface attached molecules, ligands, and recognition sites, as well as the formation of complex hybrid nanostructures by in situ transformation of unstable nanoparticle-based precursors (Figure 3.1). Alternatively, template-directed methods can be used

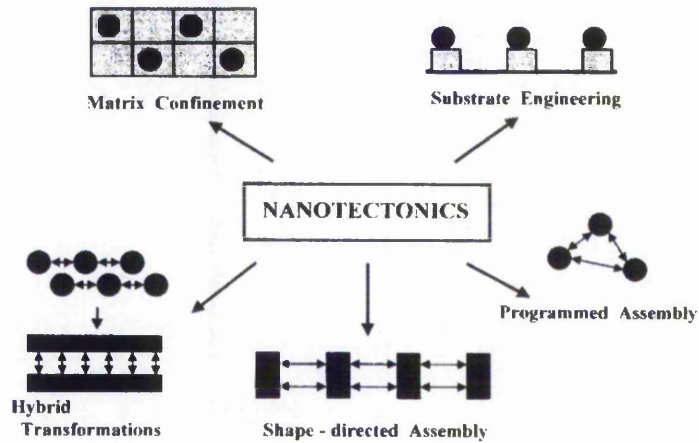


Fig. 3.1: Different strategies of the nanotectonic approach to materials synthesis [159].

in which preformed nanoparticles are confined in host structures such as bacterial superstructures, polymer sponges, and colloidal crystals, (matrix confinement) or on organic substrates such as coated polymer beads or bacterial membranes (substrate engineering) [159].

Composites synthesized using a biomimetic approach may show a number of superior properties compared to analogous conventional materials. Perhaps the most studied natural nanocomposite material is the nacre of abalone shell, an orientated coating composed of alternating layers of aragonite (CaCO_3) and a biopolymer (figure 3.2) [156]. The enhanced toughness of this nanostructured material arises both

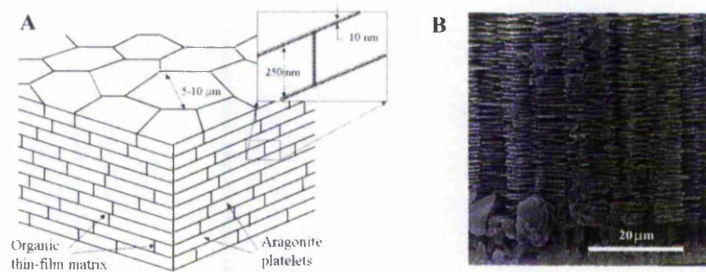


Fig. 3.2: SEM picture of the ordered structure of nacre (mother-of-pearl) giving rise to unique mechanical properties [160, 161].

from the deflection and absorption of microcracks, and from the elastic proteins hold-

ing the material together after the formation of a crack (figure 3.3) [156]. In this study we have exploited the ability of Al ions to self-assemble into large polynuclear units in aqueous solution and to provide molecular building blocks for a combined biomimetic-nanotectonic approach to the synthesis of hybrid Al-containing materials using various biopolymers. Nacre contains mainly β -chitin, silk-fibroin-like protein (Lustrin-A), and water-soluble acidic macromolecules (rich in aspartic acid residues). A protein fraction representing only 6 mol% of the total amino acid con-

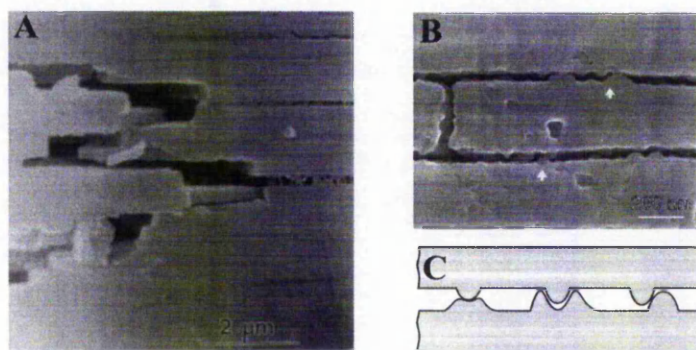


Fig. 3.3: Different explanations of the mechanical properties of nacre: (A) the presence of proteins holding the material together [162] and (B,C) the presence of microstructure giving rise to a higher energy dispersion during deformation [163].

tent has been shown to induce CaCO_3 crystallisation, this property being mimicked by synthetic Poly (Asp-Leu) and Poly-L-aspartate [164]. The conformation and microenvironment of the macromolecules might be an important requirement for the specific nucleation, as the β -sheet conformation assumed by Poly(Asp-Leu) in a 1:2 of Ca:COOH solution seems to have a crucial impact on this process. However, this prearrangement is not always necessary, as nucleation occurs in the presence of soluble polyanionic proteins [164]. Several attempts have been made to mimic the properties of nacre in synthetic materials. The fracture deflection and absorption toughening mechanism of nacre has been mimicked in a laminated material formed of ceramic and graphite co-laminated and sintered [165], whereas the elasticity of nacre protein matrix can be reproduced using a polymeric matrix.

As explained during the first part of this introduction, the aqueous speciation of aluminium and therefore the materials produced from the precursors present in solution is strongly dependant on parameters such as acidity, ionic strength or temperature. Another important parameter is the presence, in solution or on a surface, of ligands other than water-based. The theories of formation of natural materials such as nacre predict that proteins offer binding sites which are able to act as heterogeneous nucleation sites (see section devoted to Al hydroxides), promote the formation of thermodynamically unlikely crystal allotropes by provision of nucleation sites, and act as scaffolding agents for the formation of multi-level organised structures from inorganic precursor molecules or particles [166]. During his PhD project in this group, K. Shafran demonstrated the effect of small inorganic or organic ligands on aluminium and zirconium aqueous speciation, and started to look at the interactions of metal ions with an aminoacid, glycine [26]. Combined to the use of precursors such as Al polycations or monodisperse Al hydroxides, the soft complexation properties of aminoacids, peptides and proteins could lead to the formation of supramolecular entities in which the structural peculiarities of aluminium would be preserved. Due to a predictable decrease in repulsive force between the particles, these hybrid precursors would be able to assemble without leading to the dissociation of aluminium polycations. During the present work, we decided to study the soft complexation and templating processes of model Al species by proteins using a systematic approach. In a first part of the project, we tried to develop synthesis and characterisation methods enabling the obtention of pure aluminium species systems, these true building blocks being then used in conjunction with a model protein, BSA, and the bioelastomer elastin, for the preparation of bioinorganic composites in a biomimetic approach to materials synthesis.

BIBLIOGRAPHY

- [1] M. Chabanel and P. Gressier, *Liaison Chimique et Spectroscopie*, 1991.
- [2] W. L. Jorgensen and L. Salem, *The Organic Chemist's Book of Orbitals*, Academic Press, 1973.
- [3] M. Henry, J. P. Jolivet, and J. Livage, *Structure and Bonding*, 1992, **77**, 153–206.
- [4] R. Sanderson, *Science*, 1951, **114**, 670.
- [5] L. Pauling, *Journal of the American Chemical Society*, 1932, **54**, 3570–3582.
- [6] R. G. Parr, R. A. Donnelly, M. Levy, and W. E. Palke, *Journal of Chemical Physics*, 1978, **68**(8), 3801–3807.
- [7] R. G. Parr and R. G. Pearson, *Journal of the American Chemical Society*, 1983, **105**, 7512–7516.
- [8] W. Yang and R. G. Parr, *Proceedings of the National Academy of sciences of the USA*, 1985, **82**, 6723–6726.
- [9] A. Allred and F. Rochow, *Journal of Inorganic and Nuclear Chemistry*, 1958, **5**, 264.
- [10] K. Shafran, O. Deschaume, and C. C. Perry, *Advanced Engineering Materials*, 2004, **6**(10), 836–839.
- [11] J. E. Huheey, Harper and Row, 1978; p. 174.
- [12] M. Magini, G. Licheri, G. Pashina, and G. Pinna, *X-Ray Diffraction of Ions in Aqueous Solutions: Hydration and Complex Formation*, CRC Press, Boca Raton, 1988.

- [13] H. Ohtaki and T. Radnai, *Chemical Reviews*, 1993, **93**, 1157–1204.
- [14] R. E. Mesmer and C. F. Baes Jr. In ed. B. J. J. Zelinski, C. Jeffrey Brinker, D. E. Clark, and D. R. Ulrich, *Better Ceramics Through Chemistry IV (Materials Research Society Symposium Proceedings, Vol. 180)*. Materials Research Society, 1990.
- [15] D. Baes Jr and R. Mesmer, *The hydrolysis of cations*, Wiley-Interscience, 1976.
- [16] C. Jorgensen, Academic Press, 1963; p. 15.
- [17] D. Kepert, *The Early Transition Metals*, Academic Press, 1972.
- [18] G. Charlot, *L'Analyse Qualitative et les Reactions en Solution*, 6th ed., Masson, Paris, 1969.
- [19] A. Ringbom, *Les complexes en Chimie Analytique*, Dunod, Paris, 1967.
- [20] L. Sillen, *Stability Constants of Metal-Ion Complexes, Special Publication No. 17*, The Chemical Society, London, 1964.
- [21] L. Sillen, *Stability Constants of Metal-Ion Complexes, Special Publication No. 25*, The Chemical Society, London, 1971.
- [22] J. Kragten, *Atlas of Metal Ligand Equilibrium in Aqueous Solution*, J. Wiley & Sons, Chichester, 1978.
- [23] J. W. Akitt, *Progress in NMR Spectroscopy*, 1989, **21**, 1–149.
- [24] E. Matijevic, *Pure and Applied Chemistry*, 1980, **52**, 1179.
- [25] J. P. Jolivet, *From Solution to Solid State*, Wiley and Sons, 2000.
- [26] K. Shafran, *Chemical and structural studies of aluminium and zirconium aqueous chemistry*, PhD thesis, Nottingham Trent University, 2003.
- [27] L.-O. Öhman and W. Forsling, *Acta Chemica Scandinavica A*, 1981, **35**, 795–802.

- [28] F. Basolo and R. Pearson, *Mechanisms of Inorganic Reactions*, 2nd ed., J. Wiley & Sons, New York, 1958.
- [29] C. Rollinson, American Chemical Society Master Series, 1956; p. 448.
- [30] V. Baran, *Coordination Chemistry Reviews*, 1971, **6**, 65.
- [31] D. Wang, W. Sun, Y. Xu, H. Tang, and J. Gregory, *Colloids and Surfaces A: Physicochem. Eng. Aspects*, 2004, **243**, 1–10.
- [32] I. Benito, A. del Riego, M. Martínez, C. Blanco, C. Pesquera, and F. González, *Applied Catalysis A: General*, 1999, **180**, 175–182.
- [33] J. J. Fitzgerald and A. H. Rosenberg, Marcel Dekker, 1999; chapter 4 Chemistry of Aluminum Chlorohydrate and Activated Aluminum Chlorohydrates, pp. 83–137.
- [34] G. Sposito, *The Environmental Chemistry of Aluminium*, Lewis Publishers, CRC Press, 1996.
- [35] W. H. Casey, B. L. Phillips, and G. Furrer, 2002; chapter Aqueous Aluminum Polynuclear Complexes and Nanoclusters: A Review, pp. 166–190.
- [36] R. Flarend, *Aluminum and Alzheimers Disease*, Elsevier, 2001.
- [37] S. Bi, C. Wang, Q. Cao, and C. Zhang, *Coordination Chemistry Reviews*, 2004, **248**, 441–455.
- [38] J. H. Son and Y.-U. Kwon, *Inorganic Chemistry*, 2003, **42**, 4153–4159.
- [39] J.-H. Son, H. Choi, and Y.-U. Kwon, *Journal of the American Chemical Society*, 2000, **122**, 7432–7433.
- [40] J.-H. Son, H. Choi, Y.-U. Kwon, and O. Hee Han, *Journal of Non-Crystalline Solids*, 2003, **318**, 186–192.
- [41] J.-H. Son and Y.-U. Kwon, *Inorganica Chimica Acta*, 2005, **358**, 310–314.

- [42] N. Sanson, F. Bouyer, C. Gerardin, and M. In, *Physical Chemistry, Chemical Physics*, 2004, **6**, 1463–1466.
- [43] L. F. Nazar, G. Fu, and A. D. Bain, *Journal of the Chemical Society, Chemical Communications*, 1992, pp. 251–253.
- [44] G. Jander and A. Winker, *Zeitschrift für Anorganische und Allgemeine Chemie*, 1931, **200**, 257.
- [45] C. Brosset, *Acta Chemica Scandinavica*, 1952, **6**, 910.
- [46] W. H. Casey, *Chemical Reviews C*, 2006, **106**(1), 1–16.
- [47] C. Brosset, G. Biedermann, and L. Sillen, *Acta Chemica Scandinavica*, 1954, **8**, 1917.
- [48] L. Sillen, *Acta Chemica Scandinavica*, 1954, **8**, 299.
- [49] P. Hsu and C. Rich, *Soil Science Society of America Proceedings*, 1960, **24**, 21.
- [50] P. Hsu and T. Bates, *Mineralogy Magazine*, 1964, **33**, 749.
- [51] R. Stol, A. Van Helden, and P. Bruyn, *Journal of Colloid and Interface Science*, 1976, **57**, 115.
- [52] P. Hsu, *On Soil Chemistry*, Science Press, Beijing, 1986.
- [53] P. Huang, *Soil Chemistry*, Science Press, Beijing, 1991.
- [54] A. Schutz, W. Stone, G. Poncelet, and J. Fripiat, *Clays and Clay Minerals*, 1987, **35**, 251.
- [55] P. Hsu, *Minerals in Soil Environment, second edition*, Soil Science Society of America, Madison, 1988.
- [56] R. Letterman and S. Asolekar, *Water Research*, 1990, **24**, 931.
- [57] G. Johansson, *Arkiv For Kemi*, 1962, **20**(26), 305–319.

- [58] J. W. Akitt, N. N. Greenwood, and B. L. Khandelwal, *J.C.S. Dalton*, 1972, pp. 1226–1229.
- [59] J. W. Akitt and J. M. Elders, *Journal of the Chemical Society, Dalton Transactions*, 1988, pp. 1347–1355.
- [60] T. Hedlund, S. Sjöberg, and L.-O. Öhman, *Acta Chemica Scandinavica*, 1987, **41**, 197–207.
- [61] T. L. Feng, P. L. Gurian, M. D. Healy, and A. R. Barron, *Inorganic Chemistry*, 1990, **29**, 408–411.
- [62] C. Brinker and G. Scherer, *Sol-Gel Science: The Physics and Chemistry of Sol-Gel Processing*, 1990.
- [63] L. J. Michot, E. Montargès-Pelletier, B. S. Lartiges, J.-B. d'Espinoise de la Caillerie, and V. Briois, *Journal of the American Chemical Society*, 2000, **122**, 6048–6056.
- [64] W. Seichter, H.-J. Mögel, P. Brand, and D. Salah, *European Journal of Inorganic Chemistry*, 1998, pp. 795–797.
- [65] E. Morgado Jr., Y. L. Lam, and L. F. Nazar, *Journal Of Colloid And Interface Science*, 1997, **188**, 257–269.
- [66] J. F. Keggin, *Proceedings of the Royal Society of London, Series A, Mathematical and Physical Sciences*, 1934, **144**(851), 75–100.
- [67] L. C. W. Baker and D. C. Glick, *Chemical Reviews*, 1998, **98**, 3–49.
- [68] L. C. W. Baker and J. S. Figgis, *Journal of the American Chemical Society*, 1970, **92**(12), 3794–3797.
- [69] L. Allouche, C. Gerardin, T. Loiseau, G. Ferey, and F. Taulelle, *Angewandte Chemie International Edition*, 2000, **39**(3), 511–514.
- [70] W. H. Baur and T. Ohta, *Acta Crystallographica B*, 1982, **38**, 390–401.

- [71] J. Rowsell and L. F. Nazar, *Journal of the American Chemical Society*, 2000, **122**, 3777–3778.
- [72] G. Johansson, *Arkiv For Kemi*, 1962, **20**(27), 321–342.
- [73] J. Y. Bottero, D. Tchoubar, J. M. Cases, and F. Flessinger, *Journal of Physical Chemistry*, 1982, **86**, 3667–3673.
- [74] J. W. Akitt and A. Farthing, *Journal of the Chemical Society, Dalton Transactions*, 1981, pp. 1606–1608.
- [75] P. Jardine and L. Zelazni, *Soil Science Society of America Journal*, 1986, (50), 895–900.
- [76] S. Schonherr and H. P. Frey, *Zeitschrift fur Anorganische und Allgemeine Chemie*, 1979, **452**, 167.
- [77] G. Fu, L. F. Nazar, and A. D. Bain, *Chemistry of Materials*, 1991, **3**, 602–610.
- [78] L. Allouche and F. Taulelle, *Inorganic Chemistry Communications*, 2003, **6**, 1167–1170.
- [79] A. Nielsen, *Kinetics of Precipitation*, Pergamon Press, Oxford, 1964.
- [80] J. T. G. Overbeek, *Journal of Colloid and Interface Science*, 1982, **15**, 251.
- [81] A. E. Nielsen, Pergamon Press, London, 1967; p. 419.
- [82] A. Wells, *Structural Inorganic Chemistry, 5th ed.*, Clarendon Press, Oxford, 1991.
- [83] ed. H. Stanley and N. Ostrowsky, *On Growth and Form, Fractal and Non-Fractal Patterns in Physics*, number 100 in NATO Series E: Applied Sciences, Nijhoff, Martinus, 1986.
- [84] R. K. Iler, *The Chemistry of Silica*, 1979.
- [85] A. Nielsen and O. Sohnel, *Journal of Crystalline Growth*, 1971, **11**, 233.

- [86] H. Furedi-Milhofer, *Pure and Applied Chemistry*, 1981, **53**, 2041.
- [87] I. Stranski and D. Totomanov, *Naturwissenschaften*, 1933, **20**, 905.
- [88] H. Van Straten, B. Holtkamp, and P. De Bruyn, *Journal of Colloid and Interface Science*, 1984, **98**, 342.
- [89] H. Van Straten and P. De Bruyn, *Journal of Colloid and Interface Science*, 1984, **102**, 260.
- [90] D. Tchoubar and J.-Y. Bottero, *Comptes Rendus de l'Academie des Sciences Serie IIa: Geomateriaux*, 1996, **322**, 523-524.
- [91] G. Bye and K. Sing, Academic Press, London, 1973; p. 29.
- [92] M. Blesa and E. Matijevic, *Advanced Colloid and Interface Science*, 1989, **29**, 173.
- [93] P. Hsu, *Clays and Clay Minerals*, 1988, **36**, 25.
- [94] M. Axelos, D. Tchoubar, J. Bottero, and F. Fiessinger, *Journal de Physique*, 1985, **46**, 1587.
- [95] J. W. Akitt, *Journal of the Chemical Society, Dalton Transactions*, 1984, pp. 147-148.
- [96] R. F. Giese Jr., *Acta Crystallographica B*, 1976, **32**, 1719-1723.
- [97] A. Wells, Clarendon Press, Oxford, 1991; p. 635.
- [98] B. Baker and R. Pearson, *Journal of Catalysis*, 1974, **33**, 265.
- [99] B. Yoldas, *Journal of Applied Chemical Biotechnology*, 1977, **23**, 409.
- [100] A. W. Laubengayer and R. S. Weisz, *Journal of the American Chemical Society*, 1943, **65**, 247-250.
- [101] E. Matijevic, *Pure and Applied Chemistry*, 1988, **60**, 1479.
- [102] E. Matijevic, *Langmuir*, 1986, **2**, 12.

- [103] R. E. Flarend, T. Bin, D. Elmore, and H. S. L., *Food and Chemical Toxicology*, 2001, **39**, 163.
- [104] R. E. Flarend, S. L. Hem, J. L. White, D. Elmore, M. A. Suckow, A. C. Rudy, and E. A. Dandashli, *Vaccine*, 1997, **15**, 1314.
- [105] O. Guillard, B. Fauconneau, D. Olichon, G. Dedieu, and R. Deloncle, *The American Journal of Medecine*, 2004, **117**, 956–959.
- [106] C. Exley, *American Journal of Medecine*, 2004, **117**, 969–970.
- [107] G. V. Rao and K. S. Rao, *FEBS Journal*, 1992, **49**, 331.
- [108] R. A. Yokel and P. J. Mc Namara, *Pharmacology and Toxicology*, 2001, **88**, 159.
- [109] W. R. Harris, G. Berthon, J. P. Day, C. Exley, T. Peder Flaten, W. F. Forbes, T. Kiss, C. Orvig, and P. F. Zatta, *Journal of Toxicology and Environmental Health*, 1996, **48**, 543–568.
- [110] J. R. Shann and P. M. Bertsch, *Soil Science Society of America Journal*, 1993, **57**, 116.
- [111] D. R. Parker, T. B. Kinraide, and L. W. Zelazny, *Soil Society of America Journal*, 1988, **52**, 438–444.
- [112] D. R. Parker, T. B. Kinraide, and L. W. Zelazny, *Soil Science Society of America Journal*, 1989, **53**, 789–796.
- [113] C. Exley, J. S. Chappel, and J. D. Birchall, *Journal of Theoretical Biology*, 1991, **151**, 417.
- [114] C. Exley, A. J. Wicks, R. B. Hubert, and D. J. Birchall, *Journal of Theoretical Biology*, 1994, **167**, 415.
- [115] C. Exley, A. J. Wicks, R. B. Hubert, and D. J. Birchall, *Journal of Theoretical Biology*, 1996, **179**, 25.

- [116] B. Lothenbach, G. Furrer, and R. Schulin, *Environmental Science and Technology*, 1997, **31**, 1452.
- [117] G. Furrer, B. L. Phillips, K.-U. Ulrich, R. Pothig, and W. H. Casey, *science*, 2002, **297**, 2245–2247.
- [118] W. E. Dubbin and G. Sposito, *Environmental Science Technology*, 2005, **39**, 2509.
- [119] G. Furrer, B. Trusch, and C. Mueller, *Geochimica et Cosmochimica Acta*, 1992, **56**, 3831.
- [120] S. Forde and M. J. Hynes, *New Journal of Chemistry*, 2002, **26**, 1029–1034.
- [121] S. Hiradate and N. U. Yamaguchi, *Journal of Inorganic Biochemistry*, 2003, **97**, 2631.
- [122] A. Masion, F. Thomas, D. Tchoubar, J. Y. Bottero, and P. Tekely, *Langmuir*, 1994, **10**, 4353.
- [123] G. S. R. Krishnamurti, M. K. Wang, and P. M. Huang, *Clays and Clay Minerals*, 2004, **52**, 734.
- [124] P. Zhang, H. H. Hahn, E. Hoffmann, and G. Zeng, *Chemosphere*, 2004, **57**, 1489.
- [125] J.-P. Boisvert and C. Jolicoeur, *Colloids and Surfaces A: Physicochemical and Engineering Aspects*, 1999, **155**, 161–170.
- [126] G. L. Kerven, P. L. Larsen, and F. P. C. Blamey, *Soil Science Society of America Journal*, 1995, **59**, 765.
- [127] A. Masion, F. Thomas, D. Tchoubar, J. Y. Bottero, and P. J. Tekely, *Journal of Non-Crystalline Solids*, 1994, **171**, 191.
- [128] A. Masion, A. Vilge-Ritter, J. Rose, W. E. E. Stone, B. J. Teppen, D. Rybacki, and J.-Y. Bottero, *Environmental Science and Technology*, 2000, **34**, 3242–3246.

- [129] N. Yamaguchi, S. Hiradate, M. Mizoguchi, and T. Miyazaki, *Soil Science Society of America Journal*, 2004, **68**, 1838.
- [130] F. Gérard, J.-P. Boudot, and J. Ranger, *Applied Geochemistry*, 2001, **6**, 513–529.
- [131] D. Hunter and D. S. Ross, *Science*, 1991, **251**, 1056.
- [132] T. Kiss and M. Hollósi, *Aluminum and Alzheimers disease*, 2001.
- [133] T. Kiss, I. Sóvágó, I. Tóth, A. Lakatos, R. Bertani, A. Tapparo, G. Bombi, and R. B. Martin, *Journal of the chemical society, dalton transactions*, 1997, pp. 1967–1972.
- [134] P. Rubini, A. Lakatos, D. Champmartin, and T. Kiss, *Coordination Chemistry Reviews*, 2002, (228), 137–152.
- [135] R. L. Richards, C. R. Alving, and N. M. Wassef, *Journal of Pharmaceutical Sciences*, 1996, **85**(12), 1286–1289.
- [136] C. C. Perry, Wiley-VCH, 1998; chapter 11 Biomaterials, pp. 499–516.
- [137] D. Bohrer, P. Cicero do Nascimento, P. Martins, and R. Binotto, *Analytica Chimica Acta*, 2002, **459**(2), 267–276.
- [138] C. Exley, *Journal of Inorganic Biochemistry*, 1998, **70**, 195–206.
- [139] J. Powel, M. W. Whitehead, C. Ainley, M. Kendall, J. Nicholson, and P. Richard, *Journal of Inorganic Biochemistry*, 1999, **75**(3), 167–180.
- [140] G. Berthon, *Coordination Chemistry Reviews*, 2002, **228**, 319–341.
- [141] J. Aramini, J. Saponja, and H. Vogel, *Coordination Chemistry*, 1996, (149), 193–229.
- [142] B. Solomon, *Aluminum and Alzheimers Disease*, 2001.
- [143] E. Arnoys and M. Schindler, *Analytical Biochemistry*, 2000, (277), 1–10.

- [144] C. Bellingham and F. Keeley, *Current Opinion in Solid State and Materials Science*, 2004, **8**, 135139.
- [145] J. Igual and J. Dawson, *Canadian Journal of Botany*, 1999, (77), 1321–1326.
- [146] M. Schottelndreier, M. Norddahl, L. Strom, and U. Falkengren-Grerup, *Annals of Botany*, 2001, (87), 769–775.
- [147] J. Putterill and R. Gardner, *Biochimica and Biophysica Acta*, 1988, (964), 137–145.
- [148] L. Copeland and M. De Lima, *Journal of Plant Physiology*, 1992, **140**, 641–645.
- [149] T. Rufty, C. McKown, D. Lazof, and T. Carter, *Plant, Cell and Environment*, 1995, (18), 1325–1331.
- [150] S.-W. Cho and J. Joshi, *Biochemistry*, 1989, (28).
- [151] Z. Krejpcio and R. Wojciak, *Polish Journal of Environmental Studies*, 2002, **11**, 251.
- [152] J. Jan and D. Shantz, *Chemical Communications*, 2005, p. 2137.
- [153] A. Wittayanukulluk, D. Jiang, F. Regnier, and S. Hem, *Vaccine*, 2004, **22**(9–10), 1172–1176.
- [154] R. Al-Shakhshir, F. Regnier, J. White, and S. Hem, *Vaccine*, 1995, **13**(1), 41–44.
- [155] R. Al-Shakhshir, F. Regnier, J. White, and S. Hem, *Vaccine*, 1994, **12**(5), 472–474.
- [156] A. Sellinger, P. M. Weiss, A. Nguyen, Y. Lu, R. A. Assink, W. Gong, and C. J. Brinker, *Nature*, 1998, **394**(6690), 256–260.
- [157] S. Busch, U. Schwarz, and R. Kniep, *Chemistry of Materials*, 2001, (13), 3260–3271.

- [158] J. H. Fendler, *Chemistry of Materials*, 2001, **13**, 3196–3210.
- [159] S. A. Davis, M. Breulmann, K. Rhodes, H. B. Zhang, and S. Mann, *Chemistry of Materials*, 2001, (13), 3218–3226.
- [160] M. Sarikaya, H. Fong, J. M. Sopp, K. S. Katti, and G. Mayer In *15th ASCE Engineering Mechanics Conference*, 2002.
- [161] D. Chateigner, C. Hedegaard, and H.-R. Wenk, *Journal of Structural Geology*, 2000, **22**, 1723–1735.
- [162] A. P. Jackson, J. F. V. Vincent, and R. Turner, *Proceedings of the Royal Society of London, Series B, Biological Sciences*, 1988, **234**, 415–440.
- [163] R. Wang, Z. Suo, A. Evans, N. Yao, and I. Aksay, *Journal of materials research*, 2001, **16**(9), 2485–2493.
- [164] K. Naka and Y. Chujo, *Chemistry of Materials*, 2001, (13), 3245–3259.
- [165] B. Clegg, *Materials World*, 1998, **6**(4), 215–216.
- [166] A. H. Heuer, D. J. Fink, V. J. Laraia, J. L. Arias, P. D. Calvert, K. Kendall, G. L. Messing, J. Blackwell, P. C. Rieke, D. H. Thompson, A. P. Wheeler, A. Veis, and A. I. Caplan, *Science*, 1992, **255**, 1098–1097.

Part II

MATERIALS AND METHODS

4. SOLUTION STATE AND COLLOIDAL CHARACTERISATION TECHNIQUES

4.1 Potentiometric techniques

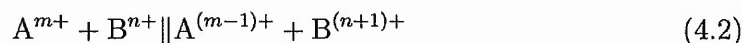
4.1.1 Definition of potentiometry

Potentiometry and potentiometric titrations are the oldest, most established and most widely used methods for speciation studies in aluminium ion solutions [1]. Potentiometry is the application of the Nernst equation to detect the unknown concentration of an analyte in solution by measuring the expressed voltage of a redox reaction when it is connected to a half-reaction with known composition (and half-cell potential) [2]. The Nernst equation can be written as follows [2]:

$$E = E^0 - \left(\frac{RT}{nF}\right) \ln Q \quad (4.1)$$

Where E is the Nernst potential of half-cell; E^0 is the standard Nernst potential; R is the universal gas constant; n is the number of electrons; F is the Faraday constant; Q is the concentration quotient of the components in a half-cell.

A potentiometric measurement is based on the principle that if one has a redox reaction:



and the cell voltage is known as well as the concentration of three of the reagents, one may determine the concentration of the fourth. The system is composed of two half-cells (one is the reference electrode, the other is the indicator electrode) and a voltmeter to measure the cell potential [3]. pH electrodes and chloride selective electrodes were used during this project.

4.1.2 Potentiometric equipment and single-point measurement procedures

pH measurements

In the case of the pH measurement setup, the indicator electrode is composed of a glass membrane on which H^+ can replace Na^+ present in the structure, giving rise to a measurable potential [3], while the reference electrode can be silver-silver halide or saturated calomel electrode [4].

During the project, pH measurements were carried out using a high-precision Radiometer potentiometer PHM 240 fitted with a Red-Rod combined glass electrode pH 2008 with internal reference and double junction. All pH measurement devices (pH meters, but also the pH meter included in the automatic titration unit) were calibrated every 24 hours at the relevant temperature and with four standard IUPAC pH buffers (pH=1.687, 4.005, 7.000, 10.012) in the case of potentiometric titrations (wide pH range needed) and with a choice of these buffers in the case of measurements carried out over narrower pH domains. Temperature was evaluated during calibration and measurements using a Radiometer temperature sensor type T201. Finally, for long experiments such as titrations, readings of pH and temperature were stored by connecting the pH meter or automatic titration unit to a PC, whereas single measurements were stored after equilibration of the reading under stirring.

Chloride ion concentration measurements

For Cl^- measurement, a chloride selective electrode (Cl.S.E.) is used together with a chloride-free Hg/Hg_2SO_4 reference electrode. The selective electrode uses a solid-state membrane of a sparingly soluble silver chloride/silver sulphide salt. In non-saturated solutions, the membrane slowly dissolves, the chloride sensitivity arising from the dissolution equilibria at the membrane surface. The sensitivity is around $1 \cdot 10^{-6}M$ and none of the ions present in our systems interferes with the measurement. In order to determine the hydrolysis ratio $h = \frac{[OH^-]}{[Al^{3+}]}$ of the model solutions prepared using the ion exchange technique, chloride ion concentration was precisely measured by means of an ion selective electrode. A PHM250 ion analyser fitted with a T201

temperature sensor, Ref621 Hg/Hg₂SO₄ reference electrode and an ISE25Cl solid-state chloride-selective electrode (all from Radiometer) was used for this purpose. Three standard sodium chloride solutions with concentrations 0.1, 1 and 10 mMol/L were prepared by successive dilutions of a chloride ion standard (0.1N solution, Fluka) in acetate buffer. The acetate buffer containing 0.2mol/L acetic acid was prepared by diluting 12g of acetic acid glacial in deionised distilled water followed by base titration to pH 4 using a 4M KOH solution. To avoid any deviation in the measurements, the electrodes were successively immersed in the 10mMol/L chloride standard and calibrated using the three standards until stable consistent readings were obtained. Calibration and sample measurements were read and recorded in a text format during 3min for each of the solutions in order to ensure the stability of the measurement. The calibration and measurement steps were all performed at 25°C.

4.1.3 *Potentiometric titrations. Principles and instrumentation*

Titrimetric analysis consists in determining the number of moles of reagent (titrant), required to react quantitatively with the substance being determined (sample). The titrant can be added:

- (a) Volumetrically, with a glass or automatic burette or with a low flow-rate pump.
- (b) Coulometrically, e.g. generated electrochemically from a proper electrolyte [3].

Various methods are available to detect the end-point of the titration: spectrophotometry, potentiometry, amperometry, conductometry [3].

In a modern analytical chemistry laboratory, automation of titration procedures has many advantages: (i) measurement becomes convenient and fast, (ii) analysis can be carried out without supervision, and (iii) there is a possibility for advanced data treatment [4]. Several devices for the automatic transfer of titrant can be used [4, 5]. Piston burettes are highly reliable, do not require calibration, but are expensive. Peristaltic pumps are of relatively low cost and highly versatile. However, they require frequent calibration due to the continual changes in the physical properties of the flexible tubes employed. Suction-stroke piston pumps (metering pumps) are as versatile as the peristaltic pumps, but are more precise and require

less calibration.

For a given point-by-point titration, stability criteria and kinetic parameters can be set to adapt the speed of titration to the system response. Moreover, cell configuration, stirring, end-point detector position and mode of titrant addition have to be optimised. Equilibrium throughout the titration curve can be attained only when the titrant is dispensed at an infinitely low rate. Two factors determine the rate at which the measurement reaches equilibrium: the kinetics of the chemical reaction involved and the electrode response time. These two factors are the slowest in the vicinity of the equivalence point, from which quantitative information can be derived. End points can therefore be delayed [4], the magnitude of this delay depending on parameters such as the analyte and titrant concentrations or the dispensing rate. Several strategies are used to virtually eliminate this artefact [5]:

(a) Modify the dispensing rate, either throughout the entire titration (monotonic mode), or solely close to equivalence (dynamic mode). In the dynamic mode, the titrant injection rate is inversely proportional to the rate of potential change, $\partial E/\partial \lambda$, where λ is the volume of titrant added [4];

(b) Perform a repetitive-monotonic titration. In this mode a series of titrations is performed in a consecutive manner, the measurements being made under non-equilibrium conditions, the titrant being provided at a fast and constant rate. Each titration is stopped some time after the end point. A new portion of sample is added to the cell and the titration is resumed at the previous rate. The new aliquot can be added also without suspending the flow of the titrant. Each end point in a series of such titrations is delayed once by a period of time depending on the titration parameters. Previous delays are not accumulated. The delay of the previous titration is always nullified a short time after a new portion of an analyte is added, since the response of the system is slow only around the equivalence point, but not far away from it.

Several methods are available to determine the end-point in titration curves [4]. For distinct and complete inflexion, the first derivative of the curve is often sufficient, whereas incomplete or broad inflexions require approaches for end-point determination such as Gran method.

4.1.4 Uses of potentiometric techniques in the present work

Potentiometric methods were employed for (a) standardisation of the stock solutions and anion exchange resin under OH^- form (back-titration of excess acid after neutralisation) using fully automated titration procedures, (b) speciation studies of Al ions in aqueous solutions using potentiometry to monitor Al^{3+} hydrolysis/condensation processes during forced hydrolysis using liquid base or anion exchanger and (c) to monitor Cl^- concentration and therefore the average Al^{3+} hydrolysis ratio during or after ion exchange experiments.

Two general strategies were employed for potentiometric titrations:

(a) single-batch mode, where small repetitive and monotonic additions of the titrant were made into one batch of sample step-wise. A relatively simple, easily automated way of performing speciation studies in metal ion solutions, this mode was however principally used for the standardisation of solutions rather than for the preparation of the samples themselves.

(b) multi-batch mode, where additions of the titrant (liquid base or anion exchanger) were made to multiple batches in order to adjust the hydrolysis ratio to a certain pre-defined level. This type of titration is harder to implement but offers a number of advantages discussed below.

4.1.5 Potentiometric titrations for standardisation of stock solutions of acids and alkalis

Commercial volumetric standard solutions of alkalis and acids were used during synthesis as well as for standardisation of the stock solutions of different bases and acids. In the case of stock solution standardisation, a volumetric solution of alkali or acid was used in a standard potentiometric titration procedure [3]. An aliquot of the stock solution was diluted with deionised water in order to be able to immerse the electrodes and injection device, as well as to avoid using too large an amount of both sample and titrant, and titrated with the volumetric standard using either an ABU91 autotitrator set in dynamic incremental mode with a 10 or 5 ml high-precision piston pump or a more modern Radiometer Titramaster using a similar

injection device and titration parameters. The concentration of the stock solution was calculated from the first derivative of the potentiometric curve. All solutions of KOH were sonicated for 15 min prior to use in standardisation procedures or any other experiments to eliminate the presence of dissolved carbon dioxide.

4.1.6 *Single-batch potentiometric titration setup*

Automated single-batch potentiometric titrations were performed during the first part of this project. The setup included a thermostated titration cell consisting of the titration vessel (round-bottom flask) adjusted to the desired temperature using a stirring-heating mantle (300-400 rpm). Titrants were delivered to the reaction vessel using an Eppendorf EDOS 5222 automatic burette. Pre-defined portions of titrant were added at chosen time intervals to the heated aluminium chloride solutions. Measurements of pH were conducted at pre-set time intervals (from 1 to 10 s depending on the time span of titration).

4.1.7 *Time-resolved potentiometric titrations*

In the course of potentiometric titrations with discrete titrant additions the system needs some time to stabilise prior to the next titrant addition. This required time is referred to as the 'stabilisation interval', 'delay time' or 'relaxation time' [4] and a time-resolved potentiometric curve during this (short) interval follows several distinct shapes.

The observation of particular shapes of the curves in 'stabilisation intervals' has been reported for studies of Fe^{3+} aqueous hydrolysis [6]. It was observed that the shapes of time-resolved (relaxation) curves during potentiometric titrations of Al-containing solutions fall into four general shapes [7].

There may be possible reasons for relaxation curves to occur: (a) insufficient mixing in the titration system, (b) slow equilibration at the working surface of the glass electrode, (c) temperature variations and (d) chemical processes occurring in the system are relatively slow. The former 3 sources of deviation can be minimised by a careful control over experimental conditions and by the use of precise equipment properly calibrated, the relaxation behavior observed between regular titrant

additions is primarily related to chemical processes occurring in these time intervals.

4.1.8 Multi-batch titrations

Multi-batch titrations are a useful alternative to single-batch titrations since they allow simultaneous and independent study of processes arising under different conditions. These conditions include reagent ratios (hydrolysis ratios in the present case), temperature, ionic strength and any other significant parameters. This approach is therefore very attractive for the systematic study of aluminium hydrolysis-condensation reactions which are known for their complexity and the numerous factors affecting the processes (see introduction). The multi-batch titrations described in the present work have been carried out using an anion exchanger under OH form as a base, the major aim the initial part of the project being the improvement of the synthesis of polycationic species, as well as to understand the pathways of their formation and collapse. Every sample was produced at a different hydrolysis ratio ranging from $h=0.5$ to $h=3.0$ by rapid mixing with the anion exchanger, as described in the following developments of this section.

4.1.9 The ion exchange experiments

Methods of ion exchange have long been known in materials science as an excellent alternative to neutralisation techniques involving strong acids or bases. Cation exchange has been successfully used to synthesise stable colloidal suspensions of molybdenum, tungsten, vanadium oxides [8–10] and silica [11]. Applications of anion exchange have been reported for the controlled condensation of $ZrO(NO_3)_2$ and $TiO(NO_3)_2$, resulting in the formation of stable colloids [12]. The anion exchange method has also been used for the synthesis of colloidal precursors to several materials including oxides of Fe, Al, Cr, Zr and Ti [12–16]. Another application of anion exchange in the synthesis of metal oxides and hydroxides has been for the removal of undesired anions (e.g. sulfate, phosphate, etc.) after reaction in solution [17, 18]. To our knowledge the route described in this thesis has not been proposed for the targeted synthesis of Al polycation solutions, even though the ion exchange method has the virtue of being environmentally friendly, low-temperature and a low cost

method for the precise control of the properties of the resulting materials and suspensions [12, 13]. There are two main operational modes used in ion exchange: a dynamic or column mode and a static or batch mode [8, 12, 13]. In the dynamic version of the ion exchange method the solution of a metal ion precursor is forced through a column containing densely packed ion exchange resin. There is no time for equilibration of the flowing solution phase with the solid phase during the process which results in a concentration gradient of species along the column due to varying degree of exchange. Often, the metal ion solution needs to be passed through the resin bed several times to achieve complete exchange, as in the case of the synthesis of V_2O_5 gels [8]. This gradient and the inferred diversity of speciation do not pose a serious problem as the target product is a relatively stable colloidal phase of an oxide or hydroxide (e.g. colloidal silica, vanadia, etc.). However, when the targeted synthesis of metastable and, especially, charged species such as Al polycations is concerned where the exact concentration ratio of the metal ion and exchanged anions is very important, the presence of a speciation gradient across the column of resin can be detrimental giving rise to 'local perturbations' similar to those induced by alkaline neutralisation. The static mode to our mind is crucial for using ion exchange as a 'soft' technique for the synthesis of pure, homogeneous solutions of polynuclear metal ions and hydroxide nanoparticles. Kinetic control of the hydrolysis condensation reactions of metal ions in solution is carried out in this case by the slower release of hydroxide ions over the whole surface of the resin available for the exchange according to the following equilibrium:



Where $-An^{n+}$ - basic groups on the surface of the anion exchanger; n - the total number of surface groups in the case of monobasic functionalities; X^{z-} - the anion (usually a halogen, sulfate or phosphate ion) exchanged for hydroxide ion at the anion exchanger surface.

The rate and extent of exchange leading to the equilibrium schematically shown in equation 4.3 depends on the charge and other properties of the anion. The exchange of hydroxide ions for chloride ions is generally not a very favourable process and occurs only when there is a significant excess of chloride ions in solution. This helps

to control the kinetics of the process which slows down as chloride ions are gradually eliminated from the reaction medium [13]. Part of the released hydroxide ions will react quickly with the protons introduced by the autohydrolysis of monomeric metal ions, leading to an increase of the pH, as mentioned in the introduction.

The larger proportion of the hydroxide ions released will favour directly or indirectly (via the change of pH) the relatively slow formation of oxo- or hydroxopolymers with high nuclearity x and polymerisation degree m during the partial neutralisation of metal ions in solution. The extent of polymerisation depends on the hydrolysis ratio h of the system ($h=[\text{OH}^-]/[\text{Me}^{z+}]$) and can be precisely controlled by the level of chloride ions in solution exchanged with hydroxide ions on the resin.

Resin standardisation and stock solutions preparation

Commercially available anion exchange resin Amberlite IRA67 (Sigma), 15–60 mesh, in the chloride form (minimum total exchange capacity $0.0023 \text{ Mol}\cdot\text{g}^{-1}$ according to the manufacturer's data) was washed using deionised distilled water and transformed to the hydroxide form using an excess of 2M KOH solution prior to a second extensive washing with water before drying for 48 h under ambient conditions. The titre of the processed resin (number of OH equivalents per gram of dry resin) was established using immersion in a known amount of a 1.0M HCl volumetric standard solution and subsequent back-titration of the excess free acid with a CO_2 -free 1.008M KOH volumetric standard solution sonicated for 15–30 min prior to use. The exchange capacity of the fully conditioned OH form of the resin was typically around $0.0024 \pm 0.0001 \text{ Mol}\cdot\text{g}^{-1}$. The stock solution of 1.0M aluminium chloride was prepared by dissolving $\text{AlCl}_3\cdot 6\text{H}_2\text{O}$ (Aldrich, 99%) in distilled, deionised water, and the concentration of this solution established using spectrophotometric measurement with 'Ferron' organic reagent (1-iodo-2,3-hydroxyquinoline, Aldrich, 83%) [19]. This measurement was validated using a gravimetric determination of the total Al ion content according to a general analytical procedure based on precipitation of Al hydroxide with ammonia and consequent calcining of the precipitate at 1000°C [20, 21].

Multi-batch titrations

The hydrolysis ratio h was the major parameter varied in the present experiment. Sixteen suspensions containing the required amount of resin necessary to reach the desired hydrolysis ratios ($h=0.5$ to $h=3.0$) in 80.0 ml of deionised, distilled water, to which 20.0 ml of 1.0 M aluminium chloride solution was added. The suspensions were stirred throughout the process by means of an overhead stirrer fitted with a glass shaft and a Teflon stirrer blade, and maintained at $25.0\pm 0.1^\circ\text{C}$ in a jacketed glass reactor. The stirring of the suspension was stopped 3 h after addition of the AlCl_3 solution and the resin removed by filtering out through a HDPE¹ Buchner filter with $70\mu\text{m}$ pore diameter.

Targeted synthesis of the Al_{13} solution

For the hydrolysis ratio $h=2.45$ which gives the highest level of Al_{13} according to previous studies [22, 23], a large batch of the Al_{13} solution was prepared by adding 200 ml of a 1.0 M Al chloride solution to a calculated amount of the OH form of the resin suspended in 800 ml of deionised water. The mixture was then processed for 3h at $25\pm 0.1^\circ\text{C}$ and the resin removed by filtering out through a HDPE Buchner filter with $70\mu\text{m}$ pore diameter.

Targeted synthesis of the Al_{30} solution

In order to produce a test batch of Al_{30} -containing solution, the Al_{13} solution was prepared first as a precursor according to the procedure described above. The precursor solution was then heated at 85°C for 42h to speed up the process of the Al_{13} conversion into the Al_{30} . The conversion from Al_{13} to Al_{30} was further studied and optimised in a dedicated study by ^{27}Al NMR spectroscopy, using temperature and hydrolysis ratios as optimisation parameters. Both the developments of the ^{27}Al NMR data treatment technique and the specific ion exchange experiment carried out during this optimisation will be described in Chapter 8.

¹ High Density Poly-Ethylene

Targeted synthesis of the Al hydroxide solution

Suspensions of Al hydroxide were prepared at hydrolysis ratios of $2.7 < h < 3.5$. The initial sols of aluminium hydroxide with particle size as low as ca. 56 nm ($h=2.7$) were aged at room temperature for up to six months. Nearly monodisperse Al hydroxide sols with mean particle size between 5 and 90 nm, as measured by DLS, were obtained using room temperature ageing. The rate of increase of mean particle size was accelerated by ageing the suspensions at higher temperature. Similarly to the Al_{13} to Al_{30} conversion, the formation and growth of Al hydroxides was monitored in a separate experiment, using aluminium concentration, hydrolysis ratio and aging temperature as parameters. we will describe the ion exchange preparation used during this optimisation in Chapter 9.

Al species-protein interactions

Al_{13} and Al_{30} solutions were prepared following the procedure described previously. Three different sols of aluminium hydroxide were prepared by adjusting the hydrolysis ratio of the stock solution of $AlCl_3$ to $h \approx 3.0$ using the anion exchange method and ageing the resulting sols according to results of the chapter devoted to aluminium hydroxide particle sols, leading to mean particle sizes 26 ± 3 , 55 ± 6 and 82 ± 8 nm respectively, as measured by dynamic light scattering (DLS). The final aluminium concentration in all model solutions was 0.4 mol/L.

Soluble elastin was obtained according to the method of Partridge et al. [24], using the treatment of insoluble elastin (97%, Sigma) in a oxalic acid 0.1M solution followed by intensive rinsing and dialysis of the resulting solutions prior to filtration and freeze-drying. An aqueous stock solution of the protein (50mg/ml) was then prepared by dissolution of the freeze-dried material in distilled deionized water.

An aqueous stock solution of bovine serum albumin (BSA) (50mg/ml) was prepared by dissolving the protein (min. 96%, from Sigma) in distilled deionized water.

Al-BSA and Al-elastin solutions were prepared at room temperature by the addition of different amounts of fresh protein stock solutions to each of the model Al-containing systems. All Al-protein solutions were efficiently stirred during and

after mixing of Al-containing and protein solutions (for 60s) using a vortex stirrer and left ageing at room temperature ($25 \pm 0.2^\circ\text{C}$) for 24 hours. The final aluminium concentration in the samples was 0.2 M, and the protein concentration was varied from 0 to 25 mg/ml for Al-BSA and from 0 to 20mg/ml for Al-elastin samples in steps of 2.5 mg/ml.

4.2 UV-Vis spectroscopy

4.2.1 Principles and instrumentation of UV-Vis spectroscopy

Spectroscopy is the measurement and analysis of electromagnetic radiation absorbed, scattered, or emitted by atoms, molecules, or other chemical species. The absorption and emission of electromagnetic radiation is associated with changes in energy states of the molecules. UV-Vis spectrophotometry uses ultraviolet and visible electromagnetic radiation in the range from ca. 200 nm to 800 nm to energetically promote valence electrons in a molecule to an excited energy state. The UV-Vis spectrophotometer measures the absorption of energy by promoted electrons at a specific wavelength or over a range of wavelengths [2]. The Absorbance A is directly proportional to the path length, b , and the concentration, C , of the absorbing species. Beer's Law states that:

$$A = \epsilon bC \quad (4.4)$$

Where ϵ is a constant of proportionality, called the molar absorptivity (or extinction coefficient).

Only chemical species having chromophore groups (functional groups which are responsible for the absorption of light in the UV-Vis region, examples include aromatics, compounds with multiple bonds, heterocycles and coordination compounds) can be analysed using UV-Vis spectroscopy. In order to be detected and quantified, molecules which do not absorb in the UV-Vis region (Al^{3+} aqueous solution species for example) will need to be complexed with reagents containing chromophore groups (organic reagents) [2].

The advantages of spectrophotometric methods are: (1) easier and faster than volumetric and gravimetric methods, (2) minimum sample preparation, (3) small amount

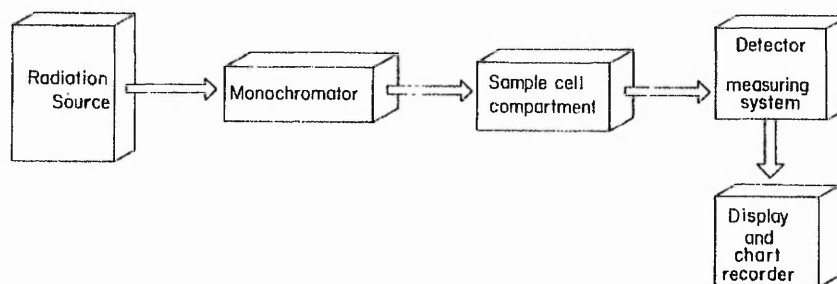


Fig. 4.1: A classical UV-Vis spectrometer arrangement.

of sample required, (4) medium sensitivity and (5) relatively high precision and accuracy. Disadvantages include possible interferences from foreign metal ions, anions and chromophores other than organic reagents.

The main requirements for spectrophotometric analysis are a sufficient stability of absorbing species and of their binding to the molecule to be determined. Moreover, colloidal and insoluble material should not be formed.

Classical single-beam UV-Vis spectrometers (Figure 4.1) are composed of a radiation source, a monochromator, a sample cell compartment, and a detector connected to an output device. In this work a UNICAM UV-Vis single-beam spectrophotometer with a beam split by a cross-section mirror was used. A tungsten-halogen lamp was used throughout this work, measurements being carried out in the 325-800nm wavelength region. The spectrophotometer contains a diffraction grating as a monochromator, a double cell compartment with reference and sample cell positions, a photomultiplier detector and is connected to a PC with Vision 32 UV-Vis software. The spectrophotometer allows for both spectrum scanning and fixed wavelength measurements. Zeroing and baseline correction of the blank sample was carried out for each sample. Plastic UV-Vis transparent cuvettes with 1 cm path length were used throughout.

4.2.2 Measurement of protein concentration

During the project, free protein concentrations were measured by a Bradford total protein concentration assay. An aliquot of 0.1 ml of the sample supernatant was

diluted in 9.9 ml of distilled deionized water. A volume of 1.0 ml of the resulting solution was mixed with 5.0 ml of the Bradford reagent containing 0.1g/L Coomassie Brilliant Blue G-250, 5.0% ethanol and 8.5% phosphoric acid (filtered before use) according to the method described in [25]. The absorbance of the solutions was integrated for 15 s at a wavelength of 590 nm 5 min after mixing and the protein concentration was calculated from the calibration curve obtained with BSA solutions of known concentration. Aluminium hydroxide particles were shown to not interfere with the measurement of BSA, as pure aluminium hydroxide sols showed near-zero absorbance at the wavelength used.

4.2.3 Aluminium quantification and speciation

As aluminium aqueous solution species do not absorb in the UV-Vis wavelength range we had to rely on the use of an adapted spectrophotometric reagent to carry out UV-Vis-based aluminium determination and speciation. As discussed previously, the main advantages of the UV-Vis technique are the ease and low price of application. In our case, an advanced data treatment technique enabled us to validate and complement the results derived from liquid-state ^{27}Al NMR using UV-Vis measurements.

Al³⁺ concentration measurement

Several spectrophotometric reagents have been proposed for aluminium determination and speciation, including aluminon, 8-hydroxyquinoline and its 7-iodo-5-sulfonic acid derivative, ferron. Ferron has been used in many studies of Al polymer formation. Its limit of sensitivity is $50\mu\text{g/L}$, and the response is linear up to $1500\mu\text{g/L}$ [26]. The background absorbance of the reagent can be reduced and the complex made more stable by using acetate buffer pH 5.2 and a reducing agent, hydroxylamine (NH_2OH , HCl) [19]. Moreover, the complexation of aluminium by ferron produces a decomposition of aluminium species at a rate related to the stability of the species in solution, enabling accurate speciation studies.

During this work, acid digestion followed by ferron spectrophotometric assay was used in order to determine accurately the total aluminium concentration. This

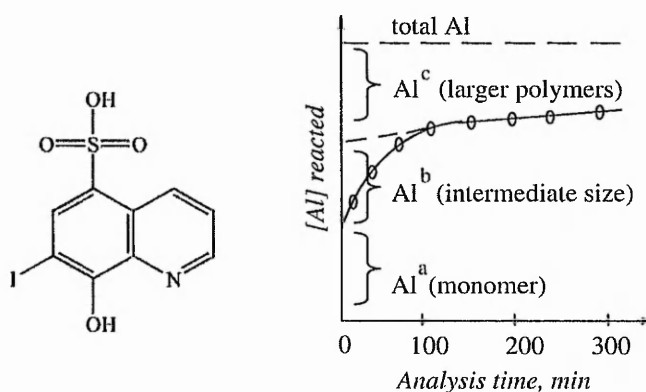


Fig. 4.2: The ferron molecule and scheme of a typical $[Al]=f(t)$ curve after mixing of Al solution with ferron, from which speciation information can be obtained.

technique has been suggested by Sposito in a review of aluminium determination techniques [26]. In an attempt to model the kinetics of surface dissolution of minerals, the proton and ligand-promoted dissociation of Al_{13} -mer has recently been investigated by Furrer [27]. In the case of the ligand-promoted dissociation, the decomposition rate of the polycation was interpreted as a function of two parallel reactions, one first-order and one second-order with respect to $[H^+]$. On the basis of available literature, the following process has been developed:

0.1 ml of the sample (0.2 or 0.4 mol/L, $h = \frac{[OH^-]}{[Al^{3+}]} = 0 \text{ to } 3$) was mixed with 2 ml HCl 1M and 7.9 ml water, and digested at $80^\circ C$ for four hours prior to ferron assay. The ferron assay was carried out by mixing the necessary amount of acid digested sample (0.2 and 0.4 ml for samples having respective initial theoretical aluminium concentration of 0.4 and 0.2 mol/L) with the ferron reagent. This technique was validated on different Al species by following the extent of acid digestion over time for different solutions of known Al concentration. The slowest kinetics of dissolution are obtained for Al hydroxide and Al_{30} -mer, however, from the figure which follows, the complete dissolution of Al hydroxide under the conditions of our determination seems to be attained after four hours (Figure 4.3).

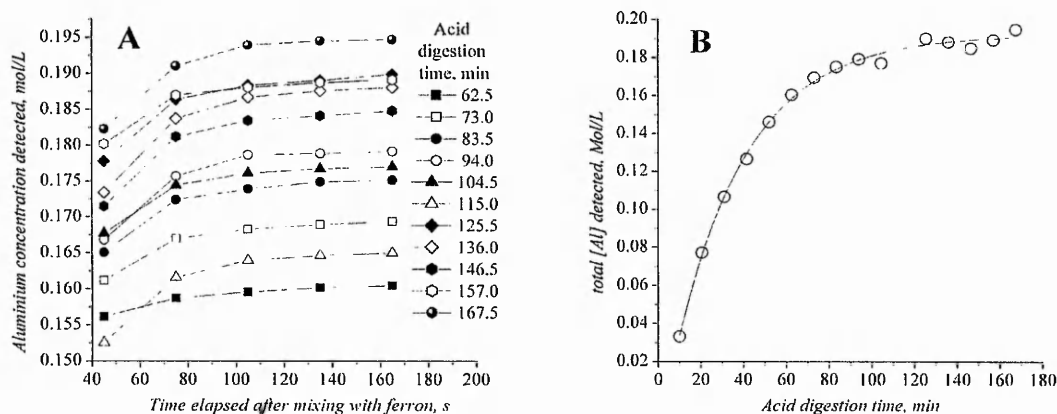


Fig. 4.3: Acid digestion monitored over time by means of ferron assay

Determination of the residual concentration of Al-ions after mixing with protein

The samples containing Al species and BSA were centrifuged for 30min at 3000rpm using a standard laboratory centrifuge. This low centrifugation speed was chosen in order to prevent free BSA or Al hydroxide sedimentation, and due to the relatively large particle size of the entities observed upon BSA addition. The supernatant of the solutions was then retained for residual aluminium and BSA concentration measurements and the solid material used for SEM characterization. In the case of Al₁₃ or Al₃₀-based samples phase separation was not observed probably due to the very small size of the particulates, and the residual protein and aluminium concentrations were therefore not measured. The concentration of free aluminium species in supernatant solutions after centrifugation was determined using a colorimetric ferron assay with preliminary acid digestion of the supernatant solutions to break down any polynuclear species and Al hydroxide that was present. For this purpose, an aliquot of 0.1ml of the supernatant solution was mixed with 2.0ml of 1.0 M HCl and 7.9ml of distilled, deionized water and digested for 48h at 60°C in a sealed tube. A 0.2 ml aliquot of the resulting solution was then mixed with 2.3ml of deionized water and 2.5 ml of ferron reagent (pH 5.2), containing $2 \cdot 10^{-3}$ M ferron (8-hydroxy-7-iodoquinoline-5-sulfonic acid, Fluka), 0.2 M acetic acid and 0.1 M hydroxylamine hydrochloride. The absorbance of the solutions was measured at 370nm, 1 hour after mixing, and the overall concentration of Al-ions in the supernatant was calculated

from the calibration curve obtained under the same conditions using an atomic absorption standard solution of Al-ions (0.986mg/L, Aldrich). In the case of Al-elastin interaction studies, the size of the composite particles formed was demonstrated to be well below the size determined in Al-BSA samples. The solutions were therefore subjected to a faster centrifugation treatment (13000rpm) to separate the composite material formed from the rest of the solution. The Al concentration in the supernatant was then determined by means of ICP² analysis after acid digestion of 0.1ml of the samples in 9.9ml HNO₃ 0.5M at 60°C for 48h. The calibration and determination of detection limits of the technique were carried out prior quantification using the atomic absorption used for the ferron assay calibration.

Ferron assay for aluminium speciation determination: a complementary method to ²⁷Al NMR

Together with potentiometry and ²⁷Al NMR, timed colorimetric methods have been the prevalent techniques applied to the study of aluminium hydrolysis and condensation [28–37]. Using 8-hydroxyquinoline, from which ferron is derived, Turner differentiated three Al fractions [30]. The fraction reacting instantaneously (Al^a) was assumed to be mononuclear species, including the hexaaqua, monohydroxo, dihydroxo and the tetrahydroxo aluminate ions. The more slowly reacting fraction (Al^b) was attributed to Al polycations, consumed by an apparent pseudo first-order reaction and transformed upon aging into a less reactive species [19, 38], which can be today attributed to the Al₃₀-mer. Finally, an Al fraction reacting slowly following a $\frac{2}{3}$ order process (Al^c), was attributed to Al hydroxides.

Subsequent investigations [31, 32] demonstrated the consistency of the method with predictions based on the nature of the synthesized hydroxy-Al solutions. Smith [33] and Smith and Hem [34] also identified three forms of Al corresponding to the results of Turner [31]. Their characterization was also based on differential kinetic reactions, although they employed a modification of the ferron-*o*-phenanthroline method [35]. Bersillon et al. [39] developed a speciation scheme for partially neutralized AlCl₃ solutions using (i) a modification of the ferron-*o*-phenanthroline procedure to es-

² Inductively Coupled Plasma

timate monomeric Al, (ii) a kinetically controlled selective adsorption procedure for the information on 'low' hydroxy-Al polymers, and (iii) a precipitation step to estimate 'medium' and 'high' hydroxy-Al polymeric species. These results were interpreted as being consistent with the hexameric ring scheme or core links model of polymer formation [39, 40]. In a study of hydroxy-Al solutions in $1 \cdot 10^{-3}$ to $10^{-2} \text{Mol} \cdot \text{L}^{-1}$ Al concentration range by ^{27}Al nuclear magnetic resonance (NMR) spectroscopy, Bertsch et al. [41–43] reported (Al_{13}) polynuclear species as the predominant polymer present in solutions. In partially neutralized AlCl_3 solutions of higher concentration (0.5M Al), the dimeric Al species was also observable by ^{27}Al NMR method [40]. In addition to Al_{13} and the monomeric species, a sizable Al fraction in these solutions that was not observable by ^{27}Al NMR spectroscopy was evidenced [44].

Ferron has also been used to differentiate Al species [34, 45, 46], the main advantage of this reagent over 8-hydroxyquinoline being its higher hydrophilicity. Smith assumed that mononuclear Al reacted instantaneously with ferron [33], intermediate polymers reacted by pseudo first-order kinetics, and large polymers or initial solid phases reacted with ferron extremely slowly or were totally inert. During our experiments, the respective stability of species towards ferron was $\text{Al monomer} < \text{Al dimer} < \text{Al}_{13}\text{-mer} < \text{Al hydroxide} < \text{Al}_{30}\text{-mer}$. On the basis of coupled ^{27}Al /ferron characterisation, the intermediate polymer fraction was later attributed to $\text{Al}_{13}\text{-mer}$ solely [47]. It has been suggested that at least four categories of soluble Al species exist in partially neutralized solutions with mononuclear Al distinguished from the others by assuming a 30s reaction with ferron [39]. Several researchers have noted the reaction of ferron with polymeric Al conformed to pseudo first-order kinetics [48, 49], with rapidly reacting polymers gradually developing into another polymeric species whose reaction with ferron was much slower [19, 48]. The arbitrary separation time for distinction of mononuclear and polynuclear Al was eliminated by Jardine and Zelazny [19, 50, 51] who modeled the kinetic reaction of ferron with partially neutralized Al solutions containing various inorganic or organic anions, and obtained the best results by assuming a first-order reaction kinetics of ferron with all the species present.

Our data treatment technique for differentiation of Al species Using calibration data, the curve of evolution of aluminium concentration reacted with ferron versus time can be calculated from the $A=f(t)$ curve, and fitted with a theoretical function (4.5).

$$C = C_{Al_1}(1 - e^{-k_{Al_1}t}) + C_{Al_2}(1 - e^{-k_{Al_2}t}) + C_{Al_{13}}(1 - e^{-k_{Al_{13}}t}) + C_{Al_{30}}(1 - e^{-k_{Al_{30}}t}) + C_{Al_h}(1 - e^{-k_{Al_h}t}) \quad (4.5)$$

With C_{Al_1} , C_{Al_2} , $C_{Al_{13}}$, $C_{Al_{30}}$, C_{Al_h} , the concentrations in aluminium monomer and dimer, Al_{13} -mer, Al_{30} -mer and Al hydroxide and k_{Al_1} , k_{Al_2} , $k_{Al_{13}}$, $k_{Al_{30}}$, k_{Al_h} , the kinetic constants for the corresponding species dissociation.

As we will see in a later section, the Non-Linear Least squares minimisation used for fitting requires initial values of the parameters. In a first implementation of the technique, the first estimates of kinetic constants were determined by reacting model solutions of each of the species individually with ferron and determining the constant by fit using a single exponential function, the goodness of the fit accounting for the purity of the system. The $C_{Al}=f(t)$ datasets for the samples were then fitted with the function presented above using the non-linear least squares curve fitting module of Microcal[®]Origin[®] 6.1 software, the kinetic constants being either fixed or allowed to vary within a narrow range. The disadvantages of this method were (a) irregularities in speciation evolution as a function of the parameter varied (time of ion exchange, hydrolysis ratio or time of temperature treatment) (b) overestimation or underestimation of the species concentrations (c) Time spent for data treatment and (d) influence of the operator carrying out the data treatment.

The second approach, used in order to attempt fixing the kinetic constant for all samples of a batch, was to carry out the fitting using the same algorithm, but carrying out the fitting on the whole dataset (several samples) sharing kinetic parameters. This approach was interesting but due to the fact that incoherent outputs and error messages were obtained from the software as well as a lack of access to the data fitting algorithm we decided to start using an alternative approach. Previous experience with MatLab[®] programming enabled us to use this language for the development of a curve data fitting and aluminium speciation analysis routine. Similarly to other fitting algorithms (GRAMS/32[®], Origin[®], Microsoft Excel[®])

our curve fitting algorithm uses the nonlinear least-squares minimisation technique for the optimisation of the fitting parameters. The difference is that MatLab enables access to the script and editing of this function. A section of this thesis is devoted to the explanation of such algorithms and of their possible artifacts.

In addition to the least-squares minimisation technique, a 'soft sharing' of the kinetic parameters was applied to kinetic constants determined for the same species present in different samples. The principle of this algorithm is presented below both as equations and as a flow chart (Figure 4.4). The philosophy behind this sharing method

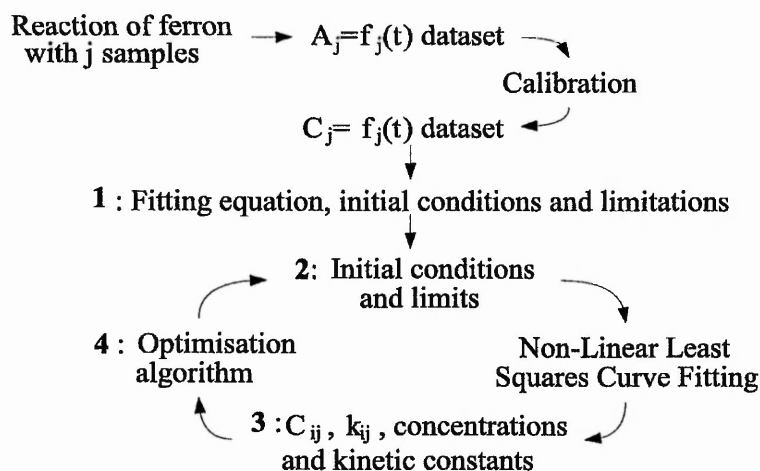


Fig. 4.4: The ferron data treatment optimisation algorithm

comes from the the nature of the system analysed. The mixture of species present in each sample is mixed with the ferron reagent at the beginning of the analysis. This reagent and the assay have been developed to 'buffer' any condition which could lead to a deviation in experimental conditions (pH, ionic strength, temperature). The kinetics of dissociation of one species should therefore be independent of the prehistory of the sample, especially in the low Al concentration range used and in the presence of acetate anions. However some authors using the ferron assay as the basis for their Al speciation determination show that a systematic variation of some of these kinetic constants occurs, for example, as a function of the hydrolysis ratio of the sample. As indicated by some of these authors, the source of this deviation must be the existence of other species with behavior similar to that of the major

species. As shown in the flow-chart of Figure 4.4, the treatment of experimental data starts with the calculation the Al fraction reacted with ferron as a function of time for each Absorbance=f(t) curve obtained. the resulting traces are modeled by the following fitting function (phase 1 in the flow chart),

$$C(t) = A_1(1 - e^{-k_1t}) + A_2(1 - e^{-k_2t}) + A_3(1 - e^{-k_3t}) + A_4(1 - e^{-k_4t}). \quad (4.6)$$

the assumption being made that the reaction of Al species with ferron obeys pseudo-first order kinetics. The initial values of the fitting parameters are input in the model, together with the variations allowed, σ (phase 2):

$$U_1 = \left(0.05 \quad 0.05 \quad 0.05 \quad 0.05 \quad k_1^1 \pm \sigma_1^1 \quad k_2^1 \pm \sigma_2^1 \quad k_3^1 \pm \sigma_3^1 \quad k_4^1 \pm \sigma_4^1 \right) \quad (4.7)$$

The total Al concentration is divided between the species (here 0.2M) and the kinetic constants k are given values in accordance with experimental and literature data. The total Al concentration is generally allowed to double but should not diverge to this extent over the iterative process.

After the fit (phase 3), new initial parameters and variations are computed from the values determined after minimisation (phase 4), the parameter p being fixed >1 if a more accentuated convergence is required:

$$k_j^n = \sum_i \frac{C_{ij} \wedge k_{ij}^{n-1}}{\sum_i C_{ij}} \quad \sigma_j^n = \frac{\max(k_{ij}^{n-1} - k_j^n)}{p} \quad (4.8)$$

With i , the sample index; j , the species index, $\max()$, the maximum of the expression in brackets and p , a parameter chosen to accentuate the convergence process.

These new parameters are then input in the fitting model

$$\left(0.05 \quad 0.05 \quad 0.05 \quad 0.05 \quad k_1^n \pm \sigma_1^n \quad k_2^n \pm \sigma_2^n \quad k_3^n \pm \sigma_3^n \quad k_4^n \pm \sigma_4^n \right) \quad (4.9)$$

and steps 2 to 4 are repeated n times, leading to a convergence of k for each species and a narrowing of the observed variations. For each iteration, a diagram presenting the different species concentration in the different samples characterised is plotted, and the final parameters estimates are stored after calculation.

4.3 ^{27}Al NMR spectroscopy

The main aluminium isotope (natural abundance of 100%), ^{27}Al , bears a spin quantum number of $\frac{5}{2}$. This isotope has a high intrinsic NMR sensitivity (Receptivity=0.206 and $1.17 \cdot 10^3$ respectively taking ^1H and ^{13}C as unity) and a high resonance frequency (26.077 MHz at a magnetic field strength where the protons of TMS resonate at 100 MHz and Al is in form Al_{aq}^{3+}). Finally, the magnetogyric ratio is estimated as $\gamma = 6.9763 \cdot 10^7 \text{rad} \cdot \text{s}^{-1} \cdot \text{T}^{-1}$. These characteristics clearly make ^{27}Al a favorable nucleus for study. Its one drawback is its quadrupole moment ($Q = 0.149 \cdot 10^{-28} \text{m}^2$) which means that its lines are in general broad [52–54].

4.3.1 Operational techniques

Due to the short relaxation time of the ^{27}Al nuclei, a Fourier transform mode of data collection is generally used and rapid pulse repetition rates with near 90° pulses gives acceptable spectra (the pulses must however be separated by at least five times T_1 to obtain quantitative results). The various parts of a complete Fourier transform (FT) system comparable to the spectrometer used throughout this work are shown on the block diagram of figure 4.5. Such a spectrometer comprises a strong, highly stable superconducting (cryo) magnet in whose gap the sample is placed and surrounded by transmitter-receiver coil. A superconducting magnet needs no current supply once the field is set up and so is inherently stable (no variation due to fluctuation in the power supply), though correcting circuits are still necessary. The magnetic field at the sample also inevitably varies throughout the bulk of the sample (i.e. the field is non-homogeneous) so that the signal frequency is not well defined and a further set of coils, known as shim coils, is placed around the sample in order to counteract these variations or field gradients and render the field as perfectly homogeneous as possible. Remaining inhomogeneities are minimized by spinning the sample tube about its long axis so that the sample molecules experience average fields. Very well defined frequencies, and so excellent resolution of close, narrow resonances is obtained in this way. The \mathbf{B}_1 field is produced by a gated (switched input) power amplifier driven by a stable, crystal controlled continuous oscillator. Because the \mathbf{B}_1

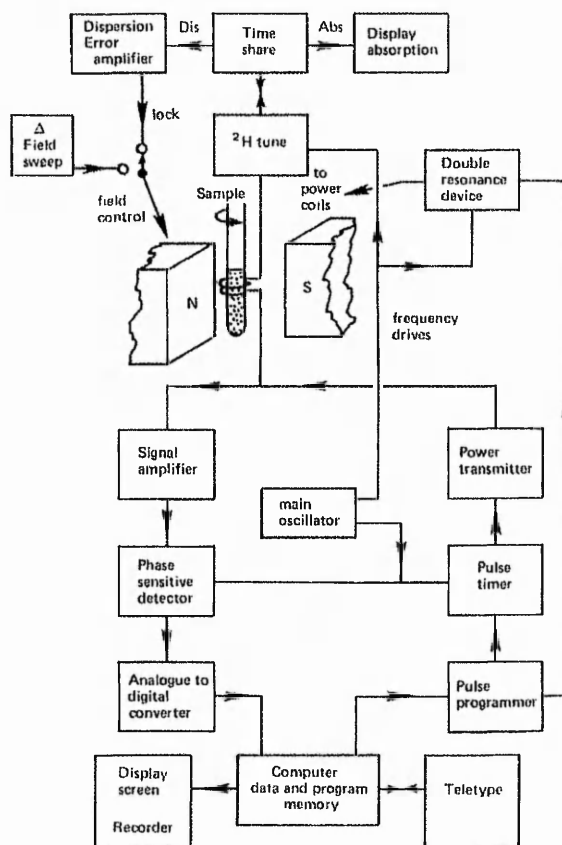


Fig. 4.5: A full FT system.

pulse is very short, its frequency is less well defined than that of the monochromatic crystal oscillator and has a bandwidth of $1/t$ Hz (t is the length of the pulse in seconds). It thus does not need to be exactly in resonance with the nuclei and indeed can cause simultaneous precession of nuclei with different frequencies. The nuclear signals are amplified and detected in a device which compares them with the crystal oscillator output (B_1 carrier) and gives a low frequency, time dependent output containing frequency, phase and amplitude information. This output is digitized and collected in a computer memory for further processing.

4.3.2 Phase correction

In principle, the technique of phase correction is no different from that with a spin $\frac{1}{2}$ nucleus. However, the first-order correction, in which the phase is varied linearly

across the spectrum, is not appropriate for broad lines. The phase of an individual line is determined by the starting point of its time domain signal and applies to the whole of that line. In the case of broad lines any phase adjustment should therefore be constant across the width of the line to avoid introducing distortion such as a sine wave into the spectrum. In order to avoid first-order phase correction, the data collection must commence immediately following the RF pulse. This is relatively straightforward to achieve since the signal emerging from the receiver is delayed one dwell time by the noise filters inserted prior to the computer digitizer and it is normal practice to commence data collection about one dwell time after the centre of the stimulating RF pulse [55]. The actual delay required depends upon the filter setting and if necessary can be found empirically by observing two well-separated resonances such as $[\text{Al}(\text{OH})_4]^-$ and $[\text{Al}(\text{H}_2\text{O})_6]^{3+}$ in a coaxial sample cell. Baseline roll is also a problem with broad line spectra which will be made worse by a first-order phase correction if there is any DC offset in either the real or imaginary component. The offset must therefore be removed carefully if a first-order correction is needed. Baseline roll can also be reduced by correct timing of the receiver enabling switch [55].

4.3.3 Missing intensity

The resonances obtained from a quadrupolar nucleus vary in breadth from quite narrow to undetectably broad. Therefore a given spectrum may not display all the responses of the nuclei present. Losses in intensity may be observed when the bandwidth of the spectrometer is close to or below the width of the observed resonances. In addition, the fact that the broader lines are defined by only a few points in a digitized FID has a major influence on the apparent intensity. The first and most intense point transforms as a DC offset assimilated to baseline in area measurements, the true skirts of the peak never descending to a true baseline level so that even if the FID is perfect, there will be a loss in line area. Quantitative measurements can be successful only if a line is less than one sixth of a sweepwidth when one expects theoretically to be able to observe about 90% of the area [54]. In order to get quantitative results, a broad bandwidth must therefore be coupled

with a very large sweepwidth. Overlapping broad and narrow lines also further confuse the baseline position of the broad component since the intensity of a narrow Lorentzian component is appreciable some distance from its centre. Moreover, when a curved baseline correction is applied too close to a broad line, the later will become narrower, leading to a significant loss of intensity. To take an example, Al_{13} gives a narrow ^{27}Al resonance at 62.5ppm from the AlO_4 nucleus and a very broad one from the twelve octahedrally coordinated aluminium atoms at about 12ppm. The AlO_4 resonance is clearly visible at room temperature whereas the octahedral component can only be fully observed if the solution is heated [56]. In this case the loss can be estimated by calculating the ratio of Al present in the two different sites, $\frac{\text{Al}_{Td}}{\text{Al}_{Oh}}$.

4.3.4 Quantification and referencing

Due to the possible losses in intensity and artifacts due to NMR equipment settings and construction, the ^{27}Al NMR analysis of any system should include quantitative estimates of the intensity of the resonance related to some external standard. For this purpose, an extrapolation of the FID or a concentric sample cell containing the sample in one compartment and a standard solution in the other can be used to determine the intensity of the signal. The $[\text{Al}(\text{H}_2\text{O})_6]^{3+}$ resonance in aqueous salt solutions and the $[\text{Al}(\text{OH})_4]^-$ resonance in aluminate solutions are two suitable standards. $[\text{Al}(\text{H}_2\text{O})_6]^{3+}$ solutions should be acidified ($\frac{[\text{H}^+]}{[\text{Al}^{3+}]} \geq 1$) to prevent self hydrolysis, and therefore give as narrow a resonance as possible, whereas an excess of alkali $\frac{\text{NaOH}}{\text{Al}} \geq 5$ has to be used in the case of aluminate to favor the complete detection of Al. The standards should in any case be calibrated against a solution of the other in a two compartment cell so as to eliminate any need for precision measurements of the cell size. The quantitative data are then extracted in the usual way by obtaining integrals. The aluminate standard is widespread as it overlaps with fewer resonances than the hexaaquo ion resonance. Baseline roll due to the broad use of aluminium in NMR tubes as well as in the ceramic bodies supporting the solenoids of NMR transducers may also interfere with the integrals and this should be minimized in setting up the spectrometer [55] or removed digitally if no broad lines are present. The background probe resonance present in many of

the new generation of high field spectrometers can be very annoying when making quantitative measurements [57]. It is generally subtracted out by running a blank sample, though the blank must have similar electrical characteristics to the sample to be measured.

4.3.5 The Spectroscopic parameters of aluminium-27

Quadrupole Relaxation

The electric charges in molecules provide field gradients at aluminium which couples the nucleus to the motion of the molecule. This mechanism provides a very efficient means of relaxation for the nucleus in liquids and for aluminium it is almost always the dominant mechanism of relaxation. For a ^{27}Al nucleus surrounded by a regular array of ligands with cubic symmetry, the nuclear resonance is narrow. Equally, if the symmetry is distorted or non-regular then the resonance will be broadened. These phenomena can be explained by quadrupole relaxation mechanisms.

The equation describing quadrupole relaxation of a single quadrupolar nucleus of spin I situated in a molecule with an isotropic tumbling correlation time τ_c is [58]

$$T_1^{-1} = T_2^{-1} = \frac{3\pi^2(2I+3)}{10I^2(2I-1)} \left(\frac{eQ}{h}\right)^2 V_{zz}^2 \left(1 + \frac{1}{3}\eta^2\right) \tau_c \quad (4.10)$$

With Q , the quadrupole moment of the nucleus; V_{zz} , the largest tensor component of the electric field gradient (EFG) at the nucleus; e , the charge on the electron and is included in the calculation of V_{zz} .

η is the asymmetry parameter of the EFG and is given by

$$\eta = \frac{V_{yy} - V_{xx}}{V_{zz}} \quad (4.11)$$

With V_{yy} , V_{xx} are the other two diagonal components of the EFG tensor.

Equation 4.10 consists of two parts; the terms involving I and Q , which are nuclear properties and are fixed for ^{27}Al , and the terms involving V_{zz} and τ_c , which are properties of the molecule in a particular solvent. It is generally assumed that all contributions to the EFG arise from the bonding electrons, an assumption that will be justified below. The molecular contribution to quadrupole relaxation contains two terms of interest, the EFG at the nucleus and the correlation time of the EFG

as it moves relative to the spectrometer magnetic field direction.

The principal interest in the latter term is that τ_c is temperature dependent and decreases with increasing temperature so that the linewidths of quadrupolar nuclei are very temperature sensitive and become narrower on heating. This reduction in relaxation rate with an increase in temperature arises because in the liquid state one is operating in the extreme narrowing region in which the rate of motion, or rather, its frequency, is much higher than the spectrometer operating frequency, and an increase in temperature increases this gap and reduces the efficiency of the relaxation process.

The EFG at a nucleus is related to the symmetry of the bonding electrons around that nucleus, so that linewidths also contain symmetry information. If one considers the nucleus to reside at the centre of a system of cartesian coordinates $(0, 0, 0)$ with charges q_i distributed around at points (x_i, y_i, z_i) there will in general be an electric field at the nucleus with three components in the x, y, z directions. The three components of this field may vary as one moves along any of x, y or z and thus nine quantities are needed to describe how the field varies in space, e.g the EFG tensor, expressed as [59, 60]:

$$EFG = \begin{bmatrix} V_{xx} & V_{xy} & V_{xz} \\ V_{xy} & V_{yy} & V_{yz} \\ V_{xz} & V_{yz} & V_{zz} \end{bmatrix} \quad (4.12)$$

where the terms are the sums of the contributions of all charges q_i with

$$V_{xx} = \sum q_i r_i^{-5} (3x_i^2 - r_i^2) \text{ etc.} \quad (4.13)$$

$$V_{xy} = \sum 3q_i r_i^{-5} x_i y_i \text{ etc.} \quad (4.14)$$

With r_i the distance of the charge q_i from the nucleus, equal to $(x_i^2 + y_i^2 + z_i^2)^{\frac{1}{2}}$

Equations 4.13 and 4.14 have an important property in that if there are two charges situated so as to be mutually inverted through $(0, 0, 0)$ so that their coordinates are x_i, y_i, z_i and $-x_i, -y_i, -z_i$, their contributions to V_{jj} or V_{jk} are of the same sign. Thus if one charge were to be moved to coincide with the other, the EFG would be unaltered. This has the consequence that if a nucleus is surrounded by an even number of equal charges paired by inversion through $(0, 0, 0)$ and their disposition

is such that the EFG is zero then it is possible to move some of the charges and maintain zero EFG. Thus one member of each inversion pair may be moved to be coincident with the other and one obtains an array of half the number of charges of doubled magnitude and, possibly with different symmetry properties but still with zero EFG. One could then halve the charge magnitude and the operation then in effect is equivalent to discarding half the charges paired by inversion. This property permits some non-cubic arrangements of ligands to have a zero EFG, contrary to accepted theory. In the case of equation 4.12 a suitable choice of axes causes all off diagonal terms to be zero and only three terms are then required to describe the EFG. Further, $V_{xx} + V_{yy} + V_{zz} = 0$ and if an asymmetry parameter is defined as in equation 4.11 then the EFG can be defined by just V_{zz} and η . If the ligands have axial symmetry around the z axis then $V_{xx} = V_{yy}$ and $\eta = 0$. It follows that in the axial symmetry case, if V_{zz} is zero then both V_{xx} and V_{yy} must be zero.

Therefore distortion is not inevitably inimical to there being a low EFG in a complex. If the reflection rule is applied to a cubic array of eight equal charges with a quadrupolar nucleus at its centre, where the EFG is zero, it is found that two structures with zero EFG can be derived. One is the well-known tetrahedron and the other is the all-*cis* half cube. These all-*cis* arrangements are clearly non-cubic and yet have a zero EFG point on their axis of rotation symmetry. This can be understood by noting that for an axially symmetrical structure the EFG tensor must be zero if the gradient along the axis is zero, so that one needs to think in terms of only one of the three components. The electric field of a number of charges symmetrically disposed in a plane about an axis will be zero at the centre of the charges and will also be zero at infinity on either side of the plane. It follows that the electric field will have two maxima, one on either side of the plane, where the gradient will be zero along the axis, and where the EFG tensor will also be zero. The charge distribution in the plane can be continuous, i.e. an annulus of charge, or can be point charges of any number down to three. Two charges are not permitted since this no longer has the required degree of axial symmetry, and where the axial gradient is zero, the transverse gradients are non-zero. It is clear from this approach that there are many combinations of planar charge and axial ligands which can give a zero or low EFG if

the balance of charge magnitudes and charge positions is correct. It would be very useful if the EFG at an atomic nucleus in a particular case could be calculated since this would allow values for the correlation time of molecules to be obtained directly from the linewidths of quadrupolar nuclei. Unfortunately this does not appear to be possible at the present time for molecules of any complexity. The reason for this is that the value of the EFG is very sensitive to the distance between nucleus and the charge generating the EFG and varies as r_i^{-3} . Thus a small charge close to the nucleus has a significant or even predominant contribution [61]. Were this not the case, it would be reasonable to expect that a charged ligand would have a marked effect upon linewidth.

Chemical Shifts

Two chemical shift references are encountered in ^{27}Al NMR spectroscopy, aqueous salt solutions which contain $[\text{Al}(\text{H}_2\text{O})_6]^{3+}$ or very-basic aluminate solutions which contain $[\text{Al}(\text{OH})_4]^-$. In both cases the symmetry of the ions is cubic and the lines are relatively narrow. Either may be used as reference, the choice depending upon which obscures least the spectroscopic region of interest. Aluminium perchlorate solutions of any concentration are the best reference [62] since the uncorrected shift is almost identical with the susceptibility corrected one. This is assigned the value of 0.00 ppm. External aluminate $[\text{Al}(\text{OH})_4]^-$ is usually accepted as having a chemical shift of 80ppm, though some measurements indicate that there is some small variation about this value, perhaps as much as $\pm 0.3\text{ppm}$ [54]. It is often convenient to prepare the standardization sample in D_2O since this can then act as both standard and lock. This does introduce an isotope shift in the ^{27}Al resonance of about 0.25 ppm, upfield for $[\text{Al}(\text{D}_2\text{O})_6]^{3+}$ [63] or downfield for $[\text{Al}(\text{OD})_4]^-$ [54]. ^{27}Al chemical shifts cover a range of about 300ppm for diamagnetic solutions. Tetrahedrally coordinated aluminium resonates between 140 and 40 ppm to low field. ^{27}Al signals from the few five-coordinate species measured come between 70 and 30ppm and octahedrally coordinated aluminium resonates between 40 and -46ppm. The overlap between these three regions complicates assignments though the shift is a very useful indication of structure.

4.3.6 Analytical procedures

^{27}Al solution NMR spectra of all samples were acquired at temperatures from 25 to 90°C using a 270 MHz JEOL FT-NMR spectrometer. Samples were placed in 5 mm NMR tubes (Goss Scientific) with coaxial inserts (Wilmad) containing sodium aluminate and potassium hydroxide dissolved in D_2O both as a lock and reference substance. Each reference solution was standardised against aluminium nitrate solution of known concentration positioned in the other compartment of the coaxial assembly, and prepared from a high purity $\text{Al}(\text{NO}_3)_3 \cdot 9\text{H}_2\text{O}$ salt (99.95%, Aldrich). The signal was digitised and stored in the memory of a silicon graphics workstation. The spectral data, initially saved as JEOL generic data format, was converted to the format required by the software chosen for the treatment. Quantification of the NMR spectra was carried out using local integration according to an algorithm developed earlier [23]. The spectral processing, local integration and peak-fitting of the spectral signals was carried out using Galactic GRAMS/32 software. Moreover, a ^{27}Al spectrum processing routine was developed with the intention to automate phasing, peak-fitting and plotting of the evolution of species concentration as a function of time of an other independent variable. This program was written in the .mat MatLab format and will be explained in more detail together with the results it enabled us to obtain.

4.4 Photon correlation spectroscopy

The methods available for particle size determination in polymer and colloidal systems can be distinguished on the basis of their main underlying measurement principle. These groups include subatomic particle scattering (small angle X-ray and neutron scattering), light scattering in the UV-Vis spectral region (photon correlation spectroscopy, turbidimetry), ultrasound attenuation, centrifugation (ultracentrifugation) and chromatographic methods (size exclusion chromatography, field flow fractionation) [64–67].

Amongst these techniques, Photon Correlation Spectroscopy was chosen to estimate the particle size of the species or bioinorganic assemblies obtained during this

project. Photon Correlation Spectroscopy (alternatively, dynamic light scattering, or quasi-elastic light scattering) provides size information in a wide particle size range (from few nm to several micrometers) in a few minutes and at a relatively low cost.

4.4.1 Principles and instrumentation of dynamic light scattering

The principle of the method is to measure the rate of diffusion of particles through a fluid [68], the rate of diffusion of a particle depending on the temperature, fluid viscosity and particle size. If temperature and viscosity are known, the size and molecular weight of scattering particles can be determined. In a typical DLS experiment, a monochromatic and coherent laser light beam illuminates a representative sample dispersed at a suitable concentration in a liquid. Since the dispersed particles are in continuous Brownian³ and/or thermal motion, the observed scattered intensity $I(t)$ will fluctuate along the time axis. Therefore, analysis as a function of time of these intensity fluctuations provides information on the motion of the dispersed particles. The light scattered by the particles at an angle (typically 90°) is recorded by a photomultiplier whose output is fed to a correlator. The correlator then constructs the time autocorrelation function (ACF) $G_2(\tau)$ of the scattered intensity:

$$G_2(\tau) = \langle I(t)I(t+\tau) \rangle \quad (4.15)$$

With $I(t)$, the intensity detected at time t ; $I(t+\tau)$, the intensity detected at time $t+\tau$ and τ , the delay time. The symbol $\langle \quad \rangle$ refers to an average value of the product $I(t)I(t+\tau)$ for various times t .

The ACF depends only on the time difference τ and is independent of the arbitrary time t at which the evaluation of $G_2(\tau)$ is started. For a large number of monodisperse⁴ particles in Brownian motion in the measuring volume V , $G_2(\tau)$ is essentially an exponentially decaying function of the time difference τ :

$$G_2(\tau) = A \left[1 + B e^{-2\Gamma\tau} \right] \quad (4.16)$$

³ Brownian motion arises from random collisions of particles.

⁴ bearing similar size and shape

With A , a time-independent constant proportional to the square of the time-averaged scattered intensity $\langle I \rangle$, sometimes referred to as baseline and B , an instrument factor with $B \leq 1$, designated as the intercept of the autocorrelation function.

The decay rate Γ is linked to the translational diffusion coefficient D of isotropic spherical particles in Brownian motion as follows:

$$\Gamma = Dq^2 \quad (4.17)$$

where q is the modulus of the scattering vector⁵:

$$q = \frac{4\pi n}{\lambda_0} \sin \frac{\theta}{2} \quad (4.18)$$

with n , the refractive index of the solvent; λ_0 , the laser wavelength in vacuo (m); θ , the angle of scattering intensity measurement.

For non-interacting, spherically shaped particles dispersed in a medium with viscosity η , the diffusion coefficient D is related to the particle diameter d by the Stokes-Einstein equation [68]:

$$D = \frac{k_B T}{3\pi\eta d} \quad (4.19)$$

With k_B , the Boltzmann constant (erg/K); T , the temperature (K); η , the diluent viscosity (poise) and d , the equivalent particle diameter (cm)

For polydisperse samples, equation 4.16 can be written as:

$$G_2(\tau) = A \left[1 + Bg_1^2(\tau) \right] \quad (4.20)$$

Where the modulus of the field autocorrelation function $g_1(\tau)$ is now related to the normalised distribution function of decay rates $G(\Gamma)$ by:

$$g_1(\tau) = \int_0^\infty G(\Gamma) e^{-\Gamma\tau} d\Gamma \quad (4.21)$$

with

$$\int_0^\infty G(\Gamma) d\Gamma = 1$$

In the ISO 13321:1996 document concerning photon correlation spectroscopy [69], the distribution of decay rates is characterised by two parameters:

⁵ The scattering vector \vec{q} is defined as the vector difference between the incident and scattered wavevectors \vec{k}_i and \vec{k}_s respectively. The modulus of both of \vec{k}_i and \vec{k}_s are equal to $\frac{2\pi n}{\lambda_0}$.

(a) The average decay rate $\langle \Gamma \rangle$, defined as:

$$\langle \Gamma \rangle = \int_0^{\infty} \Gamma G(\Gamma) d\Gamma \quad (4.22)$$

(b) A dimensionless polydispersity index PI , i.e. a measure of the broadness of the distribution, defined as :

$$PI = \frac{\mu_2}{\langle \Gamma \rangle^2} \quad (4.23)$$

where

$$\mu_2 = \int_0^{\infty} (\Gamma - \langle \Gamma \rangle)^2 G(\Gamma) d\Gamma \quad (4.24)$$

The two parameters describing particle size distribution, e.g. the average PCS diameter d_{PCS} and the polydispersity index PI are determined by a variant of the so-called cumulants method.

In the cumulants method [70], the factor $e^{-\Gamma\tau}$ in equation 4.21 is expanded around $e^{-\langle \Gamma \rangle \tau}$, yielding a polynomial in delay time. Truncating this polynomial at the second-order term, equation 4.20 can be approximated by:

$$G_2(\tau) = A[1 + Be^{-2\langle \Gamma \rangle \tau} (1 + \mu_2 \tau^2)] \quad (4.25)$$

or by

$$G_2(\tau) = A[1 + Be^{-2\langle \Gamma \rangle \tau + \mu_2 \tau^2}] \quad (4.26)$$

In order to obtain a linear regression, this equation is transformed as follows:

$$y(\tau) = \frac{1}{2} \ln[G_2(\tau) - A] \approx \frac{1}{2} \ln AB - \langle \Gamma \rangle \tau + \frac{\mu_2}{2} \tau^2 \quad (4.27)$$

or

$$y(\tau_j) = a_0 - a_1 \tau_j + a_2 \tau_j^2 \quad (j = 1, 2, 3 \dots m) \quad (4.28)$$

With j the number of the delay channel of the correlator.

For the determination of the ACF the Coulter N4Plus photon correlator utilises 80 non-equally (logarithmically) spaced channels at each measurement angle for the detection of scattered light intensity which maximises the information provided in the measurement. A typical ACF is plotted in Figure 4.6 [71].

The baseline or far point A can be determined in two ways: by the total number of photon counts in a total time duration of the considered experiment, or from

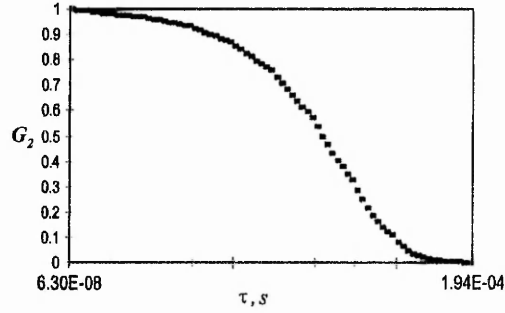


Fig. 4.6: The autocorrelation function (logarithmically spaced channels)

an estimate of $G_2(\tau)$ for delay times $\tau \gg 25/\langle\Gamma\rangle$. It is recommended that both estimates of the baseline A are determined and that the larger of both is retained. However, for relative differences between the two estimates of the baseline larger than 10^{-3} times the smallest value, measurement shall be discarded for further analysis.

The parameters a_0 , a_1 and a_2 are determined by fitting of the experimental estimates of $y(\tau_j)$ to equation 4.26 using least-squares minimisation of the following function:

$$s(a_0, a_1, a_2) = \sum_{j=1}^m w_j (y(\tau_j) - a_0 + a_1\tau_j - a_2\tau_j^2)^2 \quad (4.29)$$

In this equation, the normalised weighting factor

$$w_j = \frac{m[G_2(\tau_j) - A]^2}{\sum_{j=1}^m [G_2(\tau_j) - A]^2}$$

accounts for the nonlinear transformation of the raw data G_2 into the values for $y(\tau_j)$. The average PCS diameter d_{PCS} is calculated from a_1 by

$$d_{PCS} = \frac{1}{a_1} \frac{k_B T}{3\pi\eta} \left[\frac{4\pi n \sin(\theta/2)}{\lambda_0} \right] \quad (4.30)$$

The polydispersity index PI is related to a_2 and a_1 by

$$PI = \frac{2a_2}{a_1^2} \quad (4.31)$$

The block diagram of the N4Plus Coulter particle size meter used throughout this project is shown in Figure 4.7. In this instrument the light from an He-Ne laser passes through a cuvette containing the sample solution. Six fibre-optic receptors

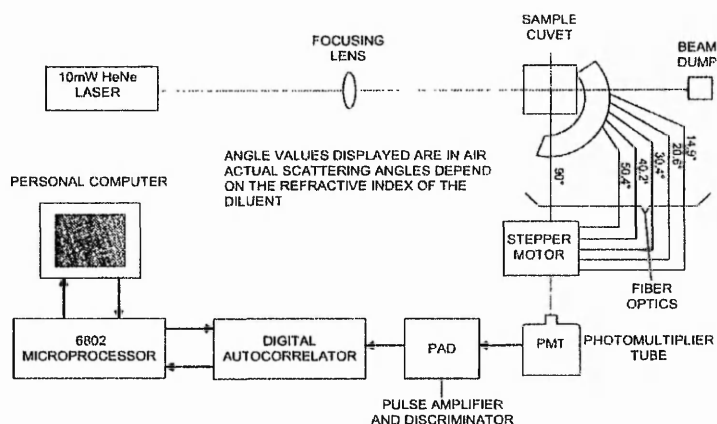


Fig. 4.7: Functional block diagram of the N4Plus DLS instrument [71].

(corresponding to measurement angles of 11.1, 15.7, 23.0, 30.2, 62.5 and 90.0°), the stepper motor and photomultiplier define the angle of scattered light detection. The digital autocorrelator computes the ACF of the current pulses obtained from the photomultiplier. The resulting ACF is sent to the computer for further analysis and particle size distribution calculated using the Fortran program CONTIN. The Analysis of the ACF also involves a subtraction of the baseline from the raw data and a calculation of the baseline error. The program CONTIN allows for unimodal (single peak in the particle size distribution) and multimodal distribution of particles to be calculated. Unimodal analysis is a faster but less accurate method. It provides only a measure of the mean size of particles in the sample. Multimodal analysis allows for the extremely polydisperse systems to be characterised. The CONTIN program, also referred to as a 'size distribution processor' (SDP) sorts the data from the autocorrelator into separate bins (17 to 31 bins are possible) from which a particle size histogram is calculated. Finally, an additional bin is devoted to the detection of dust in the sample. Standard deviation of the mean particle size in the unimodal analysis and of the particle sizes in the multimodal analysis is calculated as follows [71]:

$$SD(d) = \left[\frac{\sum_i a_i (d_i - \bar{d})^2}{\sum_i a_i} \right]^{\frac{1}{2}} \quad (4.32)$$

With d , the mean diameter of the particle distribution; d_i , the diameter corresponding to

the i th bin; a_i , the contribution to the total scattered-light intensity of particles of size d_i . Standard deviation provides a good qualitative indication of the polydispersity of the sample, though it may be not strictly accurate for extremely polydisperse systems. The SDP analysis is not able to discern between peaks of particle distributions closer than a factor of two in diameter ratio. In order to reach maximum reproducibility and correctness for particle size measurements, an adjustment of the measurement time at each angle is important. It is recommended to use longer measurement times at larger angles. It was found that the use of 240 s measurement time for scattering angle 30.2 degrees, 120 s for 62.5 degrees and 60 s for 90.0 degrees provides optimum reproducibility and precision of measurements in highly polydisperse aqueous Al species solutions [7]. DLS measurements after analysis with the SDP program CONTIN can be displayed as intensity size distributions where the magnitude of each histogram bin's content is proportional to the percent of the total scattered intensity due to particles of the corresponding bin size. The particle weight distribution (based on the approximation of spherical particles) is sometimes more useful than the intensity distribution, especially in the case of polydisperse systems. Indeed, scattering intensity is strongly related to the size of the particles, a small number of larger particles will therefore produce much more signal than a large number of small ones, causing a wrong estimation of the relative proportion of the different size peaks in the distribution [68, 71]. Moreover, weight distribution is independent from scattering angle. The SDP program uses the Mie theory [68] to convert from intensity to weight distributions. In order to obtain exact solution of the Mie equation [71], knowledge of the refractive index (a complex number) of particles is required along with the refractive index of the solvent. For dielectric (transparent) particles, the imaginary part of the particle refractive index is zero and need not to be entered. If the refractive index of particles is unknown, the SPD program uses an approximate solution of the Mie equation that holds well over a wide variety of refractive indices [71]. Another limitation of Mie theory is that the solution is not valid for strongly non-spherical particles. However, information about the shape of particles and its deviation from sphericity can be derived from the comparison of size distributions obtained at different scattering angles.

4.4.2 Standard operating procedures

Standard operating procedures recommend a sample temperature equilibration prior to measurement in order to obtain reproducible readings of the ACF and baseline. Another technique is to adjust the apparatus measurement temperature to the value of the current experiment temperature, The measurement cell of the N4Plus being thermostated (0 to $90 \pm 0.1^\circ\text{C}$). Depending on the difference between the initial sample temperature and the measurement temperature, 10-30 min equilibration is required. Since dust may have a strongly adverse effect on the results of DLS measurements, special care needs to be taken in order to eliminate dust particles from samples using high-speed centrifugation and nano-filtration of deionised water (solvent) with a peristaltic pump and Whatman cellulose nano-filters ($d_{pores}=240$ nm). The concentration of particulate material shall be above some minimum level and shall not exceed a maximum level. The minimum level is determined by the following two requirements:

- (1) The scattered intensity (count rate) of the sample containing the dispersed particles shall be at least 10 times higher than the signal scattered by the dispersion medium alone.
- (2) The number N_V of particles in the scattering volume shall be at least about 1000 (any number in the range 500-1000 is acceptable), to minimise the fluctuation of the number of particles within the measuring volume. The maximum level is mainly determined by the conditions that particles shouldn't interact with each other and no multiple scattering should be observed. Particle-particle interaction will lead to an overestimation whereas multiple scattering will produce an underestimation of the particle size proportional to particle concentration. The absence of significant contributions from multiple scattering shall be determined by the three following checks:
 - (3) The samples should look clear, or only slightly cloudy or turbid.
 - (4) The ratio of the measured intercept to its maximal value should be at least 0.8.
 - (5) If the instrument allows the laser beam passing through the samples to be viewed indirectly, a sharp parallel beam shall be observed; a spreading halo around the beam or any apparent absorbance shall not be present.

Practically, the average counts per second detected by the N4Plus from the sample should be kept between $5 \cdot 10^4$ and $1.5 \cdot 10^6$. The default range of the Coulter N4Plus submicron particle size meter is from 3 to 3000nm. However, combining rigorous standard operating procedures with an appropriate data treatment, particle sizes fractions were observed in the range 0.2-3 nm [7] when using this equipment.

4.4.3 *Dynamic light scattering in Al hydroxide suspensions and Al-elastin systems*

DLS measurements of hydroxide suspensions and Al-elastin systems were acquired using a Coulter N4Plus particle size meter at a measuring angle 90.0° and acquisition time 120 sec, temperature 25°C , equilibration time 10min, in triplicate. Particle size distribution analysis was performed using the unimodal intensity-based model from the Coulter CONTIN program.

Prior to DLS measurements the samples were diluted with distilled, deionized and nano-filtered water and treated for 1min in an ultrasonic bath to break up any loose aggregates.

4.4.4 *Dynamic light scattering and zeta potential measurements in Al-BSA systems*

DLS measurements of Al species-BSA solutions were acquired using a Coulter N5Plus particle size meter using the same sample preparation and acquisition routine as mentioned above.

Zeta potential measurements were carried out using a Malvern Zetasizer Nano ZS in complement of DLS particle size estimation, in order to obtain more conclusive results concerning the Al species-BSA interactions. Typically, 1 ml aliquot of each sample was injected into a disposable capillary cell and measurements were made at 25°C using field strengths of approximately 10V/cm. The electrophoretic mobilities of the particles were determined using phase analysis light scattering (PALS) and these were converted into zeta potentials using the Smoluchowski approximation. In order to enable this conversion and to reduce the effect of viscosity, samples of Al hydroxide-BSA were diluted 100 times with deionized water immediately before the measurements.

4.5 Conductometry

4.5.1 Principles and equipment

The conductivity of a solution is a measure of its capacity to convey an electric current. Conductivity is related to the nature and concentration of ionized substances present in the solution and to the temperature of the solution. Even pure H_2O has a measurable conductivity. After absorbing CO_2 from the air, and other substances from the glass in which H_2O is kept, the conductivity of distilled water is normally about $1\mu\text{S}\cdot\text{cm}^{-1}$. Kohlrausch has measured a value as low as $0.05\mu\text{S}\cdot\text{cm}^{-1}$. This indicates that water acts as a very weak binary electrolyte and self-dissociates. The product of the dissociation of water increases with temperature and conductivity therefore depends on temperature. The conductivity of solutions is the sum of the conductivities of the individual species of positive and negative ions. The molar conductivity of an ion is determined partly by its mobility (expressed in $\text{cm}^2\cdot\text{V}^{-1}\cdot\text{s}^{-1}$) in the electric field, mobility depending itself on temperature. Conductivity also depends on the concentration and the degree of ionization of the salts involved, and there may be a nonlinear relationship between conductivity and concentration. The conductivity gives no indication of the nature of the substances in solution but any increase or decrease in their concentration will be reflected in a corresponding increase or decrease in conductivity. The concentration of dissolved ionic matter (in mg/L) in water may be roughly estimated by multiplying the conductivity by an empirical factor, varying from 0.55 to 0.9 depending on the soluble compounds (for KCl , 0.51; for NaCl , 0.48; for $\text{Ca}(\text{HCO}_3)_2$, 1.6). Conductance can be used for conductometric titrations, the conductometric method having the advantage of using all the readings, except those close to equivalence, for end point estimation [72].

The conductance of water is measured between two parallel platinized plates and is directly proportional to plate area and inversely to plate separation. When the results are expressed as if for plates of 1cm^2 separated by 1cm then the measure becomes independent of the measuring system. This measure is the electrical conductivity, given in $\text{S}\cdot\text{cm}^{-1}$. In practice, for a given plate configuration, the factor by which conductance must be multiplied to give conductivity is measured empirically

using a standard electrolyte solution of known conductivity. This factor is called the 'cell constant'. For water with pH above about 4.5 and a temperature of 25°C,

$$c \approx 0.01\kappa \quad (4.33)$$

With κ , the conductivity expressed in $\mu\text{S}\cdot\text{cm}^{-1}$; c , the sum of concentrations of positively and negatively charged ions expressed in $\text{mMol}\cdot\text{L}^{-1}$.

Typically, the instruments all consist of two distinct parts: (a) a conductance cell containing a pair of rigidly mounted 'electrodes', usually made of Pt with a coating of Pt-black, or of carbon and (b) an instrument for measuring the electrical conductance (or resistance) between the electrodes of the cell. Most instruments consist of a low voltage alternating current generator feeding a Wheatstone bridge network, of which the cell forms one arm [72].

4.5.2 Experimental procedure

The conductivity of the samples was measured during the exchange process using a three-ring conductivity probe or a two-plate conductivity probe and a temperature sensor (all from Radiometer). The conductivity probe was calibrated using a standard NaCl solution ($1015\mu\text{S}\cdot\text{cm}^{-1}$, Radiometer).

4.6 Viscosity measurements

4.6.1 Viscosity definition

Viscosity is a measure of the tendency of a liquid to resist flow, more correctly termed the coefficient of viscosity, η . This is the ratio of the shear stress to shear rate at a simple steady shear rate. When this term is constant at different values of shear rate, then the liquid is known as Newtonian. If the coefficient varies as a function of shear rate then the liquid is known as non-Newtonian. The shear rate is the velocity difference between two liquid layers subjected to a shear stress, divided by the distance between the layers. For a rotational viscometer a high shear rate is obtained for a quick rotation and a relatively small plate spacing. Solutions of simple salts will be Newtonian fluids, and as such, the value of the viscosity measured by any

suitably accurate method can be used, whatever the shear rate. If the dispersant is non-newtonian, for example if it contains polymers, polyelectrolytes or higher molecular weight surfactants, then it is possible that the viscosity measured will depend on the measurement technique, as each method will use a different, and often unknown shear rate.

4.6.2 *Methods of viscosity measurement*

Rotational viscometer

This method uses a disk or cylinder that is rotated either in a large volume of fluid, or the fluid is contained between the rotating component and a stationary plate or larger cylinder. In both cases, the torque required to drive the disk or cylinder at a known steady rate is measured, and this is converted to the fluid viscosity. The disadvantage of this method is the number of disks or cylinders required to cover a wide range of viscosities, and the error at low viscosities can be in the order of 10%, even for the best systems.

Capillary viscometer

There are two types. One involves pumping fluid at a known rate through a capillary tube and measuring the pressure drop. The other uses gravity to cause fluid to pass down a capillary and the time for the fluid to drain through a measured length of capillary is timed. Both methods require calibration with a fluid of known viscosity. These methods are simple in principle, however in practice they are inconvenient because of the very careful cleaning procedure required. In addition, for the gravity capillary, the density must be known as the value measured is the kinetic rather than the dynamic viscosity. Each capillary will only cover a narrow range of viscosities, so a number of tubes are usually required.

Cup viscometer

The cup type viscometer, sometime called the Ford cup, is related to the capillary viscometer. It uses the time taken for a fluid in a cup of a specific capacity to

drain from a hole in the cup to give an indication of the viscosity, rather than a true viscosity reading. This technique is usually only used for viscous fluids, and is traditionally used in the paints or inks industry. A selection of cup types is required to cover a wide viscosity range.

Falling ball viscometer

This consists of a ball, needle or cylinder falling down a column of the fluid to be measured. The time to fall a marked distance is measured manually or automatically and some more expensive versions have built in temperature control. To cover a wide viscosity range, the density of the ball or needle can be changed, or the capillary can be tilted so the ball runs more slowly down the inclined plane. The latter case is mostly suitable for solutions, as particles in the fluid would interfere with the free run of the ball along the capillary

Wall Vibration viscometer

The resonant frequency of a probe vibrating at a relatively high frequency will change when immersed in a fluid. The frequency change will depend on the viscosity of the fluid. This method is simple to use, but the range of viscosities measured is narrow, typically 4 mPa·s to a few 10's of mPa·s, and the accuracy is low ($\pm 10\%$). When lower frequencies are used, a damping effect related to the viscosity of the fluid appears, reducing the amplitude of the vibration. The power required to keep the sensors vibrating at the original amplitude is measured and converted into the viscosity. The range and accuracy of measurements carried out with low frequency viscometers are therefore enhanced.

4.6.3 Viscosity measurement using the SV-10

The SV-10 vibro viscometer (A&D Ltd., Japan) (figure 4.8) was used throughout this project when viscosity measurements were required. This viscometer, using the wall vibration measurement principle to provide a 1% accuracy over the whole range of 0.3-10000mPa·s, enables the monitoring of viscosity during dynamic processes (output transfer to a PC), and combination with a jacketed reaction vessel

provides temperature control from 0 to 100°C. Its calibration can be achieved with distilled or demineralised water for most samples (carried out before every series of measurement), and a 2-point calibration is available to cover a wide sample viscosity range. The SV-10 has two gold plated paddle type sensors 12mm in diameter that

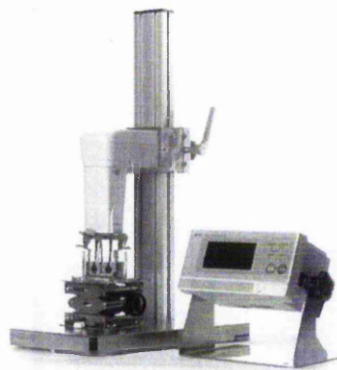


Fig. 4.8: The SV-10 Vibro viscometer.

are immersed into the sample to be measured. These paddles are in a tuning fork arrangement so when stimulated by an electromagnetic drive the paddles vibrate at a constant low frequency of 30Hz. The amplitude of vibration is detected and sufficient current is applied to the electromagnetic drive to maintain a constant amplitude. The sample viscosity causes the vibration to be damped and the current required to maintain the vibration amplitude is measured continuously, and converted into a viscosity on the display. The system takes 15 seconds to stabilise, after which a continuous reading of viscosity is displayed. The value actually measured is dependent on the sample density. Viscosity measurements were performed after temperature equilibration at $25\pm 2^\circ\text{C}$ in the 10ml polycarbonate sample cups provided by the viscometer manufacturer. Special care was taken to immerse the paddle sensors in a reproducible manner.

5. SOLID STATE CHARACTERISATION TECHNIQUES

5.1 Powder X-ray diffraction

Solid samples produced during this project were analysed by powder X-ray diffraction (PXRD). The powder X-ray diffraction technique is useful in qualitative phase analysis because every crystalline material has its own characteristic powder pattern. Since the structure of the species of freeze-dried solutions is believed to be maintained in the solid state [7], it was expected to retrieve structural data of the solution species using this technique.

5.1.1 Principles and instrumentation of PXRD

Interaction of the electric vector of X-ray radiation with the electrons of matter through which it passes results in scattering [73]. When X-rays are scattered by an ordered environment in a crystal, both constructive and destructive interference occur among the scattered rays as the distance between scattering centres is of the same order of magnitude as the wavelength of radiation. When an X-ray beam strikes a crystal surface at an angle θ , a portion of the beam is scattered by the layer of atoms at the surface. The unscattered portion of the beam penetrates to the second layer of atoms where again a fraction is scattered and so on. The cumulative effect of this scattering from the regularly spaced centres of the crystal is known as diffraction of the beam. The condition for constructive interference of the beam at angle θ is given by Bragg equation:

$$n\lambda = 2d \sin \theta \quad (5.1)$$

With n an integer; λ , the wavelength of X-rays; d , the interplanar distance in the crystal and θ , the incident angle of X-ray radiation.

Destructive interference will therefore take place at all other angles. The requirements of X-ray diffraction are: (a) spacing between layers of atoms must be roughly the same as the wavelength of the radiation; (b) scattering centres must be spatially distributed in a highly regular way. In a powder X-ray experiment, the data are collected as a powder pattern. This is essentially a plot of diffracted beam against twice the incident angle, 2θ . Hence, a diffraction pattern describes a series of peaks corresponding to coherent reflections for a given crystal. The positions of these reflections along the 2θ -axis clearly depend on the value of d which is dependant on the dimensions of the unit cell of the crystal.

A powder pattern has two characteristic features: (a) the d-spacings of the lines; (b) the relative intensities of the lines (I/I_x). From the powder diffraction data it is possible also to generate values for the mean crystallite size (d) from the observed half height line width B_b of the X-ray diffraction peaks. This may be performed using the Scherer equation [74]:

$$d = \frac{K\lambda}{\beta \cos \theta} \quad (5.2)$$

$$\beta = B_b - B_x \quad (5.3)$$

With d the mean crystallite dimension (\AA); K , the crystallite shape constant (generally taken equal to 0.9 but material-dependent); θ , the Bragg diffraction angle (radians); λ , the X-ray wavelength (usually $\text{CuK}\alpha$, $\lambda=1.5418\text{\AA}$); β , the pure diffraction breadth due to crystallite size effect and B_x , the instrument broadening.

In practice for a value of θ in degrees ($^\circ$), Equation 5.2 becomes:

$$d = 57.3 \frac{k\lambda}{\beta \cos \theta} \quad (5.4)$$

Due to various problems associated with determining mean particle sizes from PXRD data, Scherer's formula is used mainly for rough estimations [73]. If the average crystal size is less than 2000\AA then peak broadening may occur and be readily measured using Scherer's equation. The lower limit of detection occurs when the peaks become so broad that they disappear into the background radiation. For very small particle sizes it is best to use low angle peaks if possible since, for a given crystallite size, broadening increases with angle. Finally the crystallinity of

a sample can be calculated by comparing the intensity of peaks from a reference material with the intensity of the sample's peaks [75].

5.1.2 Preparation and measurement of the solid samples for PXRD

An agate mortar was used to finely grind the sample to a powder. The powder was then packed into the hollow of a cavity holder, and smoothed off by sliding a flat glass slide over the surface.

Where specified, powder XRD measurements were conducted using a Hilton Brooks modified Philips PW1050 Powder Diffractometer operated at 42.5kV/18mA with a copper source $\text{Cu K}\alpha$, $\lambda=1.540562\text{\AA}$. Scans were performed in the step mode with 0.02° step size and 0.2 to 0.4s dwell time. Data were recorded over the 2θ range $3\text{--}80^\circ$ at room temperature.

In the other cases, such as for Al-BSA experiments, X-ray powder diffraction data were acquired at room temperature using a Panalytical X'Pert Pro powder diffractometer operating with $\text{Cu K}\alpha$ radiation, continuous scans from $2\theta= 1$ to 80° , step size $0.002\ 2\theta^\circ$, scan step time 30.9s, and continuous spinning of the sample during the run.

Diffraction patterns were analysed using the Panalytical software. Data handling included background correction, spectral smoothing, determination of peak positions, peak widths, intensities, and crystallite size calculations. Comparisons of the collected data were made in conjunction with the JCPDS (Joint Committee on Powder Diffraction Standards) powder diffraction database, which consists of sets of cards containing X-ray data for most known crystalline phases, as well as the powder patterns available from the literature. The molecular structures presented in the introduction were generated from original crystal structure data provided by authors, using Mercury and Encifer softwares combined with BS software for polygonal representation [76].

5.2 Thermogravimetric Analysis

5.2.1 Design features

A thermobalance is composed of a good precision balance, a furnace capable of being programmed and a computer that will control the equipment and process the data. The computer can control the equipment to produce the most sophisticated temperature regimes, control the rate of decomposition, and carry out data processing.

The Balance

Micro-balances are balances of high sensitivity and precision designed to operate in the micro-gram range. Five types of micro-balances are defined: (a) the displacement type (beam and cantilever), (b) the torsion displacement type, (c) the beam-knife-edge type, (d) the spring balance, (e) restoration type balances [77, 78]. The equipment has to be calibrated, and small samples are generally used in order to avoid temperature gradients throughout the decomposed material. The measurements can be carried out under atmosphere or under controlled flow of a chosen gas, in order to purge the gas produced in the decomposition reaction.

The Furnace

The furnace should be able to reach about 100-200°C above the desired working temperature, be wound non-inductively to avoid possible errors in weighing, and reproduce the chosen temperature regimes precisely and accurately. Moreover, radiation and convection currents from the furnace should not affect the weighing system. Finally, if operated in the presence of a corrosive atmosphere the linings of the furnace must be made of material capable of resisting chemical attack. The most common method of measuring temperature in TG balances is a thermocouple positioned near the sample, resistance thermometers being as well used in some instances [77, 78].

5.2.2 Data presentation

When presenting the data, the equipment, crucible and temperature regime imposed should be specified, as well as the atmosphere used for the experiment. The actual TG data is initially recorded as mass plotted against the temperature regime details. In the case of linear heating, the heating rate is noted and the plot is then of mass against temperature. Additional plots include mass loss, fraction decomposed, percent mass loss or molecular composition, all plotted against the temperature. Derivative plots (DTG) can as well be used in order to show curve features more distinctly. These details are especially helpful in determining the kinetic features of the decomposition process.

5.2.3 Effects of experimental environment

Various parameters and sample characteristics can influence solid-state activity and therefore affect the kinetics and thermodynamics of decomposition.

The Solid State

Surface structure is the main factor dictating the solid state reactivity observed in TG experiments. Indeed the surface or the reaction interface structure may be quite different from the bulk structure. Moreover, the surface characteristics such as surface area are greatly affected during the TG run. Finally, the reaction often takes place at the solid-gas interface or even in the liquid phase.

The Surface State

The structure at an interface is generally distorted owing to the metastable nature and polarisability of the surface. This leads to alteration both in the extent of the surface (an extensive property) and the surface energetics associated with the surface (intensive). This results in sintering of the solid particles during decomposition. The effects of sintering causing a reduction in surface area are counteracted by thermal activation brought about by the shattering of particles due primarily to a difference in density (and hence volume) between solid reactants and solid products.

Both sintering and activation processes have rates which are temperature dependent. It would seem appropriate then in recording the surface parameters of at least the starting initial solid reactant material in terms of particle size, particle size distribution or surface area [77, 78].

Effect of the atmosphere

The environmental atmosphere around the sample can cause drastic changes in TG results. Very often an increase in the pressure of the gas produced by the reaction cause an increase in the decomposition temperature. Other effects of the environmental gas and different decomposition pathways occur depending on the atmosphere used. A well known example is the decomposition of coal, which catches fire in air but converts to coke in nitrogen.

Thermodynamic factors

During TG analysis, the material may be removed significantly from its equilibrium state. Of course in many processes the rate of reaction is significant and the end product is the thermodynamically favoured phase at the final temperature. In such instances the 'classical' thermodynamic treatment appears to fit (for example the dehydration processes), however the processes may become irreversible as they are located at the reaction interface. For polymers the technique used to start the analysis from a known phase is to modify the organisation of the material to a known structure. This is done by melting the material and cooling it down following a well defined regime.

Kinetic data

In order to obtain kinetic data in respect of the decomposition, the TG analysis is carried out at a series of temperatures, the fraction decomposed being then plotted against time at a constant temperature. One can then identify the reaction mechanism and determine the specific reaction rate constant at each temperature. The Arrhenius parameters (the pre-exponential term A and the Activation Energy E_a)

can then be calculated from a plot of $\log k(T)$ versus $1/T$ where T is the corresponding temperature of the isothermal experiment in Kelvin. Mathematical relationships have been established between the fraction decomposed and the time of heat treatment. Most of the kinetic resulting models for solid state decomposition are based upon nucleation/growth principles. Usually the nucleation takes place at the particle surface, as a consequence of the conditions applied. Subsequent growth then reflects the geometry of the contracting interface often imposed by the original shape and surface of the decomposing particles. Finally, species diffusion occurs away from or towards the reaction interface. Specific mathematical relationships have become associated with particular models, however a model can give rise to various mathematical relationships.

5.2.4 The thermal behavior of aluminium compounds

Boehmite

Boehmite has been reported to decompose from 350°C. Under reduced pressure (10^{-3} mmHg), the resulting phase is much more stable than the initial gel and starts losing water only at 300°C, although the gel has already reached the boehmite composition $2 \text{ Al}_2\text{O}_3 \cdot \text{H}_2\text{O}$ at 260°C. Since the infra-red spectrum of boehmite does not contain the bands due to water, but only those due to OH, it is perhaps better to write its formula as $\text{Al}_2\text{O}_3 \cdot 2\text{AlO}(\text{OH})_2$. An abrupt departure of water leads to a practically anhydrous alumina but this starts only at 400°C in air. The infra-red spectrum can be used to demonstrate complete dehydration by the disappearance of water bands in the residue [79].

Gibbsite

The formula given for gibbsite is $\text{Al}_2\text{O}_3 \cdot 3\text{H}_2\text{O}$, or better, $\text{Al}(\text{OH})_3$. The dehydration of this compound starts smoothly at room temperature, but half of the water escapes abruptly around 72°C. The dehydration is total at 320°C, when the plateau corresponding to the presence of the oxide begins. Other variants of this analysis are found elsewhere. The mineral loses 5/6th of its water within a very short

temperature interval and following a zero order reaction, the final reaction product being boehmite [79].

Diaspore

The dehydration of diaspore sets in suddenly around 520°C and ends at 685°C, followed by a plateau characteristic of the oxide [79].

Aluminium chloride

Aluminium chloride has the formula $\text{AlCl}_3 \cdot 6\text{H}_2\text{O}$. However, the handling necessary to place the sample into the crucible allows the salt to pick up a little moisture, whose loss at temperatures up to 38°C is observed on the thermolysis curve. The hexahydrate appears stable between 38°C and 118°C; then hydrolysis and dehydration lead to the oxide Al_2O_3 , rather rapidly up to 500°C, and very slowly thereafter. The conversion seems to be complete around 800°C [79].

Aluminium-ammonium alum

When ammonium alum is heated to 1030°C at the rate of 130°C per hour, it is stable up to 54°C. It loses all of its water around 310°C in three stages which are not very clearly separated. First there is a loss of 6 molecules of water of crystallization, up to about 126°C, then 4 molecules of water combined with sulphuric acid pass off up to around 170°C, and finally the 2 last molecules of water are lost at 310°C. The product which makes its appearance at temperatures above 524°C is a complex of the $\text{NH}_4[\text{Al}(\text{SO}_4)_2]$ type. In fact, according to preliminary studies, the ammonium sulphate may already have disappeared by sublimation and dissociation. This ammonium sulphate begins to be lost between 524°C and around 620°C. There then remains aluminium sulphate $\text{Al}_2(\text{SO}_4)_3$, which starts to decompose progressively around 620°C. The formation of Al_2O_3 is not complete even at 1030°C [79].

Sodium aluminate

The reaction of various mixtures of aluminium oxide and sodium peroxide have been studied. Below 309°C, the only losses of weight recorded are those corresponding to

a loss of water. At $309^{\circ}\text{C}\pm 18^{\circ}\text{C}$ begins a release of oxygen which continues up to $738^{\circ}\text{C}\pm 48^{\circ}\text{C}$. The heating curve contains an irregularity at $328^{\circ}\text{C}\pm 16^{\circ}\text{C}$; the reaction is very rapid at this temperature. The weight remains constant from 738°C to 1000°C . Only two reactions have been recorded: the one at the moment of spontaneous decomposition of the sodium peroxide, where there is formation of $\text{Na}_n(\text{AlO}_2)_n$ in which n denotes 2 or 3 (analysis by infrared absorption); the other, occurring at a higher temperature and producing sodium carbonate and the residual oxide.

Proteins

The hydration of various proteins has been studied using TG [79]. The investigations dealt with casein and gelatin kept for several days at $16\text{--}20^{\circ}\text{C}$ under a bell jar in an atmosphere saturated with water vapour. Two kinds of measurements were made: (1) isothermal at (80°C , 110°C , 150°C) obtained at a speed of 100°C per hour, and (2) under continuous heating from 20°C to about 250°C by raising the temperature of the furnace linearly at a rate of 50°C , 100°C or 200°C per hour. A plateau is not always observed as frequently the curve descends continuously until the end of the analysis. However, certain proteins yield isothermal levels for a greater or lesser extent along which there is no change in weight, but the quantity of water lost depends intimately on the temperature of the isotherm. Kinetic study of the loss of weight as a function of the heating rate is capable of providing information about the activation energy of the dehydration of the proteins whereas the hysteresis phenomenon occasionally introduces an ambiguity into the thermodynamic interpretation of adsorption isotherms.

Experimental procedure

The weight loss, temperature and time data arrays were collected between 20 and 900°C using a continuous heating rate of $10^{\circ}\text{C}/\text{min}$ on a Stanton Redcroft TG760 balance connected to a computer. The weight loss curve was normalized to the weight of the sample at 900°C . The dm/dT derivatives were then calculated, and the resulting DTG curves fitted using Gaussian functions in the peak-fitting module of Thermo Galactic GRAMS/32 software.

5.3 Electron Microscopy

5.3.1 Introduction

A microscope is an optical system which transforms an 'object' into a magnified 'image'. An image can be either formed by projection (Field Ion Microscope, FIM), optically (use of a lens, for example in a Transmission Electron Microscope, TEM), or by scanning, when each point of the picture is presented serially (Scanning Electron Microscope, SEM). Irrespective of the different physical principles by which an image is generated, however the concepts of resolution, magnification, depth of field and lens aberration all must be addressed.

A scanning image, similarly to a digitised image, contains a limited number of points, called pixels¹ carrying the smallest image information.

The simplest optical microscope is a single convex lens or 'magnifying glass'. The behaviour of a convex lens can be summarised by the thin lens equation;

$$\frac{1}{f} = \frac{1}{u} + \frac{1}{v} \quad (5.5)$$

With f , the focal length of the lens; u , the 'object distance' (the distance from the lens to the object) and v , the 'image distance'.

The image will be magnified, real and inverted if the object distance is $f < u < 2f$. The image is erect but virtual if $0 < u < f$. If an image is to be recorded on a photographic plate or viewed on a screen then it must be real. the magnification M produced by the single lens is given by v/u . Substitution in the lens equation gives:

$$M = \frac{f}{u - f} = \frac{v - f}{f} \quad (5.6)$$

from which it can be deduced that for large magnification $u - f$ must be small and positive. This is achieved by placing the object just outside the focal point. When high magnification is required, combinations of lenses are used, so that the total magnification is achieved in two or more stages (objective and projector lenses) in order to minimise any distortion. It is not necessary to build a light microscope with three or more stages of magnification, since the resolution of this microscope type

¹ Short for picture element

is limited to $\approx 200\text{nm}$. As objects to be observed are generally not self-luminous, an optical microscope uses an external light source. Depending on the transparency of the object to be observed, the light coming from this source is either passed through the sample (transmission arrangement) or reflected by it (reflection arrangement). The same two types of arrangement arise in electron microscopy, leading to TEM and SEM instruments.

5.3.2 Microscope characteristics

Ideally, a microscope should be a compact device. It is therefore desirable that the object and image stay in the same position, the focal length of the microscope being varied to reach the desired magnification. In the light microscope, one lens is usually exchanged for another with a different focal length, giving a limited set of fixed magnifications. In electron microscopes, all lenses are electromagnetic and the focal lengths can be adjusted without such modification.

Resolution

In optical sciences, resolution is defined as the closest spacing of two points which can clearly be seen to be separate entities. Even if all the lenses of the microscope were perfect and introduced no distortions into the image, the resolution would nevertheless be limited by a diffraction effect. In any microscope the light must pass through a series of restricted openings – the lenses themselves or the apertures. Therefore diffraction occurs so that a parallel beam of light (which would be seen as a spot) is transformed into a series of cones, which are seen as circles (Airy's rings) in the image. For light of a given wavelength the diameter of the central spot is inversely proportional to the diameter of the aperture from which the diffraction is occurring. Therefore the aperture must be as large as is feasible. The resolution of a microscope can be derived from the following equation:

$$r_1 = \frac{d_1}{2} = \frac{0.61\lambda}{\mu \sin \alpha} \quad (5.7)$$

With λ , the wavelength of the light; α , the aperture of the microscope and μ , the refractive index of the medium between the object and the objective lens.

The product $\mu \sin \alpha$ is usually called the numerical aperture (NA). In order to obtain the smallest r_1 it is possible to decrease λ or increase μ . In light microscopy λ can be decreased to 400nm with green light or 200nm with ultraviolet light, $\sin \alpha$ can be increased towards 1 by using as large an aperture as possible and μ can be increased by using an oil immersion objective lens.

Depth of field

In any microscope the image is only accurately in focus when the object lies in the appropriate plane (strictly the surface of a sphere). If part of the object lies above or below this plane then the equivalent part of the image will be out of focus, compromising the observation of three dimensional objects. The range of positions for the object for which our eye can detect no change in the sharpness of the image is known as the depth of field. In most microscopes this distance is rather small and therefore in order to produce sharp images the object must be very flat. As electron microscopes are operated at very small aperture, both resolution and depth of field are improved.

Aberrations in optical systems

Any single spherical lens suffers from chromatic and monochromatic or achromatic aberrations. The effect of each aberration is to distort the image of every point in the object in a particular way, leading to an overall loss of quality and resolution. The same types of aberration arise in electron microscopes and are very important in determining the resolution of the instrument.

Chromatic aberrations arise because a single lens causes light to be deviated by an amount depending on its wavelength. Thus a lens will have different focal lengths for light of different wavelengths and polychromatic images will appear blurred. In order to correct this aberration, single lenses are replaced with assemblies containing several carefully shaped pieces of glass with different refractive indices.

Monochromatic aberrations arise because of the different path lengths of different rays from an object point to the image point. The simplest of these effects is spherical aberration. The portion of the lens furthest from the optical axis brings rays to a

focus nearer the lens than does the central portion of the lens. The monochromatic aberrations can be reduced if only the central portion of the lens is used.

5.3.3 *Electrons versus light*

Visible light may be described in terms of photons or as radiation of wavelength 400-700nm while electrons can be considered as radiation with wavelengths between about 0.001 and 0.01nm. Electrons are very much more strongly scattered by gases than is light. Therefore the optical paths of an electron microscope must be evacuated to a pressure of better than 10^{-2} Pa. The theoretical resolution of an electron microscope is about 0.02nm, however in the transmission electron microscope (TEM) this sort of resolution cannot be obtained mainly because of spherical aberrations. The only way of minimizing spherical aberrations is to restrict the electrons to paths very near the optical axis, by using a small objective aperture. The use of a small aperture reduces spherical aberration and increases depth of field but makes the diffraction-limited resolution worse. There is an optimum size of aperture (i.e. value of α) for which the net resolution is smallest. Finally, in opposition to photons, electrons carry a charge and can be deviated by electromagnetic fields. This property is used in different ways in scanning and transmission electron microscopy.

5.3.4 *Transmission Electron Microscopy*

General view

In a transmission electron microscope (TEM), a thin specimen is irradiated with an electron beam of uniform current density. The most common types of TEM have thermionic guns capable of accelerating the electrons through a selected potential difference of at least 200keV. The electron beam is obtained by thermionic emission from tungsten hairpin cathodes or LaB₆ rods [80]. For some applications, particularly if the specimen is relatively thick or very high resolution is required, it is an advantage to use much higher electron energies. All lenses are electromagnetic and a condenser-lens system permits variation of the illumination aperture and the area of the specimen illuminated [81]. These components are assembled into a vertical

'microscope column' such as the one used throughout this project (Figure 5.1). The electron-intensity distribution behind the specimen is imaged with a three- or four-stage lens system, onto a fluorescent screen. Finally, the image can be recorded using a CCD camera and digitised to be stored in a computer file for further processing. The high aberrations of the objective lens make small apertures (10-25mrad) necessary to achieve optimum resolution (≈ 0.2 - 0.5 nm). Electrons interact strongly with atoms by elastic and inelastic scattering. The specimen must therefore be very thin, the maximum thickness depending on the density and elemental composition of the object and the resolution desired.

The condenser system

Below the electron gun are condenser lenses whose main functions are to demagnify the beam emitted by the gun and to control its diameter and convergence angle when it hits the specimen. This enables the operator to control the area of the specimen which is hit by the beam and thus the intensity of illumination.

The specimen chamber

Below the condenser lenses lies the specimen chamber, where a very small specimen must be held in the correct position but should also be capable of being moved and tilted by large amounts. These constraints are usually met by a side-entry specimen rod which holds a 3mm diameter specimen (or a smaller specimen on a 3mm support grid) between the pole pieces of the objective lens. The specimen rod enters the column through an airlock, and can usually be moved about 2mm in each of the x and y directions, in order to locate the region of interest, and by a fraction of a millimetre in the z direction in order to bring it to the object plane of the lens. It is quite easy to tilt the specimen about the long axis of the holder by up to 60° by rotating the holder itself. The mechanism which provides all these movements and tilts must ensure that when the appropriate specimen position has been selected it remains extremely stable.

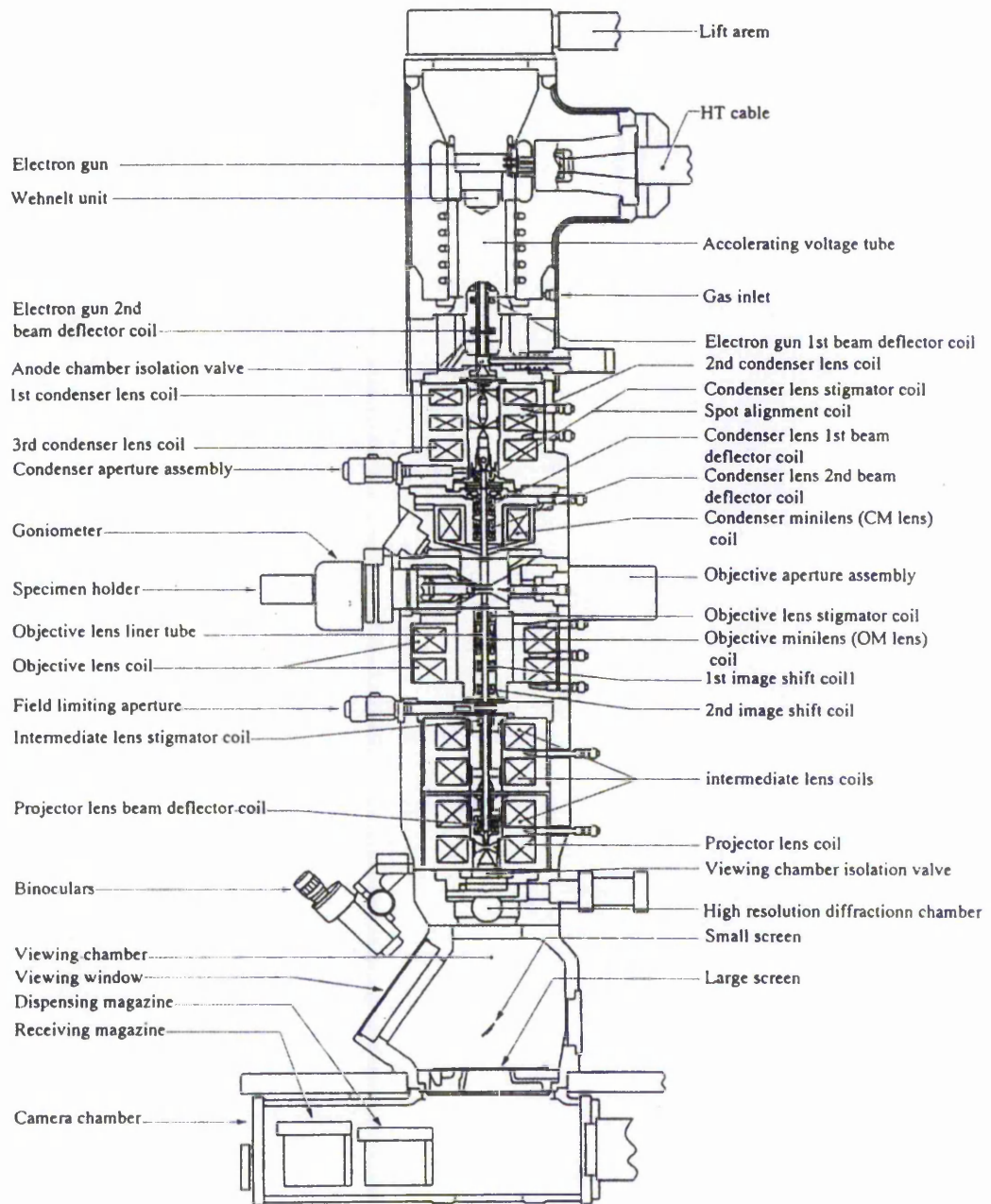


Fig. 5.1: Cross-section of the JEOL 2010 transmission electron microscope used during this project.

The objective and intermediate lenses

The role of the objective is to form the first intermediate image and diffraction pattern, one or other of which is enlarged by the subsequent projector lenses and displayed on the viewing screen. The first projector lens (often called the intermediate or diffraction lens) can usually be switched between image and diffraction modes. In the image mode it is focused on the image plane of the objective. The magnification of the final image on the microscope screen is then controlled by the strength of the remaining projector lenses. An essential feature of the objective system is the aperture holder which enables any one of three or four small apertures to be inserted into the column in the back focal plane. The diameter of the aperture is used to control the resolution, and more generally the contrast of the image.

The projector system - images

The first image produced by the objective usually has a magnification of 50-100 times. This is further magnified by a series of intermediate and projector lenses and is finally projected on the fluorescent screen. By switching on three or four lenses, each providing a magnification of up to twenty times, a total magnification of up to one million is easily achieved.

Alignment

The alignment of the electron beam along the optical axis of each lens is crucial in order to minimise the aberrations and attain the optimum resolution of the instrument. To reach this point, the electromagnetic lenses must themselves be mechanically well aligned, and this will generally have been done by the manufacturer. Minor adjustments are then performed by the operator using small electromagnetic deflection coils placed at strategic points in the column. Further coils permit small fields to be imposed to correct the effect of astigmatism in the condenser, objective and projector systems.

Electron-Specimen Interactions and Their Applications

Three major effects of electron interaction with the sample can contribute to the contrast of a TEM image. Elastic and inelastic scatterings can be considered as electron-atom interactions, whereas electron diffraction is due to electron interactions with the crystalline material lattices. In each case the important consideration is that the final image can only be formed using those electrons which pass through the objective aperture. Electrons stopped by the aperture will not contribute to the image. Clearly the size and position of the objective aperture will determine the nature of the contrast seen in the image.

Elastic Scattering and Mass-thickness contrast Elastic scattering is the most important of all the interactions that create contrast in the electron image. The Coulomb potential of a nucleus or the inner potential of a dense particle shifts the phase of the electron wave with De Broglie wavelength $\lambda = h/mv$. An electron-optical refractive index can be defined, which is proportional to the Coulomb energy. As a result, electrons are elastically scattered at the nuclei of the specimen atoms, and stopped by the aperture in the back focal plane of the objective lens [80]. If the aperture is centred about the optical axis, then in the absence of a specimen a bright background is seen. This is known as bright field imaging. Regions of the specimen which are thicker or of higher density will scatter more strongly and will appear darker in the image [81].

For large-angle scattering, or when the energy of the electrons is high, the primary electrons may lose energy. The energy transferred can exceed a threshold energy, of the order of 10-30eV, beyond which an atom can be displaced from a crystal position to an interstitial site. However small-angle scattering of electrons governs most of the scattering contrast observed. For small angles, the term elastic scattering is reserved for interactions in which the primary electrons lose no energy.

Electron Diffraction If the specimen is crystalline then an additional contrast mechanism is encountered. Diffraction of the electron beam means that the intensity of scattering is greatly increased at particular angles. The objective aperture can then

be used to stop diffracted beams, thus giving dark contrast from regions which are diffracting strongly. In bright field imaging the objective aperture is used to stop all diffracted beams and only permit undeflected electrons to contribute to the image. If the aperture is displaced it can be used to select a particular diffracted beam. This is known as dark field imaging since in the absence of a specimen the background would appear dark. However if a dark field image is created by displacing the aperture severe aberrations are likely to be introduced since all the imaging electrons are travelling far from the optical axis, where spherical aberration is large. A better method of high resolution dark field imaging is to tilt the primary electron beam, so that the chosen diffracted beam travels along the optical axis and passes through the centred aperture. The main interest in diffraction contrast arises from the ability to make visible crystal defects such as dislocations, stacking faults and precipitates [81].

Two theories can be used to explain electron diffraction. The kinematical theory, used for very thin foils (few nm), assumes that the amplitude of a Bragg diffracted wave is small compared to that of the primary wave, whereas the dynamical theory, based on the Schrödinger equation, is used for thick crystals and results in a 'pendellösung', which means that the amplitudes of the Bragg diffracted and primary waves oscillate in antiphase as a function of depth and depend sensitively on the tilt of the specimen. A theory with 20-100 or more diffracted beams has to be used if the observed phenomena are to be explained in detail. The pendellösung causes typical diffraction effects in crystal foils, which can be seen as edge or bend contours, for example. The image intensity depends very sensitively on the strain field of any lattice defects, so that a large variety of defects can be imaged and analysed without resolving the lattice structure. If the objective aperture is so large that the primary beam and one or more Bragg reflections can interfere in the image plane, an interference pattern is formed, enabling the observation of the crystal structure and its faults.

Inelastic Scattering and X-Ray Emission In inelastic scattering, the total energies and the momenta of the colliding particles are conserved, but an electron excitation

of the atom or solid is stimulated, and the primary beam loses energy. The most important electron excitations that can be observed with energy losses smaller than 50 eV are the intra- and interband and plasmon excitations near the Fermi level. The plasmons are longitudinal waves in the electron plasma and decay into either photons or phonons. Ionisation of an inner shell results in an edge-like rise in the energy loss spectrum for an energy value corresponding to ionisation of the K, L or M shell. The energy loss spectrum is rich in information regarding the electronic structure, indicated by the plasmon losses, and the chemical composition indicated by the ionisation losses. When the vacancy in an ionised shell is filled by an electron from a higher state the energy difference is emitted either as a x-ray quantum or as an Auger electron (AE). In semiconductors, electron-hole pairs are generated which can result in an electron-beam-induced current (EBIC). Electron-hole pairs recombine radiationlessly or cause cathodoluminescence (CL). All excitation energy that does not leave the specimen with the secondary electrons (SE) and photons is converted into phonons and heat.

5.3.5 *Scanning Electron Microscopy*

Principle

The electron gun, condenser lenses and vacuum system, are similar in both scanning and transmission electron microscopes. However, in contrast to the TEM, the SEM is primarily used to study the surface, or near surface structure of bulk specimens. An electron gun, usually a tungsten filament thermionic emission type, produces electrons, and accelerates them to an energy between about 2keV and 40keV. Two or three condenser lenses then demagnify the electron beam until, as it hits the specimen, it may have a diameter of only 2-10 nm.

The fine beam of electrons is scanned across the specimen by the scan coils, while a detector counts the number of low energy secondary electrons, or other radiation, given off from each point on the surface. At the same time, the spot of a cathode ray tube (CRT) is scanned across the screen, while the brightness of the spot is modulated by the amplified current from the detector. The electron beam and the

CRT spot are both scanned in a similar way to a television receiver, that is, in a rectangular set of straight lines known as a raster. The mechanism by which the image is magnified is then extremely simple and involves no lenses at all. The raster scanned by the electron beam on the specimen is made smaller than the raster displayed on the CRT. The linear magnification is then the side length of the CRT (L) divided by the side length (l) of the raster on the specimen.

Signal obtained

The most important signals are produced by secondary electrons with most probable exit energies of 2-5eV and by backscattered electrons, with energies that range from the energy of the primary electrons to about 50eV. The secondary-electron yield and the backscattering coefficient depend on the angle of electron incidence (topographic contrast), the crystal orientation (channelling contrast) and electrostatic and magnetic fields near the surface (voltage and magnetic contrast) [80]. Of the other radiations, X-rays are used primarily for chemical analysis rather than imaging. Auger electrons are of such low energy, and are so easily absorbed that they require an ultra high vacuum system and specialized equipment for their efficient use [81]. The region into which the electrons penetrate the specimen is known as the interaction volume, and throughout it, various radiations are generated as a result of inelastic scattering, although as the primary electrons lose energy the amount and type of secondary radiations will alter. The radiation generated will be detected if it escapes from the specimen, and this will depend on the radiation and the specimen. Most of X-rays produced will escape from the interaction volume, whereas electrons will not be backscattered out of the specimen if they have penetrated more than a fraction of a micron, and the backscattered signal will originate from a much smaller region than the X-rays come from. Although secondary electrons are generated both by the primary electrons entering the specimen and by escaping backscattered electrons, the former are more numerous, and therefore the detected secondary electron signal originates mainly from a region which is little larger than the diameter of the incident beam. The resolution of the SEM is closely related to the sampling volume of the signal used. Secondary electrons, having the smallest sampling volume are

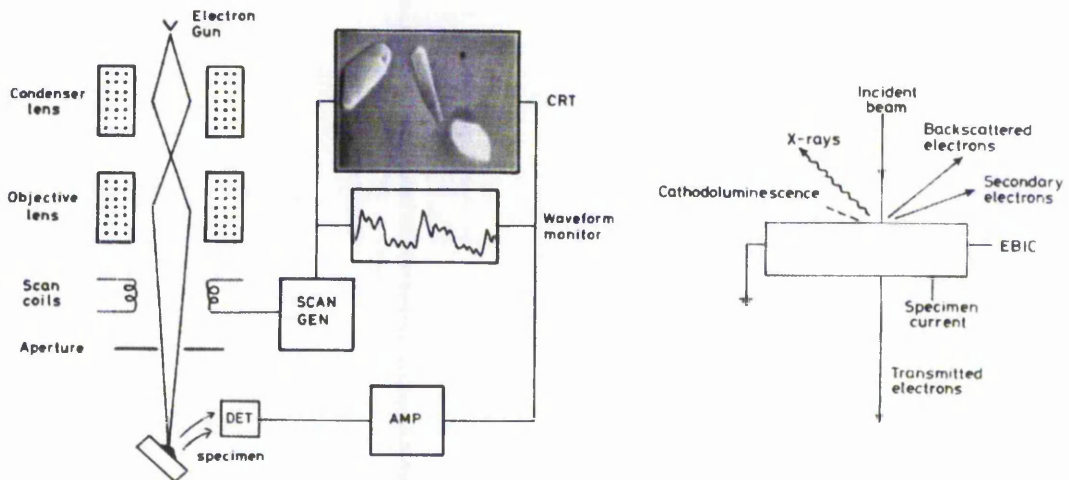


Fig. 5.2: Schematic representation of: The scanning electron microscope principle (left hand side) and the origin of the signal obtained in a SEM experiment.

therefore capable of giving a better spatial resolution than the other signals.

Secondary electrons detection

Secondary electrons are detected by a scintillator-photomultiplier system known as the Everhart-Thornley detector. The secondary electrons strike a scintillator which then emits light. The light is transmitted through a light pipe, and into a photomultiplier which converts the photons into pulses of electrons, which may then be amplified and used to modulate the intensity of the CRT. The energy of the secondary electrons (10-50eV) is too low to excite the scintillator, and so they are first accelerated by applying a bias voltage to a thin aluminium film covering the scintillator. A metal grid or collector at a potential of several hundred volts surrounds the scintillator, to prevent the high voltage of the scintillator affecting the incident electron beam, and to improve the collection efficiency by attracting even secondary electrons not moving towards the detector.

Detecting backscattered electrons

Most microscopes are fitted with purpose built backscattered electron detectors, which are of two types:

Scintillator detectors These detectors are designed to maximize the solid angle of collection (for example, the Robinson detector). They can be used in conjunction with rapid scan rates due to their rapid response time. However, they are bulky, and may restrict the working distance of the microscope, and may need to be retracted if, for example, it is necessary to detect X-rays.

Solid-state detectors When a high-energy electron impinges on a semiconductor, it produces many electron-hole pairs. Normally these will rapidly recombine, but if a voltage is applied to the semiconductor, for example, by the self-bias generated by a p-n junction, then they may be separated, thus producing a current, which can subsequently be amplified. The detector is usually in the form of a thin flat plate, which is mounted on the objective pole piece, and thus does not interfere with normal operation of the instrument. The detector consists of up to four such elements whose outputs may be measured independently. The main disadvantage of a solid-state detector is its relatively slow response time, and hence its unsuitability for rapid scan rates.

The optics of the SEM

The example of the JEOL JSM840A with which SEM images of this work have been obtained is presented in figure 5.3. The electron gun produces a monochromatic beam of electrons collected by the condenser lens which produces a demagnified image of the filament. In order to minimize spherical aberration, the entry of rays into the objective lens is restricted by an aperture. The objective lens demagnifies the filament image further, producing a probe of diameter d on the surface of the specimen. The distance between the objective lens and the specimen is known as the working distance (WD) of the microscope. The probe size in the SEM can be modified by altering the strength of the condenser lens or the working distance.

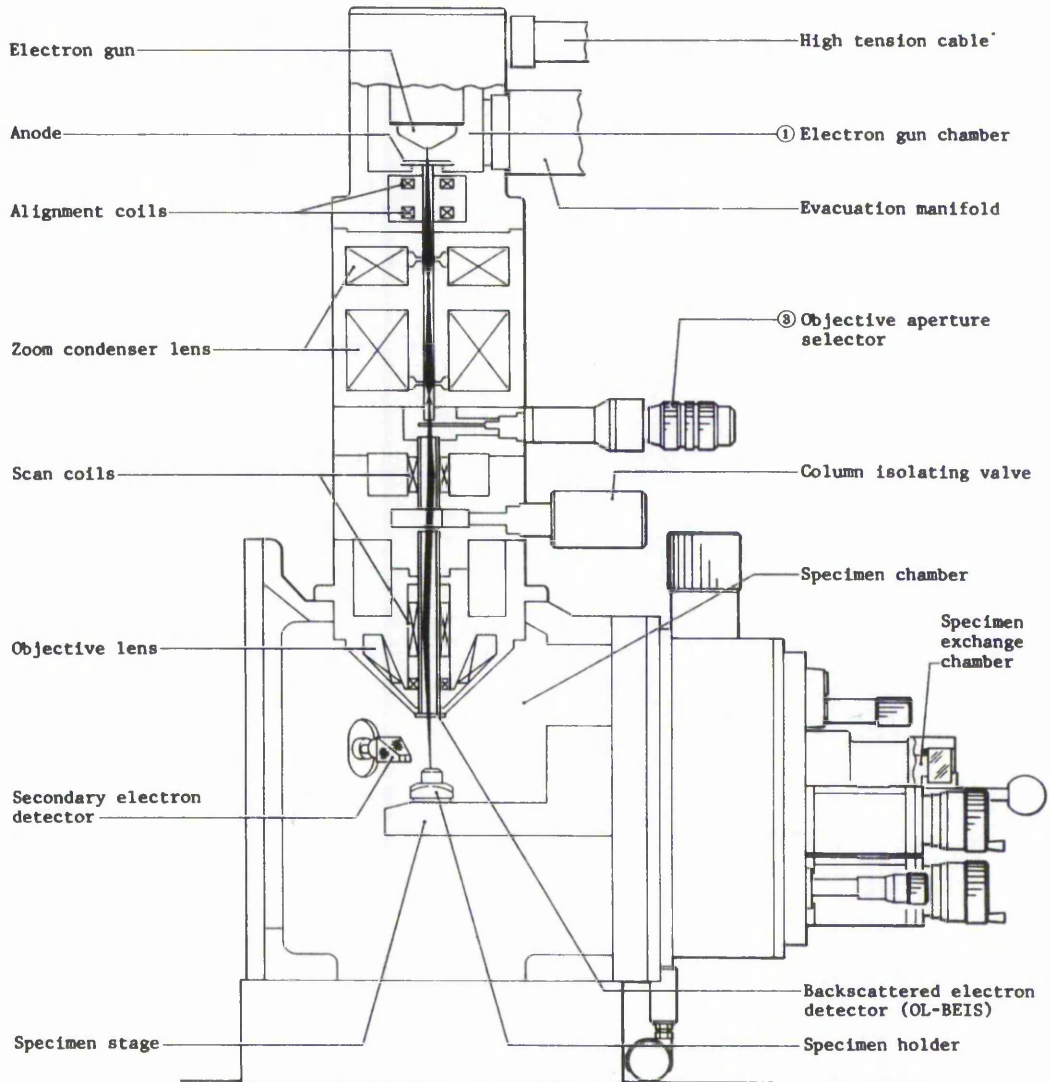


Fig. 5.3: Cross-section of the JEOL JSM 840A column.

The performance of the SEM

Pixels The amplified signal from the detector is output to a cathode ray tube, or stored as a digitised image in a computer file. Both tube and file contain a defined number of discrete image elements of pixels, each of these pixels corresponding to a pixel on the specimen. In order to resolve two features, they must occupy separate pixels. Therefore, the working resolution of the instrument can be no better than

the specimen pixel size. The size of the electron probe relative to the specimen pixel size is very important. For optimum performance of the instrument the sampling volume should be close to the specimen pixel diameter, and the probe size should be adjusted as the magnification of the microscope is altered. The resolution also depends on the signal used and for example the resolution in X-ray detection mode will be lower than in secondary electrons detection mode as the signal originates from a much larger sampling volume.

Depth of field One of the advantages of SEM over light microscopy is the large depth of field of the electron microscopy technique. Although the beam is focused on the specimen, the convergence angle is small, and, assuming a point focus, the beam diameter defocuses to a small extent with the depth of the object and the image will remain in focus as long as the probe diameter does not exceed the specimen pixel dimensions.

The minimum attainable probe size The probe size may be decreased by increasing the strength of the condenser lens, and decreasing the working distance. As the latter occurs, the beam convergence angle increases. Rays which are off the optic axis are subject to spherical aberration and the probe diameter is increased.

The minimum usable beam current In order to resolve two points on the specimen, there must be a discernible difference between the signals from these two regions. The intensity of each pixel is derived from the number of secondary electrons arriving at the detector averaged over time, to which a noise component is added. This noise component will tend to obscure the natural contrast of the specimen. Rose has determined that the human eye can only distinguish two points on a CRT for a difference in signal superior to 5 times the noise level. The mean number of electrons detected for each pixel is related to the operating conditions of the microscope, the efficiency of the detector and on the beam-specimen interactions. The Rose criterion can be expressed in terms of the critical current required to discern a contrast level in the specimen, this current increasing as the frame scan time decreases. The minimum probe size, and therefore the best resolution obtainable in terms of a

given contrast level in the specimen can be calculated as well.

Topographic images

One of the principal uses of the scanning electron microscope is to study the surface features, or topography of a sample. Topographic images are generally obtained from secondary and back scattered electrons. The backscattered electron coefficient and the secondary electron coefficient are both a minimum when the surface of the specimen is perpendicular to the electron beam. This is because of the shape of the interaction volume and its relationship to the surface of the specimen. As the specimen is tilted, electrons are increasingly likely to be scattered out of the specimen, rather than further into the specimen. The secondary electron coefficient therefore varies with the tilt of the specimen and more secondaries are produced from tilted regions of the specimen. As the efficiency of the Everhart-Thornley detector is not very sensitive to the trajectories of the secondary electrons, we expect the number of detected electrons to increase with surface tilt. It is partly for this reason that specimens being studied for topographic contrast with the ET detector are usually tilted some 20-40 degrees towards the detector. The image appears as if we were looking at the object from above, when it is being illuminated with diffuse light, the detector being the source of the diffuse light.

Topographic images may also be obtained using back scattered electrons. The yield of back scattered electrons also increases with increasing tilt angle, but only back scattered electrons going in the direction of the detector are taken into account. The image appears as if we were looking at the object from above, when it is illuminated by a light source making the same solid angle with the specimen as does the detector. Therefore in the SEM, a rough surface observed with back scattered electrons will have more shadows than the same specimen viewed with secondary electrons. Moreover, multiple detectors can be used, giving an effect comparable to multiple spotlights. This multi-element back scattered electron detector may be used to enhance the topographic image from a specimen which is almost flat, or when the suppression of compositional or crystallographic contrast is desirable.

Compositional images

The secondary electron coefficient does not depend very much on the composition of the sample, whereas the back scattered coefficient varies monotonically with atomic number and is almost independent of accelerating voltage. Two phases of different back scattered coefficients will therefore appear contrasted. Phase contrast does not exceed 5% and will be weak compared to topographic contrast which may approach 100%. The areas of compositional interest are first identified by back scattered imaging, and the phase compositions are then determined by spot analysis of the X-ray signal. It is possible to obtain quantitative compositional information by measuring the intensity of the backscattered signal from the phase of interest, comparing it with a standard element to obtain the atomic number of the phase. Although this technique is potentially valuable on account of its high spatial resolution, and for its ability to analyse phases of low atomic number which are not easily determined using X-rays, great care must be taken to exclude other forms of contrast, such as topographic or crystallographic effects, if reliable results are to be obtained.

Preparation of solid materials for scanning electron microscopy

In the case of phase separation after centrifugation of the samples (Al hydroxide-BSA) the resulting gel-like materials were rinsed with water and centrifuged again. Unlike transmission electron microscopy, special specimen-preparation techniques are rarely needed in scanning electron microscopy. Nevertheless, charging effects have to be avoided, by coating the specimen with a thin conductive film (carbon or gold) and organic specimens have to be protected from surface distortions by fixation or cryo-techniques [80]. The solid content of the samples at the bottom of the centrifuge tubes was subsequently freeze-dried for 24 hours using a Virtis freeze-drier before being mounted on SEM stubs and coated with carbon using a standard procedure. The SEM images were acquired using a JEOL-JSM-840A SEM, acceleration voltage 25KeV, working distance 8mm.

6. DATA FITTING TECHNIQUES: THE LEAST SQUARES MINIMISATION

6.1 *The objective function*

The least-squares method consists of finding those parameters that minimize an objective function. The objective function depends in some way on the parameters, on a series of experimentally measured numbers, or observations, and on a set of independent variables which are also experimental in origin.

Let us consider m observations, y_i^{obs} , ($i = 1, m$), allocated to a vector \mathbf{y}^{obs} . Similarly, we may allocate the values of the independent variables to a vector \mathbf{x} , containing the elements x_k ($k = 1, m'$). Suppose that there are n parameters. Their values will be obtained from a vector \mathbf{p} , p_j ($j = 1, n$).

We must now define a model such that corresponding to each observation, y_i^{obs} , there will be a calculated value y_i^{calc} :

$$y_i^{obs} = y_i^{calc} + e_i; \quad i = 1, m \quad (6.1)$$

Where e_i are the experimental errors.

The calculated value will depend on the parameters and the independent variables:

$$y_i^{calc} = f(\mathbf{p}, x_i) \quad (6.2)$$

x_i denotes a vector of all those values of the independent variable(s) upon which the i th observation depends. Most commonly there is only one independent variable, and we would write x_i for that scalar quantity.

A linear model is one in which the calculated values are linear functions of the parameters, i.e. each parameter is simply multiplied by a function of x , $f(x)$. The

general form of a linear model is as follows:

$$y_i^{calc} = \sum_{j=1, n} f_j(\mathbf{x}_i) p_j; \quad i = 1, m \quad (6.3)$$

In this expression the coefficients of the parameters, $f_j(x_i)$, are independent of the parameters, and this defines the system as linear. The quantities x_i are independent variables, usually assumed to be free from error.

The residual \mathbf{r} of the observation calculation can be considered as the difference between calculated and observed values, with

$$r_i = y_i^{obs} - y_i^{calc}; \quad i = 1, m \quad (6.4)$$

The simplest form of objective function is a sum of squared residuals — the term ‘least-squares’ derives from this kind of function:

$$S = \sum_{i=1, m} r_i^2; \quad S = \mathbf{r}^T \mathbf{r} \quad (6.5)$$

However, in defining the objective function in this way we are making two important assumptions. Indeed we are assuming that the independent variables x_i are not subject to experimental error, and that the errors, e_i , are all equal and independent of each other.

To be more general, we must accept that each observation is subject to a different error and that the errors for each pair of observations are connected through a covariance term. The variances and covariances are allocated to M_{hk} ; $h = 1, m$; $k = 1, m$. In this case we define the objective function as follows:

$$S = \sum_{h=1, m} \sum_{k=1, m} r_h W_{hk} r_k; \quad \mathbf{r}^T \mathbf{W} \mathbf{r} \quad (6.6)$$

The matrix \mathbf{W} is known as the weight matrix and is the inverse of the variance-covariance matrix \mathbf{M} :

$$\mathbf{W} \mathbf{M} = \mathbf{M} \mathbf{W} = \mathbf{I}; \quad \sum_{h=1, m} W_{ih} M_{hk} \quad (i = k); \quad \sum_{h=1, m} W_{ih} M_{hk} = 0 \quad (i \neq k) \quad (6.7)$$

It will be seen that equation (6.7) becomes equivalent to equation (6.5) in a special case. In the next development of this chapter, we will discuss the minimization of this objective function.

6.2 The weighted normal equations method

In the previous section, we have determined the general form of the objective function equation (6.6). When the variance-covariance matrix of the observations is a diagonal, constant matrix, i.e.

$$M_{ii} = \sigma^2, \quad M_{ij} = 0 \quad \text{for } i \neq j \quad (6.8)$$

we can say that it is a unit matrix multiplied by the constant σ^2 , known as the variance of an observation of unit weight. Thus, if we take the weight matrix to be a unit matrix, we have

$$W_{ii} = 1, \quad W_{ij} = 0 \quad \text{for } i \neq j \quad \mathbf{W} = \frac{1}{\sigma^2} \mathbf{M}^{-1} = \mathbf{I} \quad (6.9)$$

and the weights are proportional to the inverse of \mathbf{M} . The objective function becomes the sum of squared residuals:

$$S = \sum_{i=1,m} r_i^2 \quad (6.10)$$

The minimum of a function is specified when the partial derivatives of the function with respect to each parameter are zero. For the minimization, each of the n partial derivatives is therefore set equal to zero:

$$\frac{\partial S}{\partial p_k} = \sum_{i=1,m} 2r_i \frac{\partial r_i}{\partial p_k} = 0 \quad (k = 1, n) \quad (6.11)$$

These n equations are termed as the normal equations. To elaborate these equations further we need to derive expressions for the derivatives $\frac{\partial r_i}{\partial p_k}$:

$$\begin{aligned} r_i &= y_i^{obs} - y_i^{calc} \\ \frac{\partial r_i}{\partial p_k} &= - \frac{\partial y_i^{calc}}{\partial p_k} \end{aligned} \quad (6.12)$$

For a linear model,

$$y_i^{calc} = \sum_{j=1,n} f_j(x_i) p_j \quad (i = 1, m) \quad (6.13)$$

$f_j(x_i)$ can be any function of x_i such as a constant, x_i itself, x_i^2 , $\sin x_i$, $\exp x_i$, etc.

Therefore

$$\frac{\partial r_i}{\partial p_k} = - \frac{\partial y_i^{calc}}{\partial p_k} = -f_k(x_i) \quad (6.14)$$

On substituting the expressions for the residuals into the normal equation, the k th normal equation becomes, after removing the factor -2 ,

$$\begin{aligned} \sum_{i=1,m} (y_i^{obs} - y_i^{calc}) f_k(x_i) &= 0 \\ \sum_{i=1,m} f_k(x_i) y_i^{calc} &= \sum_{i=1,m} f_k(x_i) y_i^{obs} \\ \sum_{i=1,m} f_k(x_i) \sum_{j=1,n} f_j(x_i) p_j &= \sum_{i=1,m} f_k(x_i) y_i^{obs} \end{aligned} \quad (6.15)$$

These are n equations ($k = 1, n$) with the n unknown parameters p_j , values of the parameters can be found that minimize the sum of squares S . It is convenient to rearrange the double summation on the left-hand side of the normal equations. The k th normal equation can be written as

$$\sum_{j=1,n} \left[\sum_{i=1,m} f_k(x_i) f_j(x_i) \right] p_j = \sum_{i=1,m} f_k(x_i) y_i^{obs} \quad (6.16)$$

We can now denote the results of the inner summation, [...], by a single symbol, A_{kj} , the coefficient of the j th parameter in the k th normal equation

$$A_{kj} = \sum_{i=1,m} f_k(x_i) f_j(x_i) \quad (6.17)$$

Likewise, the summation on the right-hand side can be written as the single symbol b_k :

$$b_k = \sum_{i=1,m} f_k(x_i) y_i^{obs} \quad (6.18)$$

The k th normal equation can now be written in a clear form:

$$\sum_{j=1,n} A_{kj} p_j = b_k \quad (6.19)$$

6.3 Resolution of the normal equations

It is clear that once we have written down an equation defining the model we can set up and solve the normal equations to obtain values for the parameters.

The model of a linear least-squares system can be written as

$$\mathbf{y}^{calc} = \mathbf{J}\mathbf{p}; y_i^{calc} = \sum_{j=1,n} J_{ij} p_j \quad (6.20)$$

\mathbf{J} stands for the Jacobian matrix and its elements J_{ij} are the same as $f_j(x_i)$ above. It is a rectangular array with n columns ($j = 1, n$) and m rows ($i = 1, m$):

$$J_{ij} = \frac{\partial y_i^{calc}}{\partial p_j}$$

$$\mathbf{J} = \begin{bmatrix} J_{11} & J_{12} & \dots & J_{1n} \\ J_{21} & J_{22} & \dots & J_{2n} \\ \dots & \dots & \dots & \dots \\ J_{m1} & J_{m2} & \dots & J_{mn} \end{bmatrix} \quad (6.21)$$

\mathbf{y}^{calc} is a vector consisting of the values y_i^{calc} ($j = 1, n$). The normal equations become

$$\mathbf{J}^T \mathbf{J} \mathbf{p} = \mathbf{J}^T \mathbf{y}^{obs}; \quad \sum_{j=1, n} \left(\sum_{i=1, m} J_{ik} J_{ij} \right) p_j = \sum_{i=1, m} J_{ik} y_i^{obs} \quad (k = 1, n) \quad (6.22)$$

\mathbf{J}^T is the transpose of \mathbf{J} , that is $J_{ik}^T = J_{ki}$ for $i = 1$ and $k = 1, m$ and $k = 1, n$. \mathbf{y}^{obs} is a vector consisting of the observed values y_i^{obs} ($i = 1, m$). Note that the normal equations matrix \mathbf{A} is square, with n rows and columns, and is always symmetrical:

$$A_{jk} = \sum_{i=1, m} J_{ij} J_{jk} = \sum_{i=1, m} J_{ik} J_{ij} = A_{kj} \quad (6.23)$$

The i th row of the Jacobian contains the partial derivatives of y_i^{calc} with respect to each parameter, and it can be written as

$$[J_i] = \left[\frac{\partial y_i}{\partial p_1} \quad \frac{\partial y_i}{\partial p_2} \quad \dots \quad \frac{\partial y_i}{\partial p_n} \right] \quad (6.24)$$

The expressions in this row are all that is needed to form the normal equations, as follows. For the left-hand side, A_{kj} is the sum, over all rows, of the product of the k th and j th elements in the i th row. Similarly, the right-hand side is formed by summing, over all rows, the product of each element of $[J_i]$ with the vector of the observations. In this way the normal equations can be set up without storing the whole Jacobian matrix. First set all the elements of \mathbf{A} and \mathbf{b} to zero. Then, for each of point i calculate $[J_i]$ and accumulate the right- and left-hand sides:

$$b_k \leftarrow b_k + [J_i]_k y_i^{obs} \quad (k = 1, n)$$

$$A_{kj} \leftarrow A_{kj} + [J_i]_k [J_i]_j \quad (j = 1, n; k = 1, j)$$
(6.25)

This procedure forms the upper triangle of \mathbf{A} , which is all that is needed as \mathbf{A} is symmetrical. In equation (6.6), the weight matrix should ideally be taken as the inverse of the variance-covariance matrix. However, it is also acceptable, though less useful that the weight matrix be proportional to the inverse of the variance-covariance matrix. This would imply that the relationship of one experimental error to another is known, but the absolute scale of the errors is not. In this case the proportionality constant will be estimated in the least-squares process.

Introduction of weights does not greatly complicate the least-squares calculation. By following the same procedure used in the unit-weighted case it can be shown that the k th normal equation becomes

$$\sum_{i=1,m} \sum_{h=1,m} \sum_{j=1,n} f_k(x_i) W_{ih} f_j(x_h) p_j = \sum_{i=1,m} \sum_{h=1,m} f_k(x_i) W_{ih} y_h^{obs} \quad (6.26)$$

In matrix notation the normal equations are written simply as

$$\mathbf{J}^T \mathbf{W} \mathbf{J} \mathbf{p} = \mathbf{J}^T \mathbf{W} \mathbf{y}^{obs} \quad (6.27)$$

$$\mathbf{A} \mathbf{p} = \mathbf{b}$$

In many cases, and particularly where the least-squares minimisation has been used in this work, the functional relationship cannot be written in linear form, the examples in this work being models using sums of exponentials (time-resolved ferron spectrophotometric assay), or sum of peak functions (spectral ^{27}Al NMR, FT-IR) data fitting, or fitting after differentiation of raw data provided by potentiometric (pH) or weight-loss (TGA) measurements). Therefore, the use of non-linear least-squares minimisation, as well as its application and peculiarities as applied to the studies presented in this thesis will be emphasised in the following section.

6.4 The linear approximation to a non-linear system

In the case in which the observations cannot be predicted by a linear combination of the chosen parameters, we have to return to equation (6.2), which means that the observations can be calculated by a function of all the parameters p_j ($j = 1, n$) and all the independent variables x_i . This will for example be the case for the time-resolved ferron spectrophotometric assay, whose data fitting model uses a sum

of exponential functions of both parameters and independent variable terms. A 'one species' version of this model could be written $y^{calc} = p \exp(qx)$ where p and q would be the parameters (p , the species concentration and q , the kinetic constant of dissociation) and x being the independent variable (time of Al concentration measurement): the relationship is non-linear because the partial derivatives $\frac{\partial y}{\partial p}$ and $\frac{\partial y}{\partial q}$ both contain the parameters themselves. This kind of non-linear problem can be treated by the method of least squares by using a technique for successive approximations. The key to using this technique is to expand the function as a Taylor series about some value of the parameter set, \mathbf{p}^{ini} , say:

$$y_i^{calc} = y_i^{ini} + \sum_{j=1,n} \left(\frac{\partial f_i}{\partial p_j^{ini}} \right) \Delta p_j \quad (6.28)$$

In writing this expression we are making two approximations, namely that the other terms in the Taylor series expansion can be ignored and that the infinitesimal dp_j can be replaced by the finite increment Δp_j . Both of these approximations are usually very good in the limit when Δp_j becomes small, i.e. when y_i^{calc} is nearly equal to y_i^{ini} .

With this approximation for the values of y_i^{calc} we can minimize the objective function $\mathbf{r}^T \mathbf{W} \mathbf{r}$, by identifying the residuals as

$$\begin{aligned} r_i &= y_i^{obs} - y_i^{calc} \\ &= y_i^{obs} - y_i^{initial} - \sum_{j=1,n} \left(\frac{\partial f_i}{\partial p_j^{initial}} \right) \Delta p_j \\ r &= \Delta y \quad - \quad J \Delta p \end{aligned} \quad (6.29)$$

In the linear case we have $r = y_i^{obs} - Jp$, and the solution to the minimization is given by the normal equations $J^T W J p = J^T W y^{obs}$. In the non-linear case the normal equations are

$$J^T W J \Delta p = J^T W \Delta y \quad (6.30)$$

At first sight these equations look very similar to those obtained for a linear system, with p replaced by Δp and y replaced by Δy . There are, however, some very significant complications in the apparently simple substitutions.

Firstly, there is an absolute need to estimate some initial parameter values, whereas

in a linear model parameter estimation is optional. The problem of estimating values for the parameters is in general not a trivial one, and in some cases can become a major difficulty.

Secondly, the correction Δp , when added to the initial parameter values, does not usually yield the correct least-squares estimate of the parameters immediately. Rather, the process must be repeated with $p \leftarrow p + \Delta p$ as the new initial estimate of the parameters. Thus, the calculation becomes iterative, with the parameters being refined by successive approximation. This is a result of the inadequacy of the first-order Taylor series approximation.

Thirdly, the iterative nature of the process introduces other problems. Ideally the objective function S should decrease smoothly towards its minimum value as the iterations proceed, but it often happens that S may increase at some stage. This is known as divergence, and is also a result of the inadequacy of the first-order Taylor series approximation.

Finally, there is a problem of deciding when the iterations should be terminated. This is known as setting convergence criteria, and it is far from easy in the general case.

The non-linear least-squares procedure can be summarized as having two distinct phases: initial parameter estimation and then iterative refinement, guarding against divergence and checking at the end of each refinement cycle for final convergence. Many people try to program a non-linear system without protecting against divergence, and at first this may be satisfactory, but sooner or later divergence will occur. It is therefore preferable, when writing the program, to include protection against divergence in the planning stage because otherwise the program may need extensive rewriting.

At the conclusion of a non-linear refinement one obtains the usual information on parameter errors and correlation coefficients. However, it needs to be borne in mind that these values are in a statistical sense biased and should accordingly be treated with caution. The bias arises because the treatment of errors assumed a linear relationship between parameters and calculated values with neglect of the higher-order terms of the expansion.

6.5 Non-linear refinement

As seen in the previous sections, the calculation of the parameters of a non-linear model is an iterative process. Let us consider the first iteration. We begin by assigning initial values to the parameters, $\mathbf{J}^{initial}$, $\mathbf{y}^{initial}$ and the value of the objective function, $S^{initial}$. The normal equations are set up and solved for the parameter shift vector, $\Delta\mathbf{p}$ as follows. The model is linearised by means of a first-order Taylor series expansion:

$$\begin{aligned} y_i^{calc} &= y_i^{initial} + \sum_{j=1,n} \left(\frac{\partial y_i}{\partial p_j^{initial}} \right) \Delta p_j \\ \mathbf{y}^{calc} &= \mathbf{y}^{initial} + \mathbf{J} \Delta \mathbf{p}; \quad \mathbf{J} = \mathbf{J}^{initial} \end{aligned} \quad (6.31)$$

Since $\mathbf{r} = \mathbf{y}^{obs} - \mathbf{y}^{calc}$, the minimum of $\mathbf{r}^T \mathbf{W} \mathbf{r}$ is given by

$$\frac{\partial S}{\partial \mathbf{p}} = -2\mathbf{J}^T \mathbf{W} \mathbf{r} = 0 \quad (6.32)$$

and the normal equations become

$$\begin{aligned} \mathbf{J}^T \mathbf{W} (\mathbf{y}^{obs} - \mathbf{y}^{initial}) - \mathbf{J} \Delta \mathbf{p} &= 0 \\ \mathbf{J}^T \mathbf{W} \mathbf{J} \Delta \mathbf{p} &= \mathbf{J}^T \mathbf{W} \Delta \mathbf{y} \\ \Delta \mathbf{y} &= \mathbf{y}^{obs} - \mathbf{y}^{initial} \end{aligned} \quad (6.33)$$

The shift vector is then added to the initial parameter vector:

$$\mathbf{p}^{initial} \leftarrow \mathbf{p}^{initial} + \Delta \mathbf{p} \quad (6.34)$$

and the values for \mathbf{y}^{calc} and S are obtained from the new 'initial' set of parameters. If the model were linear the new value of S would be the minimum value and the new parameters would lie at the centre of the ellipsoid of constant S with respect to the parameters, which passes through the initial point, $\mathbf{p}^{initial}$. In a non-linear model, the actual contours are not ellipsoidal. We could say that the shift vector is wrong in both direction and magnitude. Assuming for the moment that S is less than $S^{initial}$, we must designate the new parameter set as $\mathbf{p}^{initial}$ and repeat the whole refinement cycle.

As the refinement proceeds the first-order Taylor series expansion of y^{calc} becomes a

good approximation. The actual contours of the objective function is as near to its minimum value as possible. We say that at this stage the refinement has converged. However, it may happen that the calculated shift vector leads to a point in parameter space where the objective function has a higher value than the point of origin. This phenomenon is known as divergence. Divergence is a problem common to all non-linear systems, and will usually occur when the initial parameter estimates are not very good. What 'very good' means varies from one system to another and it is therefore important that the refinement process should be protected against divergence.

BIBLIOGRAPHY

- [1] D. Baes Jr and R. Mesmer, *The hydrolysis of cations*, Wiley-Interscience, 1976.
- [2] D. A. Skoog and J. Leary, *Principles of Instrumental Analysis*, Fort Worth, Saunders, 1992.
- [3] E. Dahmen, *Electroanalysis: theory and applications in aqueous and non-aqueous media and in automated chemical control*, Elsevier, Amsterdam, 1986.
- [4] G. Svehla, *Automatic potentiometric titrations*, Pergamon, Oxford, 1978.
- [5] C. Brett and A. Oliveira Brett, *Electroanalysis*, Oxford University Press, Oxford, 1998.
- [6] M. Blesa and E. Matijevic, *Advanced Colloid and Interface Science*, 1989, **29**, 173.
- [7] K. Shafran, *Chemical and structural studies of aluminium and zirconium aqueous chemistry*, PhD thesis, Nottingham Trent University, 2003.
- [8] O. Pelletier, P. Davidson, C. Bourgaux, C. Coulon, S. Regnault, and J. Livage, *Langmuir*, 2000, **16**, 5295.
- [9] J. Livage, M. Henry, and C. Sanchez, *Progress in Solid-State Chemistry*, 1988, **18**(4), 259–341.
- [10] C. Falamaki, *Chemical Engineering and Technology*, 2002, **25**, 905.
- [11] R. K. Iler, *The Chemistry of Silica*, 1979.
- [12] F. Y. Sharikov, *Cryochemical synthesis of finely dispersed oxide powders using ion exchange*, PhD thesis, Moscow State University, 1991.

- [13] Y. D. Tretyakov, N. N. Oleynikov, and O. A. Shlyakhtin, *Cryochemical Technology of Advanced Materials*, Chapman & Hall, London, 1997.
- [14] Y. D. Tretyakov, V. P. Shabatin, V. R. Sokolovskii, V. G. Merkulov, and L. N. Tartakovskaya 4186083/31-02 Technical report, USSR patent office, 1987.
- [15] V. P. Shabatin, V. R. Bommareddy, V. I. Pershin, Y. D. Tretyakov, and P. E. Kazin 4749380/33 Technical report, USSR patent office, 1989.
- [16] A. A. Vertegel, S. V. Kalinin, N. N. Oleynikov, and Y. D. Tretyakov, *Journal of Non-Crystalline Solids*, 1995, **181**, 146–150.
- [17] T. Uchikoshi, Y. Sakka, K. Ozawa, and K. Hiraga, *Journal of Materials Research*, 1998, **13**, 840.
- [18] R. L. Dalton, R. K. Iler, and G. B. Alexander Us pat. no 2733205 Technical report, 1956.
- [19] P. Jardine and L. Zelazni, *Soil Science Society of America Journal*, 1986, (50), 895–900.
- [20] W. Blum, *Journal of the American Chemical Society*, 1916, **38**, 1282–1297.
- [21] Z. Marczenko, M. Balcerzak, and E. Kloczko, Elsevier, 2000; chapter Separation, Preconcentration and Spectrophotometry.
- [22] C. C. Perry and K. L. Shafran, *Journal of Inorganic Biochemistry*, 2001, **87**, 115–124.
- [23] K. Shafran, O. Deschaume, and C. C. Perry, *Advanced Engineering Materials*, 2004, **6**(10), 836–839.
- [24] S. M. Partridge, H. F. Davis, and G. S. Adair, *Biochemical Journal*, 1955, **61**, 11–21.
- [25] C. M. Stoscheck, *Methods in Enzymology*, 1990, **182**, 50.
- [26] G. Sposito, *The Environmental Chemistry of Aluminium*, Lewis Publishers, CRC Press, 1996.

- [27] G. Furrer, M. Gfeller, and B. Wehrli, *Geochimica et Cosmochimica Acta*, 1999, **63**(19/20), 3069–3076.
- [28] T. Okura, K. Goto, and T. Votuyanagi, *Analytical Chemistry*, 1962, **34**, 581–582.
- [29] J. Hem and C. Roberson, *U.S. Geological Survey, Water supply*, 1967.
- [30] R. Turner, *Canadian Journal of Chemistry*, 1969, **47**, 2521–2527.
- [31] R. Turner, *Canadian Journal of Chemistry*, 1971, **49**, 1688–1690.
- [32] R. Turner and W. Sulaiman, *Canadian Journal of Chemistry*, 1971, **49**, 1683–1687.
- [33] R. Smith, *American Chemical Society Advanced Chemistry*, 1971, **106**, 250–279.
- [34] R. Smith and J. Hem, effect of aging on aluminum hydroxide complexes in dilute aqueous solutions, u.s. geological survey water supply paper 1827-d, Technical report, U.S. Government Printing Office, Washington, Delaware, 1972.
- [35] R. Barnhisel and P. Bertsch, 1982; chapter Aluminum, pp. 275–300.
- [36] F. Blamey, D. Edwards, and C. Asher, *Soil Science*, 1983, **136**, 197–207.
- [37] H. Seip, L. Muller, and A. Naas, *Water, Air, Soil Pollution*, 1984, **23**, 81–95.
- [38] R. Turner, *Canadian Journal of Chemistry*, 1976, **54**, 1528–1534.
- [39] J. Bersillon, P. Hsu, and F. Fiessinger, *Soil Science Society of America Journal*, 1980, (44), 630–634.
- [40] P. Bertsch, G. Thomas, and R. Barnhisel, *Soil Science Society of America Journal*, 1986, **50**, 825–830.
- [41] P. Bertsch, G. W. Thomas, and R. Barnhisel, American Society of Agronomy, Madison, WI, 1982; chapter Characterization of hydroxy-Al solutions by ^{27}Al NMR Spectroscopy, p. 170.

- [42] P. Bertsch, American Society of Agronomy, Madison, WI, 1984; chapter Characterization of hydroxy-Al solutions by ^{27}Al NMR Spectroscopy, p. 170.
- [43] P. Bertsch, R. Barnhisel, G. Thomas, W. Layton, and S. Smith, *Analytical Chemistry*, 1986, **58**, 2583–2585.
- [44] P. M. Bertsch, W. John Layton, and R. I. Barnhisel, *Soil Science Society of America Journal*, 1986, **50**, 1449–1454.
- [45] M. Von Schwan, H. Gorz, and S. Schonherr, *Z. Phys. Chem.*, 1981, **262**, 953–957.
- [46] J. Buffle, N. Parthasarathy, and W. Haerdi, *Water Research*, 1985, **19**, 7–23.
- [47] D. R. Parker and P. M. Bertsch, *Environmental Science and Technology*, 1992, **26**, 908–914.
- [48] P. Tsai and P. Hsu, *Soil Science Society of America Journal*, 1985, (49), 1060–1065.
- [49] N. Parthasarathy and J. Buffle, *Water Research*, 1985, **19**, 25–36.
- [50] P. M. Jardine and L. W. Zelazny, *Soil Science Society of America Journal*, 1987, **51**, 885–889.
- [51] P. M. Jardine and L. W. Zelazny, *Soil Sci. Soc. Am. J.*, 1987, **51**, 889–892.
- [52] J. W. Akitt and A. Farthing, *Journal of the Chemical Society, Dalton Transactions*, 1981, pp. 1615–1616.
- [53] J. W. Akitt and J. M. Elders, *Journal of Chemical Society, Faraday Transactions*, 1985, **81**, 1923–1930.
- [54] J. W. Akitt, *Progress in NMR Spectroscopy*, 1989, **21**, 1–149.
- [55] D. Hoult, C.-N. Chen, H. Eden, and M. Eden, *Journal Of Magnetic Resonance*, 1983, **51**, 110.

- [56] J. W. Akitt and A. Farthing, *Journal of the Chemical Society, Dalton Transactions*, 1981, pp. 1617–1623.
- [57] R. Benn, A. Rufinska, E. Janssen, and H. Lehmkuhl, *Organometallics*, 1986, **5**, 825.
- [58] A. Abragam, *The Principles of Nuclear Magnetism*, Clarendon Press, Oxford, 1961.
- [59] O. Knop, E. M. Palmer, and R. W. Robinson, *Acta Crystallographica A*, 1975, **31**, 19.
- [60] O. Knop, *Acta Crystallographica A*, 1976, **32**, 147.
- [61] W. Gordy, *Discussions of the Faraday Society*, 1955, **19**, 14.
- [62] J.-J. Delpuech, Academic Press, New York, 1983.
- [63] J. W. Akitt and O. W. Howarth, *Journal of Chemical Society, Faraday Transactions 1*, 1989, **85**, 121–125.
- [64] A. Rosenberg In *XIV Congreso Latinoamerica e Iberico De Quimicos cosmeticos and I.F.S.C.C. International Conference, Santiago de Chile*, 1999.
- [65] A. Rosenberg and F. J.J., Marcel Dekker, New York, 1999; pp. 83–136.
- [66] M. Magnuson, *Analytical Chemistry*, 2001, **73**, 4815–4820.
- [67] ed. H. Barth, *Modern Methods of Particle Size Analysis*, Wiley-Interscience, 1984.
- [68] B. Chu, *Laser light scattering: basic principles and practice*, Academic Press, London, 1991.
- [69] Particle size analysis–photon correlation spectroscopy–iso 13321:1996(e) Technical report, International Standards Office, 1996.
- [70] D. E. Koppel, *The Journal of Chemical Physics*, 1972, **57**(11), 4814–4820.

- [71] *Coulter N₄ Plus Submicron Particle Sizer*, reference manual, 1995; Reference Manual.
- [72] H. L. Golterman, R. S. Clymo, and M. A. M. Ohnstad, *Methods for Physical and Chemical Analysis of Fresh Waters*, Blackwell Scientific Publications, 1978.
- [73] H. Klug and L. Alexander, *X-ray diffraction procedures: for polycrystalline and amorphous materials*, Wiley, New York-Chichester, 1974.
- [74] Y. Altas and H. Tel, *Journal of Nuclear Materials*, 2001, **298**, 316–320.
- [75] A. Dutschke, C. Diegelmann, and P. Lobmann, *Journal of Materials Chemistry*, 2003, **13**, 10581063.
- [76] T. C. Ozawa and S. J. Kang, *Journal of Applied Crystallography*, 2004, **37**, 679.
- [77] P. Haines, *Thermal Methods of Analysis Principles, Applications and Problems*, Blackie Academic & Professional, 1995.
- [78] D. Dollimore, Royal Society of Chemistry, 1992; chapter Thermogravimetry, pp. 31–58.
- [79] C. Duval, *Inorganic Thermogravimetric Analysis, 2nd ed.*, Elsevier, 1963.
- [80] L. Reimer, *Transmission Electron Microscopy: Physics of Image Formation and Microanalysis*, Vol. Volume 36 of *Springer Series in Optical Sciences*, Springer-Verlag, 1984.
- [81] P. Goodhew and F. Humphreys, *Electron Microscopy and Analysis, 2nd ed.*, Taylor & Francis, 1988.

Part III

RESULTS AND DISCUSSION

7. PREPARATION OF HIGH PURITY ALUMINIUM SYSTEMS BY STATIC ANION EXCHANGE

7.1 Multi-batch experiment on Al ion hydrolysis

7.1.1 the choice of conditions

In an attempt to optimise the use of ion exchange for the synthesis of model aluminium species, several options were initially tested, including different temperatures and modes of mixing of the ion exchanger with the aluminium solution, as well as different ways of processing the ion exchanger. The choice of ion exchanger went to a soft base type ion exchanger to enhance the softness of the method.

On the basis of the work carried out during previous projects and by others [1, 2], a static ion exchange using the elution of aluminium solution through a column packed with the exchanger was implemented. However turbid solutions were obtained and the difficulty of resin cleaning and regeneration directed us towards the use of dynamic ion exchange that had been used previously for the synthesis of semiconductor precursors [3] or for metal ion speciation [4]. Following this decision we designed a robust resin processing technique and optimised the synthesis of model aluminium species.

The mode of resin/Al solution mixing

A variant of the technique used by Sharikov [5] was used in which, instead of being added in portions, the resin was suspended in distilled water before aluminium solution addition, to minimise the resin aggregation observed when using the classical addition technique. The ion exchange process had therefore to be controlled differently than by slow addition and temperature was chosen as the parameter to vary to limit the exchange rate. As the condensation processes leading to the target

polycationic species were slower than hydrolytic processes, a large exchange rate and thence a quick OH^- generation could lead to the early formation of zero-charge monomeric precursors forming insoluble Al hydroxide upon condensation. This effect explains the different models required to describe Al speciation depending on base generation rates [6]. If the base is quickly generated, an early nucleation/growth process occurs leading to speciation described by the core-links theory, while slow exchange enables the system to converge towards the Keggin-type polycations.

Similarly to synthesis carried out by the addition of liquid base [7] or electrochemical techniques [8], we started by using a temperature above ambient (50°C , the use of the ion exchange resin being limited to 60°C) and the optimal hydrolysis ratio for Al_{13} preparation ($h=2.45$). The monitoring of pH during the resulting ion exchange process indicated an early pH inflexion in the pH 4.0-5.0 domain characteristic of the collapse of aluminium polycations and an associated turbidity. We therefore carried out small volume exchanges (20ml, using magnetic stirring) at 25°C and 10°C and determined the efficiency of the technique by monitoring the pH, the conductivity and the aluminium speciation of the systems to optimise the conditions for Al_{13} synthesis. The low volume of sample obtained and the poor efficiency of magnetic stirring, led us to the first scale-up of the experiment, using better temperature control and sample volume provided by a 200ml jacketed reactor with the possibility of simultaneous conductivity and pH measurement, overhead stirring and sampling during exchange. This setup enabled us to obtain the results forming the main body of the results.

Finally, in order to obtain the large amounts of solution necessary for further destabilisation studies and for the accurate monitoring of the systems by regular sampling during ion exchange or aging of the solutions, we scaled up the preparations to a volume of 2 to 3 liters. Owing to an improved mixing, the scaling up enabled better yields for the synthesis and formed a stable base for further studies.

Results of the titrations

The variation of pH during the multi-batch experiments of Al hydrolysis using static anion exchange was monitored as a function of time at 25°C (Figure 7.1A). The

derivative representation of these curves in 7.1B enabled us to identify the inflection points. At all hydrolysis ratios studied, the first 'inflection' is in fact, a rapid initial rise in pH ($t < 10$ min) arising from the early hydrolysis-condensation processes [9]. The pH plateau following the first 'inflection' arises from the formation of Al_{13}

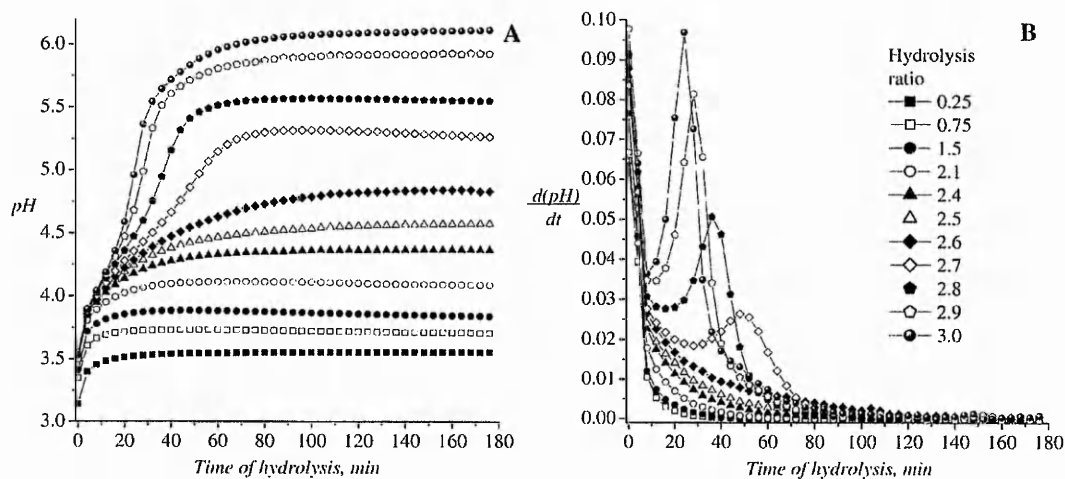


Fig. 7.1: The pH of the suspensions of anion exchange resin as a function of time elapsed after $AlCl_3$ solution addition (A). Examples of the first derivative curves calculated from the original pH data (B).

occurring in the mildly acidic range of pH [9–12]. No pH change is observed as there is no additional release of protons during the formation of Al_{13} from smaller oligomers [10, 11, 13, 14] formed in the previous stage. For samples with hydrolysis ratios $h \leq 2.5$, the pH value after reaching the plateau remains steady to the end of the experiment (Figure 7.1A). Above the hydrolysis ratio $h = 2.5$ and $pH \approx 4.2$, where formation of the Al_{13} reaches its maximum, [9, 15] another inflection occurs at much later times ($t > 20$ min, Figure 7.1A and B). This major inflection arises from the collapse of Al_{13} and similar Keggin polycations with the formation of Al hydroxide [9]. With increase of h , the second inflection becomes sharper and occurs at ever-shorter times of pH monitoring, Figure 7.1B. From the measurement of pH it is clear that static anion exchange is a very soft technique since: (a) there is no temporary pH shift due to local perturbations characteristic of strong alkali additions; (b) initial hydrolysis-condensation, the formation of the Al_{13} and the formation of colloidal

hydroxide are well separated on the time scale of the experiments; (c) there is no premature hydroxide formation below $h \approx 2.5$. Conductivity and chloride ion concentration were also monitored during the ion exchange process. Example data acquired during the titration of a sample with a final hydrolysis ratio $h=2.6$ are given in Figure 7.2. The conductivity of the sample decreases exponentially with time (Figure 7.2A) due to the steady hydrolytic condensation of Al ions into polynuclear species and, eventually, Al hydroxide. This is in contrast to classical base neutralisation,

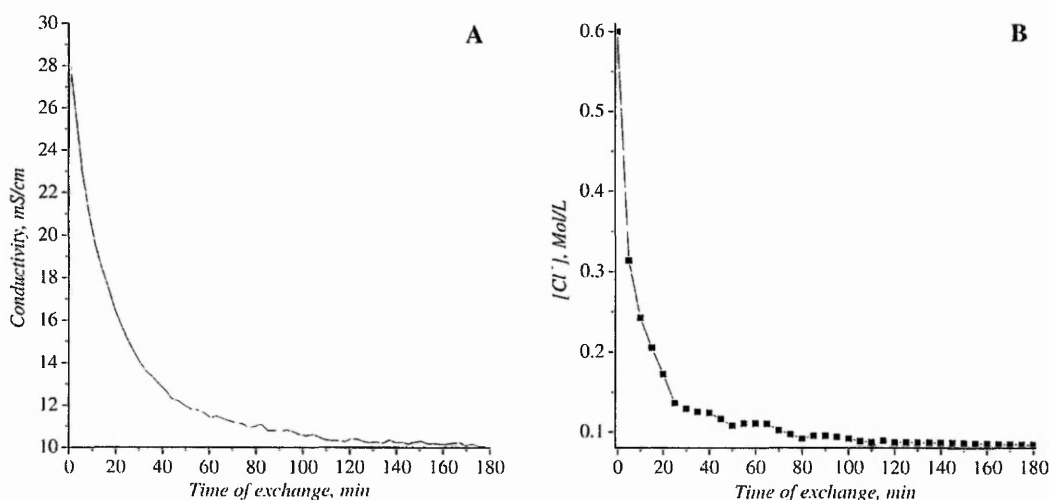


Fig. 7.2: Conductivity (A) and chloride ion concentration (B) monitored during the ion exchange synthesis of a sample with $h=2.6$ upon anion exchange process.

where conductivity variation during titration is much less profound due to the opposite process of an increase in 'spectator' ion concentration [9]. Therefore, anion exchange has the advantage of significantly reducing the amount of spectator ions present which otherwise can be a serious problem in materials synthesis [10, 11, 14]. A similar exponential trend is observed for the variation of chloride ion concentration (Figure 7.2B). This data gives indirect evidence that the reactions occurring in the Al ion solution arise mainly as a consequence of the ion exchange of chloride ions from solution with hydroxide ions on the resin surface. Conductivity and chloride ion measurements help to establish the optimum time required for completion of the ion exchange reaction. As follows from Figure 7.2, most of the reactions at $h=2.50$

are complete within 3h.

Direct monitoring of chloride ion concentration provides an additional possibility to calculate the 'actual' hydrolysis ratio of the samples:

$$h = 3 - 2 \left(\frac{[\text{Cl}^-]}{[\text{Al}^{3+}]} \right) \quad (7.1)$$

From this formula it follows that the formal hydrolysis ratio of Al ion solutions prepared by static anion exchange never exceeds $h=3.0$ (Figure 7.3)(as well as the pH value never exceeding 7 (Figure 7.1)), which is further evidence of the 'softness' of the method.

^{27}Al NMR spectra of the samples at the end of the anion exchange process were

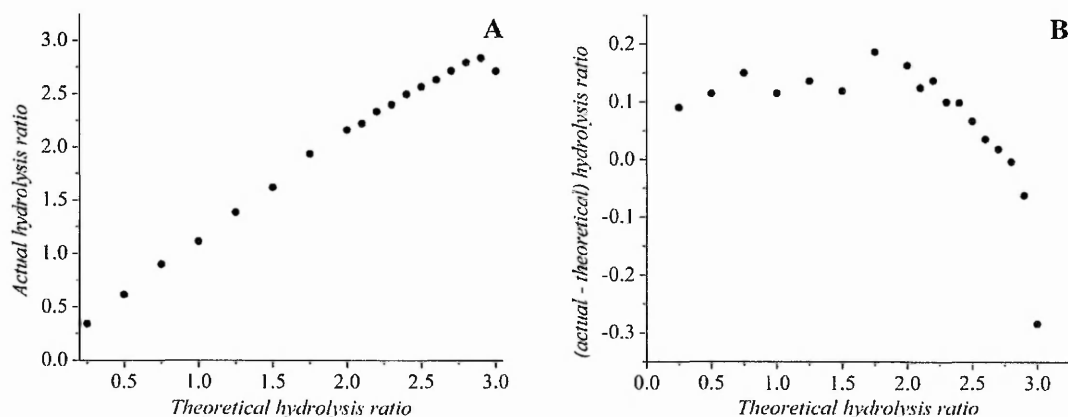


Fig. 7.3: (A) Evolution of hydrolysis ratio and (B) of the difference actual-theoretical h ratio as a function of the theoretical h . Actual h calculated from $\text{Cl}^-/\text{Al}^{3+}$ ions concentration measurements.

acquired (Figure 7.5A). Along with the signal of the aluminate ion internal reference at 80ppm, sharp peaks arising from Al_{13} ($\delta=63\text{ppm}$), Al monomers ($\delta=0.0\text{ppm}$) and a broader peak of small Al oligomers ($\delta=2-4\text{ppm}$) were observed. The data of Figure 7.5A indicates that these NMR signals vary in a systematic fashion with the increase of hydrolysis ratio of the ion-exchanged Al ion solutions. The overall quality of the spectra and consequently the higher accuracy of the calculated proportion of soluble Al species acquired in the present study is greatly improved compared to our previous study at room temperature [9] due to the absence of Al hydroxide colloids

from 'local alkali perturbations' and the low overall ionic strength of the sample solutions prepared by anion exchange. Quantification of the acquired NMR spectra was carried out with high precision ($RSD < 5\%$, $N(\text{spectra})=3$) using an algorithm described previously [16, 17].

Parallel quantification of Al speciation in the samples produced by anion exchange was performed using a 'Ferron' kinetic assay for comparison with ^{27}Al NMR. A demonstration of the ability of NMR to provide quantitative information concerning Al species concentrations in the systems produced is given in Figure 7.4. The

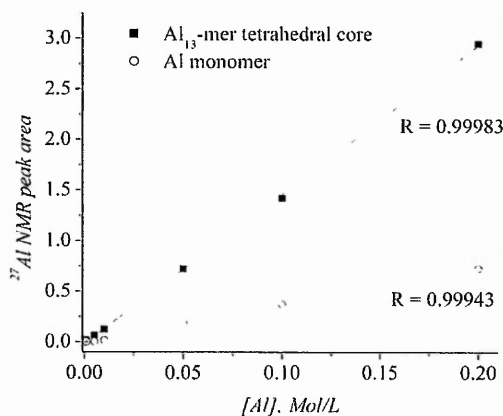


Fig. 7.4: ^{27}Al NMR peak areas from different solutions prepared by dilution of a 0.2M Al_{13} -mer solution validating the ability to carry out quantitative speciation determination. The peak areas have been determined also for solutions diluted with pH 4 (pH of the initial solution) HCl solution, and did show any major differences.

resulting speciation diagrams containing soluble Al species as well as colloidal Al hydroxide are presented in Figure 7.5B. The amount of Al hydroxide was estimated indirectly by the difference of the total concentration of aluminium and the sum of soluble species detected by NMR or the Ferron assay respectively. The concentrations of Al monomers and small oligomers ('Al dimers') measured by ^{27}Al NMR decrease in a more or less linear fashion with increasing hydrolysis ratio, reaching zero at $h=2.5-2.6$, similar to previous quantitative observations [18]. At the same time, Al_{13} concentration increases almost linearly, reaching a maximum in the range

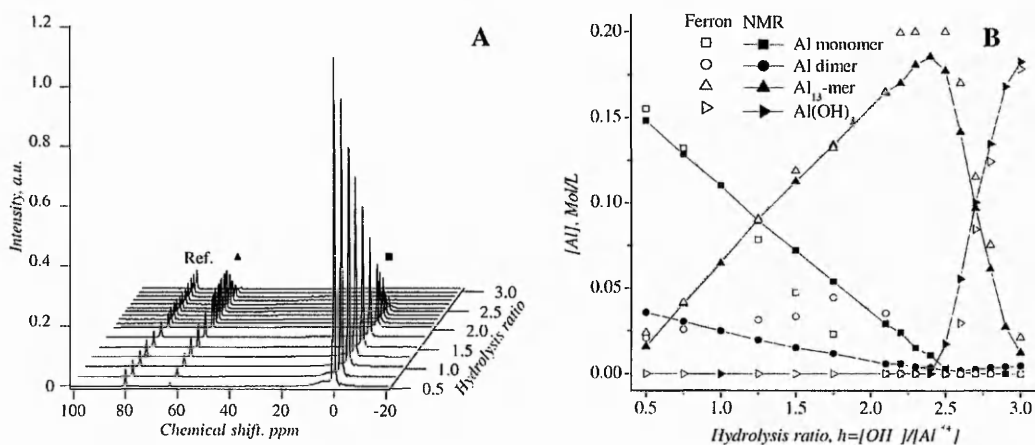


Fig. 7.5: ^{27}Al NMR spectra of the samples prepared using static anion exchange (A) and speciation diagram (B) derived from the quantification of ^{27}Al NMR spectra and ferron assay (Ref.= aluminate standard).

$2.4 > h > 2.6$ (Figure 7.5B). The Keggin polycations start to collapse at $h \approx 2.5$ and colloidal Al hydroxide forms which cannot be detected directly by ^{27}Al solution NMR [9, 19, 20]. At the maximum concentration, Al_{13} represents around 90-95% of the total soluble aluminium species, the remainder being minor quantities of Al monomers and dimer. No Al hydroxide was detected in solutions below $h \approx 2.6$, as indicated by the total concentration of soluble Al species in Figure 7.5B being very close to 100% of the overall concentration of aluminium (0.2 mol L^{-1}). Therefore, a very tight control over speciation and a high purity of the target Al species solutions (in this case, Al_{13}) can be maintained when Al hydrolysis is conducted by means of the static anion exchange approach.

The quantitative data obtained using the Ferron kinetic assay generally follows the same trends described above for the NMR data (Figure 7.5B). The best correlation between the two methods is observed for Al_{13} data. The Ferron assay tends to slightly overestimate the concentration of Al_{13} at $h > 2.0$; however, the difference does not exceed $\approx 10\%$.

The largest difference between the data of ^{27}Al NMR spectroscopy and the Ferron assay is found for Al monomers and, especially, 'Al dimers' (Figure 7.5B). This dif-

ference probably arises from minor computational errors in the Ferron assay data treatment which may occur during the iterative fit of the complex exponential function described in the materials and methods part of this work. However, the sums of Al monomers and small oligomers are nearly identical for the NMR and Ferron data at all hydrolysis ratios where these species have been detected. Therefore, the Ferron kinetic assay can be used as an alternative to ^{27}Al NMR for quantification of Al speciation in model systems. The similarity of the results obtained by quantitative ^{27}Al NMR spectroscopy and Ferron kinetic assay serves as additional validation of these independent methods for quantification of Al speciation.

7.2 Target synthesis of the Al_{13} -mer

On the basis of the multi-batch experiments described above, the optimum range of hydrolysis ratios and other conditions was established for the Al_{13} species. This enabled a targeted synthesis of the single Al_{13} species in solution on the laboratory scale in quantities of up to 5L, and Al total concentrations up to $0.6\text{Mol}\cdot\text{L}^{-1}$. It must be noted that the upper level of the Al content was limited mainly by the resin capacity. Preliminary partial acidification of the Al chloride solution and the formation of a suspension of the anion exchange resin prior to mixing was found to be an effective measure to further improve the yield of the Al_{13} species and minimise any local perturbations which may occur when significantly higher concentrations of Al solution (initial concentration of AlCl_3 solution was 1.0M) and the corresponding amounts of resin are involved in the synthesis. The target ratio of the produced batch of Al_{13} , described in this study as an example, was $h=2.45$, the final Al concentration $0.4\text{Mol}\cdot\text{L}^{-1}$ and the percentage of the target Al_{13} species $\approx 95\%$ of the total Al content, as determined by ^{27}Al NMR spectroscopy and the Ferron assay (Figure 7.6).

From the prepared batch of high-purity Al_{13} solution, a solid sample was obtained via either slow evaporation of a batch of Al_{13} solution at low temperature in a Virtis freeze-drier or at room temperature via simple ambient drying atmosphere. The materials obtained using ambient drying conditions had the appearance of glass (Figure

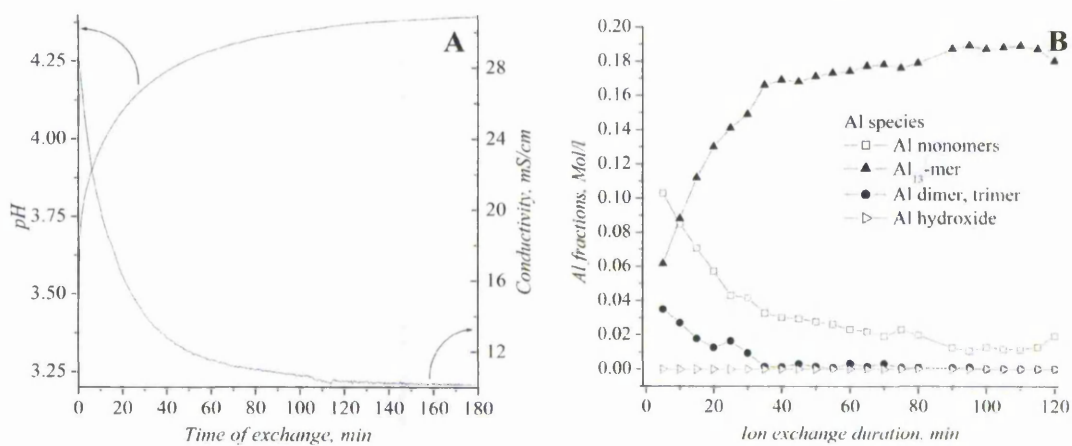


Fig. 7.6: (A) Evolution of pH and conductivity, as well as (B) Al speciation as determined from a ferron kinetic assay over the synthesis of a high purity Al_{13} -mer by means of ion exchange.

7.7). These materials were poorly soluble and likely to be composed mainly of Al

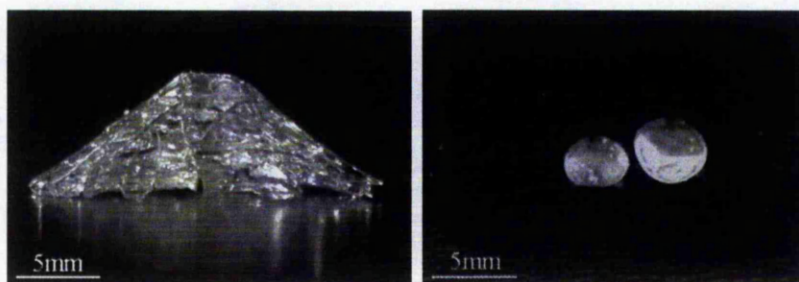


Fig. 7.7: Materials resulting from the classical drying of the Al_{13} solution in a 50ml tube (left), and on a hydrophobic surface synthesised from MTEOS(right).

hydroxide. Ambient drying conditions were therefore unadapted to the transfer of the Al_{13} -mer molecule to the solid state.

The freeze-dried sample was subjected to powder XRD analysis (Figure 7.8). The composition of the sample was checked by re-dissolution of the solid sample in distilled water, followed by acquisition of ^{27}Al solution NMR spectra (Figure 7.9B).

Powder XRD patterns of the sulfate salts of aluminium polycations are well known and have been used for the structural identification of these species [21, 22]. Comparison of the PXRD pattern in Figure 7.8 with the reference lines of the Al_{13} sulfate

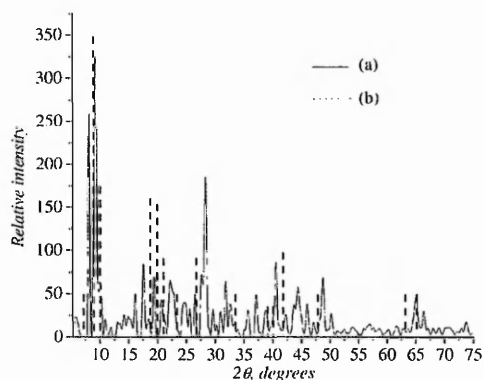


Fig. 7.8: PXRD patterns of the freeze-dried $h=2.45$ sample (a), and the major lines of the PXRD pattern of Al_{13} sulfate salt [21](b).

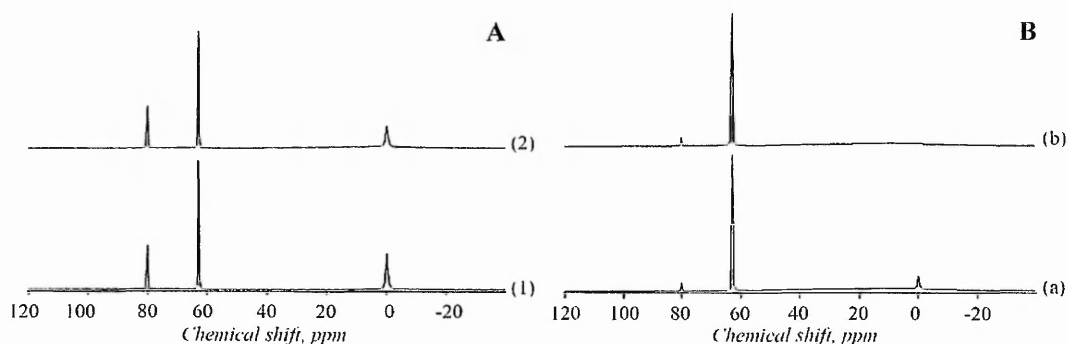


Fig. 7.9: ^{27}Al solution NMR spectra (A) of the initial (1) and re-dissolved (2) sample at $h=2.5$; ^{27}Al NMR spectra (B) obtained on an Al_{13} solution before (a) and after (b) the second ion exchange step.

salt indicates that the product obtained using the static anion exchange is highly crystalline and structurally similar to the Al_{13} sulfate salt. Deviations of the reflections observed for the Al_{13} chloride salt can be preliminarily explained by the likely structural differences in the unit cell induced by the presence of chloride ions. Summarising the XRD analysis one can conclude that Al_{13} can easily crystallise from pure solutions in the chloride form upon slow evaporation, and that it does not require the presence of sulfate ions for crystallisation, as has been mentioned in the literature [21]. In order to examine the effect of the drying procedure on the

overall speciation of the sample at $h=2.5$, the ^{27}Al solution NMR spectrum of the re-dissolved solid sample was measured and compared to the initial solution spectrum (Figure 7.9A–B). There was only a minute difference observed in the spectra, Figure 7.9A–B. The Al_{13} concentration which represents $\approx 92\%$ of the total Al content was calculated from the signal at 63ppm. For the samples before and after re-dissolution it differs by less than 0.5%, while the Al monomer concentration calculated from the peak at 0.0ppm differs by less than ca.2%. Therefore, slow evaporation did not significantly affect the speciation of the sample at $h=2.5$ and can be used for extraction of the Al_{13} from solution into the solid state. Addition of a small extra amount of the anion exchange resin to an Al_{13} containing solution (to make up the total hydrolysis ratio to $h=2.55$) led to a complete disappearance of the minor Al monomer signal at ca. 0.0ppm (Figure 7.9B). The fraction of the Al_{13} in solution of the sample treated with anion exchange in two stages reached $\approx 99\%$. The two-stage anion exchange treatment would be recommended over the one-stage procedure as it is able to produce exceptionally pure solutions of Al_{13} [23].

7.3 Target synthesis of Al_{30}

The Al_{30} synthesis requires thermal ageing of the Al_{13} solution prepared as described above. We have monitored the evolving Al_{30} species using ^{27}Al NMR spectra acquired at 85°C (Figure 7.10) as well as using a ferron kinetic assay on the same samples (Figure 7.11). The NMR spectra in Figure 7.10 show that evolution of the Al_{30} fraction with time is inversely proportional to the Al_{13} content, as indicated by the decreasing peak of the tetrahedral Al ‘core’ of the Keggin ions at $\approx 63\text{ppm}$ and the increasing signal at $\approx 70\text{ppm}$ arising from the AlO_4 ‘core’ atoms of the Al_{30} species (Figure 7.10A). After 42h the concentration of all three major species detected by NMR (Al_{30} , Al_{13} and Al monomers) stabilised (Figure 7.10B). The results of ^{27}Al NMR speciation are again very well reproduced by the diagrams obtained from the ferron assay, demonstrating the efficiency of the data treatment applied. The concentration of Al_{30} was calculated on the basis of peak-fitting of the peak at 70ppm [7], the concentration of Al_{13} and Al monomers—from the peaks at ≈ 63 and

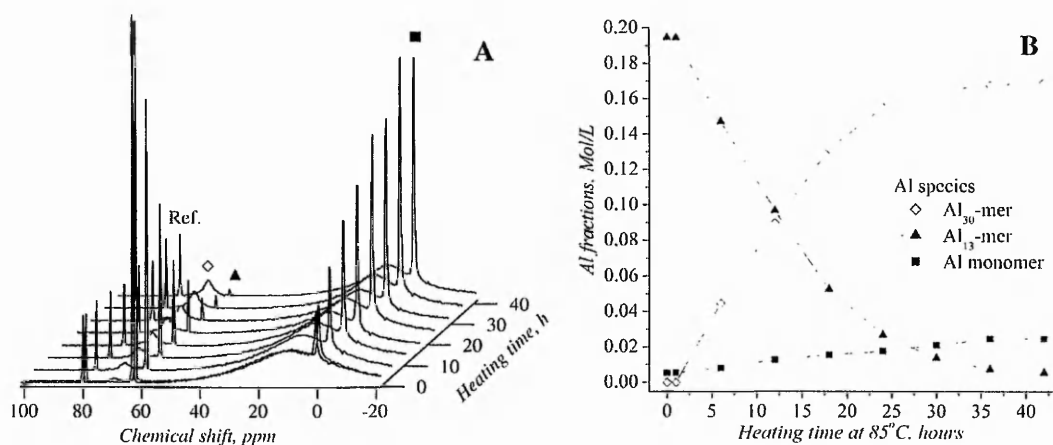


Fig. 7.10: ^{27}Al solution NMR spectra of the Al_{13} solutions aged for 42h at 85°C (A) and the dynamic diagram of Al speciation (B) (Ref.= aluminate standard).

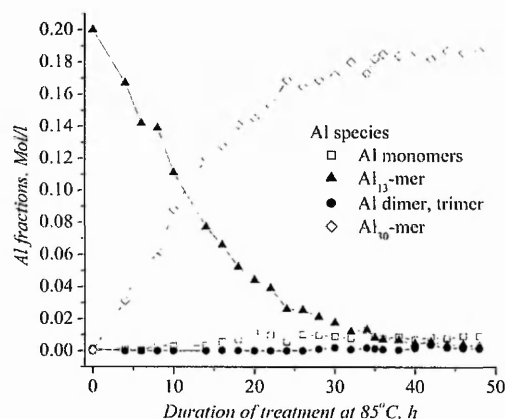


Fig. 7.11: Al speciation determined by means of ferron kinetic assay as a function of time in the Al_{13} solutions aged for 42h at 85°C .

≈ 0 ppm, as described above. The concentration of Al 'dimers' was not evaluated due to the very low concentration of these species. The sum of all mentioned soluble species accounts for $\approx 100\%$ of the total Al content, with the anion exchange synthesis rendering highly pure Al species solutions: in this case, the Al_{30} solution. Once aged, the calculated Al_{30} fraction was found to be around 90% of all the detected species. Therefore, only one additional step of prolonged thermal ageing is sufficient to convert quantitatively the highly concentrated, high purity Al_{13} species into the

Al₃₀ species.

As has been shown previously in experiments on Al ion hydrolysis at 90°C [16, 17], two major processes occur in Al ion solutions at high temperature in the vicinity of the optimum hydrolysis ratio for Al₃₀ formation ($h \approx 2.40$): conversion of the Al₁₃ to the Al₃₀ involving consumption of Al monomers and the breakdown of the Al₁₃ into Al monomers. The increasing concentration of the Al monomer observed in the dynamic speciation diagram (Figure 7.10B) indicates that the process of Al₁₃ breakdown slightly exceeds the formation of the Al₃₀ for the given conditions of the ageing experiment. Optimisation of the hydrolysis ratio, temperature, time and other parameters of the ageing process will lead to even higher yields of the Al₃₀ by further reducing the amount of the Al₁₃, Al monomers and other possible species in solution.

7.4 Synthesis of Al hydroxide nanoparticles with tuneable sizes

In order to produce Al hydroxide particles free from soluble Al species, hydrolysis ratios have to be in the vicinity of $h \approx 3.0$. Ageing time and temperature are two further parameters defining the resulting size of Al hydroxide colloids. Minor quan-

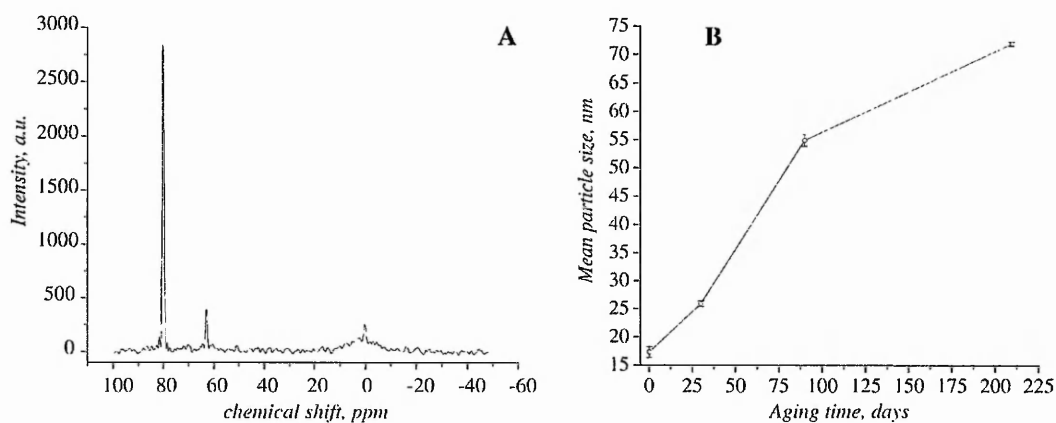


Fig. 7.12: The ²⁷Al solution NMR spectrum of the as-prepared Al hydroxide ($h \approx 3.0$) (A) and the dynamic particle size distribution of the Al hydroxide suspensions as measured with DLS aged for 200h 25°C(B).

tities of the Al_{13} ($\approx 2\%$ of total Al content), Al monomers ($\approx 0.5\%$) and small Al oligomers (presumably dimers, $\approx 1\%$) were found in a freshly prepared sample of colloidal Al hydroxide ($h \approx 3.0$), as indicated by small sharp peaks in the NMR spectrum in Figure 7.12A at ≈ 63 , ≈ 0 and a minor broad peak $\approx 4\text{ppm}$. Hydrolysis ratio is the major factor in determining the purity of the Al hydroxide samples. With increasing value of h from $h=2.6$ to $h=3.0$ the concentrations of soluble Al species reduced dramatically as shown in Figure 7.5B. The particle size evolution of the synthesised Al hydroxide suspensions as a function of time is shown in Figure 7.12B for a sample of Al hydroxide prepared at $h=3.0$ and aged for a total of 200 days at room temperature. The initial particle size of the suspension of Al hydroxide prepared by anion exchange $h=3.0$ and 25°C was around $21 \pm 4\text{nm}$ (Figure 7.12B). Further ageing of the hydroxide suspension at the same temperature led to an increase of the particle size up to $\approx 70 \pm 1\text{nm}$ after 200 days of the experiment. The following ageing of the suspension for 2 months under ambient conditions rendered hydroxide particles of 80nm size. Therefore, the particle size of the synthesised Al hydroxide sols can be very stable for significant time periods. The particle size distribution of the as-prepared Al hydroxide suspension was relatively broad as follows from the value of the polydispersity index (PI) [24] estimated to be ≈ 0.68 from the dynamic light scattering measurements. This is probably due to the presence of small primary nuclei (56nm) together with the particles of $\approx 25\text{nm}$ size. However, in the course of ageing at room temperature the particle size distribution became narrower, with the PI measuring about 0.16 by the end of monitoring (200 days). An illustrative example of a TEM image from a 200nm hydroxide suspension obtained using accelerated aging at 60°C is presented in Figure 7.13A. Upon sedimentation of the large particles of this suspension, the formation of an arrangement with optical properties (diffraction of light leading to iridescent aspect of the solid sedimented) close to the ones observed for Stöber silica mimic of opal 7.13B is obtained 7.13A, demonstrating both the high monodispersity and stability of the particles. On the basis of the results described above by varying hydrolysis ratio in the range $2.6 > h > 3.0$, temperature and ageing time, it is possible to tune the size of the Al hydroxide nanoparticles to a desired value in a very narrow range. The

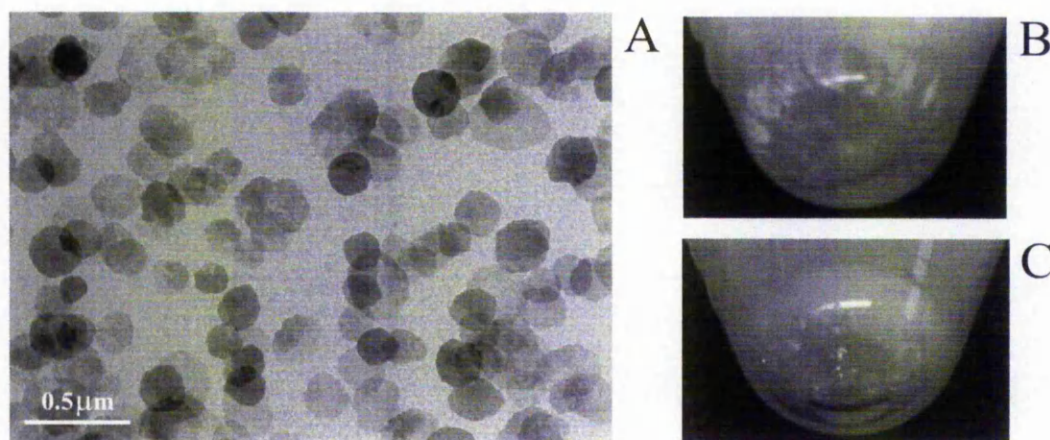


Fig. 7.13: (A) TEM image of a 200nm hydroxide particle sol obtained by means of ion exchange followed by accelerated aging at 60°C, and normal light images of the bottom of 15ml sample tubes containing (B) Stöber silica and (C) the Al hydroxide mimic of opal.

value of hydrolysis ratio or degree of neutralisation also determines the overall positive charge on the particles, thus preventing their further growth by aggregation. 'Ostwald ripening' of the Al hydroxide particles is very slow, possibly due to high monodispersity of the synthesised sols.

7.5 Concluding remarks

From the results discussed above, the static ion exchange method is an excellent route to the synthesis of aluminium (and, potentially, other metals) polycation species due to its 'softness', 'green' features, low cost, relative ease and good control over reaction factors. Using this technique it is possible to synthesise nearly pure solutions of the Al_{13} , Al_{30} and Al hydroxide from quite high concentrations of aluminium ions (up to $0.6\text{Mol}\cdot\text{L}^{-1}$ in this study), which is not possible by means of a commonly-used base neutralisation route (Figure 7.14). It is hoped that this method will eventually lead to (a) elucidation of the mechanisms of the polycation formation, breakdown and structural transformations into Al hydroxide; (b) the generation of more reliable thermodynamic and kinetic data about the polynuclear

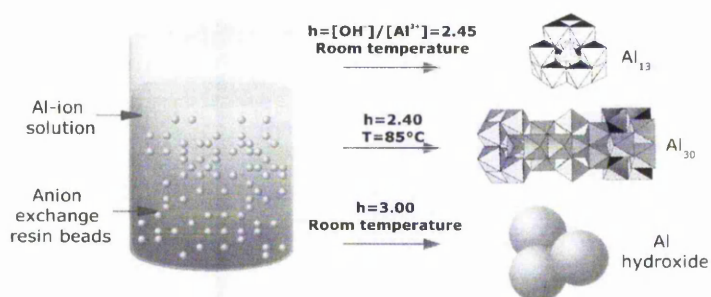


Fig. 7.14: The results of the implementation of the anion exchange technique for the synthesis of Al species model systems [25].

species; (c) represent a very important model for use in fundamental studies, such as structure-property relationships, as well as in applied studies of environmental, biomedical and geochemical interest; (d) in terms of materials chemistry, create an interesting class of manageable molecular building blocks of high purity, with known properties, structure and size precisely defined on the nanometre scale. The next chapters will concentrate on the optimisation of Al_{30} and colloidal Al hydroxide preparation, as well as on the study of aluminium-based inorganic and composite materials prepared from high-purity model species solutions.

BIBLIOGRAPHY

- [1] J. Livage, M. Henry, and C. Sanchez, *Progress in Solid-State Chemistry*, 1988, **18**(4), 259–341.
- [2] R. K. Iler, *The Chemistry of Silica*, 1979.
- [3] Y. D. Tretyakov and O. A. Shlyakhtin, *Journal of Materials Chemistry*, 1999, **9**, 19–24.
- [4] S. C. Hodges, *Soil Science Society of America Journal*, 1987, **51**, 57–64.
- [5] F. Y. Sharikov, *Cryochemical synthesis of finely dispersed oxide powders using ion exchange*, PhD thesis, Moscow State University, 1991.
- [6] S. Bi, C. Wang, Q. Cao, and C. Zhang, *Coordination Chemistry Reviews*, 2004, **248**, 441–455.
- [7] L. Allouche and F. Taulelle, *Inorganic Chemistry Communications*, 2003, **6**, 1167–1170.
- [8] G. Fu, L. F. Nazar, and A. D. Bain, *Chemistry of Materials*, 1991, **3**, 602–610.
- [9] C. C. Perry and K. L. Shafran, *Journal of Inorganic Biochemistry*, 2001, **87**, 115–124.
- [10] J. W. Akitt and A. Farthing, *Journal of the Chemical Society, Dalton Transactions*, 1981, pp. 1624–1628.
- [11] J. W. Akitt and J. M. Elders, *Journal of Chemical Society, Faraday Transactions*, 1985, **81**, 1923–1930.
- [12] S. M. Bradley, R. A. Kydd, and R. Yamdagni, *Journal of the Chemical Society, Dalton Transactions*, 1990, pp. 2653–2656.

- [13] M. Henry, J. P. Jolivet, and J. Livage, *Structure and Bonding*, 1992, **77**, 153–206.
- [14] J. P. Jolivet, *From Solution to Solid State*, Wiley and Sons, 2000.
- [15] S. M. Bradley, R. A. Kydd, and R. Yamdagni, *Journal of the Chemical Society, Dalton Transactions*, 1990, pp. 413–417.
- [16] K. Shafran, O. Deschaume, and C. C. Perry, *Advanced Engineering Materials*, 2004, **6**(10), 836–839.
- [17] K. L. Shafran and C. C. Perry, *Journal of the Chemical Society, Dalton Transactions*, 2005, pp. 2098–2105.
- [18] P. Jardine and L. Zelazni, *Soil Science Society of America Journal*, 1986, (50), 895–900.
- [19] J. W. Akitt, N. N. Greenwood, B. L. Khandelwal, and G. . Lester, *Journal of the Chemical Society, Dalton Transactions*, 1972, pp. 605–610.
- [20] P. M. Bertsch and D. R. Parker, Boca Raton, FL, 1996; p. 117.
- [21] Y. Xu, D. Wang, H. Liu, L. Yiqiang, and H. Tang, *Colloids and Surfaces A: Physicochem. Eng. Aspects*, 2003, **231**, 1–9.
- [22] G. Johansson, *Arkiv For Kemi*, 1962, **20**(27), 321–342.
- [23] J. Rowsell and L. F. Nazar, *Journal of the American Chemical Society*, 2000, **122**, 3777–3778.
- [24] *Coulter N₄ Plus Submicron Particle Sizer*, reference manual, 1995; Reference Manual.
- [25] K. L. Shafran, O. Deschaume, and C. C. Perry, *Journal of Materials Chemistry*, 2005, **15**, 3415–3423.

8. CONDITIONS OF LARGE POLYCATIONS FORMATION: AN NMR STUDY

8.1 ^{27}Al NMR treatment algorithms

8.1.1 *The local integration algorithm*

During the past years our group has build a methodology for Al speciation studies by means of ^{27}Al NMR using local integration algorithms. A first attempt to get quantitative information from NMR spectra used a local integration algorithm which was described in a recent publication [1] (Figure 8.1). This algorithm uses mainly an integration of narrow peaks, less susceptible to the missing intensity phenomena described in the materials and methods section as well as by others [2]. Despite the high quality of the results obtained using this algorithm [3], some problems persisted, including a strong user-dependency, the reduced accuracy of broad spectral features and overlapped peaks integration. Moreover, although they give reasonable results for proton spectra, commercial automatic phasing algorithms are not adapted for ^{27}Al NMR spectra treatment, phasing has to be carried out manually, adding some additional user-dependency and making the treatment very time-consuming. In order to alleviate the errors induced by integration, we started using a peak-fitting algorithm in GRAMS/32 software. Despite the good accuracy of the peak-fitting results, some pitfalls remained, namely the low stability of the peak fitting routine, the impossibility to fit the whole spectra, and the strong need for constraints in order to prevent divergence. Spectrum pre-treatment had still to be carried out manually and the program did not enable the batch-processing of series of spectra, an option very useful in the case of kinetic studies. We therefore decided to develop a fully automated treatment algorithm including apodisation, Fourier transform, phasing of narrow and broad spectral features, baseline correction, full fitting of the

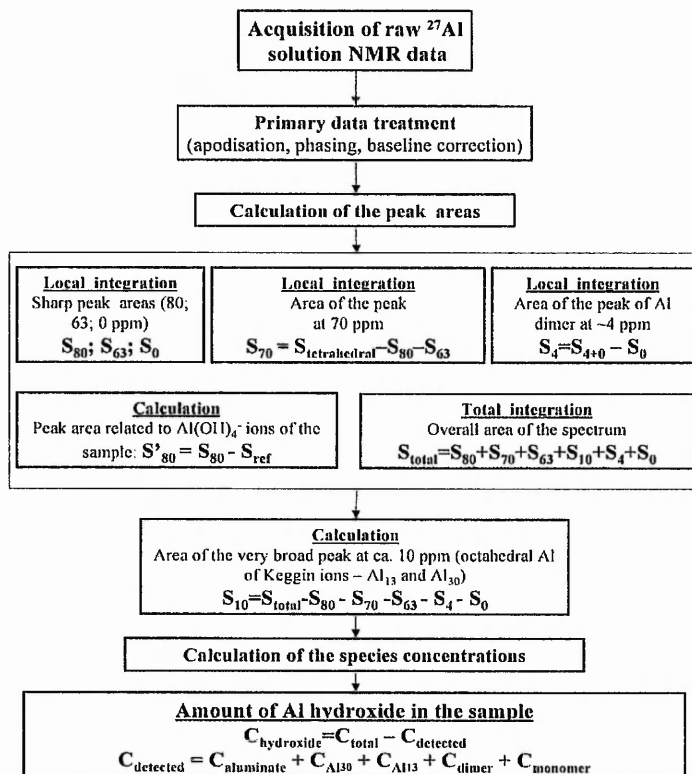


Fig. 8.1: our local integration algorithm

spectra using peaks attributed to species evidenced in the literature, construction of speciation diagrams and 3D representation of series of spectra. This algorithm was successfully programmed using MatLab programming language and used on batches of spectra acquired during very different experiments and presenting an exhaustive panel of Al aqueous species. This chapter presents the results obtained for the kinetic study of Al_{13} - Al_{30} conversion. This study included the monitoring of the conversion and was carried out on samples of different hydrolysis ratios and temperatures, to obtain a first idea of the effect of initial speciation on the kinetics of transformation as well as determine the approximate values of the activation energy for the conversion. Such a study is important for the optimisation of Al_{30} -mer synthesis as well as to get more insight into the dimerisation mechanism.

8.1.2 Automatic treatment algorithm

Our treatment algorithm uses JEOL Delta NMR acquisition and treatment software data under generic ASCII format, but can of course treat ASCII data produced by other softwares. Delta software enables the combination of spectra acquired during a single measurement session or independent sessions. Our approach is to include in a single file the FID acquired for a reference solution together with the series of FIDs to be treated. The resulting data file is then converted to ASCII format, readable by many data treatment and representation softwares, and imported in to MatLab workspace. Once the treatment function is called, each FID of the set is treated separately to lead to a set of spectra which are fitted in the second part of the algorithm.

The first step of treatment is apodisation, carried out using either an exponential or gaussian window function calculated by the program, and having a specific decay constant:

$$k = e^{-n/K}$$

With k , the resulting multiplying factor; n , the position of the number in the dataset and K , a pseudo time constant related to the size of the data treated and the rate at which it is desired to decrease the intensity of the data.

Both imaginary and real parts of the original FID are multiplied by this function, resulting in an improvement of the signal to noise ratio, together with a broadening of the peaks present in the forthcoming spectra (see figure 8.2 for the example of an exponential window function). It is important to note that gaussian window function will produce peaks with a predominantly gaussian line shape, whereas application of an exponential window function will lead to predominantly lorentzian peaks [2]. This will need to be considered when choosing the model to be used for peak fitting in the last step of our algorithm. It can be noted that the use of an exponential window combined with lorentzian peak fitting generally gave better results than gaussian window and peak fitting.

After apodisation, the frequency analysis of the FID traces is carried out using the

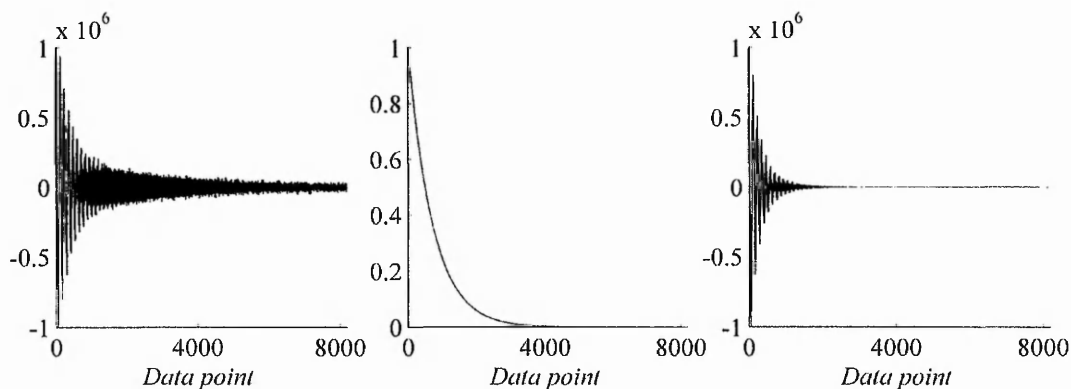


Fig. 8.2: Example of the use of an exponential window function.

built-in MatLab FFT¹ function. A complex FFT is carried out on the combined real and imaginary parts of the FID. The mathematical expression of a fourier transform can be written:

$$F(\omega) = \int_{-\infty}^{\infty} f(t)e^{-i\omega t} dt \quad (8.1)$$

Of course a discrete version of the Fourier transform is used to be able to treat the digitised information stored in the computer memory. The Fourier transform of the output data contains a real and an imaginary part, used during the phasing operation. An example of spectrum resulting from the simple FFT of an apodised FID is presented in figure 8.3. As can be seen from this figure the spectrum is initially not phased, which means it does not present the classical absorption line shapes required for quantification and peak position attribution. In order to get usable spectra a phasing treatment needs to be used in which imaginary and real output of the fourier transform of the FID traces are mixed. Several orders of phasing can be differentiated depending on how the real and imaginary components are mixed across the spectra. The 0 order phasing is characterised by an identical mixing across the spectra, whereas the amount of mixing is varied linearly for 1st order phasing. In our case, a 0 order phasing together with a minimal 1st order phasing were generally required to obtain the desired line shape. When only narrow features are present in the spectra, zero order phasing can be estimated in different positions

¹ fast Fourier transform

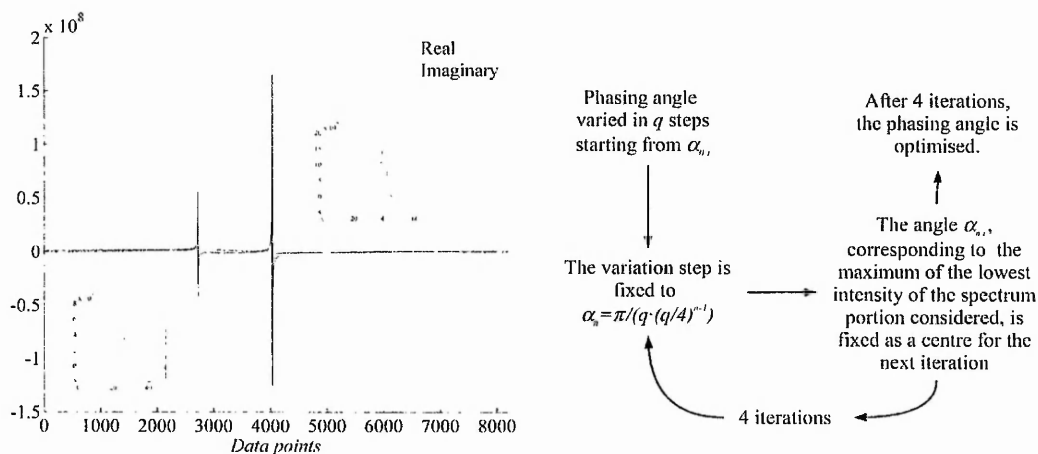


Fig. 8.3: Spectrum obtained after FFT of apodised FID trace, and the iterative phasing algorithm implemented.

of the spectrum, for example for the peaks attributed to Al in octahedral configuration of monomers and in the tetrahedral configuration of aluminate ions, and the amount of which one needs to vary the real-imaginary mixing (corresponding to 1st order phasing) is then determined by fitting a linear variation law between the two values of phasing angle obtained. The automatic phasing algorithm presented in figure 8.3 is therefore applied to the two reference peaks, leading to a full phasing of the spectrum (Figure 8.4). In the case of spectra containing broad features related to Al in the octahedral or tetrahedral environment of polycations, which is the case in most of the spectra we have to treat, the simple phasing algorithm mentioned above cannot be used anymore. 0 order phasing can still be carried out using the aluminate reference peak, but the overlapping of the broad signal from Al in small oligomers and large polycations with the signal from acidic monomers hinders the use of the corresponding narrow peak for phasing (figure 8.5). When manual phasing is used this problem is encountered as well and 1st order phasing is carried out by fixing the phasing angle of the aluminate reference peak to the 0 order value, and varying linearly the phasing angle on both sides of this peak until the broad features become symmetric. Of course this method is very biased by the operator carrying out treatment. We therefore programmed a phasing algorithm based on

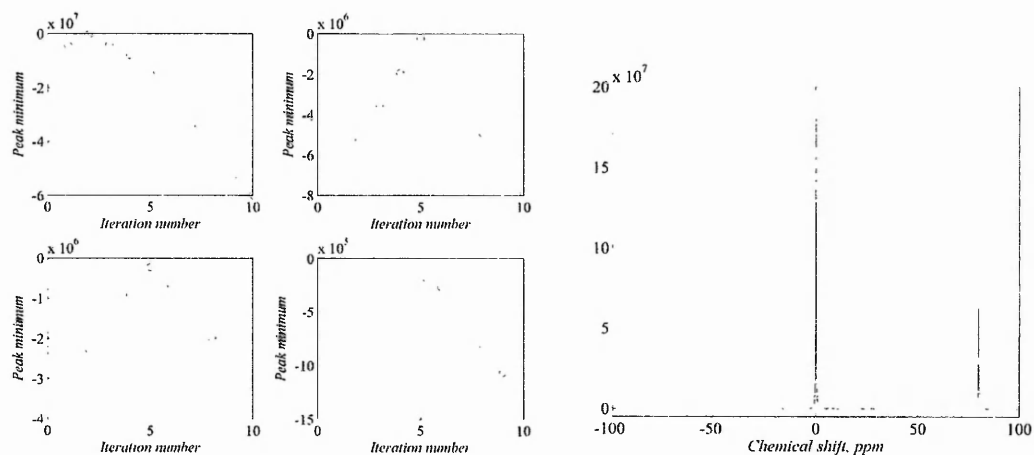


Fig. 8.4: Evolution of the minimum of the spectral window considered as a function of variation step for the four phasing process iterations, and spectrum obtained after phasing.

this visual approach: 0 order phasing angle is determined by applying the simple algorithm mentioned earlier to the aluminate peak spectral window, after which a modified version of the algorithm is used to phase the broad peak related to Al in the octahedral environment of the Al_{13} -mer. For this the center of the peak is estimated from literature data as well as from our observations, and the phasing angle for the corresponding chemical shift is varied according to the step-iteration process mentioned earlier. For each phasing angle, two small spectral windows positioned at equal distance from the peak center on both sides of it are phased considering both 0 and 1st order phasing, and their intensity subtracted from each other. The absolute value of this difference is used as an objective function (to be minimised) during the iterations, and the phasing of the broad spectral feature is accurately reached after 4 iterations (figure 8.5). The simple phasing and broad octahedral features phasing algorithms produce, efficiently and in a very reduced time, spectra of accurate phasing which can then be used for peak-fitting. The accuracy of this algorithm was tested for samples of very different Al speciation as well as for signals acquired under various temperature conditions, and can be proved both visually and from the very low residuals of peak fitting.

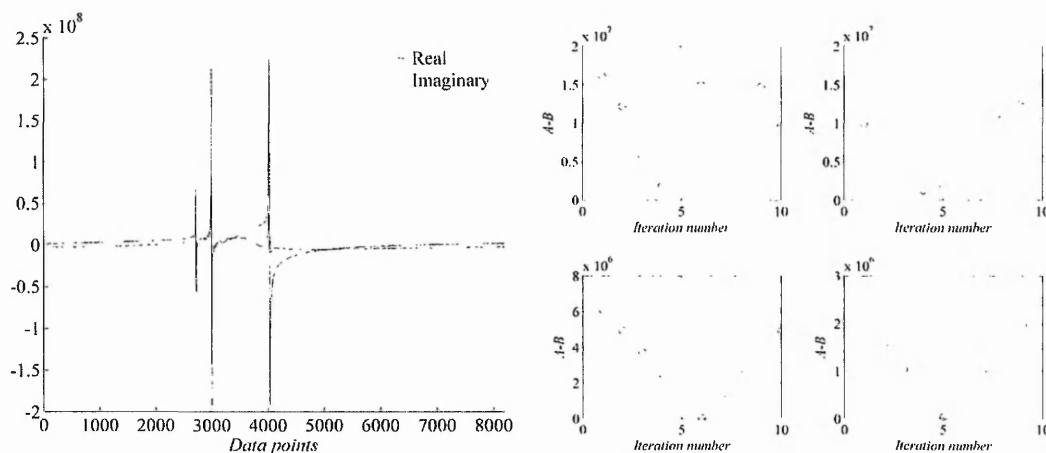


Fig. 8.5: ^{27}Al NMR spectrum of a sample containing Al monomer, Al_{13} and Al_{30} -mer prior to phasing, and the evolution of the minimisation parameter as a function of variation step for the four iterations of our phasing algorithm.

Prior to peak fitting, the raw FID spectra are zero-filled, which means the number of data points are multiplied by 2^n by adding zeros at the end of the data file, before being converted to frequency domain using FFT. The resulting spectra are phased using the angles determined during spectral pre-treatment, the ppm scale is determined on the basis of the phased aluminate peak center position and the sweep width used for acquisition. Both ppm scales and the real part of the spectra are then stored in two separate matrices necessary for the fitting step. At this point a 3 dimensional representation of the set of spectra is output by MatLab, to control globally spectra pretreatment.

Fitting is carried out on every single spectrum by using a customised and automated version of the MatLab curve-fitting toolbox, using NLLS² minimisation with initial parameters and boundaries determined from the literature, a low convergence criterion and allowing a large number of iterations to be performed. These two last choices make the fitting procedure longer, but lead to much better fitting results. Depending on apodisation parameters, gaussian or lorentzian peak (Figure

² Non-linear least squares

8.6) functions were used:

$$\begin{aligned}
 \text{Gaussian mathematical function:} & \quad f(x) = \frac{1}{\sigma\sqrt{2\pi}} e^{-(x-\mu)^2/2\sigma^2} \\
 \text{our Gaussian fitting model:} & \quad f(x) = a e^{-((x-b)/c)^2} \\
 \text{Lorentzian mathematical function:} & \quad L(x) = \frac{1}{\pi} \frac{\frac{1}{2}\Gamma}{(x-x_0)^2 + (\frac{1}{2}\Gamma)^2} \\
 \text{our Lorentzian fitting model:} & \quad L(x) = \frac{ac}{(x-b)^2 + c^2}
 \end{aligned} \tag{8.2}$$

The functions used in our algorithm are different from the mathematical expressions, but lead to the same peak shapes: Up to 10 different peaks were fitted, including

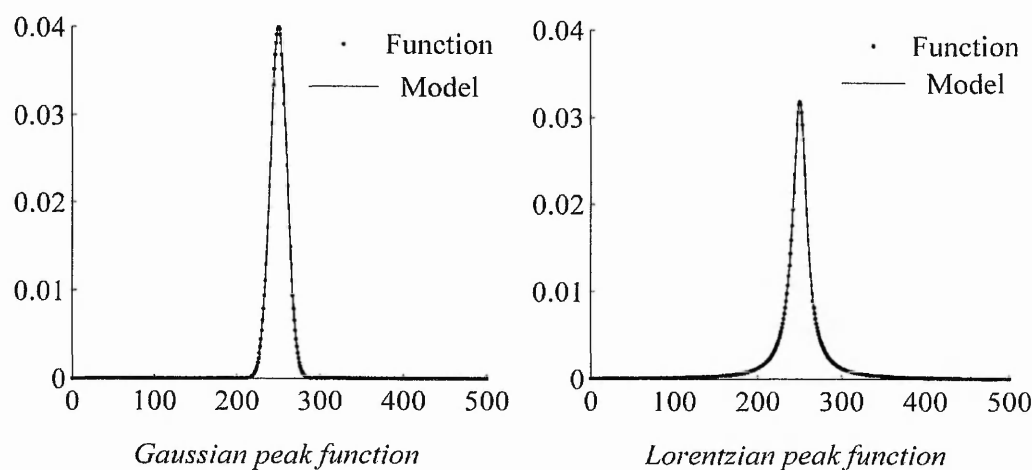


Fig. 8.6: Shape of the peak functions used for the fitting of ^{27}Al NMR spectral features

the signal arising from Al in the octahedral environment of Al monomers, dimers, trimers, Al_{13} -mer, and Al_{30} -mer, and to Al in the tetrahedral environment of aluminate ions, Al_{13} -mer, 'capped' Al_{13} -mer, Al_{30} -mer, as well as a peak, not yet clearly attributed, positioned at 73-75ppm. 30 parameters, and 1 baseline parameter were therefore optimised to minimise the difference between the actual and the fitted spectra. Figure 8.7 shows the 3D representation of a set of 43 spectra acquired during Al_{13} - Al_{30} -mer conversion, together with an example of fitting of the whole spectrum. As one can see, the full spectrum fitting results in very low values of residual, and enables an efficient deconvolution of overlapped peaks. Data processing time being drastically reduced (10 to 30s per spectrum using a 3GHz processor, 1GB RAM

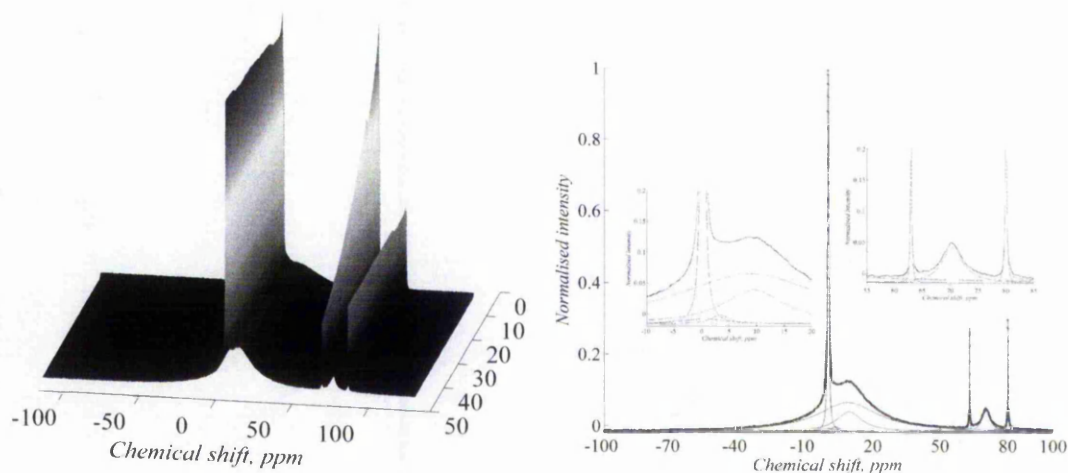


Fig. 8.7: 3D representation of a set of 43 spectra after pre-treatment, and an example of 'fit' taken among this set.

memory computer and a low convergence criterion), the measurement rate for data collection during reaction can be set to its maximum and much smoother trends obtained.

8.2 Application of Automated ^{27}Al NMR treatment to kinetic studies

The automated treatment algorithm developed is especially useful for kinetic studies such as the study of the formation of the Al_{30} -mer, which is presented below.

8.2.1 Preparation of initial samples

For the following experiment, a batch 2.5L of $h=2.5$ Al chlorohydrate solution with a final Al concentration of 0.33 Mol/L (estimated from ferron assay throughout the experiment) was prepared using the ion exchange procedure described in the previous chapter. A preacidification of both resin suspension and AlCl_3 solution was carried out to prevent any Al hydroxide formation during the early stages of ion exchange. h was chosen so that all Al monomer is consumed at the end of exchange, h being higher than the theoretical h of Al_{13} -mer. The counterpart of Al monomer

absence will therefore be the presence of a limited amount of Al hydroxide at the end of exchange. This enabled the study of the effect of hydroxide presence on the Al_{13} - Al_{30} -mer conversion.

During the ion exchange process, pH, conductivity, aluminium and chloride ion concentrations were determined in order to monitor the exchange process and the extent of neutralisation reached at any moment. Moreover, Al speciation was periodically determined by means of ^{27}Al NMR and the ferron assay, and 5ml samples were taken from the solution at times $t = 30, 50, 80$ and 180min to carry out the kinetic studies intended.

In figure 8.8 are presented the results of the Al speciation monitoring carried out by means of ^{27}Al NMR during preparation. The main peaks observed correspond to Al_{13} -mer (63 and 10ppm), Al monomers (≈ 0 ppm), Al oligomers (≈ 2 -3ppm) and Al in the external aluminate ion reference used (80ppm). As observed in the chapter devoted to ion exchange synthesis, Al_{13} -mer concentration increases at the expense of Al monomers and dimers/trimers, the small oligomers being formed during the early stages of the process. The global hydrolysis ratio of the system, determined

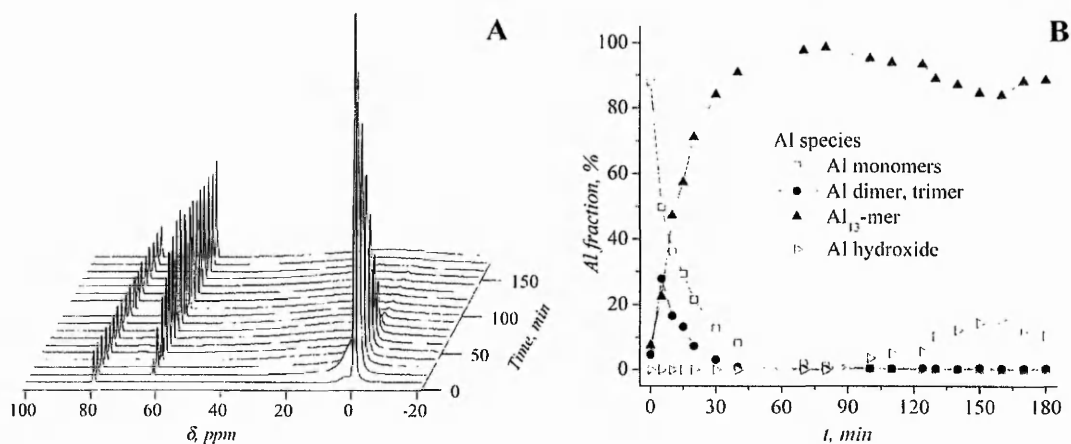


Fig. 8.8: Al speciation monitored by means of ^{27}Al NMR during the synthesis of Al chlorohydrate solutions prior to kinetic study: (A) stacked spectra and (B) Al speciation diagram, both obtained from our automatic treatment technique.

by combined $\text{Al}^{3+}/\text{Cl}^-$ concentration measurements, follows the same trend as the evolution of the Al_{13} -mer concentration (Fig. 8.9). As follows from figure 8.8, the

concentration of the Keggin ion reaches a maximum after 50-60 minutes, corresponding to a hydrolysis ratio close to the theoretical h of this species (2.45) and then undergoes a slow diminution as h exceeds 2.45. This decrease results in a drop

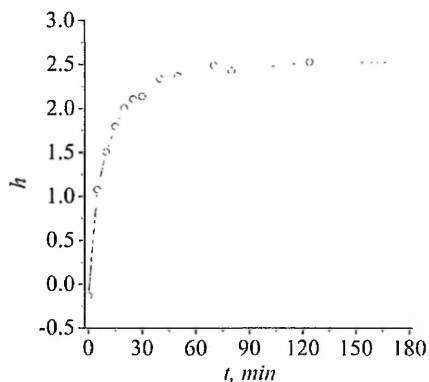


Fig. 8.9: Evolution of hydrolysis ratio over time of exchange as determined from Cl^- and Al^{3+} concentration measurements.

in the total Al concentration measured by ^{27}Al NMR, and the concentration of Al hydroxide, determined as the difference between total and measured concentration, grows while h exceeds the theoretical value of 2.45 (Fig. 8.9). After preparation, the second step of the experiment was to follow the evolution of speciation of the four large samples taken during preparation when exposed to heat treatment at 80, 85 and 90°C . The hydrolysis ratios of the samples corresponding to $t = 30, 50, 80$ and 180min were respectively estimated as $h = 2.14, 2.37, 2.43$ and 2.52 as described above.

8.2.2 The kinetic study

For the kinetic experiment, 0.5ml of one of the samples was transferred to a 5mm NMR tube fitted with a capillary insert containing the aluminate standard solution. Both acquisition parameters and standardisation procedure are described in the materials and methods section. After temperature equilibration ($\approx 1\text{min}$), FID traces were acquired every 20min for 15 hours, 42 spectra being finally obtained for every pair of measurement variables (h, T). All traces were stored in a single file and exported to MatLab workspace after addition of the FID trace acquired from

a primary reference solution under the same measurement conditions. The traces were processed as described using the automatic data treatment algorithm, the time required for treatment being 30min for 43 spectra using a 3GHz processor PC (1GB RAM memory) due to the very low convergence criterion fixed.

Figure 8.10 summarises the evolution of the spectra obtained for every pair of variables (h,T) as a function of heating time. As expected, an increase in the intensity of the peak attributed to Al₃₀-mer tetrahedral cores (70ppm) is correlated with a decrease in the intensity of the peak attributed to tetrahedrally coordinated Al in the Al₁₃-mer (63ppm). A sharpening of the peaks can be noticed upon increasing the measurement temperature, as predicted from the theory of quadrupolar line broadening [2]. At h=2.14 and 2.37, Al monomer is present at the beginning of the experiment and the concentration of this analyte is very slightly modified during the experiment. In the case of h=2.43 and 2.54, the Al monomer concentration, initially very low as predicted, undergoes a considerable increase over heating time, whereas the amount of Al₃₀-mer produced is lower than for h=2.14 and 2.37.

In order to discuss more accurately the results obtained, a precise estimation of the peak areas by fitting of the spectra was required. The results obtained from this procedure are presented in the following developments of this chapter. Figure 8.11 summarises the evolution of the compound of interest (Al₃₀-mer) as a function of heating time for different initial h solutions. As mentioned earlier, the final Al₃₀-mer concentration, together with the rate of its formation, increase as the aging temperature is raised from 80 to 90°C. The formation rate was estimated, assuming a 1st order process, and fitting the concentration evolution with a function of the type

$$y = A(1 - e^{-k(t-t_{cor})})$$

With y, the Al₃₀-mer concentration at time t, k, the kinetic constant of formation and t_{cor}, the initial time correction parameter.

The term t_{cor} being used to correct the effect due to the measurement of the different set of spectra at different times after preparation (up to two weeks). Indeed, as can be seen, the initial Al₃₀-mer concentration is not negligible in some cases and arises from its production at room temperature prior to the beginning of heat treatment.

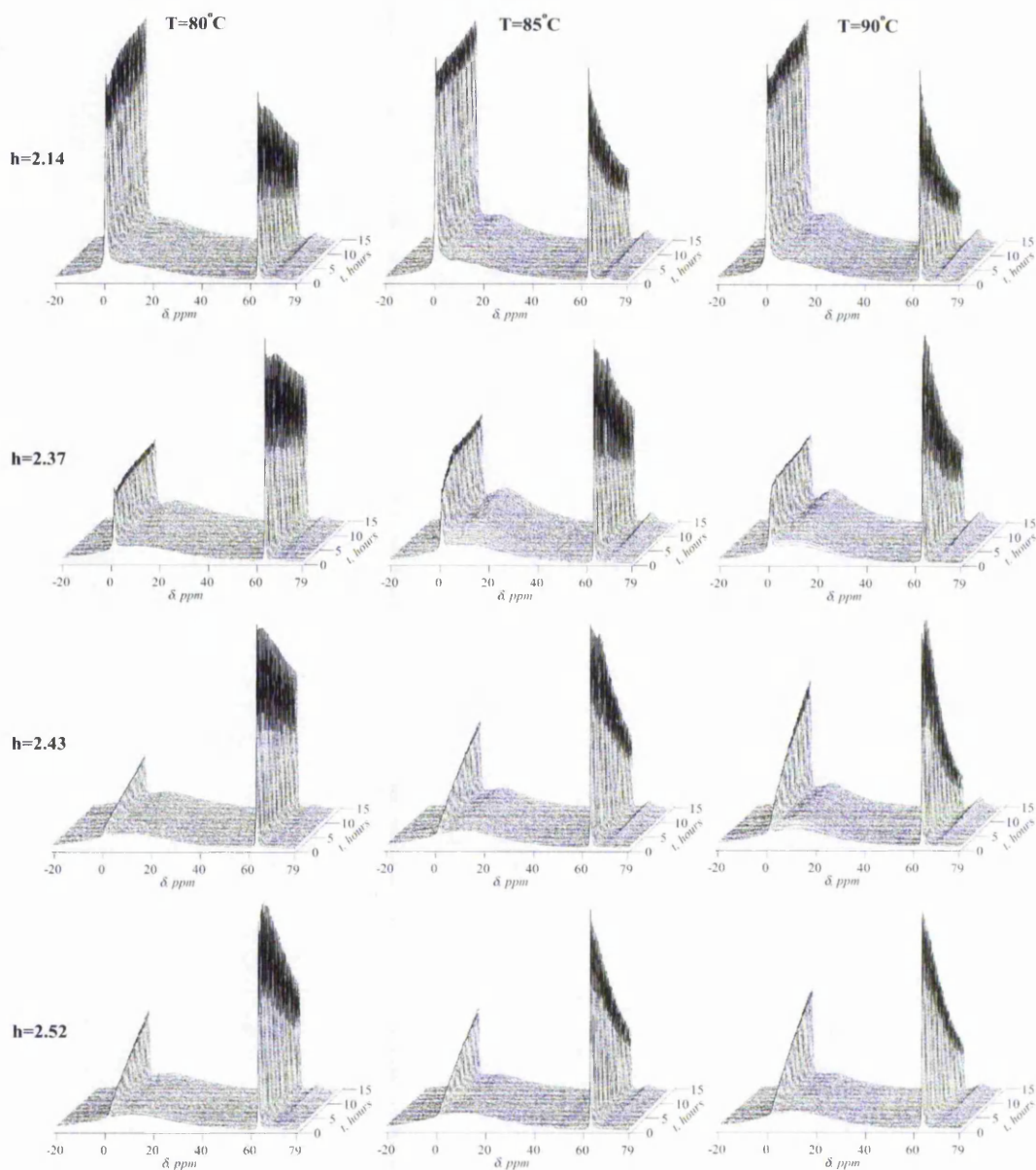


Fig. 8.10: Stacked representation of the spectra evolution over Al_{30} -mer production as a function of time at the three different heating temperatures and respective hydrolysis ratios 2.13, 2.37, 2.43 and 2.52. Spectra obtained from automatic treatment.

As the Al_{13} - Al_{30} -mer conversion has been monitored at three different temperatures, the Arrhenius equation can be used to calculate the activation energy E_a of the

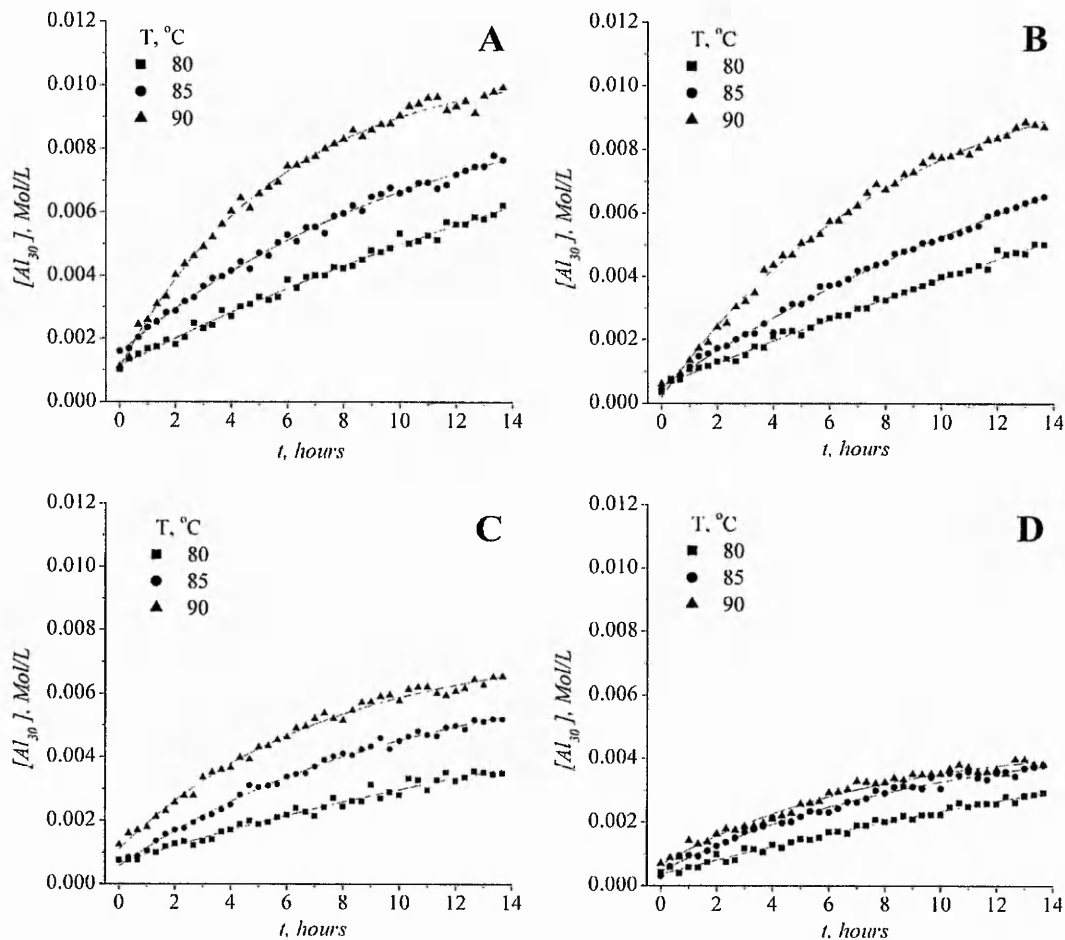


Fig. 8.11: Summary of the Al_{30} -mer production as a function of time, determined from peak-fitting of the peak positioned at 70ppm in NMR spectra acquired at three different temperatures and respective hydrolysis ratios: (a)2.14, (b)2.37, (c)2.43, (d)2.52.

conversion reaction:

$$k = Ae^{-E_a/RT} \quad (8.3)$$

With k , the rate constant; T , the temperature in Kelvin; E_a , the activation energy of the reaction (J); R , the gas constant ($8.314J \cdot K^{-1} \cdot Mol^{-1}$) and A , the pre-exponential factor.

The determination of this parameter enables the rate of reaction to be predicted for a given temperature, and is therefore important for the optimisation of synthesis both on the industrial and laboratory scale. In order to obtain an activation en-

ergy from the estimations of the kinetic constant, $\ln(k)$ was plotted against $1/T$, (T in Kelvin) (Fig. 8.12) and a linear function fitted to the resulting points. The

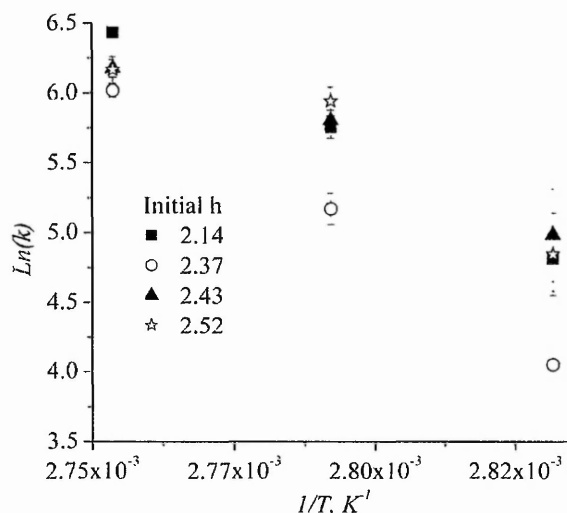


Fig. 8.12: Arrhenius plots for the $\text{Al}_{13}\text{-Al}_{30}$ -mer conversion with different initial h.

slope of the linear function obtained equals $-\frac{E_a}{R}$, and the value of $\ln(k)$ for $1/T=0$ equals $\ln(A)$. Both of the Arrhenius equation parameters are presented in table 8.1 for the different hydrolysis ratios considered. As may be predicted for a complex

Tab. 8.1: Pre-exponential factor A and activation energy E_a determined on the basis of the different kinetic constant values obtained for $\text{Al}_{13}\text{-Al}_{30}$ -mer conversion.

Hydrolysis ratio	A	E_a (kJ·Mol ⁻¹)
2.14	$1.84 \cdot 10^{25} \pm 9.69 \cdot 10^{25}$	156 ± 16
2.37	$7.40 \cdot 10^{29} \pm 5.70 \cdot 10^{30}$	189 ± 23
2.43	$5.51 \cdot 10^{15} \pm 3.45 \cdot 10^{16}$	91 ± 19
2.52	$3.50 \cdot 10^{15} \pm 2.85 \cdot 10^{16}$	89 ± 24

process such as the $\text{Al}_{13}\text{-Al}_{30}$ -mer conversion, no simple trend can be extracted from the data presented in the table above. However, interesting observations can be made. A large activation energy variation can be observed at all hydrolysis ratios, accounting for the slow conversion kinetics obtained at room temperature, and for

the necessity to increase the temperature of the system in order to obtain satisfactory reaction rates. The minimum activation energy E_a and frequency factor A , are obtained for the samples combining low monomer and high Al_{13} -mer contents, and having hydrolysis ratios close to the theoretical h of Al_{13} -mer. The fastest conversions rates are systematically obtained for the $h=2.37$ sample, containing an Al_{13} -mer concentration close to the concentration present in the $h=2.43$ sample, plus a higher quantity of monomer. This confirms that the monomer plays an important role in the Al_{13} - Al_{30} -mer conversion, but acts more as a bridging species than a catalyst, as can be seen from the evolution of activation energy upon monomer concentration decrease.

Due to the narrowing of the peak at 10ppm observed upon heating of Al_{13} -mer solutions for extended periods of time, this broad spectral feature was fitted with two different peaks, our thought being initially that each of the peaks would represent all octahedrally coordinated Al respectively present in Al_{13} or Al_{30} -mer. As can be noticed from figure 8.13, the narrower peak area is initially very low and the whole of the 10ppm feature can be fitted with a single peak attributable to octahedrally coordinated Al in Al_{13} . For increasing heating time, the area of the second, narrower peak increases, but remains lower than the area of octahedrally coordinated Al in Al_{13} even when more than 50% of total Al is present as Al_{30} -mers. The evolution of the narrowest peak at 10ppm is correlated with evolution of the peak at 70ppm, but appears to represent only part of the octahedrally coordinated Al in the Al_{30} -mer, whereas the broader peak contains the signal from the rest of the octahedrally coordinated Al in both polycations. A more careful analysis of the data indicates that the area of the small peak at 10ppm equals slightly less than 2 times the area of the 70ppm peak, which would correspond to 4 Al ions in the Al_{30} -mer structure. This matches the number of Al ions present in the bridge linking two Al_{13} -mer units within the Al_{30} -mer. The signal leading to the narrowing of the broad feature at 10ppm therefore appears to correspond to the 4 bridging monomers present in Al_{30} -mer, these nuclei experiencing electrical fields totally different from the rest of octahedrally coordinated Al of the molecule. This might have been anticipated from the structure of the Al_{30} although has not previously been identified as such.

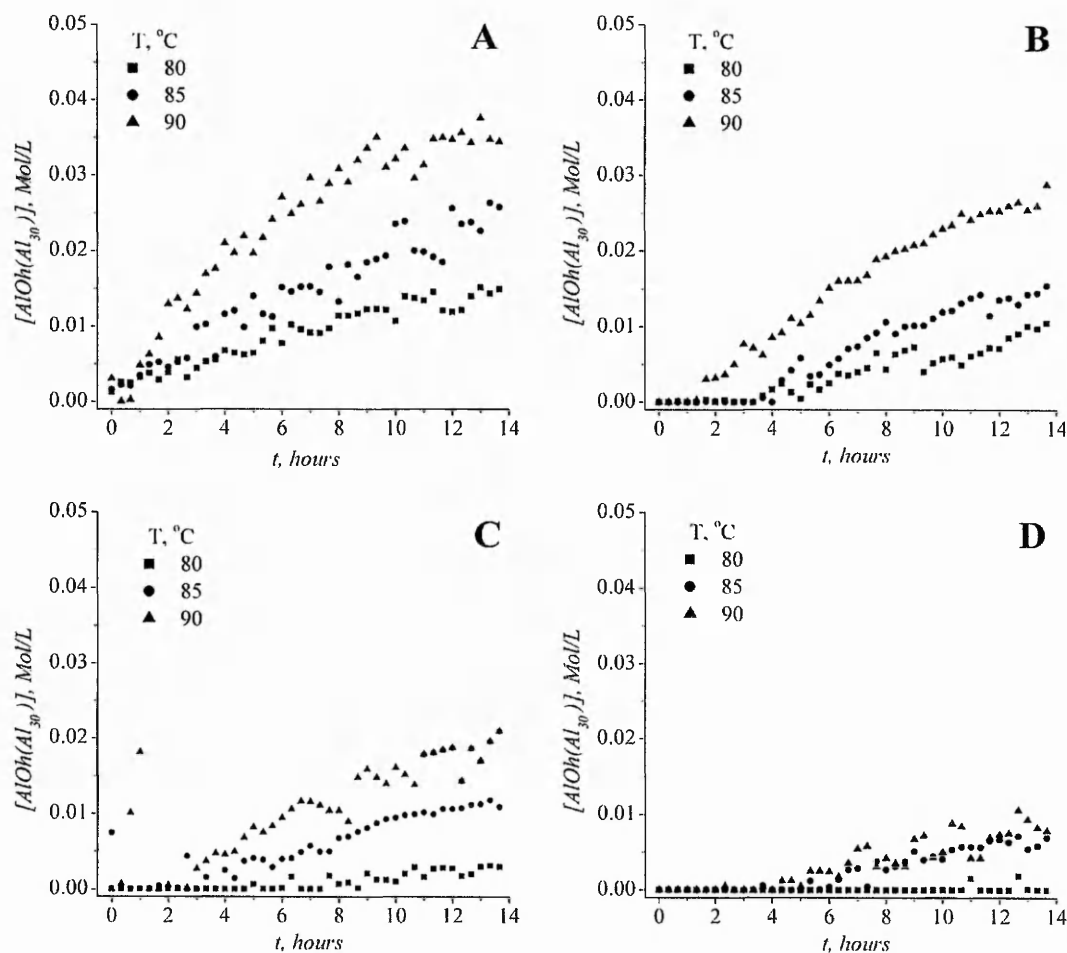


Fig. 8.13: Summary of the evolution of Al concentration corresponding the 10ppm peak attributed to part of octahedrally coordinated Al in Al_{30} -mer, for different temperatures and respective hydrolysis ratios: (a)2.14 , (b)2.37 , (c)2.43 , (d)2.52.

Peak areas together with the corresponding concentrations have been determined for species other than the Al_{30} -mer, in order to potentially clarify the observations made above. As discussed earlier, Al monomers and Al_{13} -mers are two species connected with the formation of the giant polycation (Fig. 8.14). Even so, as follows from Figure 8.14, Al_{13} -mer and Al_{30} -mer concentration evolutions are not exactly correlated during the early stages of heating treatment, and an initial increase of $[Al_{13}]$ is observed in some cases above $h=2.14$. This can be explained by a mobilisation of soluble species precipitated under the borderline conditions used for

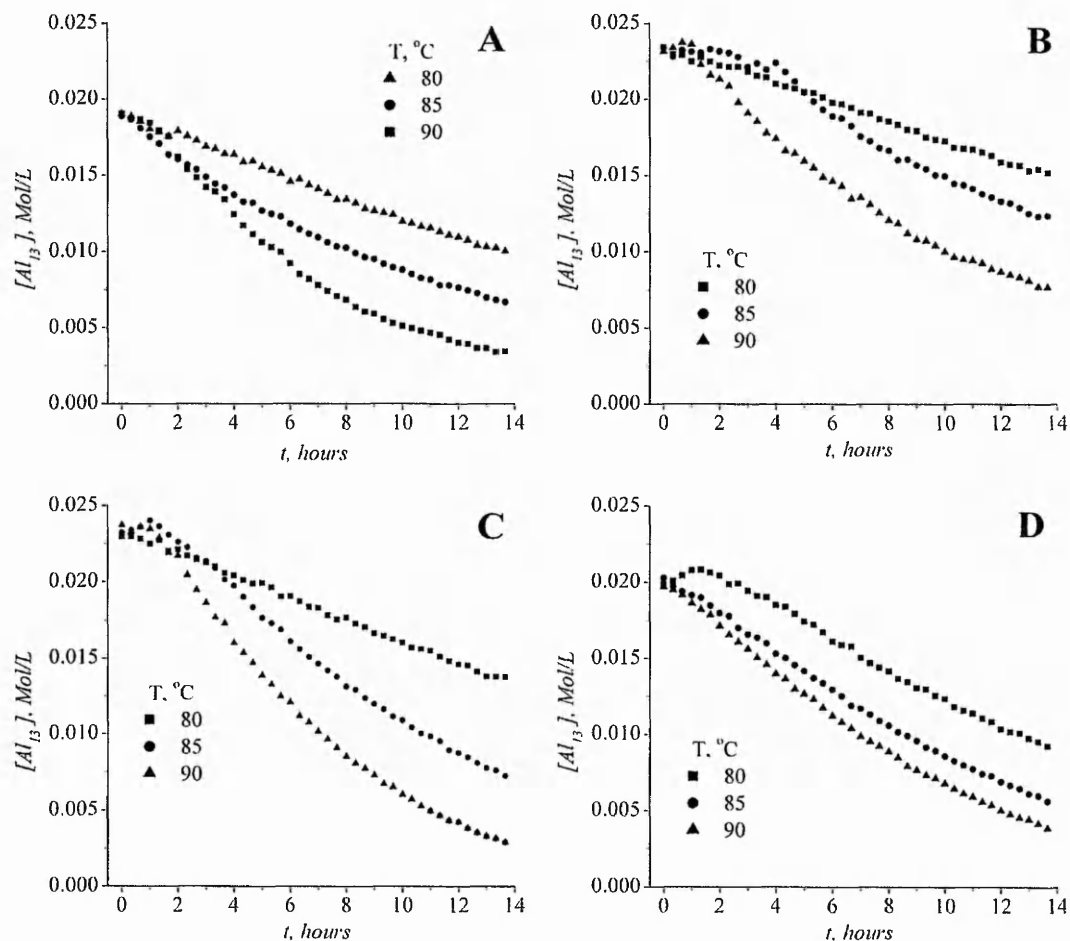


Fig. 8.14: Summary of the Al_{13} -mer concentration evolution as a function of time at three different temperatures and respectively hydrolysis ratio: (a) 2.14, (b) 2.37, (c) 2.43, (d) 2.52.

the experiment, by an additional production of the polycation or by a shift of the speciation equilibrium, all of these effects arising presumably from the temperature elevation. Nevertheless, after this initial increase, the evolution of the system follows a much more regular trend characteristic of the consumption of Al_{13} -mer by conversion to Al_{30} -mer. Moreover, the influence of initial hydrolysis ratio on the rate of the reaction consuming Al_{13} -mer is much less marked than the production rate of Al_{30} -mer, and all Al_{13} -mer consumed is visibly not converted to the larger polycation. Therefore, due to the apparent multiplicity of the processes implicated,

the evolution of Al_{13} -mer concentration upon heat treatment cannot be fitted with a simple function as in the case of the Al_{30} -mer, and further considerations need to be made before building a more appropriate kinetic model.

The diagrams of figure 8.15 describe the evolution of the 'capped' Al_{13} -mer concentration as a function of time. The signal at ≈ 64 ppm arising from this species has been identified by several groups [3-5], but not given a definite structure as for the other species quantified throughout this work. Nevertheless, due to its chemical shift and the low level at which it remains during the conversion process, 'capped'- Al_{13} -mer is generally thought to be an intermediate in the conversion mechanism. Two different evolution trends can be observed from the data plotted in figure 8.15. For samples with hydrolysis ratios 2.14, 2.43 and 2.52, 'capped'- Al_{13} -mer concentrations slightly increase before decreasing following the same trend as Al_{13} -mer concentration evolution. For $h=2.43$, a strong effect of temperature can be noticed, the concentration decrease rate being apparently proportional to temperature, whereas no strong dependency is observed for $h=2.14$ and 2.52. For the sample with $h=2.37$ treated at $T=80$ and 90°C , the concentration of the species increases for the first 6 hours of treatment, after which it remains steady, a decrease being only measured during the two last hours of treatment at $T=90^\circ\text{C}$. Data obtained for $h=2.37$ at $T=85^\circ\text{C}$ differs from the other results, a small increase following a drop in concentration arising during the first 3 hours of treatment, and data will probably need to be re-treated or discarded.

In order to clarify the evolution of the signal attributed to Al monomers and small oligomeric species during the heat treatment of the four solutions, Al monomer and small oligomers concentration as well as Al monomer peak position were estimated and plotted as a function of time in figures 8.16, 8.17 and 8.18.

As noticed earlier from spectral observation, Al monomer and oligomer concentrations remain practically constant over the time of the conversion reaction for $h=2.14$ and 2.37, whereas it increases for the higher h ratios studied (figures 8.16 and 8.17). We have seen in the previous developments that one part of Al_{13} -mer could not be accounted for by Al_{30} -mer production for $h=2.43$ and 2.52. The increasing concentration of the small species probably arises from the collapse of the

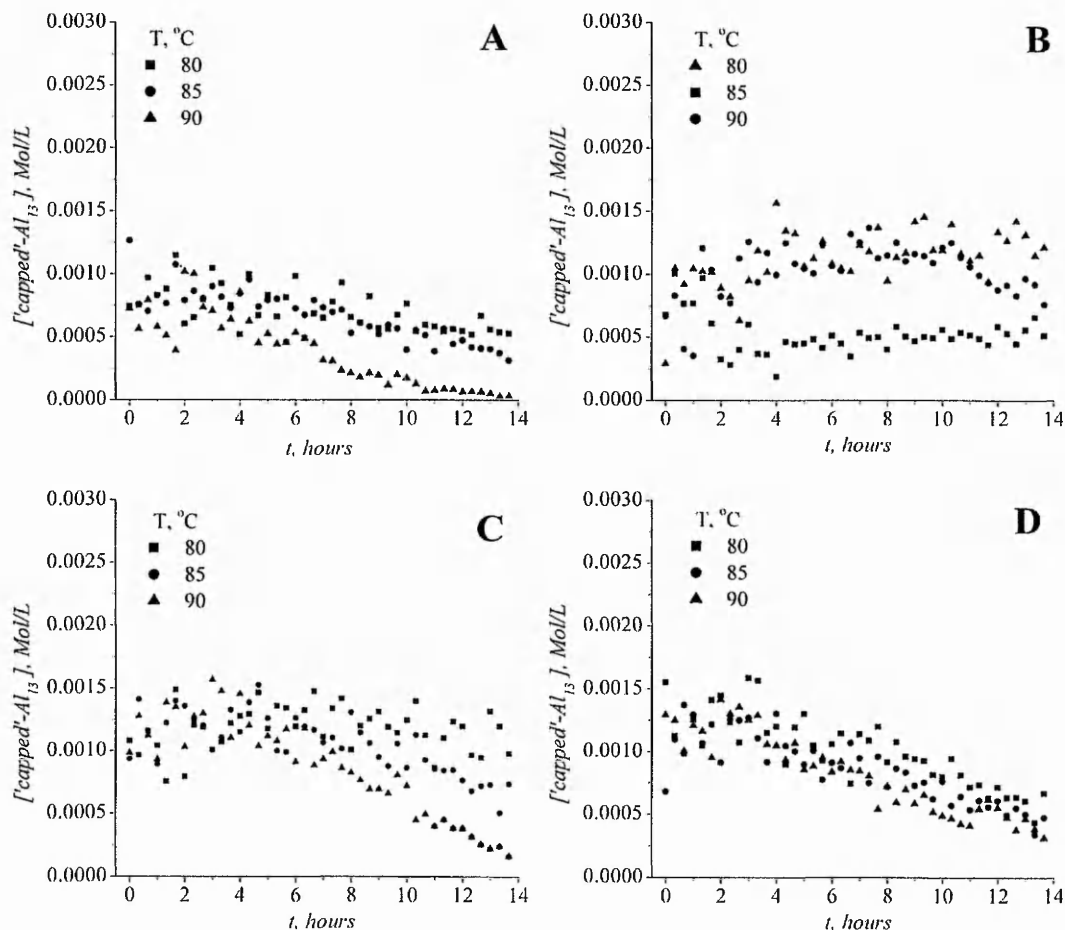


Fig. 8.15: Summary of the 'capped'-Al₁₃-mer concentration evolution as a function of time at three different temperatures and respectively hydrolysis ratio: (a)2.14, (b)2.37, (c)2.43, (d)2.52.

Al₁₃-mers, which are subsequently not reformed due to unfavorable conditions such as low precursor molecule concentrations. Under lower hydrolysis ratio conditions, the amount of small Al oligomers is higher and the Al₁₃-mer can easily be reconstituted. This explanation is supported by the concentration of small oligomers, and by the fact that Al₁₃-mer collapse should be enhanced by elevated proton concentrations [6], and the opposite trend should then be observed.

Al monomer peak position was in general correlated to Al monomer concentration evolution (Fig. 8.18). Indeed no peak shift was observed in the case of the $h=2.12$

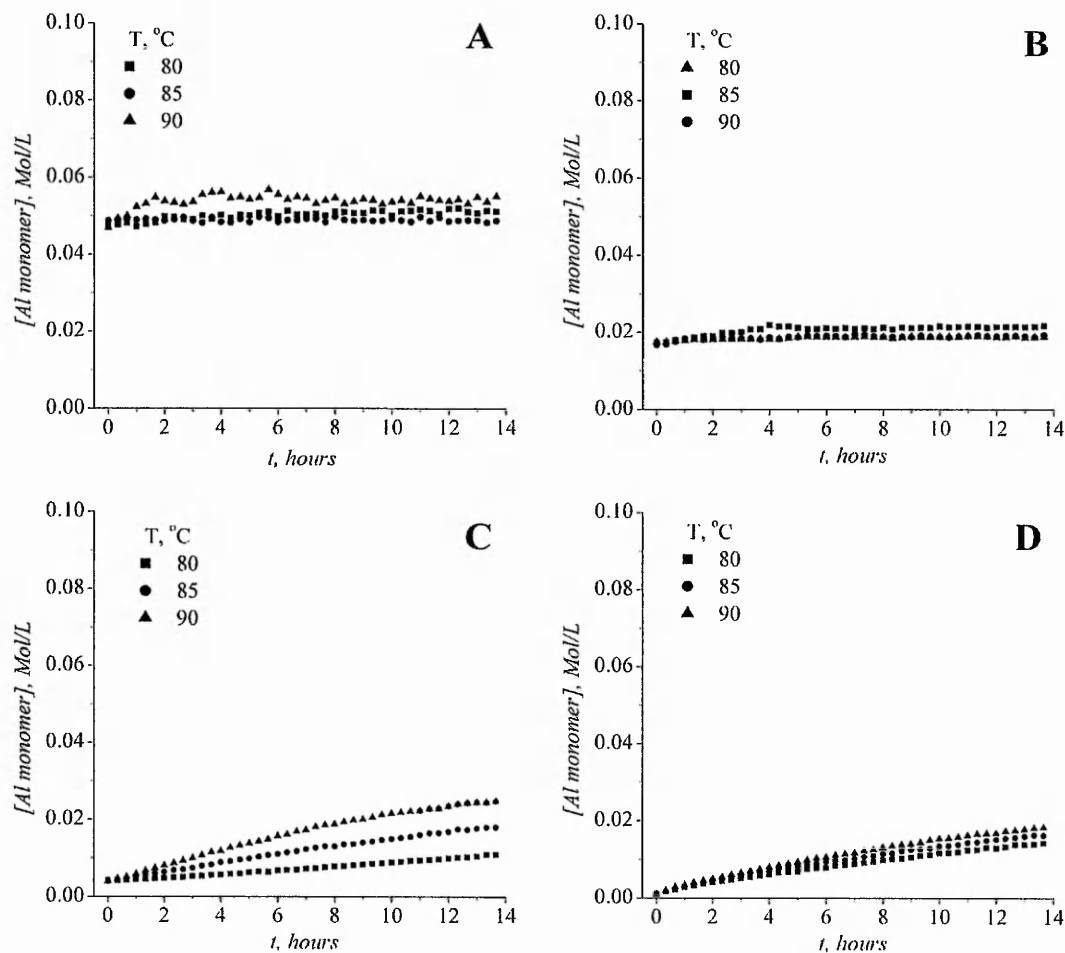


Fig. 8.16: Evolution of the monomer concentration versus heating time at three different temperatures and respectively hydrolysis ratio: (a)2.14, (b)2.37, (c)2.43, (d)2.52.

and 2.37 samples, whereas a shift of as much as 0.22ppm following an exponential decay towards low ppm values is visible for $h=2.43$ and 2.52. The initial chemical shift appears to be related to the hydrolysis ratio of the system, higher initial δ being observed as h is raised in the sample. Temperature does not seem to affect to a great extent either the peak position (less than 0.02ppm peak shift between 80 and 90°C), or the kinetics of the process leading to this peak position shift. It is too early to discuss the trends of Al monomer peak shift, however the evolution observed as well as the temperature-independent process leading to the shift demonstrate it

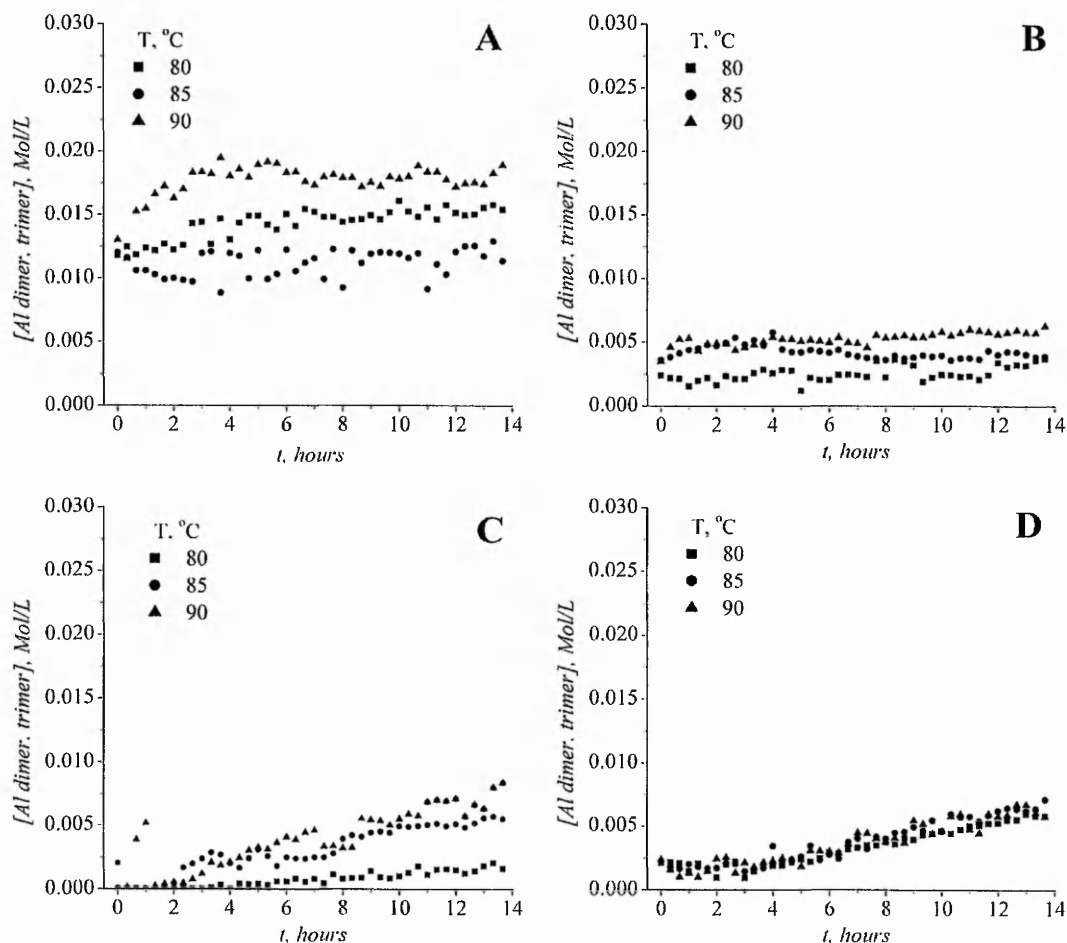


Fig. 8.17: Evolution of the concentration of small oligomeric Al species (dimers, trimers) versus heating time at three different temperatures and respectively hydrolysis ratio: (a)2.14, (b)2.37, (c)2.43, (d)2.52.

is independent from Al_{13} -mer collapse, and would rather arise from the slow release of monomers from unknown soluble species or small hydroxide nuclei present in the solution, and giving rise to the initial chemical shift. The chemical shift measured being then an average between the chemical shift of Al in small oligomers or nuclei and free Al monomer. Thus it would get closer to the chemical shift of monomer as other species are broken down with a low impact of temperature.

The ^{27}Al NMR peak at 75ppm, corresponding to the AlP_3 species, was finally fitted with our model. The AlP_3 polycation, including 3 tetrahedrally coordinated

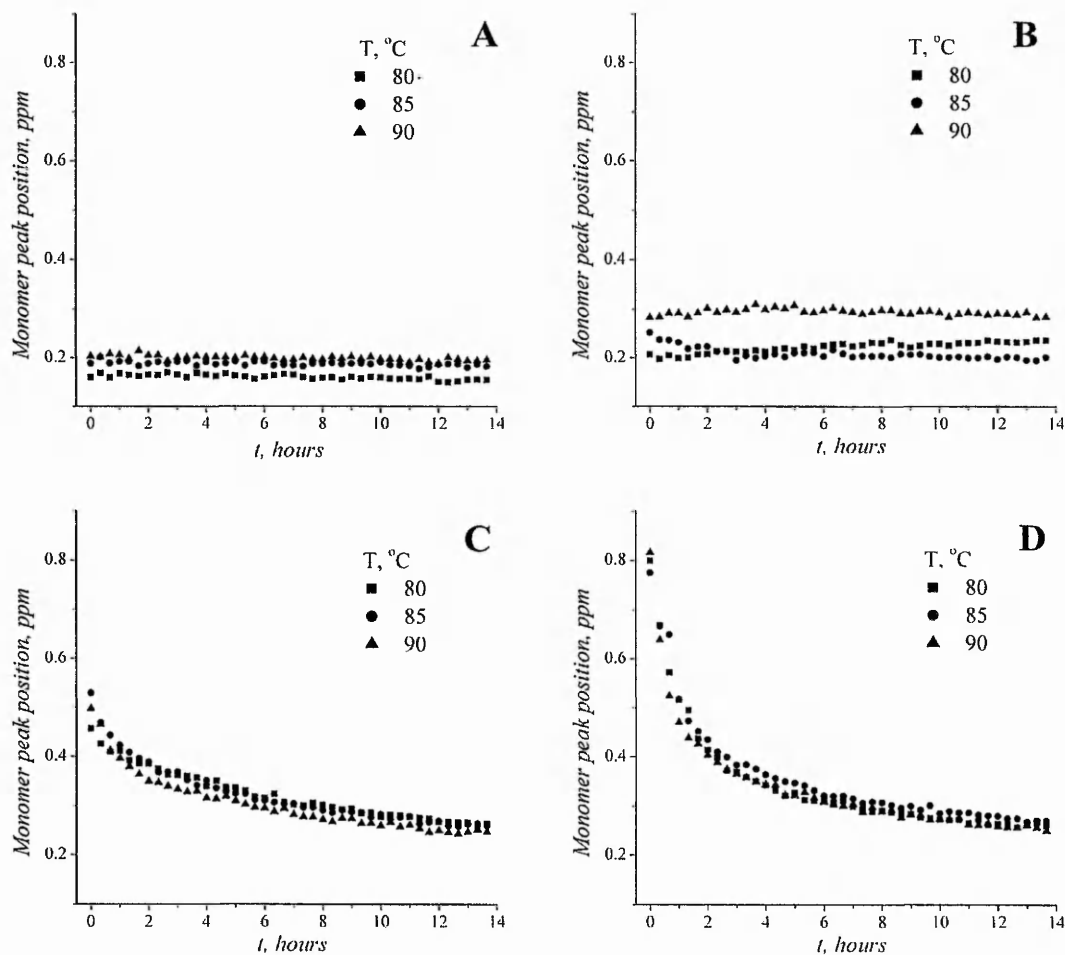


Fig. 8.18: Monomer peak position as a function of heating time at three different temperatures and respectively hydrolysis ratio: (a)2.14, (b)2.37, (c)2.43, (d)2.52.

aluminium ions in its structure, forms at an even slower rate than Al_{30} -mer, and the time span of the experiment was not sufficient to produce an elevated amount of this species. As follows from figure 8.19, the highest species concentration were obtained for the lowest hydrolysis ratios samples treated at high temperature, the maximum concentration ($6 \cdot 10^{-4} \text{Mol/L}$) being detected in the case of the heating of the $h=2.14$ sample at 90°C . This demonstrates that monomer might again play an important role in the formation of this species.

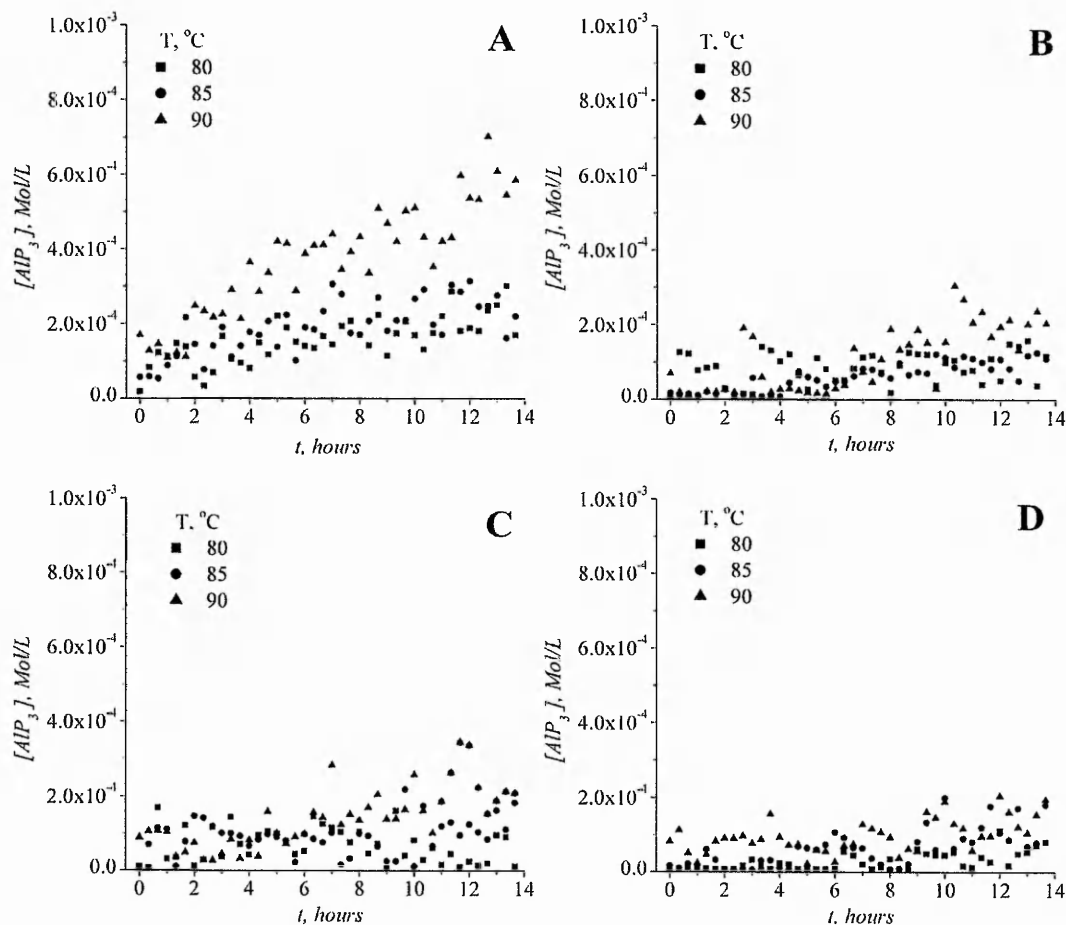


Fig. 8.19: Evolution of the AIP_3 species concentration versus heating time at three different temperatures and respectively hydrolysis ratio: (a) 2.14, (b) 2.37, (c) 2.43, (d) 2.52.

8.3 Conclusion

In this part of the work, an efficient automatic NMR data treatment algorithm programmed in MatLab environment has been described. The program was used to carry out the operations of apodisation, phasing, FFT and peak-fitting in a manner adapted to the requirements of ^{27}Al NMR, the final aim being the estimation and monitoring of species concentrations during the dynamic processes underlying Al speciation. Satisfactory phasing of both narrow and broad spectral features was achieved using an iterative process based on the principles of manual phasing. In

the second part of the chapter is described the application of the automatic data treatment to the study of Al_{13} - Al_{30} -mer conversion. Four samples of respective hydrolysis ratio 2.14, 2.37, 2.43 and 2.52 were prepared by means of ion exchange before being subjected to heat treatment, one FID trace being recorded in situ every 20min for a total time of 15 hours. Three heating temperatures were investigated (80, 85 and 90°C), enabling the estimation of both kinetic constants and activation energies of conversion corresponding to different hydrolysis ratios. Al_{30} -mer, but as well AlP_3 , are preferentially formed for a h lower than the theoretical value for each of the species. The role of different species have been demonstrated from observation of the corresponding peaks. Monomeric species promote the efficient bridging of 'capped'- Al_{13} -mer units leading to the formation of large amounts of Al_{30} . For higher hydrolysis ratios, most of the Al monomers produced by break-down of the Keggin structure do not reform the polycation in the absence of a sufficient concentration of both monomeric and small oligomeric species. Under such conditions, the formation of undetectable species (possibly hydroxide) is observed as demonstrated by a loss of signal intensity. The intermediate role of 'Capped'- Al_{13} -mer in the Al_{13} - Al_{30} conversion was verified, higher levels of this species matching high rates of reaction.

Through the years, authors noticed a narrowing of the broad spectral feature observed at 10ppm upon heat treatment. As mentioned in the materials and methods section, this peak originates from Al present in octahedral coordination in large Al polycations. Our treatment algorithm enabled the deconvolution of this spectral feature as two separate peaks, one being attributable to Al in the shell directly surrounding tetrahedral Al centers, and the second narrower one to Al ions bridging Al_{13} -mer subunits in the Al_{30} -mer structure. This conclusion can be drawn from two observations: (a) The evolution of the 70ppm peak, attributed to tetrahedrally coordinated Al in Al_{30} -mer), is correlated to the evolution and the 10ppm peak attributed to bridging monomers in Al_{30} -mer, (b) The area of the peak at 10ppm is equivalent to two times the area of the peak at 70ppm, and can be therefore attributed to four Al ions (of course the peaks at 10 and 70ppm were fitted completely independently).

In conclusion, the implementation of a fully automated ^{27}Al NMR data treatment algorithm, combined with ion exchange synthesis enabled us to gain further understanding of the Al_{13} - Al_{30} -mer conversion mechanisms and of the features observed in ^{27}Al NMR spectra, and indicated the optimum conditions required for efficient conversion.

BIBLIOGRAPHY

- [1] K. Shafran, O. Deschaume, and C. C. Perry, *Advanced Engineering Materials*, 2004, **6**(10), 836–839.
- [2] J. W. Akitt, *Progress in NMR Spectroscopy*, 1989, **21**, 1–149.
- [3] K. L. Shafran and C. C. Perry, *Journal of the Chemical Society, Dalton Transactions*, 2005, pp. 2098–2105.
- [4] G. Fu, L. F. Nazar, and A. D. Bain, *Chemistry of Materials*, 1991, **3**, 602–610.
- [5] L. Allouche, C. Gerardin, T. Loiseau, G. Ferey, and F. Taulelle, *Angewandte Chemie International Edition*, 2000, **39**(3), 511–514.
- [6] G. Furrer, M. Gfeller, and B. Wehrli, *Geochimica et Cosmochimica Acta*, 1999, **63**(19/20), 3069–3076.

9. PREPARATION OF MONODISPERSE AL HYDROXIDES

9.1 *Introduction*

For decades, researchers and industrial groups have been working at preparing monodisperse sols of oxides or hydroxides for diverse applications. As demonstrated in the well documented case of monodisperse silica spheres obtained from the process developed by Stöber, the preparation of such sols is generally poorly reproducible, strongly dependant on a large number of parameters, with several batches needing to be prepared in order to reach the desired particle size range [1]. In the case of Al hydroxides and oxides, alkoxide routes prevail for the production of particle sols, the disadvantage of these being the use of non-aqueous solvents as well as expensive precursors [2–4].

The stability and monodisperse nature of our aluminium hydroxide sols prepared using an aqueous route were demonstrated during the initial ion exchange experiments described earlier in this thesis [5]. In all cases the produced suspensions reached equilibrium after a few months of aging at room temperature, with both stability and average particle size being then unaffected by years of normal storage (sols prepared at the beginning of this project).

The experiment which follows is intended to reduce the time required for this equilibrium to be reached and to develop a robust and reproducible method for the preparation of stable monodisperse hydroxide sols. The approach involved studying the effect of the initial hydrolysis ratio of the sols as well as the aging temperature and aluminium concentration. In addition, the experiments were performed to (a) get more insight in the mechanisms of growth of the Al hydroxide previously observed and (b) determine the behavior of Al_{13} -mer in the presence of this thermodynamically more stable solid phase, demonstrating the way the polycation affects

the growth processes. As we will see, the experiments carried out unveiled the large complexity of the hydroxide growth processes in the presence of polycations, and enabled us to draw some conclusions concerning the optimisation of monodisperse hydroxide sol preparation routes.

Two types of initial aluminium hydroxide sols were synthesized by means of ion exchange, the two differing by the extent of their neutralisation ($h=2.62$ and 2.82) and therefore, as will be noticed in the following developments of this section, by the amount of Al_{13} -mer remaining after initial preparation. Aluminium speciation, pH, conductivity and chloride concentration were monitored during this preparation process. In each case two batches were prepared at 12 hour intervals following identical procedures in order to check the reproducibility of the synthesis and enable the full monitoring of the system evolution over aging.

Following preparation, the resulting sols were diluted to different extents (0.05, 0.2 and 0.4M Al) and aged for 60h at three different temperatures (25, 40 and 60°C), the batches being characterised every 4h over the aging process by an arsenal of techniques including pH, conductivity, viscosity, DLS measurements as well as speciation monitoring by means of the ferron assay.

For each extent of neutralisation, we will present the results of characterisation during preparation to then study in more detail the aging processes.

9.2 Results and discussion: for low degree of neutralisation

This section describes the evolution of the hydroxide sols aged in the presence of a fairly elevated concentration of polycations ($h=2.62$). The aging temperatures were chosen so that the heat treatment did not promote the production of Al_{30} -mer so that the changes observed during the experiment are entirely related to the processes of Al hydroxide growth and interaction with Al_{13} . Al speciation was monitored by means of ^{27}Al NMR and ferron assay prior to aging, during the initial preparation process. In figure 9.1 are presented the NMR spectra and Al speciation diagram. In order to obtain the concentration of the different species present as a function of exchange time, our automatic NMR spectra processing/fitting algorithm was im-

plemented in order to clearly differentiate between monomeric and small oligomeric species present in solution and get a clear picture of Al speciation. One can observe the presence at 63ppm, of the peak attributed to the Al₁₃-mer tetrahedrally coordinated Al core. The intensity of this peak increases abruptly during the first 30min of exchange, together with a decrease in intensity of both monomer (0ppm) and small Al oligomers peaks (3-4ppm). As mentioned earlier this observation is characteristic of the formation of the Al₁₃-mer. After reaching a maximum the intensity of the 63ppm peak decreases together with the other species peaks, to reach a stable value after 2 hours of treatment. After the end of the ion exchange process, the system is therefore governed by Al₁₃-mer and Al hydroxide, as shown in the speciation diagram derived from NMR spectra analysis. The effects of the processes identified

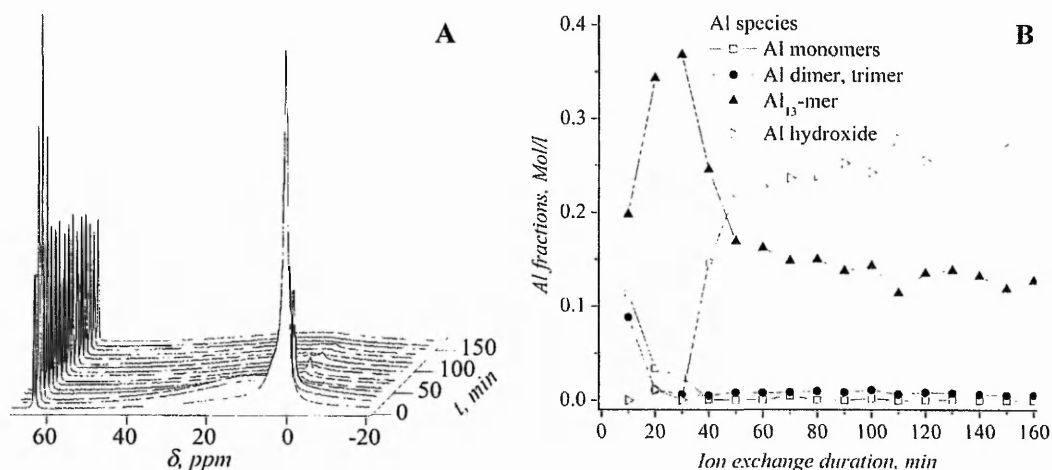


Fig. 9.1: ²⁷Al NMR spectra (A) and derived speciation diagram (B) over ion exchange synthesis of the initial Al hydroxide sol.

by ²⁷Al NMR can also be followed by pH and conductivity measurements (Figure 9.2). Thus, after the different inflexions attributed to polycations production and collapse, pH and conductivity measurements indicate that relative stability of the system is reached at the end of the ion exchange process. However the system is just stable in appearance and slowly evolves after preparation, leading for example to a decrease in pH and an increase in hydroxide particle size under ambient conditions. In the second part of the experiment, devoted to the study of the aging process,

the relative equilibrium attained at the end of the ion exchange process was perturbed by the introduction of dilution and heating. Figure 9.2B shows the effect of this perturbation on the pH of the sols prepared. As predicted, the initial pH of the sols depends on their dilution, and is in the order $5.21(0.4\text{M Al}) > 5.19(0.2\text{M Al}) > 4.94(0.05\text{M Al})$. In all cases the pH of the sols decreased during aging, the fastest changes being observed for the first 4 hours of the experiment. The rate of decrease appears to depend mainly on temperature, whereas the pH reached at the end of the monitoring depends mainly on total Al concentration. The largest pH evolutions over heating time are observed in the case of the sols heated at 60°C , this variation decreasing for lower aging temperatures. The conductivity of the sols

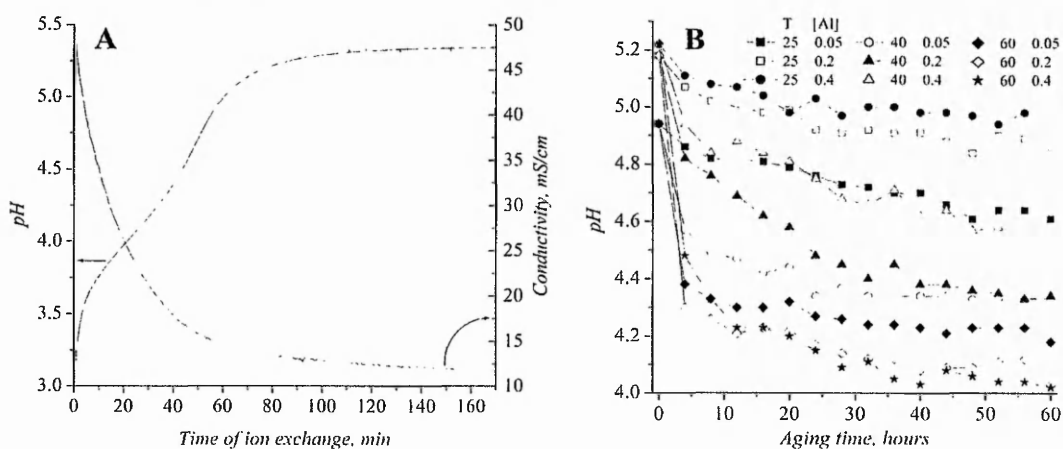


Fig. 9.2: (A) pH and conductivity of the solution over the ion exchange process, and (B) evolution of the pH on aging the sols at different Al concentrations and temperatures for 60h.

is proportional to Al concentration throughout the experiment (Figure 9.3). As in the case of pH, the largest changes are observed for the highest Al concentrations over the first 10 hours of aging. Conductivity is much less affected than pH by aging after this time and the variation in conductivity must originate from proton release as demonstrated by pH measurements. Viscosity was the only parameter from which a difference could be observed between the two batches prepared to check the reproducibility of the synthesis. This difference probably arises from the difference in time for the sampling of the two batches. Indeed sampling started

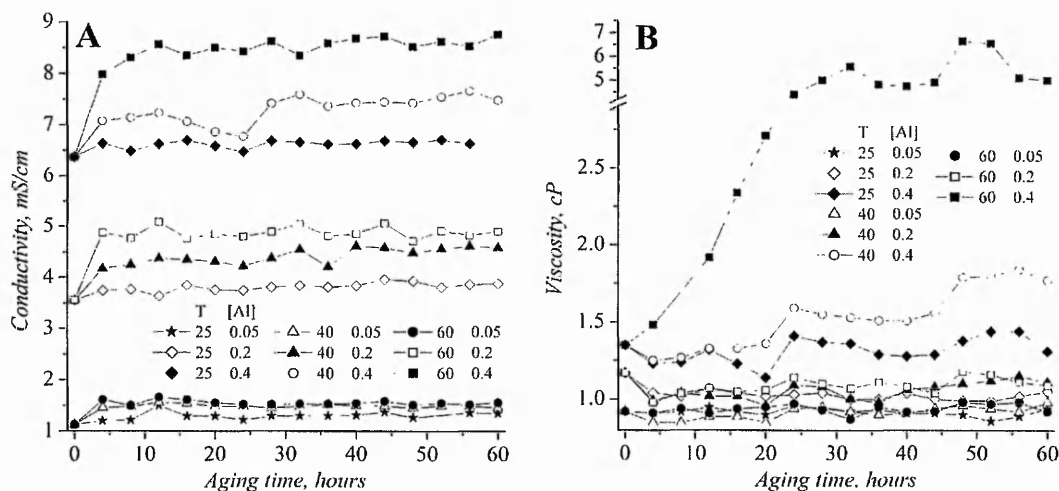


Fig. 9.3: (A) Evolution of conductivity and (B) viscosity in the sols during aging at different Al concentrations and temperatures for 60h.

12h after preparation in the case of the first batch, whereas it started straight after preparation for the second batch. The 12 hours of heat treatment of the first batch without any shaking of the containers probably allowed the gel network to form in the very concentrated sols prepared, leading to a larger viscosity of the preparations. Nevertheless the variation observed was not considerable and was mainly evidenced in the samples of highest Al concentration, independent of the aging temperature. The general trend observed during aging was a slight decrease in viscosity following preparation, after which an increase can be observed. In the case of the most dilute sols (0.05 and 0.2 Mol/L Al), viscosity remains close to the solvent viscosity, whereas a substantial jump is observed at higher concentration. This jump became larger as the temperature of aging was increased. At 60°C, the viscosity of the sols stabilised to 5-7cP after following a sigmoidal trend over the 30hours following preparation. The gelation observed probably originates from the formation of weak bonds between hydroxide particles, promoted by heat treatment and high particulate matter concentration or by the destabilisation of Al polycations at the beginning of the process, which generally leads to a similar increase in viscosity. Indeed the gels were easily peptised by simple dilution/sonication carried out prior to particle size analysis, as demonstrated by as determined particle size remaining

below 150nm. The gelation of the sols correlated with an increase in particle size (Figure 9.4). Great care was taken with diluting and sonicating the suspensions that

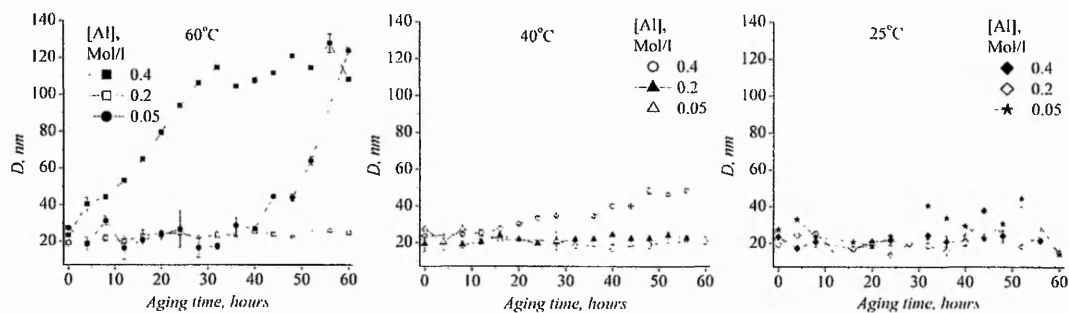


Fig. 9.4: Evolution of Al hydroxide particle size after dilution to 0.4, 0.2, and 0.05Mol/L Al over aging of the resulting sols at 25, 40 and 60°C for 60 hours.

were characterised by DLS in order to prevent multiple scattering and any viscosity or gelation-dependant artifacts. Moreover the diluted samples were equilibrated at the measurement temperature for at least 20 minutes after cooling to room temperature to alleviate the effect of temperature on particle diffusion. The particle size measured over time is therefore the size of primary particles forming the sols, and not that of loose aggregates. Similarly to viscosity, evolution in particle size followed a sigmoidal trend and is more evident in the case of the highest Al concentrations and heating temperatures. The 0.05M sol treated at 60°C shows a very peculiar behavior, as the sol characterised seems to undergo an abrupt growth starting after 40 hours of treatment, which led to the sedimentation of solid material. Further experiments will need to be carried out under similar conditions to study further this peculiar behavior which might arise from a change in growth mode in this concentration range or to an accidental introduction of impurities at some point of the sampling procedure. Apart from this case, the growth rate seems to be related to the amount of material available for growth, either under the form of soluble species (mainly Al_{13} -mer as demonstrated by initial NMR results), or smaller hydroxide particles undergoing solubilisation/precipitation or aggregation (for aging processes, see introduction). The aggregation model remains valid as stronger bonds might be formed within the gels formed, leading to denser aggregates resisting peptisation.

These suppositions concerning the origin of Al hydroxide particles growth can be further assessed by the observation of changes in Al speciation over aging. Indeed, as noticed both from ferron and ^{27}Al NMR monitoring of the system, the sols contained a large amount of Al_{13} immediately after preparation. The evolution of this species, as well as other species concentration is plotted in Figure 9.5 against time at different temperatures, for the most concentrated of the sols studied. A corre-

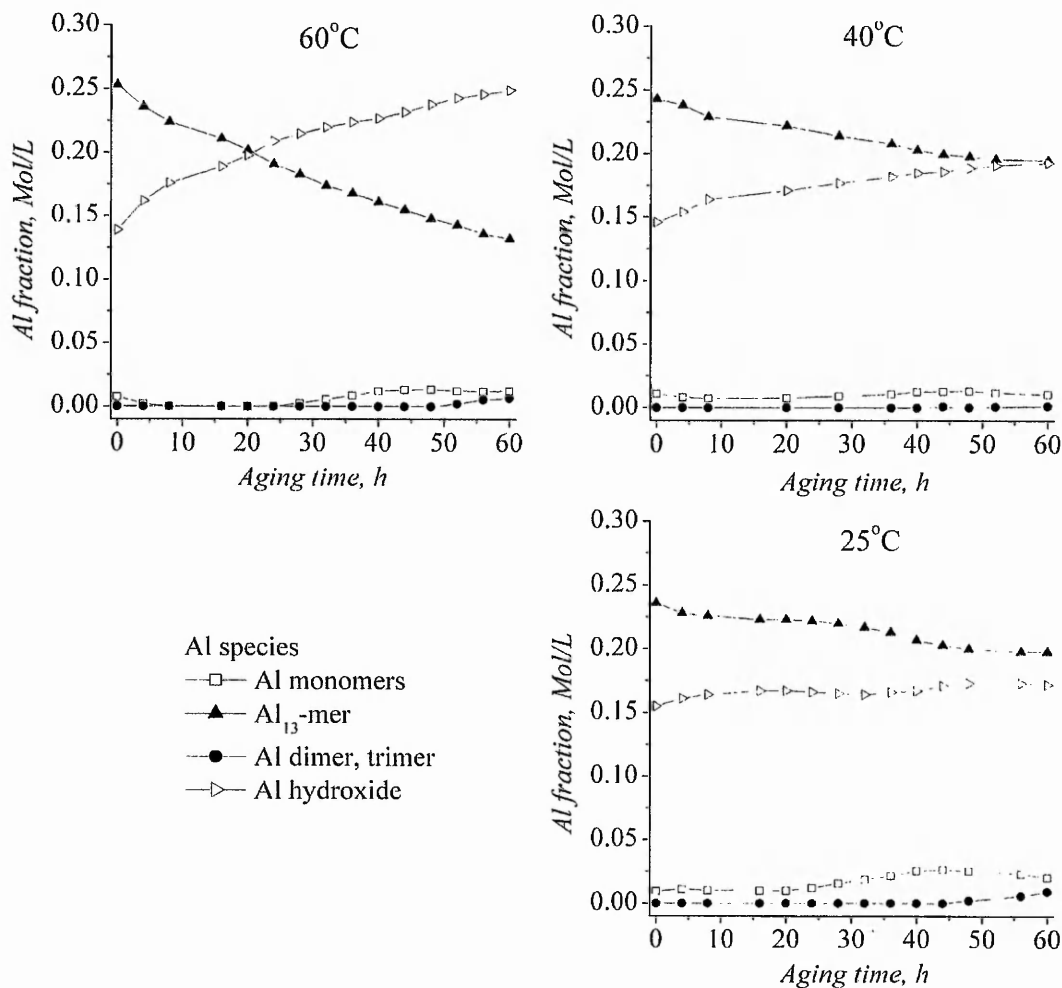


Fig. 9.5: Evolution of Al speciation as determined from ferron kinetic assay in 0.4 Mol/L Al sols aged at 25, 40 and 60°C for 60 hours.

lation between an increase in hydroxide concentration and a decrease in Al_{13} -mer concentration measured can easily be identified from this data. This evolution is

accentuated at higher temperatures and follows exponential trends as observed for the case of Al_{30} -mer formation from Al_{13} -mer dimerisation. However the decrease in the Al_{13} -mer concentration is much faster than in the case of Al_{13} - Al_{30} conversion carried out under similar temperature conditions. The evolution observed therefore probably derives from a dissolution-precipitation process in which Al_{13} -mers collapse with the resulting oligomers precipitating quickly on the more thermodynamically stable hydroxide surface, promoting growth rather than an increase in the number of the particles observed. This model would explain the correlation between DLS and speciation data. Another demonstration of our hypothesis resides in the changes in pH of the systems during aging. The pH evolves quickly from the instability to the stability domain of the polycation (the borderline of this domain can be estimated at 4.5) over the first 5 hours of aging. After this time a dissolution-reformation of the polycation [6] can occur in the absence of hydroxide. However in the presence of the thermodynamically more stable solid, the precursors do not reform Al_{13} and precipitate on neighbouring particles.

9.3 The case of more extensive neutralisation

A second series of experiments have been performed to study the evolution of hydroxide sols in the presence of a low polycation fraction, with initial preparation being performed at a higher hydrolysis ratio ($h=2.82$). As in the previous case, the inflexions relating to the build up and collapse of polycations are observed from the first parts of the pH curve (Figure 9.6). As observed for ion exchange experiments carried out for lower Al concentrations, the speed and extent of neutralisation are higher when a larger amount of exchanger is introduced in the system. The pH observed in the present case stabilised to 6.5 at the end of the process, a value close to the isoelectric point of Al hydroxide. This can be further evidenced by the higher viscosity of the sols produced both after ion exchange and aging that results from larger inter-particle interactions in the most concentrated dispersions (Figure 9.8). The evolution in speciation determined from ^{27}Al NMR spectra fitting emphasises again the mechanism of Al hydroxide formation going through a step of Al polycat-

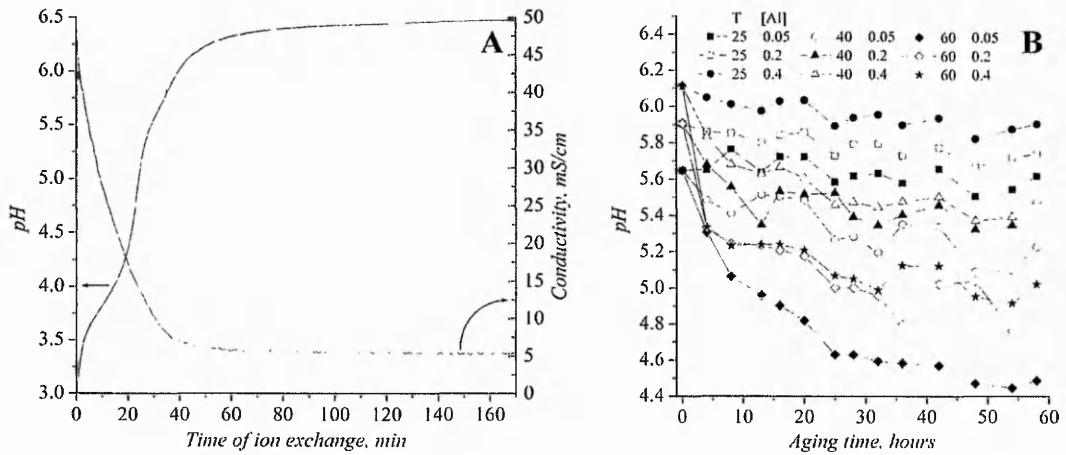


Fig. 9.6: (A) pH and conductivity of the solution over the ion exchange process, and (B) evolution of the pH over aging of the sols at different Al concentrations and temperatures for 60h

tions predominance (Figure 9.7). The speed and extent of the process are however different, the Al_{13} concentration being at a maximum after 18min of treatment and decreasing to virtually zero after 60min. The batches of material are therefore composed mainly of the solid phase at the end of the exchange process. The pH and

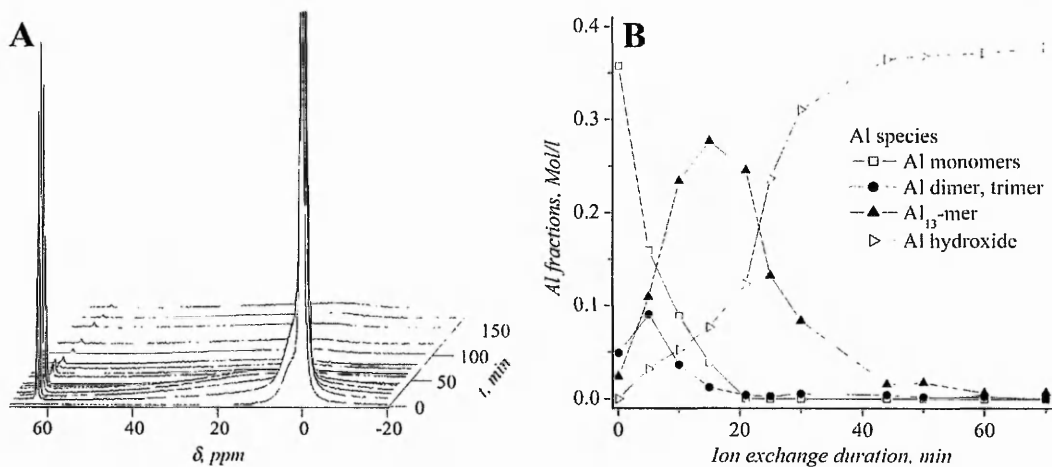


Fig. 9.7: Al Speciation monitored by means of ^{27}Al NMR over ion exchange time leading to an Al hydroxide batch virtually free of Al_{13} -mer: (A) Stacked spectra and (B) corresponding speciation diagram from automated spectra treatment.

conductivity evolution during aging followed trends similar to the ones observed during the first aging experiment, however the pH decay and the conductivity increase appeared slower and last until the end of monitoring. Again, viscosity measurement suffered poor reproducibility over aging between the two batches prepared, despite the good agreement observed from conductivity and pH measurements. The sigmoidal trend observed earlier is hardly observable in the highest concentration sols, but is however more apparent from DLS measurements (Figure 9.9). The dif-

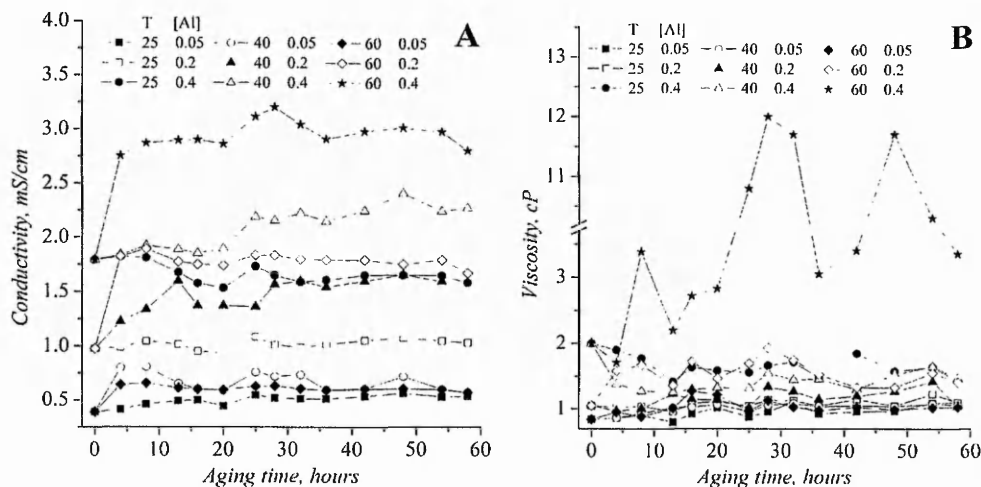


Fig. 9.8: (A) Evolution of conductivity and (B) viscosity in the sols over aging at different Al concentrations and temperatures for 60h.

ference in particle size in the two batches demonstrate a lower reproducibility of particle synthesis for the higher neutralisation of the sols, the maximum particle size obtained being lower than for previous experiments. An increase in particle size is again observed over aging time, the growth being accentuated at elevated Al concentrations and temperature, but with a much less well defined sigmoidal trend. The lower particle size reached might arise from the lower availability of soluble precursors available to feed the hydroxide particle growth, as well as from the higher viscosity slowing down diffusion processes. The Al speciation monitored using ferron assay, which could enable us to seek for some clarity or explanation of the growth process in the initial absence of polycations unveils a higher complexity than predicted (figure 9.10). In the case of the less concentrated sol (0.05M), the very

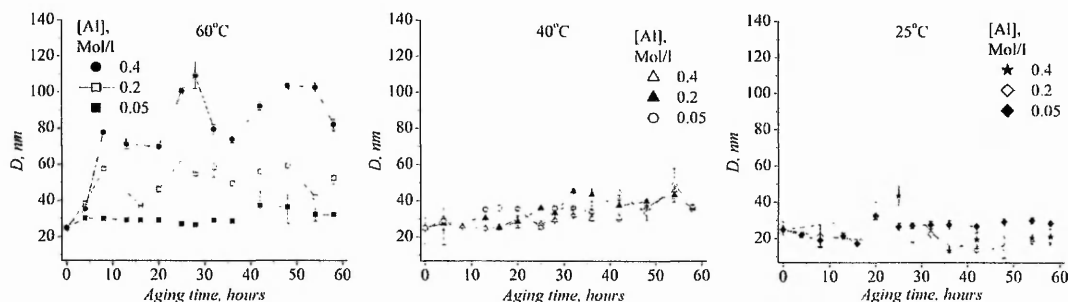


Fig. 9.9: Evolution of Al hydroxide particle size after dilution to 0.4, 0.2, and 0.05Mol/L Al over aging of the resulting sols at 25, 40 and 60°C for 60 hours.

low Al_{13} -mer concentration present initially is converted to the hydroxide phase in the first few hours of aging. A peculiar behavior appears starting from the medium concentrated sols (0.2M): instead of increasing at the expense of the Al_{13} -mer concentration, the Al hydroxide concentration evolution follows the opposite trend and progressively decreases while Al_{13} -mer is formed. This trend is pronounced during the first 12 hours of aging of the most concentrated dispersion (0.4M), however, the concentrations stop following this trend after 20h, to then adopt the same evolution as the one observed in the case of the first hydroxide aging experiment. Under slow and soft neutralisation conditions, as in the case of our first aging experiment, Al polycations formed during the first step of the process slowly convert to hydroxide after production of a critical size nucleus, the solid being mostly composed of a thermodynamically more stable phase. However, in the case of the faster neutralisation carried out during the second experiment, a portion of the Al_{13} -mer formed during the first minutes of ion exchange do not have time to convert to the stable hydroxide phase and is converted into a metastable phase such as a basic salt, which undergoes a very slow transformation to the stable hydroxide at room temperature. Indeed, on the basis of SAXS studies of Al hydroxide gel formation, some authors assume a mechanism of hydroxide formation proceeding through the aggregation of Al_{13} -mer units followed by reorganisation of the latter [7–9].

During our own experiments, we demonstrated that when the conversion from polycation to hydroxide is slowed down, for example by cooling down the system below

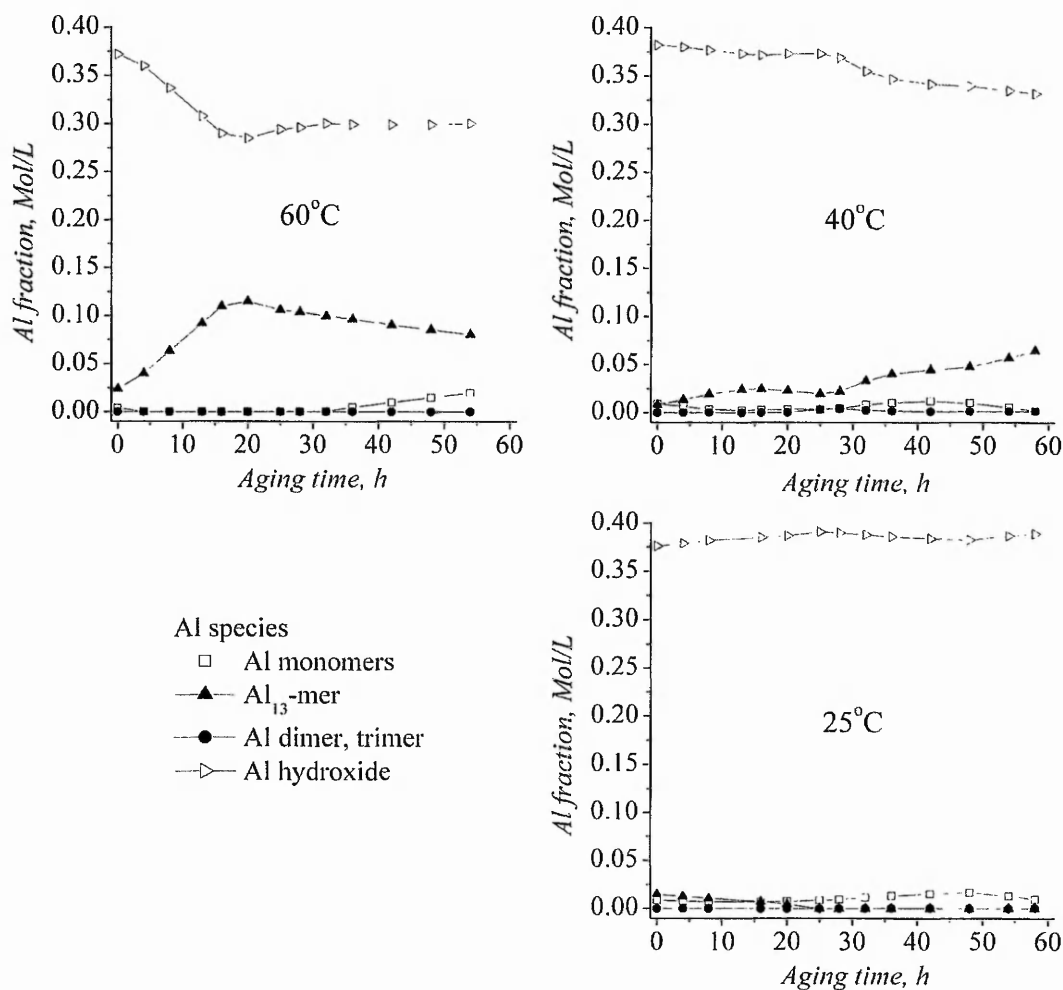


Fig. 9.10: Evolution of Al speciation as determined from ferron kinetic assay in 0.4 Mol/L Al sols aged at 25, 40 and 60°C for 60 hours.

5°C, a gelation phenomenon occurs and the NMR signal attributed to polycations disappears, whereas these species are still detected from the ferron kinetic assay. When the pH of the solution is decreased by acid addition, a large portion of Al polycations (Al₁₃ or Al₃₀) are again detected by liquid-state ²⁷Al NMR, demonstrating the composition of the precipitated phase. At high temperature, the decrease of the solution pH might lead to the release of Al₁₃-mer from this metastable phase. Al₁₃-mer concentration increases until all the metastable precipitated phase is dissolved. The polycation concentration is then observed to decrease, feeding the growth of

the stable hydroxide phase.

9.4 Conclusions

In this chapter were described different experiments aiming at obtaining additional information concerning the formation of Al hydroxide from solution of high Al polycations content, as well as at the optimisation of monodisperse hydroxide sol preparation. The preparation and aging of two different types of hydroxide, either partially or fully neutralised was monitored using both solution and colloidal state characterisation techniques. The results enabled us to demonstrate the better quality and reproducibility of hydroxide sols prepared from partially neutralised solutions. For low neutralisation levels, stable hydroxide nuclei are formed during the initial preparation and their growth is fed during aging by the slow collapse of Al₁₃-mer, as demonstrated from ferron assay results. The best growth is obtained for the highest Al content samples, and this phenomenon greatly accelerated as the temperature of suspensions is increased. For a more extensive initial neutralisation, the formation of a large number of stable hydroxide nuclei is hindered by the precipitation of a metastable solid phase, which dissolves upon aging as indicated by the release of Al polycations. The simultaneous presence of Al hydroxide and of the metastable solid leads to a more intricate growth mechanism accounting for the poorly reproducible results obtained in this case. In this part, the possibility to use polycations as precursors to monodisperse hydroxide sols has been demonstrated. The growth of such sols can be efficiently accelerated when a slow partial neutralisation is initially carried out. Growth of the hydroxide particles is then slowly fed by Al polycations collapse. The resulting particle sols have a high stability, with hexagonal sheet-like particles bearing an elevated surface charge with interesting potential for the formation of auto-assembled nanocomposites.

BIBLIOGRAPHY

- [1] K. Nozawa, H. Gailhanou, L. Raison, P. Panizza, H. Ushiki, E. Sellier, J. P. Delville, and M. H. Delville, *Langmuir*, 2005, **21**, 1516–1523.
- [2] N. Yao, G. Xiong, Y. Zhang, M. He, and W. Yang, *Catalysis Today*, 2001, **68**, 97–109.
- [3] Y. K. Park, E. H. Tadd, M. Zubris, and R. Tannenbaum, *Materials Research Bulletin*, 2005, **40**, 1506–1512.
- [4] K. Wefers and C. Misra Oxides and hydroxides of aluminum Technical report, Alcoa Laboratories, 1987.
- [5] K. L. Shafran, O. Deschaume, and C. C. Perry, *Journal of Materials Chemistry*, 2005, **15**, 3415–3423.
- [6] W. H. Casey, B. L. Phillips, and G. Furrer, 2002; chapter Aqueous Aluminum Polynuclear Complexes and Nanoclusters: A Review, pp. 166–190.
- [7] J. Y. Bottero, D. Tchoubar, J. M. Cases, and F. Flessinger, *Journal of Physical Chemistry*, 1982, **86**, 3667–3673.
- [8] D. Tchoubar and J.-Y. Bottero, *Comptes Rendus de l'Academie des Sciences Serie IIa: Geomatériaux*, 1996, **322**, 523–524.
- [9] J. P. Jolivet, *From Solution to Solid State*, Wiley and Sons, 2000.

10. DESTABILISATION OF AL SPECIES: EFFECT OF BSA AND SOLUBLE ELASTIN, RESULTING MATERIALS

During this study, Al-BSA and Al-elastin samples were prepared from model solutions of aluminium species (Al_{13} , Al_{30} , and Al hydroxide sols with different particle sizes) and different amounts of BSA or soluble elastin. The composite samples were analyzed using a range of solution and colloidal techniques including pH, conductivity, viscosity measurements together with solution ^{27}Al NMR and quantification of the free protein/Al fraction after centrifugation of the phase-separated materials. The samples were finally freeze-dried and analyzed using several solid-state techniques as well as solution techniques after re-dissolution of the obtained materials.

10.1 Al-BSA systems

10.1.1 Physical properties and pH of the Al-BSA solutions

Conductivity, pH and viscosity measurements of the samples prepared from Al species and BSA were carried out simultaneously, after ageing the samples for 24 hours. The data are presented in Figure 10.1. As follows from Figure 10.1A, initial conductivity of the pure aluminium species solutions varies in the following order: $\text{Al}_{30}\text{-mer} > \text{Al}_{13}\text{-mer} > \text{Al hydroxide (26 nm)} > \text{Al hydroxide (55 nm)} > \text{Al hydroxide (82 nm)}$. With increasing BSA concentration, solution conductivity decreases for Al polycations ($\approx 5\%$ decrease for the Al_{13} and $\approx 10\%$ - for the Al_{30}), while remaining practically unchanged for the samples prepared from Al hydroxide (Figure 10.1A). The initial pH of the three hydroxide mixtures with BSA (Figure 10.1B) shows an inverse trend to that of conductivity, the $\text{Al}_{30}\text{-BSA}$ system showing the lowest initial pH of 3.9. The pH of $\text{Al}_{13}\text{-BSA}$ solutions increases with increasing BSA concentration, reaching the upper pH limit of $\text{Al}_{13}\text{-mer}$ stability ($\text{pH} \approx 4.6$) [1]. The

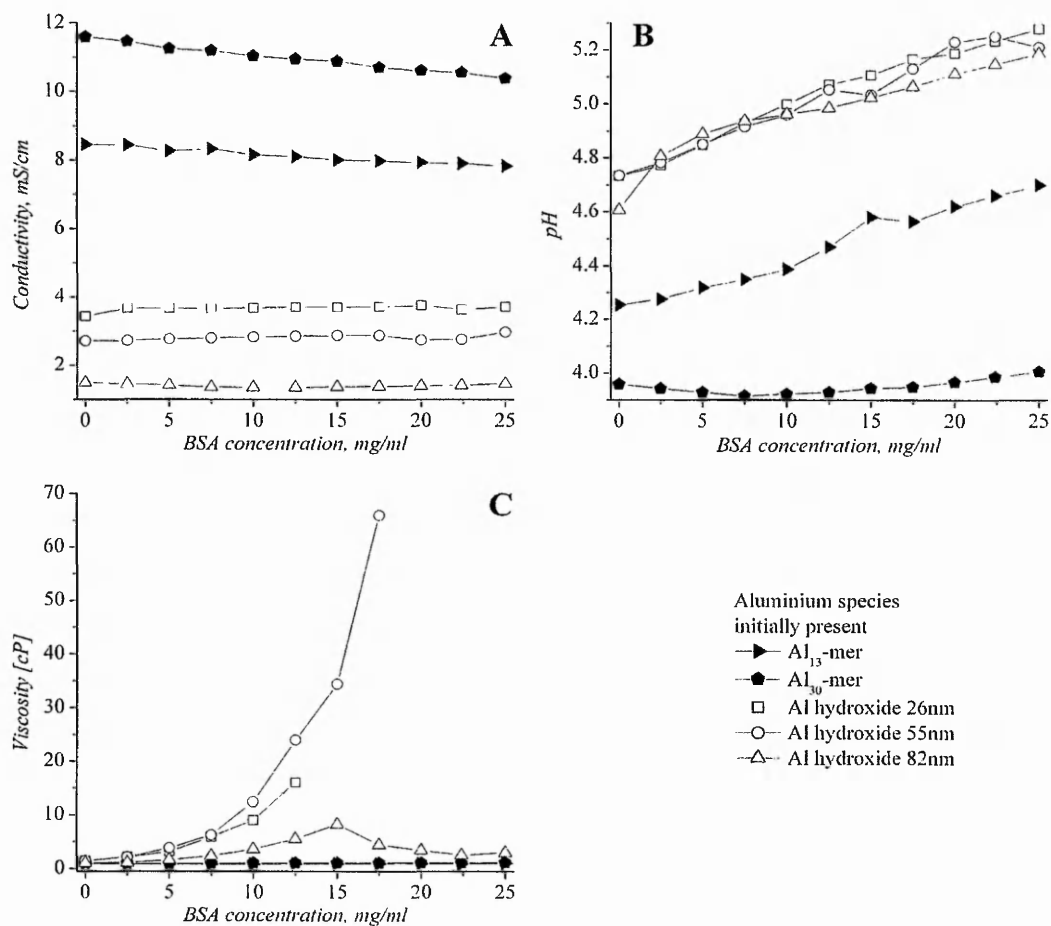


Fig. 10.1: Conductivity (A), pH (B) and viscosity (C) of Al species-BSA samples prepared with various BSA concentrations.

pH of the Al₃₀-BSA samples decreases slightly when BSA concentration increases from 0.0 to 7.5 mg/ml, and then tends to increase for higher BSA concentrations. However, the overall pH change in the case of the Al₃₀-BSA systems does not exceed 0.1 units of pH, and the pH value never exceeded pH \approx 4.0. The initial pH of the Al hydroxide-BSA systems is systematically higher than that of the Al polycations and BSA, and continues to increase with increasing BSA concentration. There is no substantial difference between the values of pH for the Al-hydroxide-BSA solutions prepared from the three hydroxide sols. According to the data of Figure 10.1C, the initial viscosity of Al hydroxide without BSA is approximately the same as that of

pure water (0.98 ± 0.02 cP at 25 °C). The viscosity of the Al hydroxide-BSA mixtures increases exponentially with increasing BSA concentration up to 17.5 mg/ml of BSA in solution, reflecting the increasing gelation processes. The growth of viscosity is much steeper for the samples prepared from Al hydroxide particles with 26 and 55nm diameter. For these samples, the strong gel obtained inside the reaction vessels above a certain BSA concentration could not be transferred into the viscometer cell without damaging the gel structure and biasing viscosity readings. Therefore, no measurements of viscosity were made for the samples with BSA content above 12.5 mg/ml. Both Al polyoxocation-containing systems (Al₁₃-BSA and Al₃₀-BSA) showed no significant increase of viscosity whatever the BSA concentration, in drastic contrast to hydroxide-containing systems (Figure 10.1C), indicating little or no gelation for the systems in question.

10.1.2 Dynamic light scattering

DLS measurements were performed in order to follow particle size evolution in the model Al-BSA systems. The results of these measurements are presented in Figure 10.2 as a function of BSA concentration. The relative standard deviation of the particle size data presented in Figure 10.2 did not exceed $\approx 5\%$ for the Al₁₃-based systems; $\approx 3\%$ for the Al₃₀-based systems and $\approx 2\%$ for all Al hydroxide-based systems. In the case of samples prepared from the three different Al hydroxide sols, the measured particle sizes increase with increasing BSA concentration (Figure 10.2A). The relative slope of the inclining particle size curve as well as the largest particle size measured appears to be inversely related to the particle size of the initial Al hydroxide suspension. For the 26nm Al hydroxide sol, the particle size growth is most rapid and the largest particle size observed by DLS (≈ 1200 nm) is the highest. In contrast, the Al hydroxide system initially containing 82 nm particles shows the slowest growth of particle size with increasing BSA concentration, and the largest particle size is between 200 and 400nm at BSA concentrations of 22.5-25mg/ml (Figure 10.2A). Therefore, the propensity of Al hydroxide particles to aggregate in the presence of increasing concentrations of BSA, possibly acting as a coagulation agent [2], arises from the overall surface area of the suspension, which in turn de-

depends on particle size. In the case of the 82nm Al hydroxide sols, the evolution of

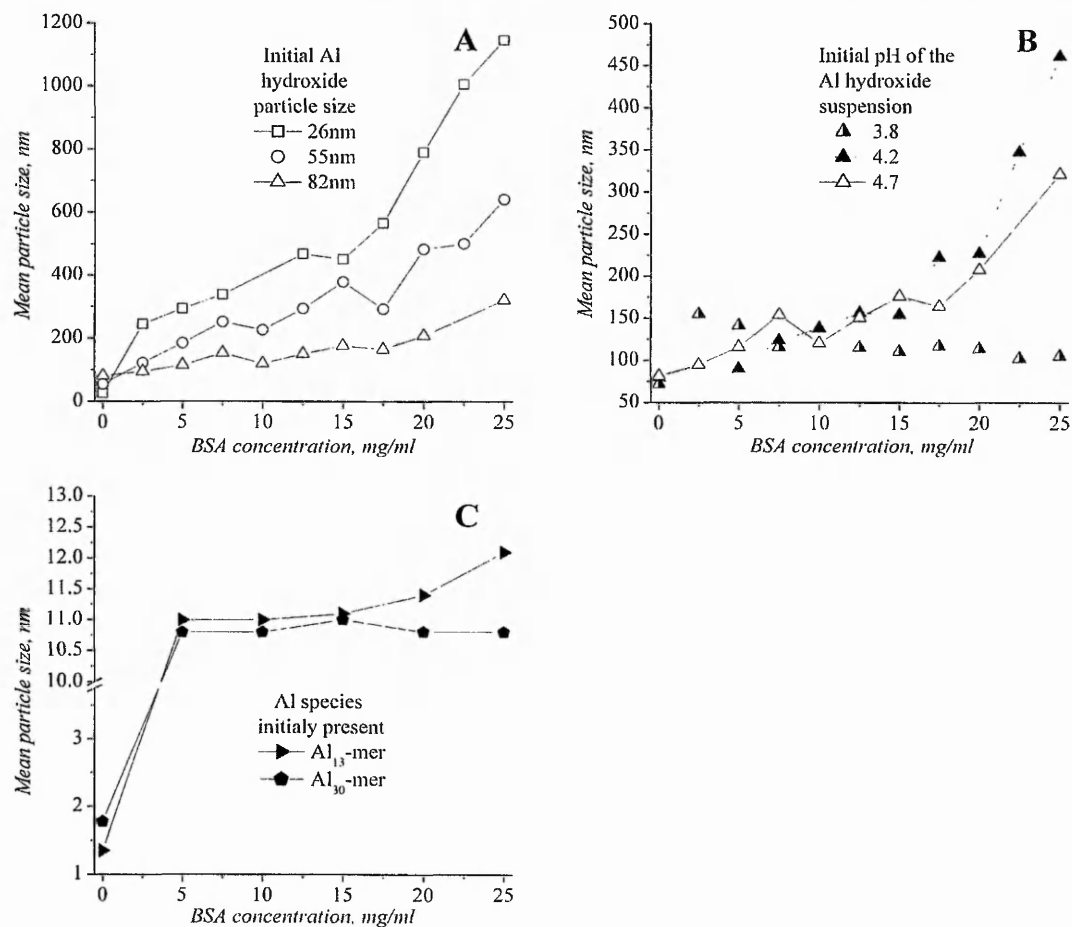


Fig. 10.2: Evolution of mean particle sizes of Al species-BSA samples as a function of BSA concentration measured by DLS at a scattering angle of 90° . (A) Al hydroxide-BSA samples with different Al hydroxide particle sizes, (B) Al hydroxide-BSA samples prepared from 82 nm Al hydroxide with adjusted pH; (C) Al₁₃-mer-BSA and Al₃₀-mer-BSA samples.

particle size with BSA concentration has been followed for three initial values of pH of the initial Al hydroxide sol (Figure 10.2B). At an initial pH of 3.8, the particle size varies over a relatively narrow range (100-150 nm) above a BSA concentration of 2.5 mg/ml and tends to decrease with increasing amounts of BSA. When the Al hydroxide sol was adjusted to a higher pH (4.2 or 4.7), the particle size increases with BSA concentration according to a pre-set value of the pH, especially at high BSA concen-

trations ($>15\text{mg/ml}$). The data of Figure 10.2B indicates that pH is an important parameter governing the aggregation-gelation process in the Al hydroxide-BSA systems. At $\text{pH} < 4.0$ these systems show only limited aggregation, while at higher pH the system is allowed to aggregate and thence to gel, especially in the presence of high BSA concentrations. As follows from Figure 10.2C, the particle size of the pure Al_{13} -mer and Al_{30} -mer solutions was found to be close to the actual sizes of these species (1 ± 0.3 and 2 ± 0.7 nm respectively [3]). Once BSA is added, the average particle size in all cases immediately increases to $\approx 10.75 \pm 0.5$ nm. For the Al_{13} -BSA samples the mean size of the suspension does not change profoundly with further increase of BSA concentration, while in the case of the Al_{30} -containing solutions the average particle size tends to increase at BSA concentrations above 17.5 mg/ml (Fig. 10.2C). The mean diameter of the BSA molecule alone was estimated to be $\approx 8\text{-}9$ nm from preliminary DLS measurements (the actual size of the BSA molecule is $4\text{nm} \times 4\text{nm} \times 14\text{nm}$ [4-6]). The larger mean particle size observed could arise from the formation of a few larger aggregates of BSA in the presence of highly charged Al species or from the absorption of Al polycations on the 'surface' of BSA molecule, which is negatively charged in mildly acidic conditions ($\text{pH} < 5.0$). The hypothesis above can be supported by zeta-potential measurements of the model systems in question (Figure 10.3). The value of the zeta-potential for Al polyoxocation-BSA systems is positive for the BSA concentration range considered and only a minute difference between Al_{13} - and Al_{30} -containing samples is observed (Figure 10.3A). Zeta potential measurements of pure Al_{13} and Al_{30} solutions failed, the size of polycations lying below the measurement range of the equipment used. Therefore, the values of ζ -potential measured arise from the presence of BSA molecules, which in pure solutions exhibit a negative potential ($\approx -8.6 \pm 0.08\text{mV}$). The observed charge reversal of BSA could only be explained by the adsorption of Al polyoxocations on the surface of the protein. With increasing concentration of BSA, the ratio of Al polyoxocations to protein falls constantly, resulting in a ζ -potential decrease (Fig. 10.3A). In the case of Al hydroxide, the value of the ζ -potential of all particles in the system is also positive, but more than two times higher than for the Al polyoxocation-BSA solutions at similar concentrations (Fig. 10.3B). The ζ -potential

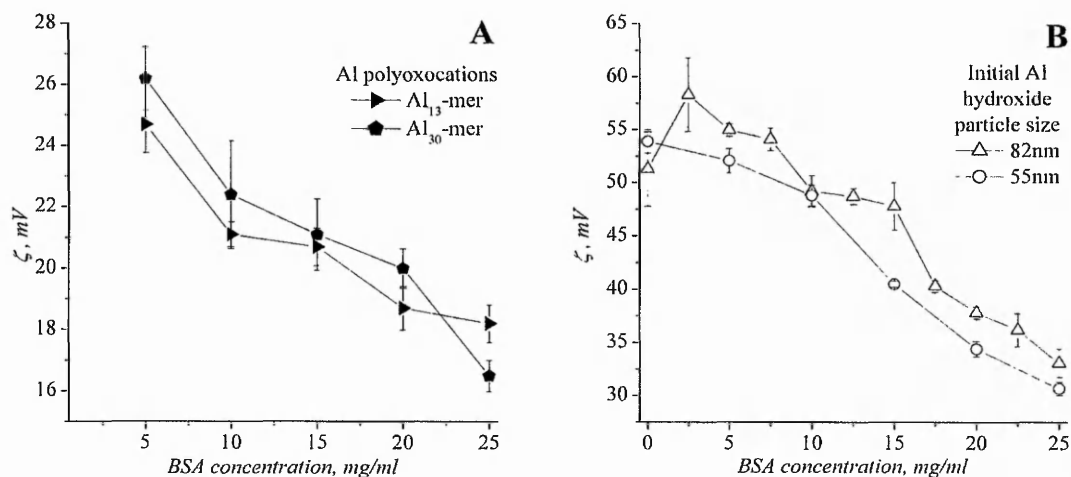


Fig. 10.3: Zeta potential measurements carried out on (A) Al polycations-BSA systems and (B) 82nm Al hydroxide-BSA.

of the Al hydroxide-BSA system also tends to drop with increasing amounts of BSA. This could be explained by the adsorption of negatively charged BSA molecules on highly charged particles of Al hydroxide with resulting charge cancellation.

10.1.3 Residual concentrations of BSA and aluminium ions

In order to clarify the extent of Al hydroxide-BSA composite formation after ageing of the samples, free supernatant concentrations of BSA and aluminium were measured as a function of BSA concentration after removal of the insoluble matter by centrifugation as described in the experimental section. The results are presented in Figure 10.4 for the samples prepared from Al hydroxide sols with varying particle sizes. The average measurement error did not exceed 12% for BSA and 9% for Al-ions. As follows from Figure 10.4A, the free BSA concentration in the supernatant of the Al hydroxide-BSA samples expressed as percentage of the total BSA concentration decreases with the increase of the total protein concentration for all three Al hydroxide suspensions. For the samples containing Al hydroxide with 26 nm particles, the 'free' BSA concentration is the lowest and decreases most rapidly to reach zero levels at $[BSA] > 15$ mg/ml. For the system containing 82nm Al hydroxide particles, there is possibly a decay of BSA concentration above a concentration of \approx

15 mg/ml. The system containing 55 nm Al hydroxide particles appears to follow an intermediate trend. 'Free' total aluminium concentration in the centrifugate solution continuously decreased with increasing total BSA concentration in the systems containing Al hydroxide (Figure 10.4B). This decrease was equally substantial for all three suspensions tested (from $\approx 100\%$ to $\approx 35\%$ of the total Al concentration which was 0.2 mol/L initially). The curves generally followed a sigmoidal trend indicating that association of BSA and Al hydroxide particles occurs in a 'titration-like' fashion. The trends discussed above probably arise from the formation of colloidal,

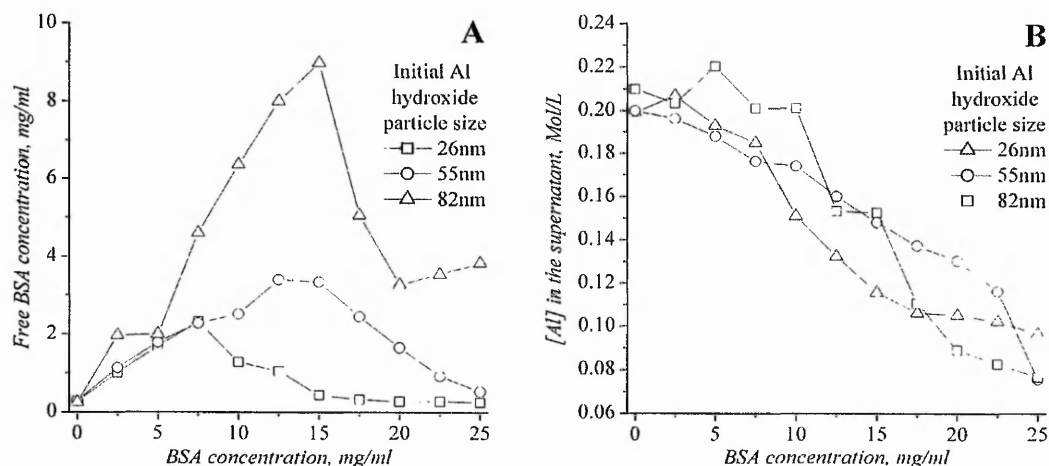


Fig. 10.4: Free BSA concentration (A) and aluminium ion concentration (B) in the supernatant solutions of the Al hydroxide-BSA samples after centrifugation.

self-assembled composites in BSA-Al hydroxide mixtures. The extent of the hybrid composite formation is indicated by the sedimentation of these particles by centrifugation and, consequently, lower 'free' concentrations of Al species and BSA in the supernatant. One can hypothesize that for low BSA concentrations, the particle size is probably below the sedimentation threshold set by the gentle centrifugation speed of 3000rpm, whereas for higher BSA amounts, the Al hydroxide-BSA 'conjugates' are quickly separated and the increase in total BSA produces a decrease in free aluminium concentration. This hypothesis is supported indirectly by the DLS data (Figure 10.2A) and viscosity measurements (Figure 10.1C) which show the particle size and the viscosity in the Al hydroxide-BSA systems increasing with increasing

total BSA concentration.

10.1.4 Re-dissolution experiments and ^{27}Al solution NMR

The results described above were concerned with the solution characterization of the obtained Al-BSA model systems. In the case of the Al polycation-BSA systems, a fraction of these solutions was freeze-dried to obtain solid products. Freeze-drying was chosen as a suitable method for quenching all reactions in solution and the gentle, non-destructive transformation of solution species into solid state species. For Al hydroxide-BSA systems, the part sedimented by centrifugation was subjected to freeze-drying. As has been shown by measurement of the residual Al and BSA concentrations (Figure 10.4), a large part of the protein and Al hydroxide was in the insoluble phase (centrifuged out). In the case of Al polycations-BSA mixtures, there was no significant phase separation after centrifugation. Therefore, a part of native solution was freeze-dried and analyzed in the solid state. For the Al hydroxide-BSA systems, no measurable amounts of soluble Al species were detected by ^{27}Al NMR spectroscopy (data not presented). In contrast, all samples prepared from Al polycations and BSA were soluble. The first step of analysis of the freeze-dried samples was to re-disperse them in pure water, to identify and measure amounts of individual Al species in re-dissolved samples. Such analysis has been carried out using quantitative ^{27}Al solution NMR spectroscopy according to the procedure developed earlier [1, 3, 7]. The NMR spectra of all of the Al polycation-BSA systems before and after the freeze-drying/re-dissolution procedure were acquired. The spectra of the initial Al polycation-BSA samples (before freeze-drying) are presented in Figure 10.5, as an illustrative example. Re-dissolution was carried out with accurately weighed amounts of solid materials in a fixed volume of distilled, deionized water (normally, 1 or 2ml). ^{27}Al NMR spectra acquired from the Al_{13} -mer-BSA solutions show peaks at $\approx 63\text{ppm}$ (tetrahedral core of the Al_{13} -mer) and $\approx 0\text{ppm}$ (octahedral signal of Al monomers) along with a signal at 80ppm arising from aluminate-ions of the internal reference solution [8], Figure 10.5A. In the spectra of the Al_{30} -mer-BSA systems (Figure 10.5B), along with the signals at $\approx 63\text{ppm}$ and $\approx 0\text{ppm}$, a broad signal at 70ppm is observed, which corresponds to the tetrahedral 'core' Al atoms

of the Al₃₀-mer [9]. The width of the peak at 70ppm arises from the conditions at which ²⁷Al NMR spectra were acquired, the 25°C temperature used leading to considerable quadrupolar line broadening. However the position and attribution of the peak was verified using variable temperature NMR, which may cause denaturation of the protein but which enabled confirmation of the spectral features. On

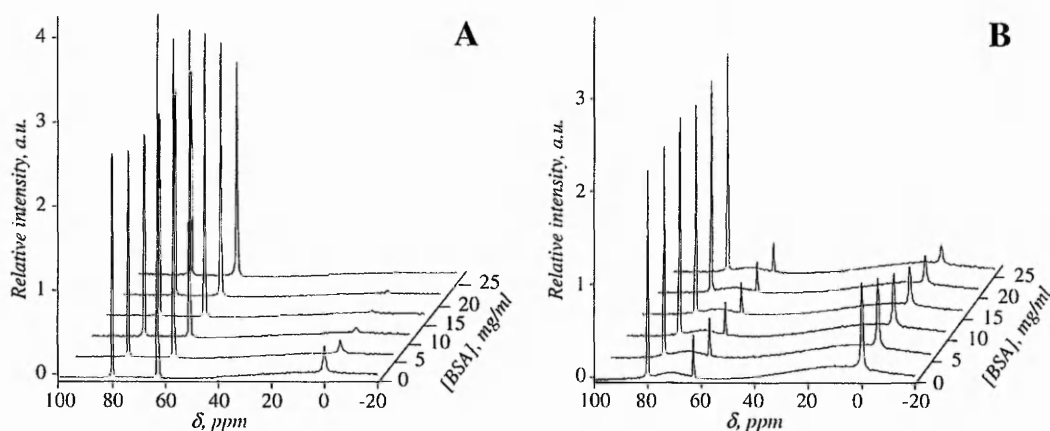


Fig. 10.5: ²⁷Al solution NMR spectra of the Al₁₃-mer-BSA (A) and Al₃₀-mer-BSA (B) samples as a function of total BSA concentration. T=25°C. The peak at 80ppm arises from internal reference solution of aluminate-ions in D₂O.

the basis of the ²⁷Al NMR spectra of the Al polycation-BSA samples before and after freeze-drying/ re-dissolution Al speciation diagrams were calculated using an algorithm described previously [1, 3]. The diagrams, which include Al monomers, Al₁₃-mers, Al₃₀-mers and Al hydroxide, are presented in Figure 10.6. The amount of Al hydroxide, normally undetectable by means of ²⁷Al solution NMR, was estimated indirectly as the difference between the total Al content (either in solution or in the solid state, depending on the experiment) and the sum of the fractions of all soluble species (Al monomers, Al₁₃-mers and Al₃₀-mers). Further investigation will need to be carried out using solid state NMR or another characterisation technique in order to attribute more precisely the undetectable fraction assigned to Al-hydroxide. Indeed, the binding of polycations to a protein might produce a broadening of ²⁷Al NMR peaks resulting in an apparent decrease of the polycation concentration. The concentration of small Al oligomers (e.g. Al dimers or trimers)

was not taken into account in the present study due to the very low concentration of these species, as indicated by the absence of the associated broad peak at ≈ 2 -4ppm or its strong overlap with larger peaks at ≈ 0 and ≈ 10 ppm (cf. Figure 10.5). The immediate conclusion following from the data of Figure 10.6 is that generally there is a good correlation between all measured species in the samples before and after the freeze-drying/re-dissolution procedure. Therefore, such a procedure does not significantly disturb the distribution of soluble species in the Al polycation-BSA samples. The concentration of the major species, the Al_{13} -mer in the initial Al_{13} -mer-BSA samples before and after freeze-drying/re-dissolution decreases from ≈ 98 -99% to $\approx 90\%$ upon increasing BSA from 0 to 25mg/ml. This decrease is correlated with a decline of Al monomer concentration (from $\approx 2\%$ to $\approx 0.2\%$) and anti-correlated with the increase of insoluble matter (from $\approx 0\%$ to $\approx 12\%$), probably due to an increase of solution pH (Figure 10.1B). However, these hydroxide particles do not aggregate strongly due to the presence of BSA in solution, as supported indirectly by the constant viscosity of the samples with various BSA concentrations (Figure 10.1C). The data of Figure 10.6B indicates that in the case of the Al_{30} -mer-BSA

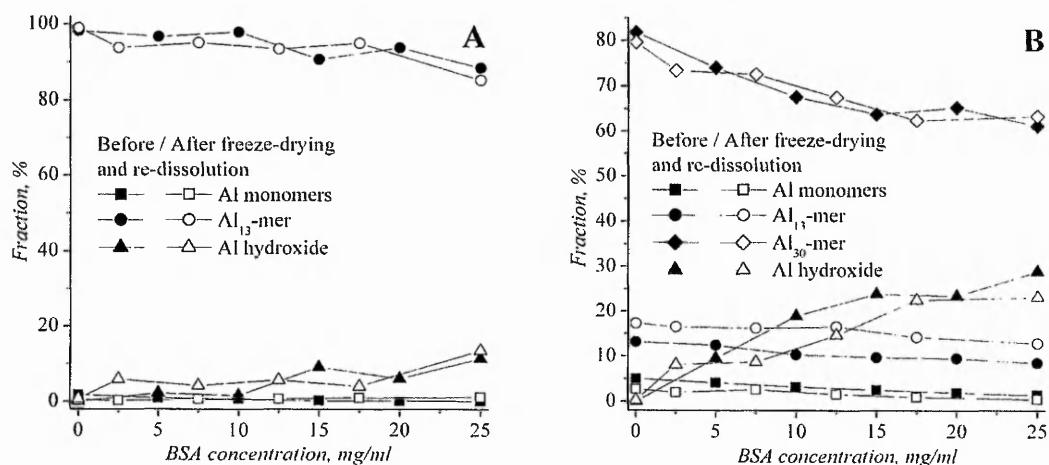


Fig. 10.6: Quantification of the ^{27}Al solution NMR spectra of the Al_{13} -mer-BSA (A) and Al_{30} -mer-BSA (B) samples as a function of total BSA concentration. $T=25^\circ\text{C}$.

systems, there is a strong effect of increasing BSA concentration on the initial and freeze-dried samples. The concentration of the major species (Al_{30} -mers) decreases

from ≈ 80 - 86% to ≈ 62 - 65% upon increase of BSA concentration. A similar trend, but to a lesser extent, is observed for the minor quantities of the Al_{13} -mer and Al monomers. The general trends observed for the fractions of soluble species detected in the Al_{30} -mer-BSA (Figure 10.6B) samples do not correlate with the corresponding pH trends in Figure 10.1B. The apparent contradiction is probably due to the stronger acidity of the Al_{30} -mer or higher concentration of Al monomers in the Al_{30} -mer-containing solution, compared to the Al_{13} -mer samples. Higher acidity makes the Al_{30} -mer solution more sensitive to BSA additions, and it would require higher BSA concentrations or a base stronger than BSA in order to increase the pH substantially.

10.1.5 TGA measurements

As mentioned above, the model systems containing pure Al hydroxide and BSA could not be investigated directly using re-dissolution experiments and ^{27}Al solution NMR. Therefore, solid-state techniques such as X-ray diffraction, thermogravimetry and SEM were employed in order to shed light on the speciation of these systems. The result of thermogravimetric analysis of the solid samples of Al hydroxide (26nm)-BSA model systems with various BSA content prepared by freeze-drying of the respective solutions are presented in Figure 10.7 and Table 10.1.

The original TGA data was normalized to the final 'dry' weight of the samples, Figure 10.7A. It varied in a systematic fashion with increasing BSA concentration. The data were smoothed using an FFT algorithm (Origin 6.1 software) and the first derivative (DTG) curves were calculated (Figure 10.7B). The DTG curves revealed several peaks with the maxima indicated in the legend, which were fitted using Gaussian functions in ThermoGalactic Grams/32 software as shown in the illustrative example in Figure 10.7C. The position of the maxima of the fitted DTG peaks at 49 ± 4 , 157 ± 20 , 239 ± 12 and 354 ± 33 , 459 ± 63 , and $604 \pm 87^\circ\text{C}$ remained relatively constant, i.e. within 10-15%, with increasing BSA in the initial samples. Following the treatment of the TGA data described above, a semi-quantitative analysis of the peak areas of the DTG profiles was performed. As can be noticed from Table 10.1, areas of the DTG peaks at 49, 157 and 239°C tended to increase with increasing BSA

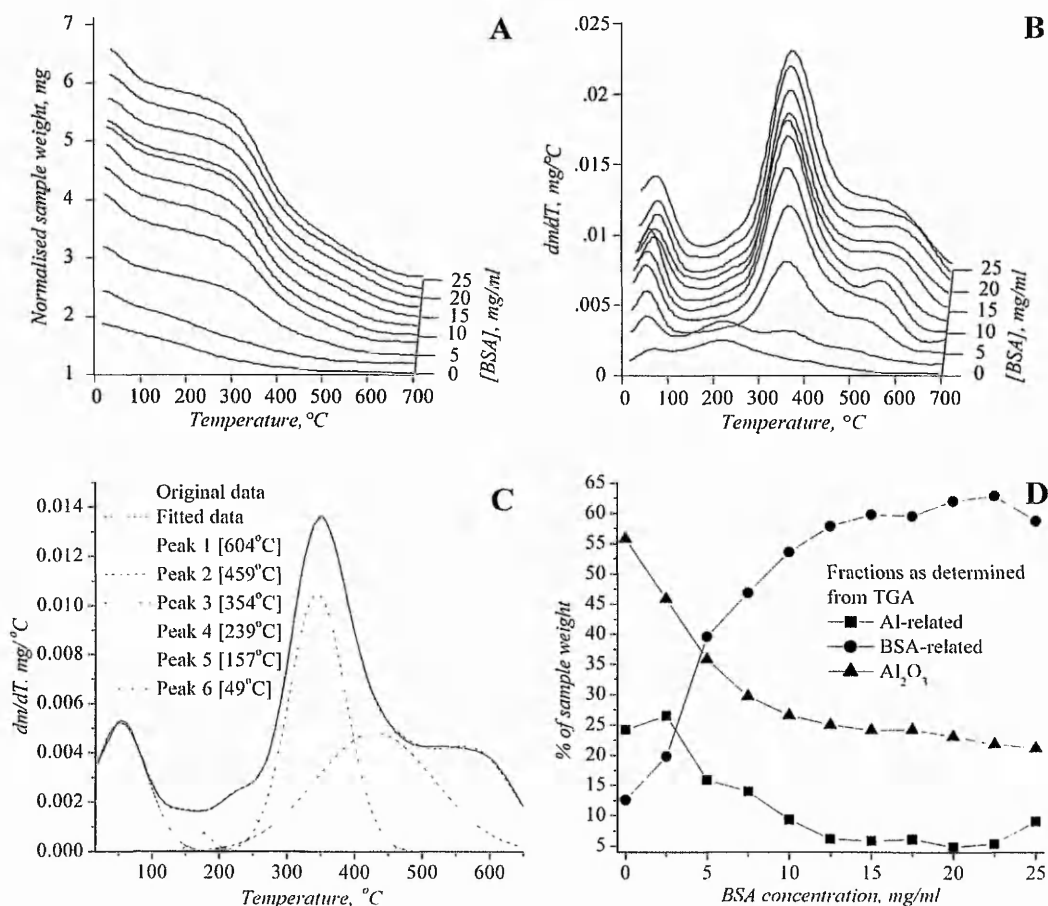


Fig. 10.7: Thermogravimetric 'weight loss' curves (A)(normalised against final weight), the first derivative thermogravimetric (DTG) curves (B), an example of the peak fitting used for semi-quantitative analysis of the DTG curves (C), and DTG peak areas as a function of BSA concentration (D).

content of the samples, which suggests their association with the thermal degradation of BSA. The other three peaks showed a different trend and, therefore, can be preliminarily attributed to the inorganic component of the analyzed composites (Al hydroxide). By summing the areas of the DTG peaks proposed to have arisen from BSA and from Al hydroxide it was possible to reconstruct the trends observed for the bioorganic and inorganic components of the composites, as shown in Figure 10.7D. The Al-related DTG trend associated with Al hydroxide correlates quite well with the mass fraction of the dry residue which is most probably pure Al₂O₃. The

Tab. 10.1: Evolution of weight loss fractions corresponding to the detected weight loss peaks and residual fraction after heat treatment (expressed as percentages of total sample weight) as a function of the initial BSA content of the sample.

BSA, mg/ml	49°C	157°C	239°C	354°C	459°C	604°C	residue
0	2.1	12.7	0.3	0.6	19.6	9.2	55.4
2.5	5.9	12.9	1	2.1	21.5	11.4	45.2
5	5.9	33.5	2.7	2.1	6.1	11	35.3
7.5	9.7	35.8	5.4	2.3	7.4	11.1	28.3
10	10.3	36.6	7.8	1	7.1	11.2	25.9
12.5	12.5	37.8	7	2.6	4.2	11.5	24.4
15	15.8	36.4	8	2	3.9	10.3	23.5
17.5	16.7	35.6	8	1.9	4	10.1	23.7
20	17.9	35.5	8.9	1.5	3.8	9.9	22.5
22.5	16.6	37.1	9.8	1.8	3.5	9.9	21.4
25	14.2	39.3	9.4	1.1	4.1	11.6	20.4

sum of BSA-related DTG peaks shows an opposite trend to that of the inorganic component (Figure 10.7D) which, in turn, is in good agreement with the data on the concentration of BSA and Al in solution after centrifugation (Figure 10.4).

10.1.6 Results of powder X-ray diffraction

Selected samples of the Al-BSA systems containing various Al species and different amounts of BSA were analysed using X-ray diffraction (Figure 10.8). XRD patterns of the Al₁₃-mer-BSA system (25mg/ml of BSA) shown in Figure 10.8 contains an intense peak composite peak at ≈ 9.6 degrees 2θ and several other very broad features which possibly indicate the presence of a crystalline phase with extremely small crystallite size. We have compared the diffractograms (a) and (b) in Figure 10.8 with the PXRD data available for the Al₁₃-mer sulfate salt [10] and our own PXRD measurements of the Al₁₃-mer chloride salt [7]. However, there was no complete match with any of these patterns. Therefore, the exact identification of the crystalline

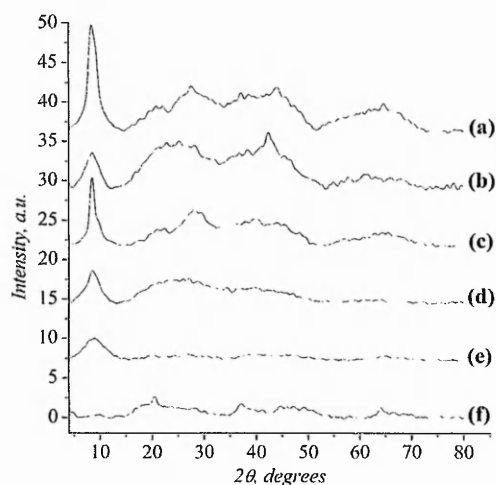


Fig. 10.8: XRD patterns obtained from the Al-BSA materials prepared. (a) Al_{13} -BSA 0 mg/ml; (b) Al_{13} -BSA 25 mg/ml; (c) Al_{30} -BSA 0 mg/ml; (d) Al_{30} -BSA 25 mg/ml; (e) Al hydroxide ($d \approx 26$ nm)-BSA 0 mg/ml; (f) Al hydroxide ($d \approx 26$ nm)-BSA 25 mg/ml.

phase was not possible in this case. Perhaps the presence of high amounts of BSA completely prevents crystallization of the Al_{13} -mer chloride, although the crystallite size in this case is likely to be much lower than for the pure freeze-dried Al_{13} -mer solution [7]. For the Al_{30} -mer containing samples (Figure 10.8), high amounts of BSA apparently prevent crystallization of the Al_{30} -mer in the chloride form, as follows from comparison of the PXRD patterns of pure (c) and BSA-containing (d) freeze-dried samples. On the basis of the re-dissolution experiments and ^{27}Al NMR measurements described above (Figure 10.6B) we assume that the Al_{30} -mer phase in Figure 10.8(c) may be partially crystalline with extremely small crystallite size, close to the dimensions of the Al_{30} itself. However, further structural characterization of the solid material is necessary for more conclusive assignments. PXRD patterns acquired for the systems containing Al hydroxide (≈ 26 nm) indicate that the samples are predominantly X-ray amorphous, whatever the amount of BSA, Figure 10.8(e) and (f).

10.1.7 SEM observations

The solid products obtained by freeze-drying of various Al species-BSA samples were subjected to SEM analysis. When observed by SEM, the pure 82nm hydroxide-based samples without BSA revealed morphology characterized by sheets covered with equally spaced parallel ribbons (Figure 10.9). At increasing BSA concentration, the ribbons disappear and the sheets become increasingly disorganized. For the highest BSA concentrations, the sample consists only of disorganized flakes and small sheets. For the samples obtained from 26nm Al hydroxide and BSA, a sim-

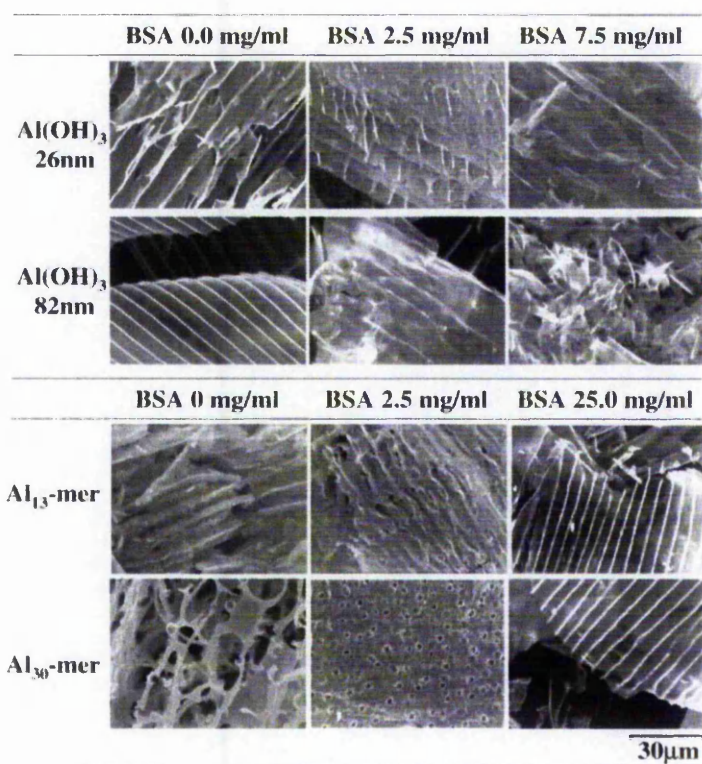


Fig. 10.9: SEM pictures of Al-BSA hybrid materials prepared by freeze-drying from Al hydroxide and Al polycations with various BSA amounts.

ilar observation can be made (Figure 10.9). However, the sheets obtained from pure 26nm Al hydroxide are more disorganized in comparison with the ones prepared from larger particles, and the spacing between the nano-ribbons is larger. For the lowest BSA concentrations, a stacking of the sheets is observed, the spacing

of the ribbons becoming more chaotic. Finally, at the largest BSA concentration used, the sheets are much smaller and completely disorganized. Summarizing the SEM observations of the morphology of Al hydroxide-BSA systems, the effect of hydroxide particle size is important. With increasing particle size of Al hydroxide, the nano-ribbon morphology gets sharper and more ordered (at least in the two dimensions of the sheets). In the case of pure Al₁₃-mer, the freeze-dried material is largely disorganized on the micrometer level, although relatively thick (30-60nm wide) ribbons can be observed by SEM (Figure 10.9). Upon BSA addition, the samples containing Al₁₃-mers change progressively until finally they exhibit the same morphology as for pure hydroxide-based materials. A similar picture is observed for the Al₃₀-mer-based materials. Freeze-drying of pure Al₃₀-mer solutions leads to a mixed fibrous and sheet-like structure which progressively disappears at higher BSA concentrations. An increasing amount of large stacked sheets comprising 3-5nm diameter holes is then observed. As BSA concentration increases, sheets with ribbons similar to those observed for pure hydroxide samples dominate. SEM observations made on samples prepared from Al polycations support the idea that increases in BSA concentration leads to partial transformation of polycations into aluminium hydroxide. The fact that the Al₁₃ and Al₃₀-based materials obtained by freeze-drying were soluble in water over the whole BSA concentration range could be explained by either the relatively small fraction, or the extremely fine size of the Al hydroxide particles formed in both cases, especially in the Al₃₀-mer-based systems, as detected indirectly by the characteristic nano-ribbons in SEM images. The reason for the 'nano-ribbon - sheet' morphology of Al hydroxide-containing samples is not clear. This morphology could arise either from the freeze-drying procedure itself or from the preferential packing of Al hydroxide particles into symmetrically located two-dimensional structures. Further morphological and spatial chemical analysis is required in order to explain this phenomenon. Nevertheless, whatever the origin of the nano-ribbon morphology, it remains a good 'fingerprint' of the presence of significant amounts of Al hydroxide.

10.2 Al-Elastin systems

10.2.1 Physical properties and pH of the Al-Elastin solutions

Conductivity, pH and viscosity measurements of the samples prepared from Al species and elastin were carried out as described above for Al-BSA samples. As follows from Figure 10.10A, initial conductivities are similar for the pure aluminium polycation solutions (≈ 8.8 mS/cm), but much lower for the pure Al hydroxide suspension (1.05mS/cm). With increasing elastin concentration, solution conductivity decreases continuously for both Al polycations, while for samples prepared from 70nm Al hydroxide an initial increase (0.1mS/cm) for the smallest elastin addition was observed followed by a steady decrease back to the initial value measured for Al hydroxide alone (Figure 10.10A). The Al₁₃ and Al₃₀ based solutions shows similar initial pH value but upon increases in protein concentration split (Figure 10.10B), the pH of Al₁₃-based solutions increased very slightly, whereas it decreased (0.18pH units) following an exponential decay (first 10mg/ml added) for the Al₃₀-elastin systems. The pH of the Al hydroxide-elastin mixtures is lower than for polycation-based solutions and pH decreases following a trend similar to the pH evolution observed for Al₃₀-elastin systems. It should be noted that the pH of the solutions remains in the domain of stability for Al polynuclear species, opposite to the behavior observed earlier for experiments performed in the presence of BSA, causing differences in speciation between Al-BSA and Al-Elastin systems. The initial viscosity of pure Al species solutions is again approximately close to that of pure water (10.10C). The viscosity of the Al hydroxide-Elastin mixtures increases steadily up to additions of 10mg/ml of elastin in solution, but not as dramatically as for Al-BSA systems, reflecting an increase in inter-particle interactions probably arising from cancelation of repulsive forces stabilising the hydroxide dispersion. In both Al polyoxocation-containing systems, viscosity follows a peculiar and similar trend including a decrease for the first 5mg/ml of protein added followed by a steady and moderate increase for higher concentrations (Figure 10.10C), hallmark of the existence of complex interaction phenomena between both parts of the systems.

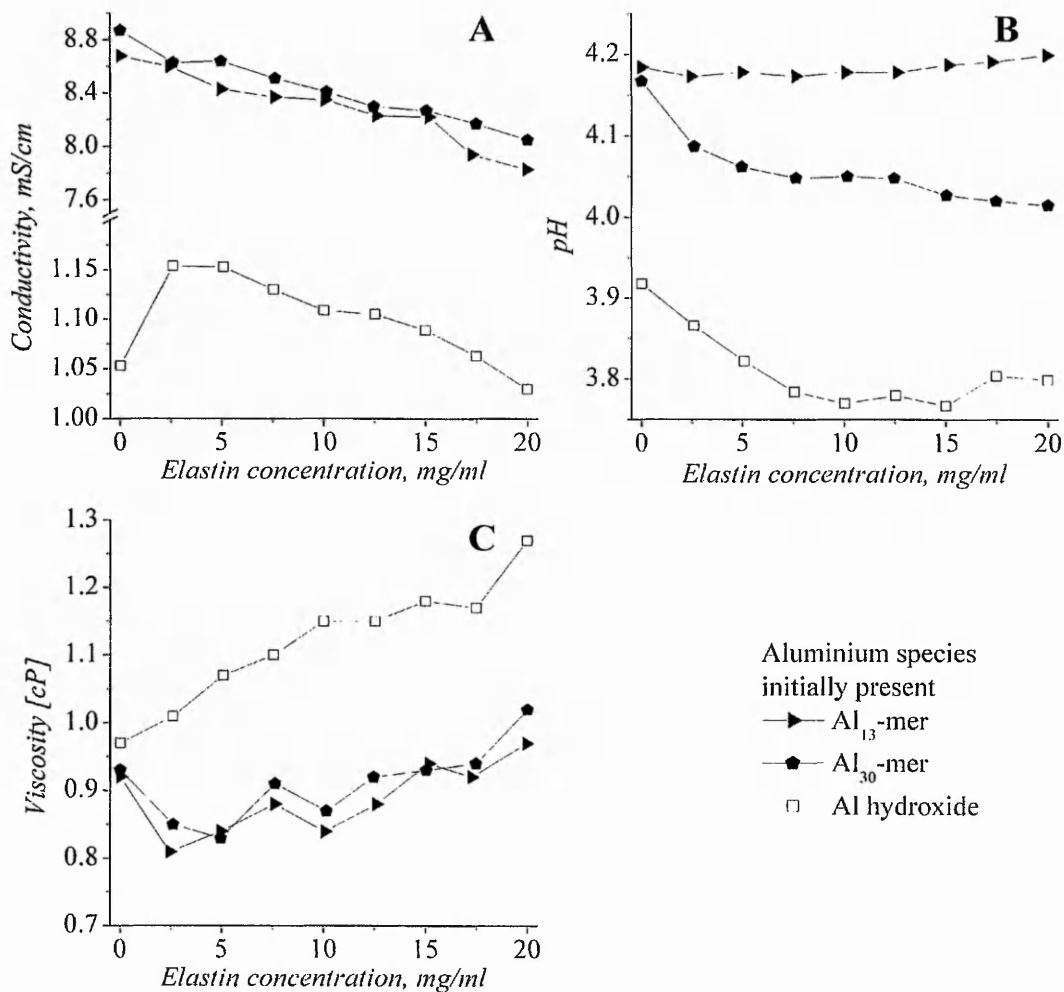


Fig. 10.10: Physical Measurements carried out on the Al-Elastin systems.

10.2.2 Dynamic light scattering

The results of these measurements are presented in Figure 10.11 as a function of elastin concentration. As previously described, the sols were diluted before measurement, in order to eliminate the effect of viscosity variations. In all systems the measured particle size increases for low protein concentration, to stabilise to a value around 100nm in Al hydroxide or Al₃₀-Elastin and 125nm in Al₁₃-Elastin mixtures (Figure 10.11), whereas the average particle size measured in a pure 10mg/ml elastin solution is 25nm. In polycation-based systems this increase is especially sharp as was observed during Al-BSA experiments, and the size of the particles reaches a maxi-

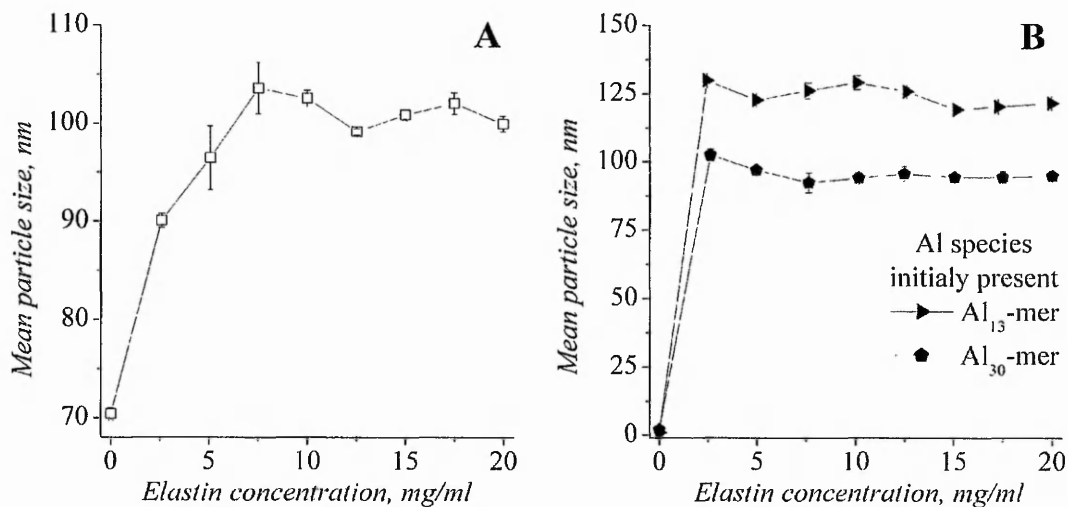


Fig. 10.11: Evolution of average particle size as a function of Elastin concentration in the systems: (a) In the presence of Al hydroxide, (b) In the presence of Al polycations.

imum for the lowest elastin concentration. The initial size of polycations estimated from DLS has been taken from Al-BSA experiments results, obtained using a more sensitive instrument. The mean particle size of the initial hydroxide suspension was estimated to be 70nm, and stabilised near 100nm for elastin concentrations higher than 7.5mg/ml (Figure 10.11A). This observation in Al hydroxide-Elastin systems is close to the one made in the case of BSA interactions with Al hydroxide sols of initial pH 3.8 and initial particle size 82nm. These observations in Al polycation- and Al hydroxide-Elastin might again be caused by the formation of a few larger elastin aggregates in the presence of Al species, or by the formation of Al species-elastin assemblies based on electrostatic interactions. The particle sizes observed in the case of polycation-elastin system however suggests more an assembly of elastin fragments linked or not by polycations rather than the formation of a coating by polycations as formulated in the case of experiments performed with BSA. The size difference observed between Al₁₃-elastin and Al₃₀-elastin still requires explanation.

10.2.3 Residual concentrations of elastin and aluminium after centrifugation

In order to determine the amount of elastin and Al present in the $\approx 100\text{nm}$ particles formed in the mixtures prepared, free supernatant concentrations of elastin and aluminium were measured as a function of total elastin concentration after removal of the higher particle size fraction by centrifugation. In this case both Al hydroxide- and Al polycation-elastin systems led to particles separable from the initial species by centrifugation. A 13000rpm centrifugation was applied for 30min to all systems after which Al and elastin concentrations were determined in the supernatant respectively by means of ICP and a Bradford assay, whereas the solid centrifuged was washed with distilled water and re-centrifuged prior to freeze drying for solid state characterisation. The results of residual concentrations measurements are presented in Figure 10.12 for the samples prepared from the different Al model systems. As follows from Figure 10.12A, the free elastin concentration in the supernatant of the Al-elastin samples increases with the increase of the total protein concentration for all three systems. Free elastin detected is lower in Al₁₃-mer than in Al₃₀-mer based systems for the whole concentration range studied, the concentrations measured in the two cases becoming closer as total elastin concentration is raised. For equal initial elastin concentrations, the amount of protein detected after centrifugation of Al hydroxide-based systems is systematically lower, probably due to the larger size of Al hydroxide, leading to a more extensive sedimentation of Al hydroxide-elastin than Al polycation-elastin assemblies. Indeed the residual Al concentration measurements provide evidence that most of the pure Al hydroxide can be separated by the 30min 13000rpm treatment, this separation remaining largely effective in the presence of protein additions (Figure 10.12B), except for a slight decrease for the first 2.5mg/ml added. This observation, in contradiction with the increasing mean particle size in the system, may be explained by the simultaneous increase in viscosity of the sample that would lead to slower sedimentation. In the case of Al polycation systems, the amount of Al₁₃- and Al₃₀-mer separated are low over the whole range of protein concentration studied, which means that a large number of small particles are still present in the systems, and the particle size observed by DLS is only an average between these small entities and larger aggregates which, sepa-

rated by centrifugation, will be characterised in the solid state. As for the Al-BSA

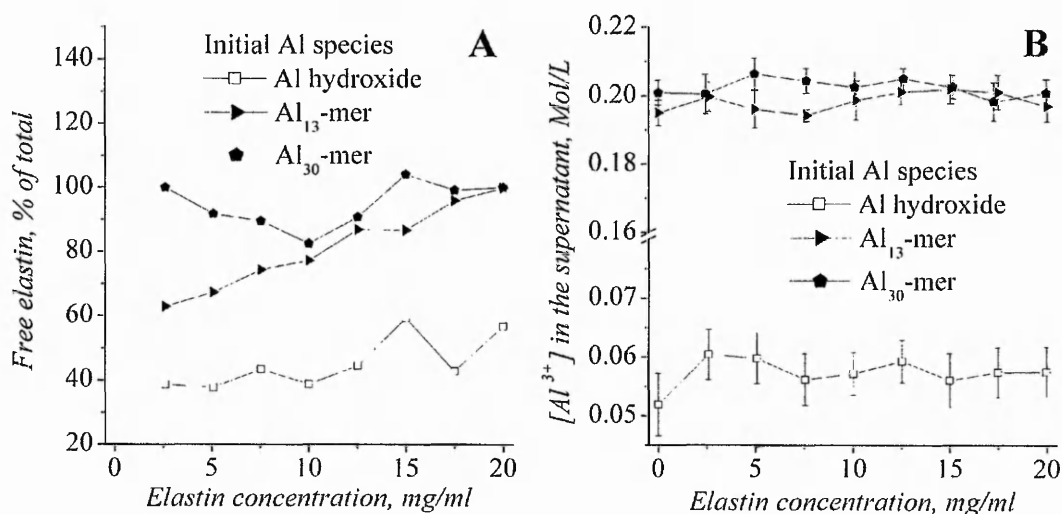


Fig. 10.12: Residual concentrations observed in the supernatant of samples centrifuged at 13000rpm for 30 min as a function of total elastin concentration (A) Elastin concentration as a percentage of elastin added, measured by a Bradford assay (B) Al concentrations measured by means of ICP.

systems, The trends observed in the evolution of free elastin concentration arise from the formation of colloidal, self-assembled composites in Elastin-Al species mixtures, which can also be observed from DLS measurements.

10.2.4 ²⁷Al solution NMR

During the previous sections as well as other works, freeze-drying has been shown to be a reliable method for the quenching of solution processes and the transfer of solution speciation to the solid state without alteration. In the case of Al-elastin systems the redissolution of freeze-dried samples has not been so far carried out, and ²⁷Al NMR characterisation of the mixtures has only been applied on the initial solutions. The composition of the solid samples will therefore be trusted to be preserved from the liquid state until further work can be accomplished. The spectra of the initial Al polycation-elastin samples (before centrifugation) are presented in Figure 10.13. Again the peaks attributed to the tetrahedral cores of the Al₁₃- and Al₃₀-mers),

together with the signal of Al monomers in octahedral configuration and the signal of aluminate-ions contained in the internal reference solution [8] are observed in the Al polycations-elastin sample spectra. The speciation diagrams obtained from local

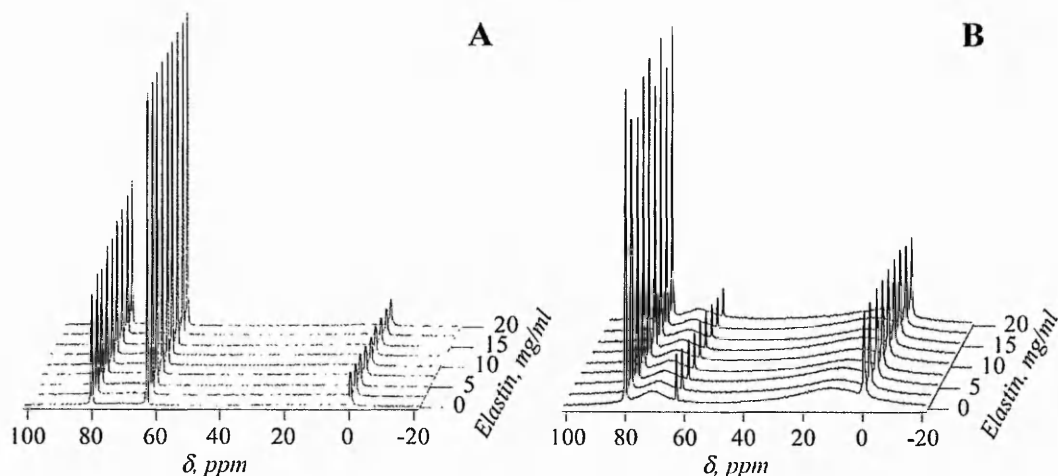


Fig. 10.13: ^{27}Al NMR spectra of (A) Al_{13} -elastin and (B) Al_{30} -elastin samples at 25°C .

integration of the spectra presented above are presented in Figure 10.14. The poly-

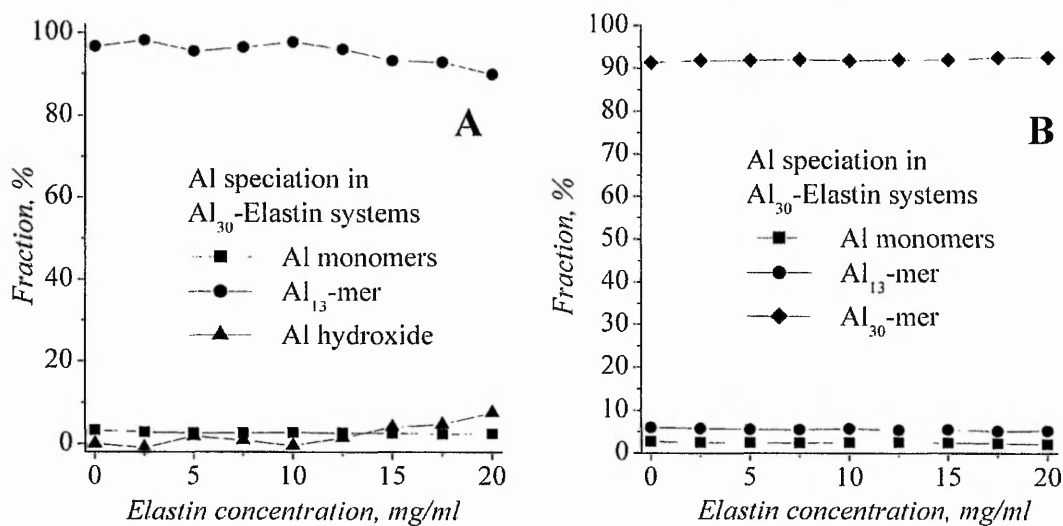


Fig. 10.14: Al speciation determined by local integration of the ^{27}Al NMR spectra of A Al_{13} -elastin and B Al_{30} -elastin samples.

cationic and monomeric species concentration appears to be much less affected by

the increase of the elastin content than upon BSA addition. The concentration of the Al_{13} -mer in the initial Al_{13} -mer-elastin samples decreases slightly from $\approx 95\%$ to $\approx 90\%$ upon increasing Elastin concentration from 0 to 20mg/ml (Figure 10.14A). The effect of the protein on speciation is even less marked in the case of Al_{30} -elastin systems as the Al_{30} -mer concentration remains practically unaffected in the protein concentration range studied (Figure 10.14B). These observations are verified by the low pH variation monitored upon increase of the protein content of the solutions. We indeed noticed earlier that the solution pH remained within the domain of stability of Al polycations, which was not the case for Al-BSA systems. the continuity in Al speciation observed could be therefore expected

10.2.5 SEM observations

The solid products obtained by freeze-drying or classical drying of various Al-elastin samples as well as pure freeze-dried elastin were subjected to SEM analysis. When observed by SEM, the pure hydroxide sample prepared by centrifugation followed by freeze-drying revealed a ribbon morphology (Figure 10.15) instead of the sheets covered by ribbons observed in Al-BSA samples. This difference is probably due to the faster centrifugation treatment applied during the Al-elastin interaction experiments, which causes the disturbance of colloids within the solution. Indeed a sheet morphology is observed when solutions are not subjected to centrifugation (Figure 10.15C). Images of the freeze-dried solids obtained both before and after centrifugation for each system will be therefore presented in the next developments. At increasing elastin concentration, small sheets progressively appear in the general morphology of the centrifuged samples (Figure 10.17A), larger sheets apparently coated by elastin filaments being observed without centrifugation (Figure 10.17B). The morphology of elastin, which generally consists of small interconnected filaments (Figure 10.16), is not observed in the centrifuged samples despite the presence of an increasing amount of carbon as detected by elemental mapping of the observed samples and the indirect evidence of the presence of elastin in the solid material arising from residual concentration measurements. The filaments observed in the non-centrifuged sample must therefore account for excess elastin coating composite

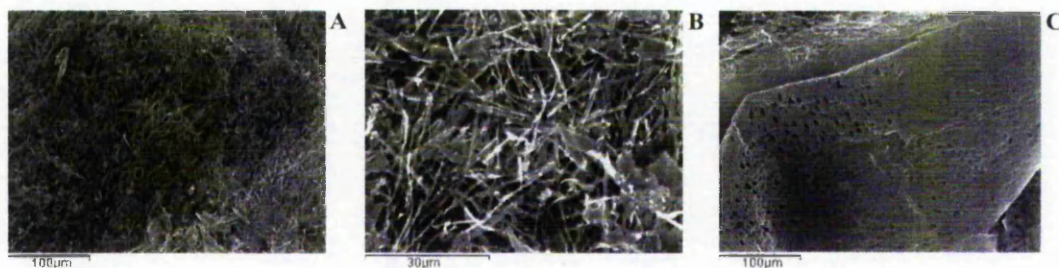


Fig. 10.15: SEM images of the freeze-dried pure Al hydroxide suspension (A-B) centrifuged at 13000rpm for 30min and (C) Without preliminary centrifugation.

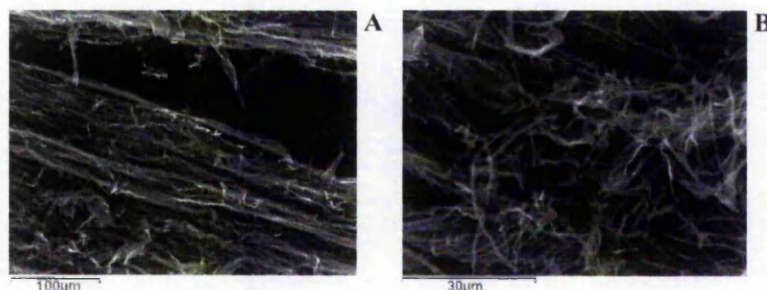


Fig. 10.16: SEM images of freeze-dried pure elastin solution.

sheets. In the case of pure Al₁₃-mer, the freeze-dried material is largely disorganized

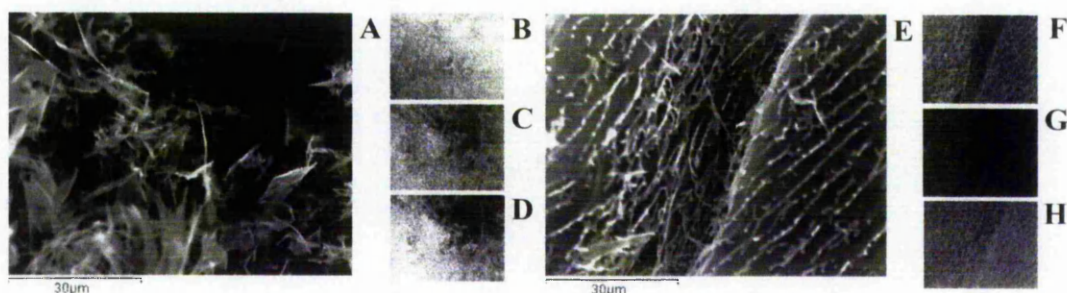


Fig. 10.17: SEM images of the freeze-dried Al hydroxide-elastin 20mg/ml sample (A) centrifuged at 13000rpm for 30min and (E) Without preliminary centrifugation; elemental mapping of the same regions using respectively (B-F) CK α_{1-2} , (C-G) OK α_1 and (D-H) AlK α_1 energies.

on the micrometer level, although relatively thick ribbons can be observed in the non-

centrifuged sample(Figure 10.18E). Upon elastin addition, an increasing number of

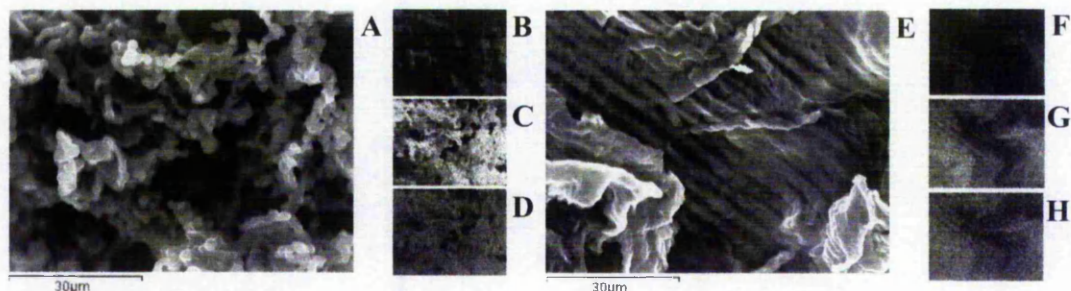


Fig. 10.18: SEM image of the freeze-dried pure Al₁₃-mer sample (A) centrifuged at 13000rpm for 30min and (E) Without preliminary centrifugation; elemental mapping of the same regions using respectively (B-F) OKα₁, (C-G) AlKα₁ and (D-H) ClKα₁ energies.

filaments characteristic of elastin appear in the centrifuged samples containing Al₁₃-mers, whereas the non centrifuged samples change progressively until they exhibit the same 'nano-ribbon' morphology as observed in the case of Al polycations-BSA materials, close to the pure hydroxide morphology (Figure 10.19a). Elemental mapping enables one to demonstrate that the filaments are not only formed of elastin but that a measurable amount of Al-based material is associated with these structures(Figure 10.19B, C, D). Complementary TEM characterisation will be required

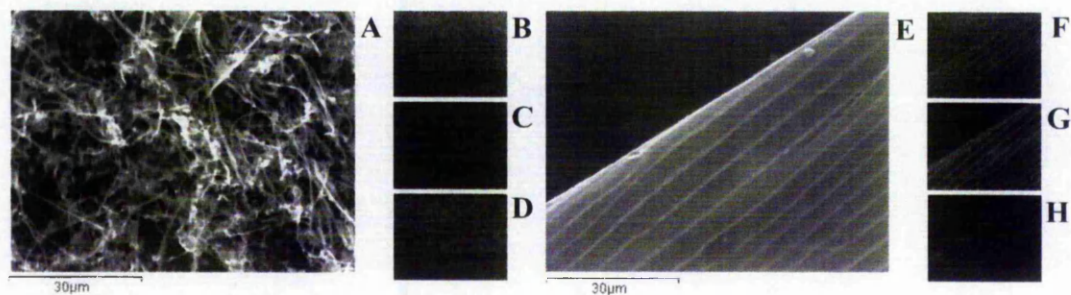


Fig. 10.19: (a)SEM image of the Al₁₃-mer-elastin 20mg/ml sample (A) centrifuged at 13000rpm for 30min and (E) Without preliminary centrifugation; elemental mapping of the same regions using respectively (B-F) OKα₁, (C-G) AlKα₁ and (D-H) ClKα₁ energies.

to demonstrate the position of the Al fraction within the filaments. Again similar observations are obtained in Al₃₀-elastin materials. Freeze-drying of pure Al₃₀-mer solutions leads to a mixed fibrous and sheet-like structure (Figure 10.20B) which progressively disappears at higher elastin concentrations in the non-centrifuged samples (Figure 10.21E).

Sheets with ribbons similar to those observed for pure hydroxide samples dominate

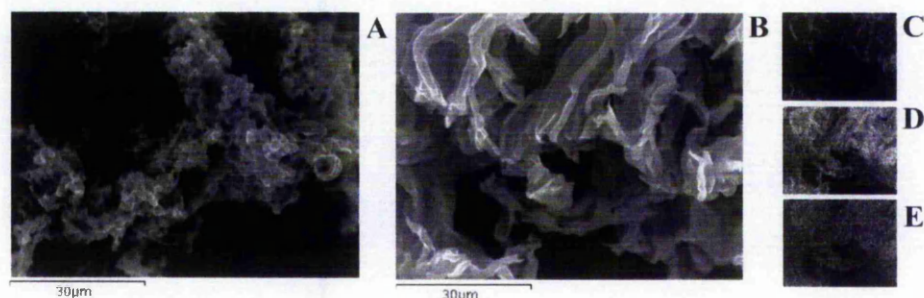


Fig. 10.20: SEM image of the pure Al₃₀-mer solid-state sample (A) after centrifugation treatment, (B) without centrifugation; elemental mapping of the region (B) using respectively (C) OK α_1 , (D) AlK α_1 and (E) ClK α_1 energies.

in non centrifuged samples, whereas filaments characteristic of elastin but presenting a high Al and Cl concentration are present in the centrifuged portion (Figure 10.21A).

10.3 Conclusions of Al-protein interactions study

Nanohybrid materials have been obtained by mixing aluminium hydroxide sols, as well as Al₁₃-mer or Al₃₀-mer solutions with varying amounts of BSA and soluble elastin. The composition and formation mechanisms of these materials have been investigated using various solution and solid-state characterization techniques. The chosen time scale of ageing of Al-protein mixtures (24 hours) allowed us to concentrate on the long-term interactions of Al species with proteins at conditions close to equilibrium.

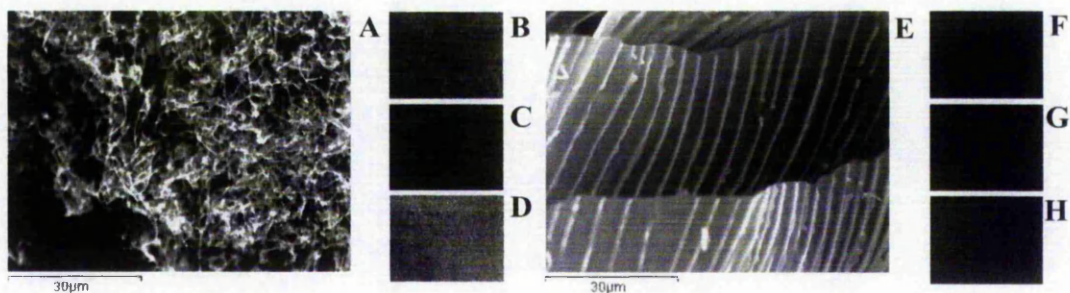


Fig. 10.21: (a) SEM image of the Al_{30} -mer-elastin 20mg/ml sample SEM image of the freeze-dried pure Al_{13} -mer sample (A) centrifuged at 13000rpm for 30min and (E) Without preliminary centrifugation; elemental mapping of the same regions using respectively (B-F) $\text{OK}\alpha_1$, (C-G) $\text{AlK}\alpha_1$ and (D-H) $\text{ClK}\alpha_1$ energies.

10.3.1 Al-BSA interactions

All five Al-containing precursors used in this study possess significant positive surface charge which correlates well with the initial pH of the corresponding solutions (suspensions) and decreases in the following order: Al_{30} -mer (pH=3.85) > Al_{13} -mer (pH=4.26) > Al hydroxide 1 (26nm, pH=4.61) > Al hydroxide 2 (55 nm, pH=4.73) > Al hydroxide 3 (82 nm, pH=4.75). The formal charges of Al_{30} -mer (+18) and Al_{13} -mer (+7) are known, while the exact charge on the Al hydroxides is not. The assumption of the charge variation of Al hydroxide suspensions was made intuitively, according to their mean particle sizes, which must be limited by the overall charge of the particles [11], as well as from initial pH values and a systematic character of the interactions with BSA observed in the present study.

The BSA molecule with isoelectric point at $\text{pH}\approx 4.67\text{--}5.0$ represents a very weak polyacid with relatively wide range of acidities of functional groups and, therefore, inhomogeneous distribution of negative charges [6]. This enables us to assume that in most cases studied in the present work the interaction between BSA and positively charged Al polycations or Al hydroxide nanoparticles is predominantly electrostatic. Electrostatic interaction presumably leads to coverage of BSA molecules by smaller Al polycations. The resulting particles are slightly larger than the original BSA molecules according to the DLS data (Figure 10.2C). The overall charge of these

agglomerates would depend on BSA concentration. At a certain point, when the concentration of BSA is high enough to partially cancel the charge of Al polycations, some properties of the system become similar to those of Al hydroxide, as evidenced indirectly by the identical morphology of the freeze-dried samples (Figure 10.9). However, unlike in Al hydroxide-BSA systems, the hybrid particles of Al polycations with protein remain soluble. Therefore, the charge on Al polycations adsorbed on the surface of BSA is still positive. The increasing concentration of BSA appears to force Al₁₃-mers, and especially Al₃₀-mers, to convert partially into Al hydroxide, apparently, as a result of an acid-base reaction. This is strongly supported by ²⁷Al solution NMR data showing progressive decrease of the concentration of soluble Al species (Figures 10.5, 10.6). We assume that Al polycations act as acids due to their high charge-per-Al atom ratio, while BSA acts as a base, which is possible, taking into account the heterogeneity of the functional groups on the surface of this protein [5, 6]. The possibility of acid-base interaction of Al polycations with BSA is also supported by the conductivity and DLS data (Figures 10.1A and 10.1C) indirectly indicating the formation of Al hydroxide with increasing concentration of BSA. Substantial decrease of conductivity and increase of detected particle sizes is observed. These changes are more profound for the Al₃₀-mer which is a stronger acid than for the Al₁₃-mer as follows from the lower formal hydrolysis ratio and pH of solutions of the Al₃₀-mer. The extent of Al hydroxide formation and its particle size should be limited, as follows from the absence of gelation and large aggregates, according to viscometry and DLS results (Figures 10.1C and 10.2C). Zeta-potential measurements of Al species-BSA systems generally support the predominantly electrostatic character of the interaction of Al polyoxocations and Al hydroxide with BSA. Correlation of increasing BSA concentration with decreasing zeta-potential indicates that the negative charge of BSA is being cancelled by either Al polyoxocations or Al hydroxide (Figure 10.3). When solutions containing Al polycations and BSA are forced into the solid state by freeze-drying, there is no significant change in Al speciation, as shown by ²⁷Al NMR spectroscopy after re-dissolution of freeze-dried materials in water (Figures 10.5A and B). Powder XRD provides a hint that crystallization of the Al₁₃-mer and Al₃₀-mer salts is suppressed in the presence of high

BSA concentrations (Figure 10.8). The overall result of interactions between BSA and Al hydroxide is most probably the formation of a hybrid material in which BSA molecules are adsorbed on the surface of larger Al hydroxide particles. This process is promoted by increasing BSA concentration, as supported by the dramatically growing average size of the mixtures (Figure 10.2), and higher values of viscosity and pH (Figures 10.1B and C). The conductivity of these model systems does not change in this case (Figure 10.1A), as there are practically no soluble Al species involved in the process. Measurements of free BSA concentrations indicate (Figure 10.4) that a large part of the protein is involved in the formation of a composite gel-like structure that was amorphous to X-rays after centrifugation and freeze-drying (Figure 10.8). Free Al concentration varies as a function of BSA content in a titration-like manner for all three Al hydroxide systems studied. Therefore, increasing amounts of BSA cover the surface of Al hydroxide particles gradually, neutralizing positive surface charge and creating suitable conditions for aggregation. Semi-quantitative thermo-gravimetric analysis (Figure 10.7) shows a systematic increase of the BSA content and a corresponding decrease of Al hydroxide in the freeze-dried samples with increasing BSA concentration (Figure 10.7D). However, this trend is not linear and reaches a 'steady state' above $\text{BSA} \approx 15 \text{ mg/ml}$. This data could reveal a 'saturation limit' of the surface coverage of Al hydroxide by BSA molecules. The fact that the largest particle size increase observed by DLS is for the system with smallest initial hydroxide particles (26 nm, Figure 10.2A) indicates that the surface area of the Al hydroxide particles (which is higher for the 26 nm suspension) plays an important role in the aggregation-gelation process induced by BSA. The value of pH also strongly affects the size of the resulting Al hydroxide-BSA aggregates (Figure 10.2B), formed as a result of predominantly electrostatic interactions. The scheme in Figure 10.22 serves to summarize the suggested mechanisms of interaction of various Al species and BSA and to relate them to the morphology of the freeze-dried materials. As follows from the scheme, Al hydroxide is gradually covered by BSA molecules and aggregation probably proceeds via protein molecules having their effective charge reduced to zero. In contrast, Al polycations cover the surface of BSA molecules leading to charged hybrid 'core-shell' particles with organic 'core'

and inorganic 'shell'. The positively charged 'shell' protects the hybrid particles from aggregation. These mechanisms of interactions are in a complex interplay with

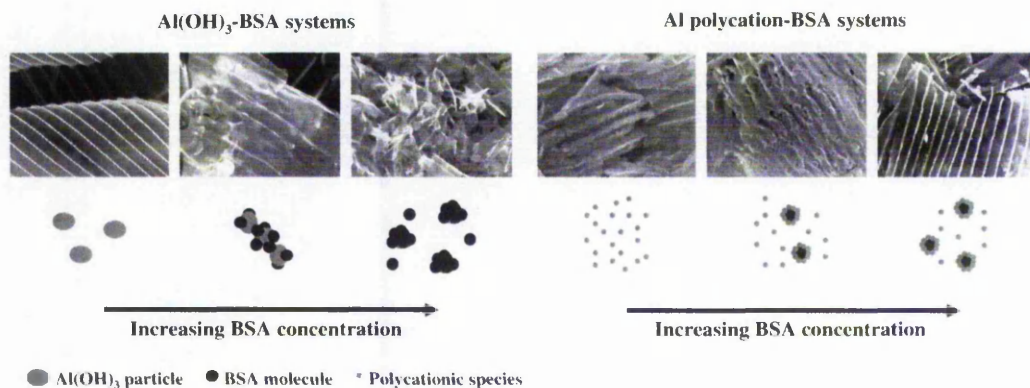


Fig. 10.22: Schematic representation of the interactions of BSA with various Al species.

the morphology of the resulting Al species-BSA materials. For Al polycation-BSA materials the morphology undergoes significant changes on increasing the amount of BSA present, being highly disorganized at low BSA content and becoming structured in two dimensions as very thin sheets with 'nano-ribbons' at higher BSA levels. The Al hydroxide-BSA system shows an opposite trend (Figure 10.22). Hydroxide particles become surrounded by adsorbed BSA molecules and at some point all hydroxide particles are separated from one another. This process results in the destruction of the 'nano-ribbon' morphology and complete 'randomization' of the solid materials at high BSA concentrations. In this case Al hydroxide particles are completely covered by BSA molecules and are separated from each other. Therefore, interaction between particles occurs through BSA layers. The occurrence of the nano-ribbon morphology which was reproducibly observed in pure Al hydroxide and Al polycation-BSA systems cannot be explained from a purely chemical or structural point of view. Perhaps, this morphology is, at least partially, a result of the freeze-drying process used for preparation of the solid materials. Nevertheless, the reproducibility of the pattern suggests its use as a 'fingerprint' of the systems from which this morphology was obtained.

10.3.2 Al-elastin interactions

Al-elastin samples were prepared using an experimental design similar to the one used for Al-BSA experiments. However the effects of an increase in elastin concentration on the properties of the systems are much less noticeable, with only a limited increase in the viscosity of the systems. SEM observation again provided evidence of the association of Al species with the protein, as demonstrated by the difference in morphology between the pure protein and the composite. In the case of the classical drying of Al-Elastin materials, elastin has enough time to aggregate and form filaments which are visible in the final material. These filaments have a large structural and toughening potential, elastin belonging to the class of bioelastomers. ^{27}Al NMR results demonstrated that elastin addition is leading to a much less extensive conversion of Al polycations into Al hydroxide than BSA, probably due to the weaker basicity of the bioelastomer, as pointed out by pH measurements. Further characterisation will be performed after redissolution of the freeze-dried materials in order to confirm Al speciation in the solid state samples characterised. Moreover TGA data for these systems is awaiting treatment, but clearly demonstrates the existence of composite materials in the fractions extracted by centrifugation. Especially in the case of Al hydroxide-based materials, the formation of this hybrid compound can be evidenced by the amount of protein sedimented with inorganic particles during centrifugation treatment (Figure 10.12), as well as by the increasing particle size (Figure 10.11) and viscosity observed (Figure 10.10).

The centrifugation treatment at 13000rpm proved to be efficient for the separation of Al hydroxide and Al hydroxide-elastin conjugates from the solution. However this treatment led to an inconsistency of SEM characterisation between Al-BSA and Al-elastin systems, whereas complementary observation without preliminary centrifugation enabled us to observe again a passage from random to 'nano-ribbon' morphology upon elastin addition in Al polycation-based systems (Figure 10.21). In the case of Al hydroxide-elastin samples, a very peculiar morphology was observed, in which elastin filaments appear to be present at the surface of Al hydroxide-based sheets (Figure 10.17).

In the case of Al-elastin interaction, only one Al hydroxide particle size and one sus-

pension pH has been considered. The studies will have to be extended to a broader range of conditions in order to demonstrate the likely effects of pH and particle size on the Al hydroxide-protein interaction.

These interactions observed are even more complex than when BSA is used, as soluble elastin demonstrates a strong tendency towards self-aggregation. The mechanism of protein aggregation can indeed be strongly affected by the addition of species bearing high surface charge such as Al polycations and hydroxide, as observed in studies devoted to interactions of the Al ion with other structural proteins.

BIBLIOGRAPHY

- [1] K. Shafran, O. Deschaume, and C. C. Perry, *Advanced Engineering Materials*, 2004, **6**(10), 836–839.
- [2] J. Novak and C. Park, *Water Science and Technology*, 2004, **49**, 73.
- [3] K. L. Shafran and C. C. Perry, *Journal of the Chemical Society, Dalton Transactions*, 2005, pp. 2098–2105.
- [4] A. Wright and M. Thompson, *Biophysical Journal*, 1975, **15**(2), 137–141.
- [5] J.-i. Anzai, B. Guo, and T. Osa, *Bioelectrochemistry and Bioenergetics*, 1996, **40**, 35–40.
- [6] K. Rezwan, L. P. Meier, M. Rezwan, J. Voros, M. Textor, and L. J. Gauckler, *Langmuir*, 2004, **20**, 10055–10061.
- [7] K. L. Shafran, O. Deschaume, and C. C. Perry, *Journal of Materials Chemistry*, 2005, **15**, 3415–3423.
- [8] J. W. Akitt, *Progress in NMR Spectroscopy*, 1989, **21**, 1–149.
- [9] L. Allouche, C. Gerardin, T. Loiseau, G. Ferey, and F. Taulelle, *Angewandte Chemie International Edition*, 2000, **39**(3), 511–514.
- [10] G. Johansson, *Arkiv For Kemi*, 1962, **20**(27), 321–342.
- [11] J. P. Jolivet, *From Solution to Solid State*, Wiley and Sons, 2000.

Part IV

CONCLUSIONS AND FURTHER WORK

In this part the most important findings of this PhD project will be assembled together with possible refinements and further work which should be undertaken to extend the present achievements. Clearly, most of the work undertaken, spanning Al-biomolecule interaction studies, optimisation of analytical techniques, development of data handling and mining algorithms, and the additional insight gained into the mechanisms underlying Al speciation would have been much less successful without the development of synthetic procedures for the obtaining of high purity Al species.

- *Ion exchange and the synthesis of model systems*

The preparation of Al chlorohydrate solutions was carried out over a range of hydrolysis ratios using a novel synthesis procedure implementing the use of ion exchange (Chap. 7). This experiment revealed the superiority of ion exchange for the synthesis of model Al species systems, including Al₁₃-mer and stable monodisperse hydroxide sols of low particle size (the smallest of the particles detected by our equipment being $\approx 20\text{nm}$). The resulting samples were characterised using a wide range of liquid and solid-state characterisation techniques including classical solution chemistry methods (potentiometry, conductometry, measurement of ion concentrations), a colloidal characterisation technique (DLS), together with ²⁷Al NMR. The yield of Al polycations synthesis, usually reaching 70-80% following a classical synthesis route to Al₁₃-mer, was found to exceed 95% by means of ion exchange, due to the softness and decaying base generation rate occurring during exchange time, in contrast to the case of classical techniques using liquid base addition, where local pH gradients account for the poor yields. The low yields obtained using classical techniques can be attributed to the early production of Al-hydroxide, which can be evidenced from ²⁷Al NMR and DLS. Our ion exchange synthesis of Al-based model systems received great interest from the industrial and academic community [1], it has been the object of several communications in international conferences, a publication [2] and an international patent [3].

Al₃₀-mer solutions and monodisperse Al-hydroxide preparations require the use of additional treatment after ion exchange for their synthesis to be performed. Al hydroxide requires aging for the desired particle size to be reached, whereas Al₃₀-mer

synthesis has to be carried out from high purity Al_{13} -mer solutions at elevated temperatures ($>70^\circ\text{C}$) in order to reach a full conversion after few days of treatment. Therefore, the optimisation of Al_{13} - Al_{30} conversion and monodisperse Al-hydroxide preparation has been the following stage of our work.

The preparation of Al_{30} -mer was carried out using temperature and hydrolysis ratios as optimisation parameters, an advanced data treatment of ^{27}Al NMR data enabling the monitoring of conversion mechanisms. For the first time, a broad signal at 10ppm, strongly overlapped with a similar signal from Al present in octahedral coordination in Al_{13} , and appearing upon build up of the Al_{30} -mer concentration was found to be proportional to the giant polycation concentration when data were analysed by independent peak fitting. This peak however does not reflect the totality of octahedrally coordinated Al within the structure but rather the Al atoms bridging two 'capped'- Al_{13} sub-units. Al_{30} -mer concentration evolution has been monitored at three different temperatures, enabling the calculation of the conversion activation energy, important for process optimisation. The large activation energies derived account for the slow reaction observed in the absence of heating. Activation energy combined with kinetic rate evolution upon variation in monomer concentration imply a direct role of these species in the conversion rather than a catalytic effect. Faster conversion rates were obtained for samples combining elevated Al_{13} -mer content and an initial Al monomer concentration sufficient to promote the efficient bridging of 'capped'- Al_{13} -mer units leading to the formation of Al_{30} . For these low hydrolysis ratios, a dynamic equilibrium appears to exist between Al_{13} -mer and Al monomer/Al oligomers, the concentration of the latter species remaining constant over the experiment time. At lower initial Al monomer concentrations, corresponding to higher h, this dynamic equilibrium is absent and most of the Al monomers produced by break-down of the Keggin structure do not reform to give the polycation in the absence of a sufficient concentration of the required species. Other reactions, and most probably the formation of the thermodynamically more stable hydroxide also occurs as demonstrated by a loss of signal under such conditions. Although the optimisation experiment enabled us to make interesting observations concerning Al_{30} -mer formation, the time span of the experiment did not enable us to

draw extensive conclusions regarding the conditions required for synthesis of larger species such as AlP_3 . However the formation of this species is favored at the lowest hydrolysis ratios studied, corresponding to the theoretical h of the species. The optimisation of AlP_3 synthesis and its full characterisation will therefore probably be part of our future challenges. From these results, prerequisites for the formation of Al_{30} -mer and larger species appear to be satisfied for hydrolysis ratios slightly lower than the hydrolysis ratio of Al_{13} -mer, some monomer and oligomers needing to be present, both to get a fast rate of reaction as a result of the bridging ability of Al monomers, and to compensate for the excessive break-down of Al_{13} -mer into its constituting parts at elevated temperature.

Further optimisation of the synthesis of monodisperse Al hydroxide suspensions was carried out in order to (a) speed up the synthesis processes, (b) reach desired particle sizes and (c) get further insight into the mechanisms of formation of the solid phase. For this purpose aging of hydroxide sols was performed at three different temperatures and aluminium concentration, starting from suspensions neutralised to different extents. The most reproducible results were obtained for partially neutralised solutions, apparently due to the lower viscosity of the sols in the presence of larger interparticle repulsion forces, leading to a free migration of the species feeding particle growth. In addition to the reproducible synthesis of Al hydroxide sols in the range 20-200nm, these studies enabled us to get further insight into the mechanisms leading to hydroxide particle growth in the presence of polycationic species. In the case of a partial neutralisation, the decrease in Al polycation concentration is correlated with an increase in the particle size of the Al hydroxide particles. This consumption of soluble species by the growth of the solid phase is enhanced at elevated temperatures but remains steady, avoiding secondary nucleation phenomena leading invariably to polydisperse sols. In the case of complete neutralisation, the Al polycations, initially absent from the medium, are slowly released from the solid phase as demonstrated by the ferron kinetic assay. After reaching a maximum, their concentration decreases, indicating that their production stops and they become a source of building blocks for the solid phase. The resulting sols were observed by means of TEM, demonstrating the hexagonal plate-like structure, these parti-

cles having the possibility to organise themselves in arrays as demonstrated from the formation of opal-like sols and by the direct observation of the stacking phenomenon by TEM and SEM. Nevertheless, the particles obtained bear an elevated surface charge (zeta-potential results), guarantee their stability in solution and the possibility of their organisation when brought into contact with oppositely charged building blocks or templates, such as the two proteins studied in the latter part of the project, or the organic polymers which will be studied in the future.

• *Optimisation of analytical techniques and data treatment algorithms*

Two techniques were optimised during this project for the characterisation of aluminium containing systems, and advanced data treatment techniques were emulated in both cases. Ferron kinetic assay and ^{27}Al NMR have been used for decades for the determination of Al speciation in various fields including soil science, cosmetology, biology and water treatment. However treatment and quantification of the data obtained using these two key techniques have still to be improved. We therefore developed data treatment algorithms including non-linear least squares minimisation for model optimisation, using information from the literature as well as our own expertise in the field for initialisation of the models, choice of the fitting functions and treatment steps as well as to protect our models from divergence. We especially addressed the issue of batch data processing, yet too poorly addressed in data treatment software but granting high-throughput analysis. On this basis, Ferron kinetic assay and ^{27}Al NMR analysis produced highly complementary and cross validated results.

Authors agree on the differentiation of at least four different aluminium fractions on the basis of the ferron kinetic assay, including Al monomers, Al_{13} -mer, Al oligomer, Al hydroxide and a slower reacting fraction appearing upon aging of an Al_{13} -mer solution. However variations in the kinetic constant for single species are observed despite the buffered conditions used for the assay, indicating the presence of additional species, or a lack of data treatment, proper data fitting techniques being rarely used at this end. We therefore decided to develop a data fitting algorithm enabling the treatment of sets of UV-Vis absorbance evolution curves, acquired in

order to monitor a dynamic process such as Al_{13} , Al_{30} or Al hydroxide formation. The algorithm uses an iterative fitting process of the whole dataset, enabling the kinetic constant and species concentrations to be allowed to vary to a large extent, but making the kinetic constants estimated for each species converge to a narrow range. The results of this approach were an increasing smoothness of the speciation patterns obtained, which became close to NMR characterisation results. In addition data treatment was made user-independent and therefore highly reproducible. To our knowledge the monitoring of Al_{13} - Al_{30} -mer conversion by means of the ferron assay, which gave results in excellent agreement with ^{27}Al NMR data, had not been carried out in the past. The use of the ferron assay enabled us to point out the existence of species or mechanisms inaccessible to ^{27}Al NMR, either due to peak broadness or to disturbance of the systems arising from elevated acquisition temperatures. Ferron kinetic assay is a precious alternative to NMR, giving the possibility to obtain from moderate cost equipment excellent speciation information, and preserving Al speciation. An excellent illustration of this is the observation of the intermediate species appearing upon Al_{13} -mer collapse and probably assembling to form the hydroxide phase.

^{27}Al NMR data treatment was also greatly improved during this project, the time of data treatment being drastically reduced by the introduction of automatic data treatment and peak fitting procedures. Starting from raw FID traces output by JEOL Delta data acquisition software, our data treatment algorithm carries out automatic apodisation, FFT, phasing of both narrow and broad spectral features observed from liquid-state ^{27}Al NMR, automatic referencing on the basis of the aluminate ion peak position, zero-filling and finally the simultaneous automatic fitting of 10 different peaks combined to baseline computation (31 parameters) for quantification of the corresponding species concentrations. The reduction of time devoted to data treatment enables the maximisation of data acquisition rate during kinetic runs, the best example of this algorithm application being the monitoring of Al speciation during Al_{30} -mer synthesis optimisation experiments mentioned earlier. In addition, we are currently developing a background subtraction algorithm to alleviate spectra from the contribution of the spectrometer hardware and NMR tube

Al content signal, effects causing large artifacts in the case of low Al concentration samples (biological samples).

Both in the case of ferron and NMR data treatment, an automatic estimation of the number of species or of the peaks number and positions, together with the statistical analysis of the species dependency using data mining techniques would be interesting additions to the present algorithms. In the case of NMR, 2D-correlation of the set of spectra could be carried out prior to fit to obtain an estimation of the peak numbers and positions, together with information concerning species relationships. For 2D-correlation we are already using a two-dimensional correlation package integrated in the MatLab environment, which greatly reduces the time required to compute correlation maps from large datasets. This algorithm can be readily included in the NMR treatment algorithm, the only missing link being the programming of reliable 2D peak-picking applicable to correlation maps.

- *Al-Biomolecules interactions: Novel materials from biomimetic routes*

In order to perform careful studies of the interactions triggering the production of hybrid Al-biomolecule composites, we decided to use a systematic approach, and examine separately the interactions of isolated species with the biomolecules of interest. This approach was successful in view of the variety and complexity of phenomena arising from the interaction of proteins with single Al species.

Our work was focused on two different proteins. BSA was chosen as a model negatively charged protein to enable a careful development of the different methodologies to be used for the characterisation of Al-protein systems and on the basis of preliminary screening experiments leading to positive results (gelation of the systems). Elastin was chosen due to its autoassembly and mechanical properties. The interaction of these proteins with Al species were characterised by means of potentiometry, DLS, conductometry, viscometry, and ^{27}Al NMR. The phase-separated materials were characterised by means of thermogravimetry, powder-XRD, SEM, and redissolved to check their Al speciation. The freeze-drying procedure used for obtaining the solid state materials proved to be a convenient technique for the quenching of dynamic processes and for the preservation of Al species in the solid state. In the

presence of an increasing BSA concentration, a strong gelation effect is observed in Al hydroxide-BSA systems, with an increase in primary particle size correlated to increases in viscosity and decrease in zeta-potential of hydroxide particles, proving the Al hydroxide-BSA association. This association can also be proven in the case of BSA-Al polycations systems. Again zeta potential measurements, carried out this time with respect to BSA molecules, verifies the association of the negatively charged protein to the positively charged polycations. For a high BSA concentrations, BSA acts as a stabiliser, the effect reflected both in particle size and viscosity evolutions. However BSA causes a destabilisation in the speciation equilibria which can be predicted according to the values of pH obtained in the Al polycations-BSA systems. The effect is especially marked in the case of Al₃₀-BSA systems, where a 10-20% decrease in polycation concentration is evidenced from ²⁷Al NMR for the highest BSA concentration explored. We interpreted this observation by the formation of Al hydroxide upon BSA addition, the supposition being in accordance with the morphology of the resulting dried materials. The strong effect of BSA on Al₃₀ concentration can be explained by the higher acidity of Al₃₀ compared to Al₁₃, BSA acting meanwhile as a soft base. The decreasing area of the peaks observed may as well arise from a broadening effect upon BSA binding or interaction with the polycationic species. This broadening would give rise to a more perceptible effect on broader peaks. The existence of a bioinorganic composite was demonstrated by both liquid-state (DLS, Zeta potential measurements) and solid-state characterisation (TGA) in the case of Al hydroxide-BSA. Interesting sheet/ribbon morphology materials were obtained from Al/BSA systems, which will require further characterisation including mechanical testing.

The effect of Elastin on the model systems was much milder, and the interactions of the protein with Al species resulted only in a limited increase in the viscosity of Al-hydroxide-elastin systems. The association of the protein with Al species is however a reality as demonstrated from protein concentration measurements carried out both on liquid samples after centrifugation of the phase-separated materials and on the separated solids after freeze-drying and TGA analysis. SEM observation again provided evidence of the association of Al species with the protein, as demonstrated

by the difference in morphology of the pure protein and of the composite. In the case of the classical drying of Al-Elastin materials, elastin has enough time to aggregate and form filaments which are visible in the final material. These filaments have a large structural and toughening potential, elastin belonging to the class of bioelastomers.

From our results, Al polycationic species and Al hydroxide were confirmed to be true building blocks of high stability and surface charge, able to assemble with oppositely charged entities such as proteins, and form intricate structures on the basis of simple, water-based synthesis under mild conditions. For the synthesis of Al hydroxide and pure Al ceramic materials, polycations can provide a slow monomer release feeding the growth of particles (Chap. 9). Tuning their conversion to hydroxide by means of temperature variation of alkali addition rate, different hydroxide particle sizes can be achieved, the monodispersity and stability of the resulting suspensions being comparable to results obtained from the alkoxide synthesis routes. Al polycations can be crystallised as their chloride salt, and undergo a conversion to Al hydroxide both in the solid state or with intermediate soluble species under specific conditions, but can also be assembled with other polyoxometallates [4, 5] or organic molecules [6], leading to the formation of 3D structures or particles. The species synthesised during the present project have therefore a true potential for the biomimetic synthesis of novel materials. The analogy between the materials synthesised and biomaterials such as nacre is clear, especially in the case of elastin-Al-hydroxide materials, based on the auto-assembly of hexagonal sheet-like ceramic precursors with a bioelastomer having high structure-reinforcing potential. However properties such as toughness and scratch-resistance of our materials need to be assessed both on bulk materials and after coating on a suitable substrate.

In addition to materials science, the work carried out is valuable and necessary to many domains of application or study of Al species, due to the paradox existing between the widespread use of Al-based materials and the ignorance of their role or effect on natural processes. The methodology developed during this project for the characterisation of Al-protein interactions will therefore be used for extended studies in a more biological context, the resulting materials being considered for their

materials applications. Further work will be performed to obtain a more extensive characterisation of the organic component of the systems. We hope this goal will be achieved by working in parallel on the characterisation of simple organic molecules and proteins included in our model systems.

BIBLIOGRAPHY

- [1] W. H. Casey, *Chemical Reviews C*, 2006, **106**(1), 1–16.
- [2] K. L. Shafran, O. Deschaume, and C. C. Perry, *Journal of Materials Chemistry*, 2005, **15**, 3415–3423.
- [3] Process of preparing aluminium species-unilever patent j3797, copyright europe, 05252011.1/epo5252011 Technical report, European Patent Office, 2005.
- [4] J. H. Son and Y.-U. Kwon, *Inorganic Chemistry*, 2003, **42**, 4153–4159.
- [5] J.-H. Son, H. Choi, and Y.-U. Kwon, *Journal of the American Chemical Society*, 2000, **122**, 7432–7433.
- [6] N. Sanson, F. Bouyer, C. Gerardin, and M. In, *Physical Chemistry, Chemical Physics*, 2004, **6**, 1463–1466.

APPENDIX

Publications, proceedings and patents

1. O. Deschaume, K. Shafran and C. C. Perry, Interactions of bovine serum albumin with aluminum polyoxocations and aluminum hydroxide, *Langmuir*, Submitted.
2. K. Shafran, O. Deschaume, C. C. Perry, The static anion exchange method for generation of high purity aluminium polyoxocations and monodisperse aluminium hydroxide nanoparticles, *J. Mater. Chem.*, 2005, 15, 3415-3423.
3. Process of Preparing Aluminium Species-Unilever Patent J3797, copyright Europe, March 2005, 05252011.1/EPO5252011.
4. O. Deschaume, K. Shafran, C. C. Perry, Bio-inspired Nano-materials on the Basis of Giant Aluminium Polycations and Proteins, Nano and hybrid coatings conference proceedings, January 2005.
5. K. Shafran, O. Deschaume, C. C. Perry, High-Temperature Speciation Studies of Al-Ion Hydrolysis, *Adv. Eng. Mater.*, 2004, 6(10), 836-839.

Posters and Presentations

1. Al Polycations as Precursors to Aluminium Hydroxide Colloids, oral presentation, Euromat 2005 conference, 09/2005, Prague, Czech Republic.
2. Synthesis of Model Aluminium Polycation-Containing Solutions and Solid Materials, poster and oral presentation, Keele meeting, 02/2005, Brussaco, Portugal.
3. Bio-inspired Nano-materials on the Basis of Giant Aluminium Polycations and Proteins, oral presentation, nano and hybrid coatings, 01/2005, Manchester, United Kingdom.
4. Preparation of Model Aluminium Polycation Solutions and Solids, poster and oral presentation, Junior Euromat, 09/2004, Lausanne, Switzerland.
5. Spectrophotometric Assay for Aluminium Speciation studies in Aqueous Solution, poster presentation, School of Science seminar, 06/2004, Nottingham, United Kingdom.
6. High-temperature speciation studies of Al-ion hydrolysis, oral presentation, Euromat 2003, 09/2003, Lausanne, Switzerland.